

---

# Improved Methods for Functional Neuronal Imaging with Genetically Encoded Voltage Indicators.

---

Peter Quicke

*Supervised by*

Professor Simon R. Schultz, Professor Mark Neil,  
& Professor Thomas Knöpfel

*A thesis submitted in partial fulfillment of the requirements  
for the degree of Doctor of Philosophy*

*in the*

Department of Bioengineering,  
Imperial College London

## **Declaration of Authorship**

I declare that, except where explicitly acknowledged, this thesis and the work presented within is my own, done under the guidance of my supervisors and mentors and with the help of my collaborators.

## Copyright Declaration

The copyright of this thesis rests with the author. Unless otherwise indicated, its contents are licensed under a Creative Commons Attribution-ShareAlike 4.0 International (CC BY-SA).

Under this licence, you may copy and redistribute the material in any medium or format for both commercial and non-commercial purposes. You may also create and distribute modified versions of the work. This on the condition that: you credit the author and share any derivative works under the same licence.

When reusing or sharing this work, ensure you make the licence terms clear to others by naming the licence and linking to the licence text. Where a work has been adapted, you should indicate that the work has been changed and describe those changes.

Please seek permission from the copyright holder for uses of this work that are not included in this licence or permitted under UK Copyright Law.

“[...] In a scientific pursuit there is continual food for discovery and wonder.”

Mary Shelley, *Frankenstein; or, The Modern Prometheus*. 1818

## **Improved Methods for Functional Neuronal Imaging with Genetically Encoded Voltage Indicators.**

by Peter Quicke

Voltage imaging has the potential to revolutionise neuronal physiology, enabling high temporal and spatial resolution monitoring of sub- and supra-threshold activity in genetically defined cell classes. Before this goal is reached a number of challenges must be overcome: novel optical, genetic, and experimental techniques must be combined to deal with voltage imaging's unique difficulties.

In this thesis three techniques are applied to genetically encoded voltage indicator (GEVI) imaging. First, I describe a multifocal two-photon microscope and present a novel source-localisation control and reconstruction algorithm to increase scattering resistance in functional imaging. I apply this microscope to image population and single-cell voltage signals from voltage sensitive fluorescent proteins in the first demonstration of multifocal GEVI imaging. Second, I show that a recently described genetic technique that sparsely labels cortical pyramidal cells enables single-cell resolution imaging in a one-photon widefield imaging configuration. This genetic technique allows simple, high signal-to-noise optical access to the primary excitatory cells in the cerebral cortex. Third, I present the first application of lightfield microscopy to single cell resolution neuronal voltage imaging. This technique enables single-shot capture of dendritic arbours and resolves 3D localised somatic and dendritic voltage signals. These approaches are finally evaluated for their contribution to the improvement of voltage imaging for physiology.

## *Acknowledgements*

I am incredibly lucky to have had the privilege of learning from and working with so many fantastic scientists. I would first like to thank my supervisors: each one has provided a different perspective and rich experience, without which none of this could have happened.

I would like to thank Simon Schultz for instigating the whole project and welcoming me into his lab. I am extremely grateful for him encouraging me to get stuck in to lab work and not worry about breaking things (too much!). His infectious enthusiasm has cultivated a fantastic lab culture and enabled me to develop and explore my interests.

I would like to thank Mark Neil for his optics expertise. His advice invariably leads me to things I have never explored, leaving me excited and with lots to understand. Mark re-kindled my interest in optics and modelling and his first mention of RL deconvolution has inspired literally tens of thousands of hours of computing!

I would also like to thank Thomas Knöpfel - the GEVI guru. I will never forget the first GEVI transients I imaged in his lab, or how he taught me to play lego with genetics. He provided me with my first opportunity to build a microscope which has clearly left quite an impression! It is fantastic to work with someone who finds such obvious joy in their work.


I would also like to give particular thanks to Amanda Foust, who took me under her wing and whose mentorship has allowed me to flourish. Among an infinity of things she taught me to patch cells, point lasers, and paint slices. Most importantly, when all else fails: get a bigger laser! I look forward to seeing her as an astronaut.

I am really grateful to everyone in the Schultz, Knöpfel, and Foust labs, you all have been a pleasure to work with. Caroline Copeland, Subhojit Chakraborty and Renaud Schuck really helped me to settle in and showed me the ropes, Yu Liu is unfailingly friendly and helpful, an organisational machine and PCR master, and Chenchen Song is a husbandry expert and all round VSFP expert. Kate Hobson's logistical skills and bureaucracy navigation support has been invaluable. Thank you all so much! Massive shoutouts in particular to Carmel Howe and Jeevan Soor for both the science and the social - may the katsus continue!

Science is great because you get to work with experts in so many different things. Thanks so much everyone who worked with me on different projects, in particular Srdjan Antic, Pier Luigi Dragotti, and their lab members, especially Steph Reynolds, Pingfan Song and Herman Verinaz Jadan.

I would like to thank the many nodes of the CX1 cluster for their hard work churning through my data - without you all I would still be waiting for my results. I'm sorry you had to redo it so many times because of my mistakes. I also need to thank the contributors to the amazing open source software that fuelled this thesis - Python, Numpy, Scipy, tiff file, neo, ImageJ, etc... I hope to contribute someday.

I have been funded by a CDT studentship from the EPSRC Centre for Doctoral Training in Neurotechnology for Life and Health (EP/L016737/1) and would like to gratefully acknowledge this support.

Thanks to the pit 'o snayks a.k.a ULF, Deathhard Crüe and all me mates for your support, even when I was a recluse. You are the best bunch around <sup>1</sup>.

My family are an endless well of love and support and I am so lucky to have them - thank you so much Mum, Dad, Ellie and Tim.

Finally I would like to dedicate this thesis to my favourite beamlet, Emma. I couldn't have wished for a better partner to share my life with. I look forward to the next chapter!

# Contents

<b>Declaration of Authorship</b>	<b>1</b>
<b>Abstract</b>	<b>4</b>
<b>Acknowledgements</b>	<b>5</b>
<b>1 Introduction</b>	<b>14</b>
1.1 Thesis outline	14
1.2 Overview	15
1.3 Optical sensing of neural activity	19
1.3.1 Fluorescent imaging of neural activity	21
1.3.2 A comparison of calcium and voltage indicators	23
1.3.3 Genetically Encoded Indicators	26
Genetically encoded calcium indicators	26
Genetically encoded voltage indicators	27
1.3.4 Optogenetic expression strategies	30
1.4 Optical Microscopy & its application to Neuroscience	33
1.4.1 Optical Imaging Fundamentals	33
Resolution in Microscopy	35
Quantum description of light	36
1.4.2 Imaging in biological tissue	36
<i>In vivo</i> vs slice scattering	37
1.4.3 Functional imaging techniques in neuroscience	38
Two Photon Scanning Strategies	43
Two photon parallelisation approaches 1: Fluorescence excitation constraints	44
Two photon parallelisation approaches 2: techniques	47



	8
1.4.4	Light field imaging . . . . . 48
1.4.5	Deconvolution . . . . . 53
1.5	Advanced optical methods in GEVI imaging: state of the art . . . . . 55
<b>2</b>	<b>Methods</b> . . . . . <b>57</b>
2.1	Introduction . . . . . 57
2.2	Slice preparation . . . . . 57
2.2.1	Solutions . . . . . 58
2.2.2	Protocol . . . . . 59
<b>3</b>	<b>Multifocal Two-photon Microscopy</b> . . . . . <b>60</b>
3.1	Introduction . . . . . 60
3.2	Development and testing of a source localisation algorithm . . . . . 60
3.2.1	Introduction . . . . . 60
3.2.2	Methods . . . . . 62
	Multifocal two-photon setup . . . . . 62
	Image reconstruction . . . . . 65
	Analysis of depth penetration . . . . . 68
	Modeling the effect of foci separation on contrast at depth . . . . . 68
	Preparation of brain slices for functional imaging . . . . . 69
	Analysis of calcium imaging videos 1: Pixel crosstalk . . . . . 70
	Analysis of calcium imaging videos 2: Signal-to-noise ratio . . . . . 71
3.2.3	Results . . . . . 73
	Source localization increases contrast at depth . . . . . 73
	Source localization decreases functional crosstalk . . . . . 74
	Source localization's impact on PSNR is labeling and frame rate dependent 75
3.2.4	Conclusion . . . . . 78
3.3	Multifocal two-photon voltage imaging . . . . . 79
3.3.1	Introduction . . . . . 79
3.3.2	Methods . . . . . 81
3.3.3	Results . . . . . 82
	Predictions of laser performance . . . . . 82
	Voltage responses are resolved at sub optimal excitation wavelengths . . 84

	2P voltage signals are larger than 1P voltage signals . . . . .	86
3.4	Chapter Conclusion . . . . .	86
<b>4</b>	<b>Wide-field single-photon voltage imaging with sparse indicators</b>	<b>89</b>
4.1	Introduction . . . . .	89
4.2	Methods . . . . .	94
4.2.1	Animals . . . . .	94
4.2.2	Slice Preparation . . . . .	94
4.2.3	Imaging . . . . .	94
4.2.4	Image analysis . . . . .	95
	Frame rate analysis . . . . .	96
	Crosstalk analysis . . . . .	96
	Experimental autocorrelation measurements . . . . .	98
4.3	Results . . . . .	100
4.3.1	Voltage imaging with densely and sparsely targeted GEVIs . . . . .	100
4.3.2	Signal-to-noise ratio . . . . .	102
4.3.3	Effect of sampling rate . . . . .	104
4.3.4	Signal spread . . . . .	108
4.4	Discussion . . . . .	110
4.5	Chapter conclusion . . . . .	113
<b>5</b>	<b>Lightfield voltage imaging</b>	<b>114</b>
5.1	Introduction . . . . .	114
5.2	Methods . . . . .	119
5.2.1	Light field microscope design . . . . .	119
	Light field microscope misalignment . . . . .	119
5.2.2	Imaging . . . . .	122
5.2.3	Light field reconstruction . . . . .	124
	Lightfield PSF calculation . . . . .	124
	Volume reconstructions . . . . .	132
5.2.4	Volume time series analysis . . . . .	133
	Effect of reconstruction on SNR . . . . .	133
	Comparison of light field and wide-field SNR . . . . .	133

5.3	Results . . . . .	133
5.3.1	Light field microscopy enables simultaneous imaging of axially separated dendrites. . . . .	133
5.3.2	Comparison of the effect of different reconstruction methods on SNR . . .	134
5.3.3	Comparison of wide-field and light field SNR . . . . .	137
5.3.4	Light field microscopy resolves 3D localised voltage signals . . . . .	137
5.4	Conclusion . . . . .	141
5.5	Prospects for synaptic mapping . . . . .	143
<b>6</b>	<b>Conclusion and future directions</b>	<b>145</b>
6.1	Summary of novel contributions . . . . .	148
6.2	List of publications arising from this thesis . . . . .	148
	<b>Bibliography</b>	<b>150</b>
<b>A</b>	<b>Copyright permissions</b>	<b>169</b>

# List of Figures

1.1	Poisson noise and SNR . . . . .	22
1.2	The difficulties of voltage imaging . . . . .	23
1.3	FRET-based voltage indicators . . . . .	25
1.4	GEVI lineages. . . . .	28
1.5	The Cre - Lox system. . . . .	31
1.6	Tissue optical properties . . . . .	38
1.7	Imaging in three dimensions . . . . .	39
1.8	One- and two-photon excitation . . . . .	41
1.9	Light field microscope diagram . . . . .	49
1.10	Light field images . . . . .	50
1.11	Synthetic refocusing . . . . .	52
3.1	The multifocal apparatus. . . . .	63
3.2	Optical characteristics of the multifocal array. . . . .	64
3.3	The source localization process. . . . .	67
3.4	Characterization of the increased depth penetration from source localization. . . . .	72
3.5	The predicted effect of changing foci separation on depth penetration. . . . .	73
3.6	Source localization decreases the functional crosstalk between adjacent neuronal structures. . . . .	74
3.7	The effect of source localization on PSNR is labeling and frame rate dependent. . . . .	76
3.8	Multifocal two-photon voltage imaging . . . . .	80
3.9	VSFP-Butterfly two-photon excitation spectra . . . . .	83
3.10	Two-photon voltage responses . . . . .	85
3.11	Comparison of one- and two-photon voltage responses. . . . .	87
4.1	Comparison of densely and sparsely expressed GEVIs. . . . .	93

4.2	d-Cre modulated sparse expression strategies enable single-cell resolution functional imaging. . . . .	99
4.3	Imaging reveals dendritic structure . . . . .	101
4.4	Signal and noise levels. . . . .	103
4.5	Effect of frame rate on SNR and spike timing estimation. . . . .	105
4.6	Theoretical treatment of sampling rate. . . . .	109
4.7	Signal spread. . . . .	111
5.1	Light field microscopy of sparse GEVI cells . . . . .	118
5.2	Light field chromatic aberration . . . . .	120
5.3	Light field misalignment . . . . .	123
5.4	PSF calculation method . . . . .	126
5.5	Numerical PSF calculation . . . . .	128
5.6	Modelled and measured PSFs . . . . .	131
5.7	Comparison of the effect of different reconstruction methods on light field SNR. . . . .	135
5.8	Comparison of light field and wide-field SNR. . . . .	136
5.9	Light field microscopy resolves 3D localised voltage signals. . . . .	138
5.10	Mapping dendritic signals. . . . .	140

# List of Tables

2.1 Na-ACSF recipe. . . . .	58
2.2 Secondary Na-ACSF recipe. . . . .	58
2.3 NMDG-ACSF recipe. . . . .	58
2.4 Intracellular solution recipe. . . . .	59
4.1 Sparse imaging SNR results. . . . .	104

## Chapter 1

# Introduction

### 1.1 Thesis outline

This thesis describes novel optical approaches in neuroscience which were developed with the aim of enabling slice synaptic connectivity measurement with voltage indicators. The main results are included in four relatively self-contained chapters, of which two chapters are adapted from journal publications.

The introduction discusses important concepts in optics, neuroscience and genetics that help to motivate many of the methods and techniques used and developed in this thesis. It also surveys and describes some of the general literature relevant to the broader concepts in the thesis. Further deeper and more specific literature surveys are included along with results in relevant chapters. The second chapter describes general methods which can be referred to from the results chapters so as to minimise the need for repetition of descriptions.

The first results chapter describes the design and build of a multifocal multiphoton microscope along with a novel image acquisition and analysis technique to improve performance at depth in scattering samples by reducing functional crosstalk and increasing image contrast. This technique is tested using an acute brain slice preparation with neurons containing the functional calcium dye Cal-520 (Tada et al., 2014). This section is adapted from results published in Quicke et al., 2018. The multifocal microscope system is then tested to explore whether it can be used to image excitatory post-synaptic potentials (EPSPs) in slices in conjunction with the VSFP family of genetically encoded voltage indicators (GEVIs). This would be advantageous over 1-photon excitation due to the greatly reduced bleaching caused by 2P microscopy enabling 3D search for EPSPs. Different laser systems and excitation wavelengths are explored to try and find the most efficient excitation regime for voltage sensors with the Förster resonant

energy transfer (FRET) pair consisting of mCitrine-mKate2. We compare the signal size when using 1- and 2-photon excitation and compare aggregate and single cell signals. We conclude from these experiments that 2-photon excitation generates insufficient emission flux to resolve single cell signals with anywhere near the signal-to-noise required to resolve EPSPs.

In the second results chapter we show that a novel sparse transgenic expression strategy enables single cell voltage signals to be resolved in densely packed neuronal classes such as cortical pyramidal cells. We use 1-photon standard epifluorescent microscopy and measure the spatial localisation of signal in scattering tissue. We also discuss optimal sampling rates for voltage indicators under different imaging conditions. This chapter is adapted from results published in Quicke et al., 2019.

In the third results chapter we present the first use of light field microscopy to image single-neuron voltage signals in brain slices. We show that voltage imaging with light field indicators enables single-shot 3D imaging of axially separated dendrites in GEVI expressing cells. We introduce a novel method for calculating light field microscope PSFs for high NA objective lenses. We discuss SNR and examine the feasibility of measurement of EPSPs using this technique.

In the final chapter we will summarise the novel contributions of this thesis and discuss future prospects of GEVI connectivity mapping.

## 1.2 Overview

Is intelligence an emergent property? Single neurons act in some ways as complex integrators, spiking in response to the summation of synaptic inputs from many other cells. The properties arising from networks of such neurons depend critically on the properties of the synaptic connections. In nature, the way cells connect together can be seen to change over timescales from milliseconds to years (Tetzlaff et al., 2012; Weishaupt, 2016). The dynamics and statistics of this likely underpin learning and behaviour, pathological states, and everything that we experience.

Attractor networks formed from recurrent neural networks are an intriguing model of mental function dating back to Hopfield (Hopfield, 1982). In this theory patterns of neural activation form stable states that could represent memories, and neuronal computation is an emergent property of connected cells (Yuste, 2015). Connectivity is fundamental to neural networks;



attractor dynamics arise from recurrent activation of sets of neurons that are strongly connected (Amit, 1989).

To test theories like these we need to interrogate cellular interconnections on a large scale. Neurons are anatomically connected if there is a synapse linking them. This connectivity can be measured by testing if voltage responses in post-synaptic neurons are elicited by action potentials in pre-synaptic neurons (Reyes et al., 1998). The gold standard for measuring this connectivity is paired- or multi- patch recordings, an extremely low throughput and challenging technique where multiple neurons are patched simultaneously. Action potentials (APs) are evoked in one cell and any post-synaptic response is measured in the others. This has provided fascinating insights into, for example, how local connectivity patterns differ from random networks (Song et al., 2005), however the technical challenge of performing these experiments has precluded the gathering of large datasets spanning different cortical areas. The difficulty of the experiments increases dramatically when increasing the number of patch-clamped cells, with no more than twelve simultaneous recordings currently mastered with considerable effort (Perin, Berger, and Markram, 2011).

Alternative methods to measure synaptic connectivity include non-functional techniques such as electron microscopy (Denk and Horstmann, 2004), synaptic reconstitution of green fluorescent protein (GFP), (called mGRASP, Kim et al., 2012) and viral synaptic tracing (Ginger et al., 2013). Electron microscopy can directly image the synaptic cleft and vesicles in the presynaptic terminal, however reconstructing tissue volumes is extremely time consuming due to the exceptionally fine resolution. mGRASP uses genetic expression of non-fluorescent split GFP molecules which can reconstitute over the synaptic cleft, enabling visualisation of synaptic terminals with fluorescence microscopy. Viruses and some small molecules can be used to infect the presynaptic or postsynaptic terminals of cells at a specific location, before they travel antero- or retrogradely to the somata of the terminals (Oztas, 2003). This labels the input or output of specific brain areas. Alternatively, some viruses such as rabies can naturally travel across synaptic connections (Ginger et al., 2013; Ugolini, 2010), labelling whole circuits. These non-functional techniques are able to identify the presence of synapses but cannot determine if the synapse is functional, although they can be combined with, e.g., optogenetic channel expression for functional mapping. In addition, histological techniques cannot measure the strength of the synaptic input or the dynamics of facilitation and depression (Zucker, 2006) in response to pulse trains and paired pulses.

Good progress has been made by combining optical stimulation of pre-synaptic cells with electrophysiological readout of post-synaptic response, techniques which require patch-clamping a single cell and inducing action potentials in pre-synaptic cells via optogenetic (Pala and Petersen, 2015; Hooks et al., 2011) or uncaging based (Boucsein, 2005; Schnepel et al., 2015) actuation. These measurement techniques can, more quickly than traditional electrode methods, measure the strength of incoming synaptic connections onto a single cell. A disadvantage is that as the membrane voltage of the presynaptic cells is not being monitored, and the optical stimulation can be non-specific (although techniques continue to improve, e.g. Baker et al., 2016), it is uncertain exactly what activity is causing the post-synaptic response. Secondly, with glutamate uncaging methods ascertaining the functional class of the stimulated pre-synaptic cell would be exceptionally difficult. Finally, glutamate uncaging studies are also unable to investigate facilitation and depression.

It has recently been suggested (Antic, Empson, and Knöpfel, 2016) that a different optical technique, voltage imaging using GEVIs, could offer a complementary view of connectivity by mapping the synaptic targets of a single cell. A single cell in an area of tissue labelled with voltage indicators could be patched and action potentials elicited, and the readout of post-synaptic response could be achieved through optical monitoring of the voltage signal. This cannot replace the full control enabled by whole cell recordings, but can offer massively increased throughput for a subset of measurements made by them. In particular, optical recording of synaptic input avoids space-clamp issues inherent to electrode recordings (Anastasiades, Marques-Smith, and Butt, 2018), where synaptic inputs are attenuated between the synapse and the recording location at the soma. Additionally, the specific location of the synaptic input onto the dendritic arbour provides additional information unobtainable without troublesome multi-patch electrophysiological experiments. Synaptic input location on the dendritic arbour affects activity induced synaptic plasticity changes (Sjöström and Häusser, 2006), and this location information is collected automatically whilst imaging voltage.

During this project we aimed to test new optical imaging methodologies with a view towards this scientific application. A number of barriers need to be overcome to achieve this goal. As we shall see, voltage imaging is a challenging electrophysiological technique. Sophisticated genetic and optical tools are required to maximise GEVI utility. This thesis describes the application and testing of a number of such techniques with an aim to find a suitable combination to enable simple and robust GEVI assisted synaptic mapping.

This would enable us to address, for example, how synaptic strength varies with distance from the pre-synaptic cell. Schnepel et al., 2015 looked at this question using glutamate uncaging for presynaptic stimulation and found a weak anti-correlation between distance and input strength in input connectivity. This technique is not fine grained enough to distinguish individual cells in the optical stimulation and cannot identify the cell class of the input cells - it could be stimulating a mixture of excitatory and inhibitory cells. GEVI based techniques would resolve this ambiguity through intrinsic cell-class specific labelling. GEVI synaptic mapping could also enable us to more easily test if the distribution of output connectivity differs from the input connectivity in a neural network, which is predicted as a marker of networks at maximal storage capacity (Brunel, 2016).

Over this next chapter we will describe the state of the art in the field of GEVI voltage imaging alongside a description of fundamental concepts and the field-specific background. Throughout this chapter we will motivate many of the design choices and describe most of the trade-offs behind the techniques used to obtain the thesis results.

We start with a discussion of fundamental concepts in cellular neuroscience and continue with a brief overview of electrophysiological instrumentation. We then focus on optical sensing of neural activity, introducing fluorescent activity sensors and compare and contrast the two main types: calcium and voltage sensors. We then introduce genetically encoded indicators, which have revolutionised neuroscientific functional optical imaging, and survey the different expression strategies which, particularly for voltage imaging, affect what they can be used for.

Having described the sample to be imaged, we then switch gears and discuss the optical set up. We again start with fundamentals, describing how physical and geometric optics arise from classical electromagnetic theory and can be used to describe and understand different aspects of imaging. We then discuss how imaging in complex biological tissue differs from the linear, isotropic and homogeneous medium often assumed in physical systems, and how we can approximate the propagation of light through it by bulk scattering and absorption coefficients. We survey broadly the classes of imaging techniques in neuroscience from 1-photon wide-field imaging to 2-photon laser scanning microscopy. Of particular interest to this thesis are two-photon parallelisation approaches and light field microscopy, and these are described in more detail. Finally, as it arises a number of times throughout this thesis, we give a brief description of deconvolution in imaging and describe the motivation behind a particular approach, Richardson-Lucy deconvolution.

### 1.3 Optical sensing of neural activity

The desire to understand neuronal physiology has driven the creation of a vast range of instrumentation. Studying neurons from the cellular to the systems level requires measuring, directly or indirectly, the neuronal membrane potential. The membrane potential is the difference in electrical potential between the extracellular space and the inside of the neuron, caused by concentration gradients of ionic species and maintained by selective active transport of ions into and out of the cell. The membrane potential varies due to the effect of ion channels in the membrane which can be sensitive to chemicals or the membrane potential itself. Voltage sensitive ion channels lead to neurons being electrically excitable, where an increase in the membrane potential can lead to an action potential, where the membrane potential transiently rapidly increases before returning to baseline. Action potentials can be thought of as the output of neuronal cells; neurons are structurally polarised, and can be divided into three parts: the input area, called dendrites, the cell body and the output connection, the axon. Neurons receive input from other cells onto their dendrites and cell bodies, and if the input causes a depolarisation above their action potential threshold, they will fire an action potential which initiates in the axon initial segment, propagates back into the soma and dendrites, and propagates forward through the axonal arbour. The axonal arbour forms contacts called synapses onto the dendrites, somata, or axons of other neurons. When an action potential reaches a synapse the membrane depolarisation triggers release of neurotransmitter molecules which diffuse across the synaptic cleft to the post-synaptic cell. These molecules activate ligand-gated ion channels, which then depolarise or hyperpolarise the postsynaptic cell depending on the channel type, and so the cycle continues.

The membrane potential of single cells can be measured with good signal-to-noise ratio (SNR) and temporal resolution through whole cell current clamp recordings. To do this a glass microelectrode filled with a solution mimicking the internal contents of the cell is placed in contact with the cell. The electrode adheres to the cell membrane, forming a gigaohm seal, and the patch of membrane inside the electrode is perforated by a pulse of suction. This provides electrical continuity between the inside of the glass electrode and the inside of the cell. The current flowing through the cell membrane at a specific membrane voltage ('voltage clamp') or the voltage across the cell membrane in response to a specific current injection ('current clamp') can then be measured for the cell.

Alternatively, electrodes can be inserted into the extracellular matrix surrounding cells to measure local potential differences that can be related to either bulk ion flow due to populations of electrically active cells (the 'local field potential'), or currents associated with the firing of individual neurons ('multi-unit activity'). This enables the recording of the activity of multiple cells at the loss of the exquisite precision and resolution of whole cell recording.

Whilst electrode-based methods of measuring bioelectric signals have proven incredibly useful, there remain significant fundamental limitations which have prompted the development of other techniques. The electrical contact required means that sensing is either highly invasive (e.g. multi-electrode arrays and patch electrodes) or highly non-specific (e.g. electroencephalograms). Remote sensing of neuronal activity-linked signals have been explored to overcome some of these limitations using electromagnetic radiation from many different parts of the spectrum. The blood oxygen level depletion (BOLD) signal, associated with increased neuronal metabolic activity and therefore probably action potential firing, is measured using radio-frequency radiation during functional magnetic resonance imaging using radio frequency magnetic fields (Grover et al., 2015). Positron emission tomography (PET) can also measure the BOLD signal by detecting gamma rays emitted from positron-electron annihilations and can also detect radio-labelled ligands of neuronal receptor subtypes (Jacobs et al., 2003). These methods are able to indirectly measure neuronal activation through their slow metabolic consequences deep inside even large organisms, but suffer from poor temporal and spatial resolution.

Optical-frequency radiation provides a powerful tool with which we can probe neural activity. Visible light enables us to resolve structures the size of neuronal processes, is manipulated relatively easily, and is minimally intrinsically toxic. Optical signals relating to underlying neuronal processes can be almost as fast as the processes themselves, with the limiting factor the specific dye or imaging technique used. As a species we rely on vision as our primary sensory modality; it seems natural to use the same frequency light to probe deeper into nature.

The first functional neuronal optical imaging experiments in the 1940's and '50s measured the changes in the scattering and birefringence of crustacean nerve fibre bundles or squid giant axons during action potential (AP) firing (Hill and Keynes, 1949; Hill, 1950; Bryant and Tobias, 1952; Cohen, Keynes, and Hille, 1968), since determined to be caused by swelling due to water influx into interstitial spaces (Foust and Rector, 2007). These changes, although following fairly faithfully simultaneous membrane voltage measurements, are extremely small ( $\sim 10^{-5}$

for scattering and  $\sim 10^{-4}$  for birefringence (Cohen, Keynes, and Hille, 1968)), and so require averaging across thousands of trials to resolve. Secondly, these measurements are mainly suited for thin *ex vivo* preparations such as excised nerves as they are measured in transmission.

Fluorescence, the emission of light by a substance excited by absorption of light, radically increased the scope of functional imaging in neuroscience. Fluorescence emission is isotropic, enabling the 'epifluorescent' imaging configuration in thick biological samples, where the excitation and emission light are delivered by a single objective. The discovery of the first voltage and calcium sensitive dyes (Davila et al., 1973; Tsien, 1980; Shimomura, Johnson, and Saiga, 1962) lead to a revolution in optical physiology by providing direct and indirect fluorescent readouts of electrophysiological activity.

### 1.3.1 Fluorescent imaging of neural activity

Voltage sensitive dyes offered a tenfold increase in sensitivity to membrane potential, enabling single-sweep recording of APs in individual neurons (Davila et al., 1973). Much work has been done since improving voltage sensitive dyes in order to improve their brightness, sensitivity and membrane targeting, widening their applicability (Kulkarni and Miller, 2017). A necessary (but likely not sufficient!) condition for creating an understanding of the function of the brain is likely to be the simultaneous monitoring and perturbation of all neurons in the intact brain of an organism during behaviour. Optical imaging has already got us part way to this goal through calcium imaging of *C. Elegans* (Prevedel et al., 2014; Nguyen et al., 2015), although whole-brain, single-cell resolution electrophysiological control is still to be achieved.

The design and improvement of fluorescent indicators since their first invention has enabled these achievements. The SNR in functional fluorescent imaging is inextricably linked to the brightness and sensitivity of the indicator to the process monitored (see Box 1). Imaging with a brighter or more sensitive sensor enables faster frame rates whilst maintaining SNR. Individual sensor fluorophore brightness does not vary much with the type of indicator (with notable exceptions discussed in section 1.3.3), as in organic indicators the fluorescent motifs are often similar, and genetically encoded indicators are generally based on similar fluorescent proteins. The sensitivity does vary widely depending on the type of sensor used due to different physical and biological mechanisms and constraints. The sensitivity of fluorescent indicators is often characterised by the fractional change in fluorescence in response to a relevant physiological event, such as a 100 mV change in membrane potential for a voltage indicator, or a

## 1: The Fundamental Limit on SNR in Optical Imaging

The statistical nature of photon detection places a limit on the maximum achievable SNR for functional optical imaging. Fluorescent indicators transduce a change in their environment into a change in their fluorescence brightness, leading to a change in the mean rate of photons detected. We would like to accurately estimate the relative fluorescence intensity,  $F$ , at a rate fast enough to resolve the dynamics of our indicator. Reducing the variance of the intensity reduces the number of samples required to estimate it within a certain accuracy. The probability of detecting  $k$  photons in a certain interval when the mean rate is  $\lambda$  is given by the Poisson distribution,

$$P(F = k|\lambda) = \frac{e^{-\lambda}\lambda^k}{k!}. \quad (1.1)$$

Both the expected value and the variance of  $F$  are equal to  $\lambda$ . Our signal,  $S$ , is given by  $\Delta F$ , the change in fluorescence brightness, and so our signal to noise ratio is given by

$$SNR = \frac{S}{\sigma} = \frac{\Delta F}{\sqrt{F}} = \frac{F' - F}{\sqrt{F}} \propto \sqrt{F}. \quad (1.2)$$

This is illustrated in the figure below. Two traces have been generated by drawing samples from a Poisson distribution with a rate increased by 10% in the central samples. The top trace shows a baseline brightness of 10000 counts/sample, whilst the bottom trace has only 1000. The SNR is clearly increased by a factor of  $\approx \sqrt{10} \approx 3$  in the top trace. The right hand graph shows theoretical maximum achievable SNR for a given brightness, for different relative changes in fluorescence from the signal of interest,  $\Delta F/F_0$ . This treatment assumes all other noise sources, such as detector read noise or fluctuations in illumination intensity as negligible, commonly true in the high brightness regime.

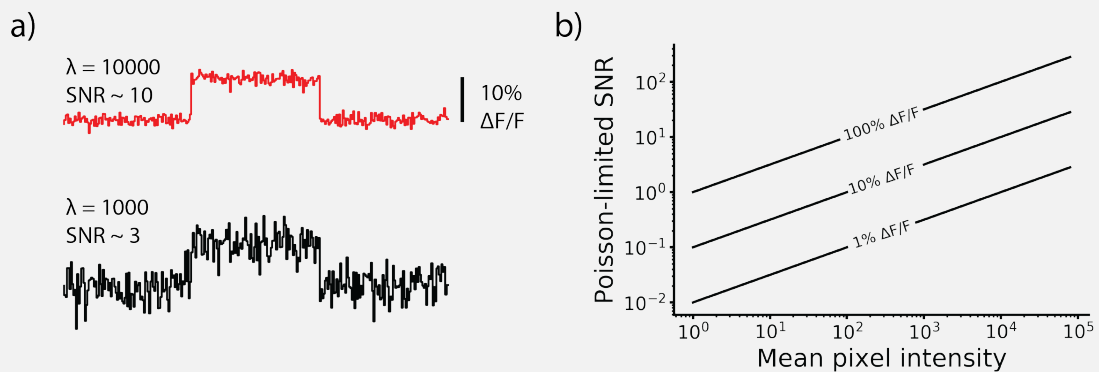


**Figure 1.1:** Demonstration of the effect of Poisson noise on SNR.  
Inspired by Djurisic et al., 2003.

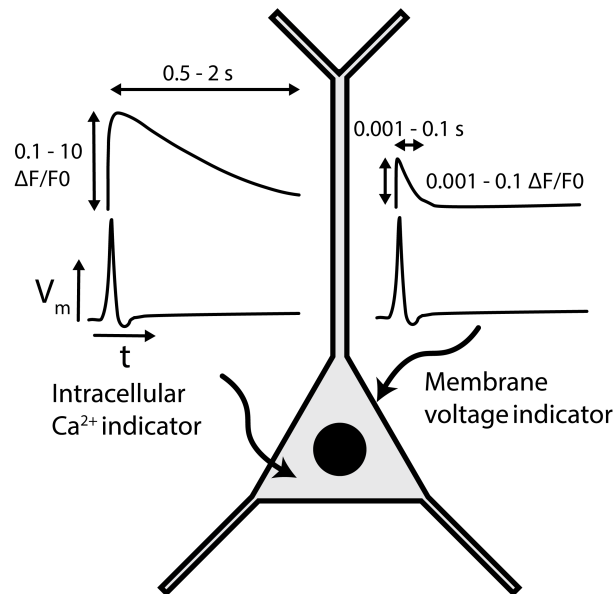


**Figure 1.2: The challenges of voltage imaging** Three issues make voltage imaging more challenging than calcium imaging. Firstly, faster intrinsic kinetics limit the photon integration period. Secondly, voltage indicators must lie in the membrane or degrade the signal; this limits the volume of indicators that can be integrated to measure the signal. Lastly, membranes where signal arises are tightly packed in the brain; fluorescent signals from overlapping membranes wash out single-cell signals.

single spike calcium transient for a calcium indicator. This fractional change,  $\Delta F/F_0$ , is defined as  $(F - F_0)/F_0$ , where  $F$  is the maximum (or minimum) fluorescence intensity during the event and  $F_0$  is the baseline intensity. In the following section I compare the two most commonly used classes of functional sensors and their sensitivity.

### 1.3.2 A comparison of calcium and voltage indicators

Although membrane potential is of primary interest when developing an electrophysiology alternative, voltage indicators have not become the most widespread sensors of neuronal activity. A number of challenges are faced by investigators attempting to use voltage indicators, summarised in Figure 1.2. Firstly the kinetics of the physiological signals involved are fast; action potentials occur on the order of milliseconds and therefore the optical signal must be sampled at a high rate. This limits the available photon integration time, demanding brighter indicators for adequate SNR as discussed in Box 1.

Secondly, the indicators must be confined to the membrane. Membrane potential changes by around 100 mV during an action potential, leading to a change in the electric field across the 3 nm thin plasma membrane of around  $3 \times 10^7$  V/m. Although this field is large, a molecule must lie across a cell's external plasma membrane to be affected. This limits the performance



of voltage indicators in multiple ways. The plasma membrane molecular density is limited by the possibility of physiological disruption. Increasing the number of charged or polarisable molecules in the plasma membrane increases membrane capacitance and can abolish action potentials altogether if too many are present (Blunck, Chanda, and Bezanilla, 2005). Secondly, high membrane affinity dyes or poorly targeted genetic constructs are prone to stain all membranes, including internal membranes that see no changing field. This increases the background without increasing the voltage dependent signal, decreasing the SNR.

Thirdly, membranes from adjacent cells overlap in the microscope depth of field, mixing their signals. Single cell voltage transients are 'washed out' by the bright background fluorescence excited from other cells. This problem is discussed at length in Chapter 4, where a genetic technique is shown to overcome it.

Calcium indicators have become ubiquitous in neuroscience as indirect indicators of AP firing as they do not suffer from many of the drawbacks associated with voltage indicators. These molecules modulate their fluorescence when they bind free  $\text{Ca}^{2+}$  ions. In many neurons, AP firing is accompanied by a rapid influx of  $\text{Ca}^{2+}$  ions into the cell, which can be 'amplified' by the release of internal stores (Berridge, Lipp, and Bootman, 2000). Calcium indicators can report this change in intracellular concentration and thereby indirectly report on neuronal firing patterns. Intracellular  $\text{Ca}^{2+}$  concentration can rise by an order of magnitude after an action potential and the rise decays slowly compared to membrane voltage, taking hundreds of milliseconds (Berridge, Lipp, and Bootman, 2000; Kulkarni and Miller, 2017). This effective low pass filter of supra threshold electrical activity enables longer integration times without signal aliasing, increasing photon counts per sample. As calcium concentration changes throughout the soma many calcium indicators can be loaded into a cell, meaning many more fluorophores can report the signal, increasing the signal brightness. These factors combine to make imaging calcium with a high SNR in neurons a much easier prospect than imaging membrane voltage.

Despite their widespread use, calcium indicators have significant drawbacks that limit their applicability to some questions. Calcium transients are not exclusively linked to action potential firing in all neurons (Grienberger and Konnerth, 2012; Manita, Miyazaki, and Ross, 2011; Miyazaki, Manita, and Ross, 2012). The slow kinetics of both indicators and physiological calcium concentration dynamics, although beneficial for imaging, limit the accuracy of estimation of underlying electrophysiological activity even when the link between APs and calcium

transients is clear. Indicator saturation, intrinsic and indicator buffering, and diffusion biophysics further complicate the link between indicator brightness and electrophysiology. As the technology for increasing indicator concentration has developed, pathology due to unwanted calcium buffering from indicators has also been reported (Steinmetz et al., 2017). Perhaps most significantly, although calcium indicators can be used to image calcium influx related to synaptic events (Bloodgood and Sabatini, 2007), when imaging in the soma they can only be relied upon to report on supra threshold activity, and are non-responsive to the sub threshold activity which causes it. These factors have spurred investigators to develop better optical, chemical, and biological techniques for imaging voltage in neurons.

## 2: Förster resonance energy transfer: FRET

Chromophores where the excitation spectrum of one overlaps the emission spectrum of the other can undergo Förster resonance energy transfer (FRET), where energy is non-radiatively transferred from the chromophore with the larger transition energy (the donor) to the other (the acceptor) (Förster, 1965). For fluorescent molecules this process is illustrated in the Jablonski diagram in the figure below. The donor is excited with blue light; the molecule can either emit a fluorescence photon or transfer energy to a nearby acceptor. FRET probability is highly sensitive to the donor and acceptor's separation,  $r$ , and relative orientation, with the efficiency scaling as  $1/r^6$ . Measurement of the relative proportion of donor and acceptor fluorescence emission in response to donor excitation enables estimation of the relative separation and orientation of the fluorophores. This mechanism has found widespread application in detecting protein co-localisation in biological samples and has also been used in the design of voltage and calcium sensors in neurons. Attaching two fluorophores to a calcium or voltage sensitive protein such that the FRET efficiency is modulated as the protein changes in response to physiological events provides a readout of these underlying processes.

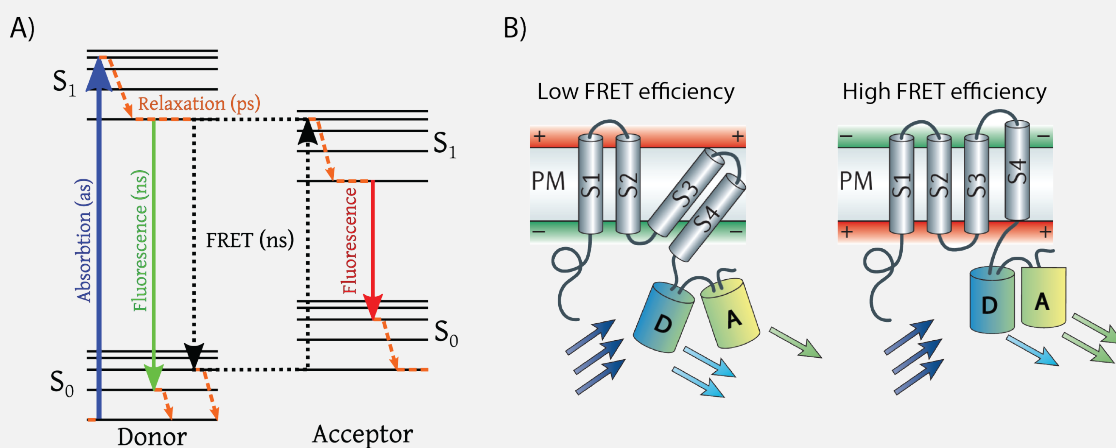


**Figure 1.3:** a) A Jablonski diagram of FRET.<sup>a</sup> b) A voltage indicator based on FRET.<sup>b</sup>

<sup>a</sup>By Alex M. Mooney, CC BY-SA 3.0.

<sup>b</sup>Reprinted by permission from: Nature, Nature Reviews Neuroscience, "Genetically encoded optical indicators for the analysis of neuronal circuits", Knöpfel, 2012

### 1.3.3 Genetically Encoded Indicators

Genetically encoded indicators offer many advantages over organic dyes loaded into cells. Organic dye loading methods generally fall into two different categories - bulk loading, where a large volume of tissue is indiscriminately labelled with an indicator that crosses cell membranes, and single cell loading, where a patch pipette is used to fill the interior of a single cell with a dye. Bulk loading enables labelling of multiple cells, but also results in large background staining of non-neuronal structures and interstitial tissue. This background contributes photons, and therefore noise to the recording without signal and so decreases SNR. Furthermore, the cell type being recorded is unknown unless further experimental steps are taken. The background labelling is particularly troublesome in multi-cell voltage imaging. The voltage signal arises from cells' plasma membranes, which, in a non-specifically labelled preparation, overlay each other. Recording from a single cell's membranes is virtually impossible and so bulk loaded voltage indicators can generally only be used for population imaging. Single cell labelling via patch pipette, on the other hand, labels a single cell without affecting the surrounding tissue. Although identification of the loaded cell type still requires further steps, single cell responses with high SNR are easily seen, even with low SNR voltage dyes. The drawback, however, is that each cell to be labelled must be patched, limiting experimental throughput. Genetic strategies can overcome many of these issues by hijacking cellular protein synthesis to generate indicator molecules.

#### Genetically encoded calcium indicators

The first widely used calcium dyes were synthetic and developed specifically for the purpose (Tsien, 1980). Interestingly, the first fluorescent protein was also the first genetically encoded calcium indicator (GECI). Green fluorescent protein (GFP), discovered in the jellyfish *Aequorea Victoria* in the 1960s (Shimomura, Johnson, and Saiga, 1962), had a fluorescent yield sensitive to the local calcium concentration, however the sensitivity was too low to use in its raw form. After the demonstration that its heterologous expression induced fluorescence in cells (Chalfie et al., 1994) and that mutations greatly improved the spectral and fluorescent properties of the protein (Heim, Cubitt, and Tsien, 1995) its usage became widespread as a non-functional marker. The first synthetically designed genetically encoded calcium sensor, Cameleon, was

developed by fusing mutant fluorescent proteins derived from GFP, the calcium binding protein calmodulin, and the calmodulin binding peptide M13 (Miyawaki et al., 1997). When  $\text{Ca}^{2+}$  ions bound to the calmodulin the two fluorescent proteins (FPs) were brought closer together, increasing the FRET efficiency (see box 2) and changing the emission spectrum.

Since then, there have been multiple rounds of optimisation of existing calcium sensor designs and development of novel sensors (Knöpfel, 2012). The most prominent among the sensors are the GCaMP family (Nakai, Ohkura, and Imoto, 2001), whose latest iterations come in a host of different varieties to suit large number of experimental paradigms and whose sensitivities can be over 100% for a single action potential (Chen et al., 2013; Dana et al., 2018). As this thesis focuses on GEVI voltage imaging, I shall not discuss the different GECIs in depth, but will survey the different GEVIs in detail in the next section.

### Genetically encoded voltage indicators

The first genetically encoded voltage sensor was developed in 1997 (Siegel and Isacoff, 1997). Since then a number of different GEVIs have been developed based on a variety of voltage sensing principles (Fig. 1.4, Xu, Zou, and Cohen, 2017; Knöpfel, 2012). Within the last year especially fantastic advances have been made in the field of GEVI design and, along with advanced transgenic expression strategies, *in vivo* GEVI imaging is poised to become a widespread tool for studying physiology, as calcium imaging has. *In vivo* single-cell resolution imaging of multiple cells is the goal of GEVI development, and requires bright signals from sparse but strongly expressing cells to overcome shot noise and signal mixing from overlapping membranes as discussed above. Until fairly recently, GEVI imaging was limited to population signals *in vivo*, however key advances have been made that have enabled imaging of  $\sim 30$  cells simultaneously in layer 2/3 of the mouse cortex *in vivo* (Abdelfattah et al., 2018).

GEVIs can be classified into two subgroups according to their protein lineage (Xu, Zou, and Cohen, 2017, Fig. 1.4a). The first group consists of fluorescent proteins fused to a voltage sensing domain (VSD) arising either from ion channels or a voltage sensing phosphatase protein (Murata et al., 2005). The voltage sensing protein can be fused to a FRET pair, a circularly permuted fluorescent protein or surprisingly even a lone fluorescent protein to transduce the conformational change in the VSD to a change in fluorescence brightness. Of these GEVIs the VSFP family has been extensively used in intact brain tissue (Lundby, Akemann, and Knöpfel, 2010; Empson et al., 2015; Mishina et al., 2014; Akemann et al., 2012), both in slice and *in vivo*,

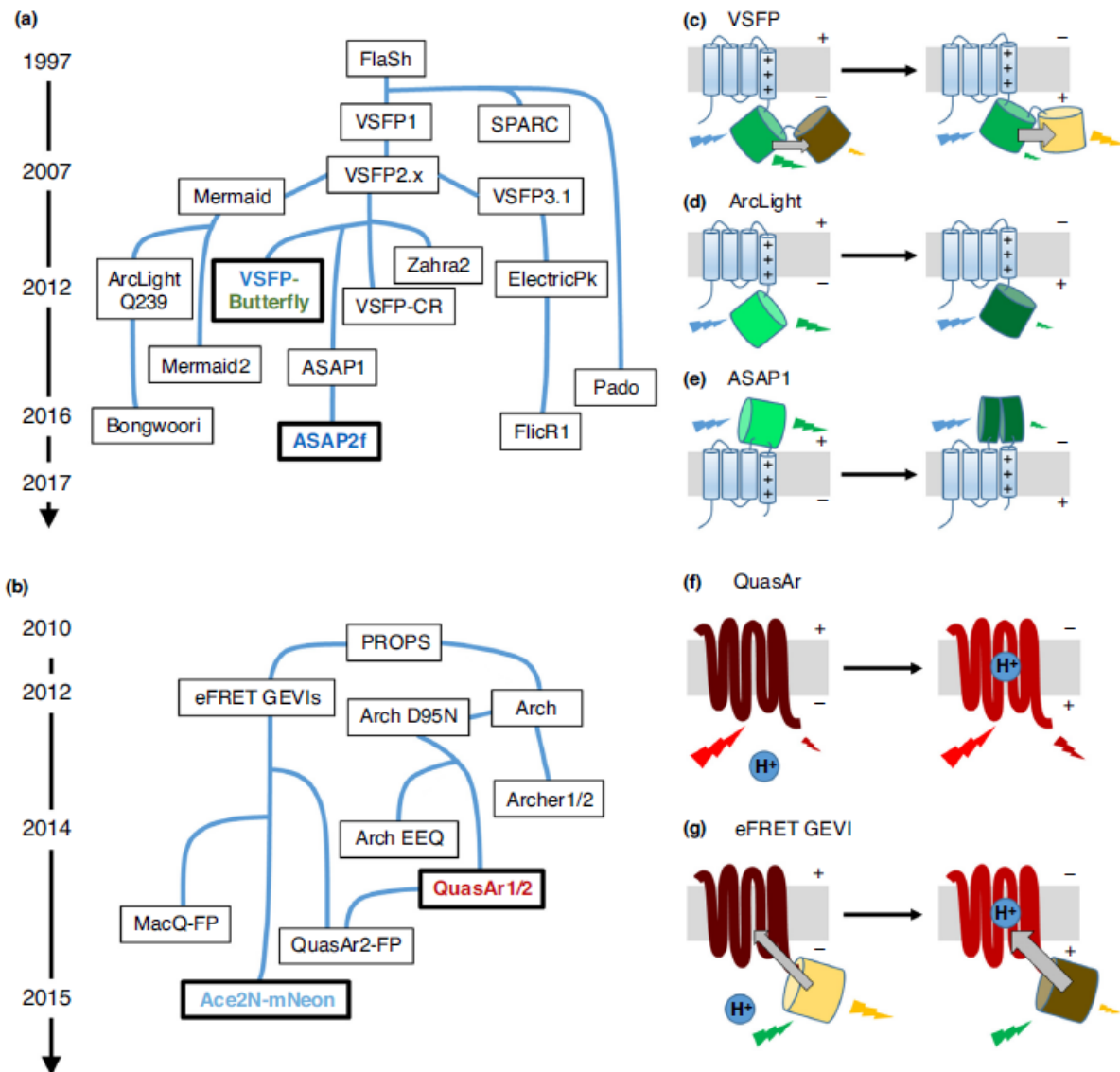


**Figure 1.4: GEVI types and lineages.** a) The first GEVI family translate conformational change of a voltage sensing domain into a change in the fluorescent yield of a single fluorescent protein or FRET efficiency of a pair of proteins. The GEVIs used in this study, variants of VSFP-Butterfly, come from this family. b) The second family use the intrinsic voltage sensitivity of microbial rhodopsins to report voltage. These offer increased sensitivity, but are very dim in their basic form. Fusing a fluorescent protein to the rhodopsin (as in g) greatly increases the brightness of these probes. Reprinted from Current Opinion in Chemical Biology, 39, Xu, Zou and Cohen, Voltage imaging with genetically encoded indicators, 1-10, Copyright (2017), with permission from Elsevier.

although without single cell resolution. The latest VSFP protein, nirButterfly (Monakhov et al., 2019), fluoresces in the near infrared, improving scattering resistance, and enables single trial AP detection in cultured cells, although its use has not been demonstrated in intact mammalian tissue. The recently reported dimeric GEVI Ilmol is also a promising new candidate, despite not having been shown to function *in vivo* (Yi et al., 2018). ASAP3 has been used to image at single cell resolution at different depths in layer 1 and layer 2/3 in mouse cortex simultaneously using two-photon excitation and has fast kinetics due to it being based on a circularly permuted FP (Chavarha et al., 2018). This family of voltage sensors suffers from slower kinetics and low sensitivity to voltage fluctuations compared to the next, but has the advantage of the use of bright fluorescent proteins.

The second family derive their voltage sensing ability from microbial rhodopsin proteins (Kralj et al., 2011a). Originally studied for their use in neuronal optogenetic control, they were also shown to exhibit endogenous voltage sensitive fluorescence that could report voltage changes when expressed in mammalian neurons (Kralj et al., 2011b). These sensors exhibit much higher sensitivity and faster kinetics than FP-based sensors, however they are extremely dim and so require phenomenally high excitation intensities (up to  $1000 \text{ W/cm}^2$  (Adam et al., 2018)) to generate enough signal photons to resolve voltage signals. The exemplar GEVIs of this type are Archon (Piatkevich et al., 2018), which in its soma-restricted version (Piatkevich et al., 2019) enabled imaging of up to 8 cells simultaneously *in vivo*, and paQuasar3 (Adam et al., 2018), which enabled imaging of up to 3 cells simultaneously *in vivo*. These GEVIs are seriously limited in intact brain tissue by the power requirements of the illumination; each cell requires around 5 - 10 mW of illumination power to generate enough signal photons to resolve their fast kinetics with high SNR. This limits the number of cells both by maximum available laser power, but also tissue heating and photodamage, especially *in vivo*.

Fusing a FP to the rhodopsin improves signal brightness without slowing the indicator kinetics. The FP undergoes electrochromic FRET (eFRET) with the bacterial rhodopsin when it undergoes membrane-depolarization induced spectral changes, varying the brightness during neuronal activity. Notable GEVIs of this family include Ace2-mNeon (Gong et al., 2015), which has been shown to report single cell action potentials in mouse cortex *in vivo*, VARNAM (Kannan et al., 2018), a redder and more sensitive eFRET GEVI, and the very recently reported Voltron (Abdelfattah et al., 2018), which uses a synthetic dye as the FRET donor, greatly improving the photostability and brightness. The latter is the most promising of the new GEVIs

and is the first and only GEVI so far to demonstrate imaging of large numbers of cells (around 30) in the mouse cortex *in vivo* at single cell resolution.

Genetic manipulations are required to induce cells to ectopically express GEVIs or GECIs, and particularly advanced manipulations are required to enable voltage imaging due to the increased challenges. It is possible to bring to bear a wide range of genetic tools to control spatio-temporal expression patterns. In the next section I will discuss these and their relative advantages and disadvantages.

### 1.3.4 Optogenetic expression strategies

The power of optogenetics derives not only from relatively non-invasive monitoring and activation, but also from the increasingly precise control of their expression within both cell classes and the individual cells themselves. In order to induce a cell to ectopically express a particular optogenetic protein, the recombinant DNA encoding the protein must be introduced into the cell. At the most basic level, short lengths of gene fragments encoding the protein of interest ('plasmids' (Finbarr Hayes, 2003)) can be introduced into cells by perfusing the cells with them whilst permeabilising the cell membrane either chemically, physically or electrically (Kim and Eberwine, 2010). If the recombinant DNA is properly designed the DNA fragments are transcribed by the cell, which then expresses the encoded protein. This type of expression is simple and requires no organism germ-line manipulation but is not hereditary and is highly variable to the transfection conditions. Furthermore, physical or chemical access to the cell is required to introduce the DNA.

A second approach to induce expression in cells is to use viruses' naturally evolved mechanisms to hijack cells' protein synthesis machinery. Viruses introduce foreign DNA into cells as part of their natural reproductive cycle. DNA encoding optogenetic proteins can be packaged into a virus and introduced into the brain, where they infect cells and transduce protein expression. This allows protein expression in an area localised to the introduction site, and multiple viruses or transgenic lines can be combined to take advantage of the intersectional strategies discussed below. Viruses can be injected to a specific location in the brain through a craniotomy, or engineered to cross the blood-brain barrier (Chan et al., 2017). Viruses do not require breeding, however if injected they cannot drive brain-wide expression and require invasive surgery in order to deliver them. Intravenous delivery of the virus enables brain wide expression, but struggles to deliver the viral load necessary to drive high enough expression

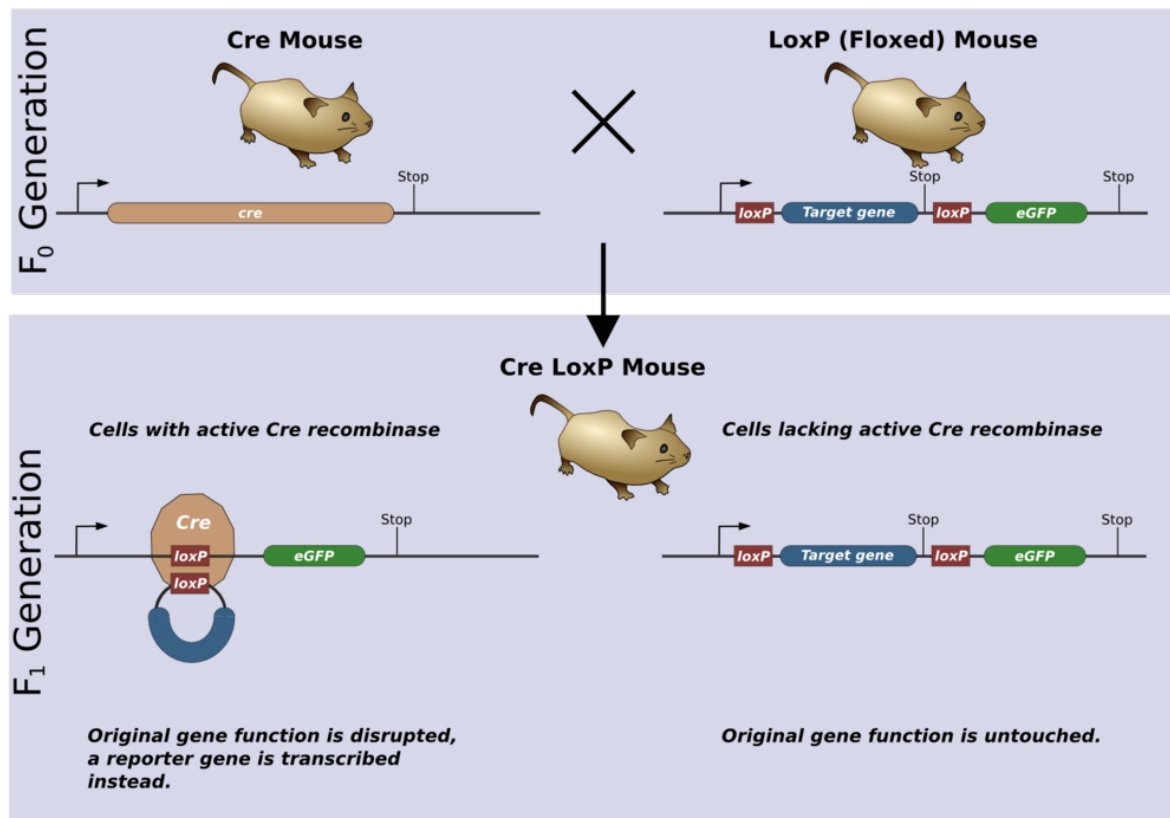


**Figure 1.5: The Cre-Lox system.** Strong non-specific promoters can drive expression in subsets of cells via intersectional Cre-Lox targeting. Mice expressing *cre* under a weak, cell type specific promoter are crossed with a mouse with a ‘floxed’ stop codon preventing expression of a downstream cassette. In cells expressing Cre recombinase the enzyme removes the floxed gene, enabling transcription of the downstream sequence.

By Matthias Zepper CC BY-SA 3.0.

for functional studies, and so has not been used for optical physiology. The expression from both delivery methods is also time limited, as the viral transfection can be cytotoxic (Kim and Eberwine, 2010).

A third approach is to generate a transgenic organism, where recombinant DNA is introduced into the organisms germline so that it is passed on to descendants. A colony of organisms can be set up to generate multiple transgenic generations. Doing this means that all cells in the organism carry the DNA encoding the protein of interest. Different strategies can then be used to ensure that the protein is expressed in specific cell classes. In order to restrict expression of a protein to a specific cell class, recombinant DNA is inserted into the genome after promoters which are active in only specific cell types. Promoters are regions of DNA which initiate gene transcription and can be used to restrict expression to specific cell types (Zeng and Madisen,



2012). Promoters consist of binding sites which are bound by specific RNA transcription factors. The protein encoded by the gene section following the promoter is only expressed in cells which contain the transcription factors corresponding to the promoter binding site. The promoter CaMK2A, for example, is active in excitatory neurons in the cortex, but not inhibitory ones (Wang et al., 2013). Inserting a gene into the genome preceded by the CaMk2A promoter would mean that the gene would be expressed exclusively in excitatory cells in the cortex.

Different promoters drive different levels of expression in cells (Zeng and Madisen, 2012). Optogenetic proteins often require very high level expression in order to be useful; strong indicator expression increases fluorescence and therefore SNR, whilst strong ion channel expression means a greater effect with less delivered light power. Some synthetic and natural promoters, such as CAG (Miyazaki et al., 1989) and HCMV (Muller et al., 1990), are able to drive extremely high levels of protein expression in a broad range of cell types. This makes them useful for optogenetic approaches, but their broad expression patterns require a second component to restrict the expression to only a single cell class of interest. The most common way of doing this is shown in Figure 1.5 and is based on an enzyme called cre recombinase (Sauer and Henderson, 1988). Cre recombinase (Cre) is an enzyme that can cut and recombine DNA at specific sites, known as LoxP sites. Depending on the relative orientation and site number Cre can remove a section of DNA between these sites or reverse it. This enables strong expression in specific cell classes using a 'double transgenic' approach. A generic protein organism line can be generated which expresses an optogenetic protein under a ubiquitous, strongly expressing, promoter, but which is unable to express the protein due to a genetic 'stop signal' or STOP codon, which is flanked by LoxP sites. This line can then be bred with another transgenic line which expresses cre recombinase under a highly specific but low expression level promoter. In cells where the specific promoter is active, Cre is produced and removes the genetic 'stop signal', enabling high level protein expression. In all other cells, the stop signal prevents any optogenetic expression.

More advanced expression strategies include intersectional targeting of cell-class subtypes (Madisen et al., 2015) and activity induced expression (Guenther et al., 2013). Of particular interest in this thesis is the triple transgenic intersectional approach using destabilised cre recombinase along with the tetracycline response element (TRE) based promoter which drives expression of a GEVI in a random subsample of a cell type (Song et al., 2017). This system

takes advantage of the extremely high expression driven by the TRE promoter. This is an inducible promoter derived from *E. Coli* which consists of several repeats of a tetracycline operator (TetO) which, when bound to the transcriptional transactivator (tTA) tetracycline protein drives strong expression of its downstream protein (Gossen and Bujard, 1992). In the strategy discussed, this promoter is prevented from driving expression of the downstream GEVI sequence by a STOP codon. A second transgenic line drives tTA expression under the excitatory neuron specific promoter Camk2A (Mayford et al., 1996). A third line is introduced which expresses destabilised-Cre (dCre) under the layer 2/3 excitatory cell-specific promoter RasGRF2A (Harris et al., 2014). dCre is a form of Cre recombinase which has been mutated so that it is unable to function unless it is re-stabilised by binding with the antibiotic Trimethoprim (TMP, Sando et al., 2013). In a mouse with all three of these genes, no expression will be driven unless a dose of TMP is given, which stabilises the dCre, which can in turn remove the STOP codon in that cell, enabling the TRE promoter to drive expression. By titrating the dose to a heavily sub saturation level, the Cre will be able to turn on expression in only a sparse subset of cells where the TMP has been able to stabilise it. In these cells however, extremely strong expression will be driven. More effective and controlled expression such as this relaxes the demands on imaging methodology.

## 1.4 Optical Microscopy & its application to Neuroscience

In this section I shall briefly review the basics of optics, before discussing in detail some aspects of optical microscopy especially relevant to the results in the thesis.

### 1.4.1 Optical Imaging Fundamentals

Unlike our understanding of the brain, our understanding of the behaviour of light is detailed and enables us to make clear and accurate predictions. Our most complete understanding of light is formulated in quantum field theory, which describes photons as excited states of the underlying electroweak field. This theory is far too complex to model most of our day to day interactions with light and provides little additional accuracy. As with all scientific models, it is therefore important to choose the correct level of approximation required by the problem at hand.

In many cases we can ignore the quantum nature of light and work purely with the classical electromagnetic field. This theory is founded upon Maxwell's equations, expressed in differential form in an linear, isotropic and homogenous material as

$$\nabla \cdot \mathbf{E} = \frac{\rho}{\epsilon} \quad (1.3)$$

$$\nabla \cdot \mathbf{B} = 0 \quad (1.4)$$

$$\nabla \times \mathbf{E} = -\frac{\partial \mathbf{B}}{\partial t} \quad (1.5)$$

$$\nabla \times \mathbf{B} = \mu \left( \mathbf{J} + \epsilon \frac{\partial \mathbf{E}}{\partial t} \right), \quad (1.6)$$

where  $\mathbf{E}$  and  $\mathbf{B}$  are the electric and magnetic fields,  $\rho$  is charge density, and  $\mathbf{J}$  is the current density.  $\epsilon = \epsilon_0 \epsilon_r$  and  $\mu = \mu_0 \mu_r$  are the permittivity and permeability of the studied material respectively, each of which can be expressed as the permittivity or permeability of free space,  $\epsilon_0$  and  $\mu_0$ , multiplied by a material-specific factor denoted by the subscript  $r$ . In the absence of free charges both  $\rho$  and  $\mathbf{J}$  are 0 and we can derive the electromagnetic wave equation. Taking the curl of 1.5 and 1.6, using the identity  $\nabla \times \nabla \times \mathbf{A} = \nabla(\nabla \cdot \mathbf{A}) - \nabla^2 \mathbf{A}$  and noting that  $\nabla \cdot \mathbf{B} = \nabla \cdot \mathbf{E} = 0$  we can derive the two equations

$$\mu\epsilon \frac{\partial^2 \mathbf{E}}{\partial t^2} - \nabla^2 \mathbf{E} = 0 \quad (1.7)$$

$$\mu\epsilon \frac{\partial^2 \mathbf{B}}{\partial t^2} - \nabla^2 \mathbf{B} = 0, \quad (1.8)$$

which are 3D wave equations for a wave propagating at  $v = 1/\sqrt{\mu\epsilon} = c/n$ , where  $c = 1/\sqrt{\mu_0\epsilon_0}$  and  $n = \sqrt{\mu_r\epsilon_r}$ , the familiar quantities of the speed of light in a vacuum and refractive index. If we can ignore coupling between the  $\mathbf{E}$  and  $\mathbf{B}$  fields, which is negligible when we consider the fields further than a few wavelengths from any boundaries (Joseph W. Goodman, 2005), then each vector component,  $u$ , of the electric and magnetic field obeys a scalar wave equation,

$$\frac{n^2}{c^2} \frac{\partial^2 u}{\partial t^2} - \nabla^2 u = 0. \quad (1.9)$$

It is with this scalar wave equation with which we describe the propagation of light through most optical systems.

In some cases we can further simplify the treatment of optical systems by considering light

as geometric rays propagating through the system. A light ray can be understood as a line perpendicular to the field wavefront. Rays can well model reflection and refraction as they pass into a medium with a different refractive index, however they are unable to capture effects arising from the wave nature of light such as diffraction and interference. These approximations remain accurate as long as the features with which the rays are interacting remain much larger than the wavelength of light. By further assuming that the angles the ray makes with the optical axis remain small (the 'paraxial approximation'), the transformations of geometric rays by optical elements such as lenses and mirrors become linear, enabling the description of optical systems as matrix operators.

Diffraction of light becomes important as electromagnetic waves interact with features that are similar in size to the wavelength of light. Physical optics theory enables us to model the behaviour of light in such situations. Huygens first proposed a wave theory of light in 1690, likening his vision of light to the waves 'seen to be formed in water when a stone is thrown into it' (Huygens, 1690). Huygens theorised in his Treatise that a secondary wavefront could be calculated by treating each point on a primary wavefront travelling through an aperture as a source of spherical waves and summing these together. This theory has been since formalised in a number of ways under different regimes, enabling us to predict the form of an electric field after it has been occluded or passed through an aperture accurately (Gu, 1999).

### Resolution in Microscopy

Geometric optics states that converging rays from a lens come to a point where the path length from the object is exactly equal for all rays. This would predict that microscope resolution is infinite, as an image would be a perfect magnified copy of the object. Unfortunately, due to the wave nature of light, this is not the case. Rays arising from a point object will constructively interfere with each other if the path length difference is less than half a wavelength. This 'smears out' spots in the image, increasing their size and thus limiting our ability to resolve closely spaced spots in the object. Diffraction from the finite lens aperture gives us a quantitative description of this effect. We can show by solving the diffraction problem of a wavefront passing through a circular aperture that the wavefront at the focal plane of a lens is proportional to the two dimensional Fourier transform of the waveform into the lens aperture (Gu, 1999). For a flat, uniform wavefront into a circular aperture this gives a field intensity of the form of the classic 'Airy disk', the width of which can be characterised as  $\sim \lambda/2NA$  (Hecht,

2017), where NA is the numerical aperture of the microscope and  $\lambda$  is the wavelength of light. A point source in a sample will be imaged into a finite width Airy disk in the image plane. This produces a minimum distance by which two points must be separated before they are recognised as such on the sensor. Similarly, collimated light will be brought to a finite width focus of the same shape when put through the same lens. This limits the maximum achievable power density in laser scanning microscopy which is especially important in two-photon microscopy as discussed below.

### Quantum description of light

There are some situations where a quantum mechanical description of light is required to describe a systems behaviour. In general, these consist of occasions where light interacts with matter such as a fluorescent molecule or a semiconductor. In these cases the arrival of light in quanta of energy is important. Fluorescence absorption spectra along with semiconductor absorption bands are non-zero over a finite band of light wavelengths. This represents the requirement that a photon of energy greater than the minimum transition energy must be absorbed by an electron in the system, the electron cannot continually absorb energy from the classical field until it overcomes the transition energy. Two photon imaging (discussed further in section 1.4.3) exploits the quantum nature of light to achieve optical sectioning. In this case, two photons of below the minimum transition energy are absorbed to enable an electron transition to a higher energy state; however they must be absorbed within the very short lifetime of a virtual interband state. The quantum nature of light also gives rise to the main source of noise in optical imaging in neuroscience, Poisson noise (see box 1). The absorption of photons by the imaging detector is subject to inherent quantum randomness. The absorption of the discrete particles can be described as a Poisson random process and so measurement of even a constant intensity semi-classical field will be subject to random Poisson noise.

### 1.4.2 Imaging in biological tissue

Whilst the optical heterogeneity of biological tissues was the original contrast agent for microscopical studies, the properties of tissue also provide additional challenges for biologists wishing to image deep inside them. Biological tissues are complex structured from far sub-wavelength ( $\sim 10$  nm) to the metre scale. When describing the propagation through the tissue we can therefore no longer assume the linear-isotropic-homogeneous properties that underpin

the previous descriptions of the propagation of light. The complexity of tissue precludes an exact description of propagation. Instead, the effect of these heterogeneities are often bundled together and quantified in terms of a number of coefficients describing different aspects of the response. These can then be measured from tissue samples or computed from models of tissue as scattering from different sized spheres using Mie theory or using continuum scattering theory based on the autocorrelation function of the fluctuating tissue refractive index (Jacques, 2013). Tissue optical properties are firstly described by the absorption and scattering coefficients,  $\mu_A$  and  $\mu_s$  ( $\text{cm}^{-1}$ ), length constants for scattering and absorption modelled as an exponential process. The angular dependence on scattering,  $p(\theta, \phi)$  ( $\text{steradian}^{-1}$ , where  $\theta$  describes elevation and  $\phi$  azimuth for a ray propagating along  $\hat{z}$ ), describes the propensity for a scattered ray to scatter in a particular direction. This is approximately symmetric about azimuthal angle when averaged over multiple scattering events and there are no large scale inhomogeneities, and so is often parameterised as  $p(\theta)$  ( $\text{radian}^{-1}$ ). An average parameter,  $g$ , the proportion of forward to backwards scatter, is often used to compare between different regions. Tissue scattering in the brain (and most biological tissue) is highly anisotropic, with  $g \approx 0.9$  (Yaroslavsky et al., 2002), and so a reduced scattering coefficient  $\mu'_s = (1 - g)\mu_s$  is often reported in studies as it is easier to measure due to the difficulty of distinguishing singly forward scattered photons from unscattered photons when the forward scattering anisotropy is high. Finally, the real refractive index,  $n'$ , is used to characterise refraction at the tissue-immersion interface. In brain tissue at the optical and near infrared (NIR) wavelengths used in this thesis scattering dominates over absorption (Yaroslavsky et al., 2002). These parameters vary as a function of wavelength and a measurement in human grey matter can be seen in Figure 1.6.

### ***In vivo* vs slice scattering**

As all experiments in this thesis were carried out in slice preparations, it is interesting to ask if the tissue parameters are varied by the slicing process. Although no specific study directly compares the two, it is possible to compare values measured in independent studies. Nishidate et al., 2015 measured the reduced scattering coefficient *in vivo* in a rat brain using a single reflectance fibre probe to be approximately  $\mu'_s = 9.9 \text{ cm}^{-1}$  at 800 nm. Oheim et al., 2001 measured the scattering length in acute *ex vivo* slices such as those used in our experiments to be  $l_s = 47 - 87 \mu\text{m}$  at 800 nm depending on the age of the rat. The rats used in Nishidate et al.'s study are likely in the central age bracket from their quoted weight. As  $l_s = 1/\mu_s$ , this corresponds

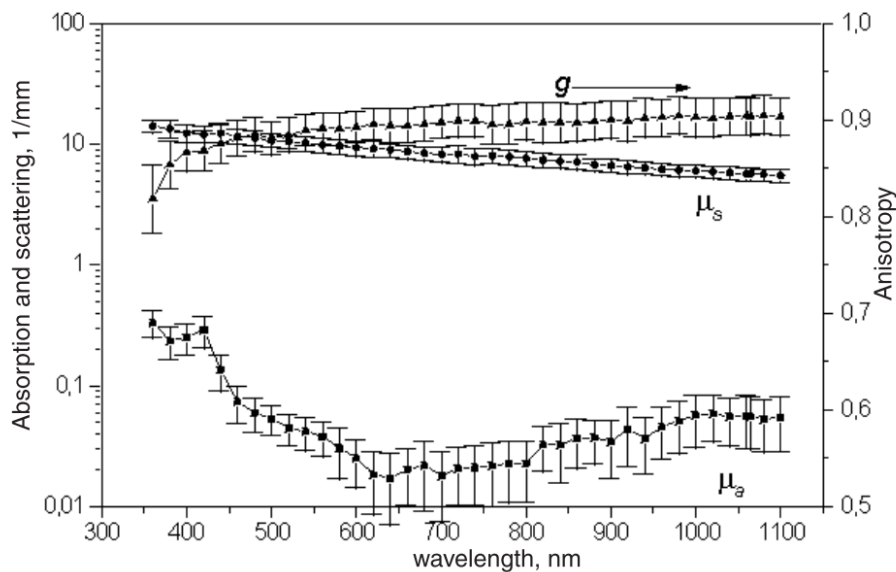


**Figure 1.6: Tissue scattering, anisotropy and absorption as a function of wavelength in the visible, NIR and NUV spectral range** The coefficients of the dominant optical interactions in Human brain gray matter. Note that scattering dominates absorption by multiple orders of magnitude in the visible, and anisotropy remains  $\sim 0.9$  throughout spectrum, as the scattering of rays is extremely forward biased. Reprinted with permission from Yaroslavsky et al. (2002). *Phys. Med. Biol.*, 47(12), 2059-73. ©Institute of Physics and Engineering in Medicine. Reproduced by permission of IOP Publishing. All rights reserved

to a range of  $\mu_s = 114 - 213 \text{ cm}^{-1}$ . The reduced scattering coefficient,  $\mu'_s = (1 - g)\mu_s$ , and  $g$  is around 0.9 in brain tissue at these wavelengths (Rupprecht et al., 2015; Yaroslavsky et al., 2002). This leads to  $\mu'_s = 11.4 - 21.3 \text{ cm}^{-1}$  in an acute slice preparation for rats, with the equivalent value likely in the centre of this range. This would put the scattering in slice to be 50% higher than *in vivo*. This interesting result, although requiring confirmation in a direct comparison, would impact upon the applicability of technologies developed in slices to *in vivo* studies.

### 1.4.3 Functional imaging techniques in neuroscience

Having described what we would like to image and then the concepts underpinning the theory of imaging, we can now turn to the specific imaging implementations used in neuroscience. There are a broad set of competing requirements on the techniques used to image indicators. We would firstly like to image fast enough to resolve the indicator and network dynamics with a high SNR. As discussed previously this means we would like to be able to excite as much fluorescence as possible from our sample within the normal bounds of photobleaching and phototoxicity. To collect as much data as possible from the biological system in its natural setting, we would like to monitor many cells in the intact brain. This creates further requirements

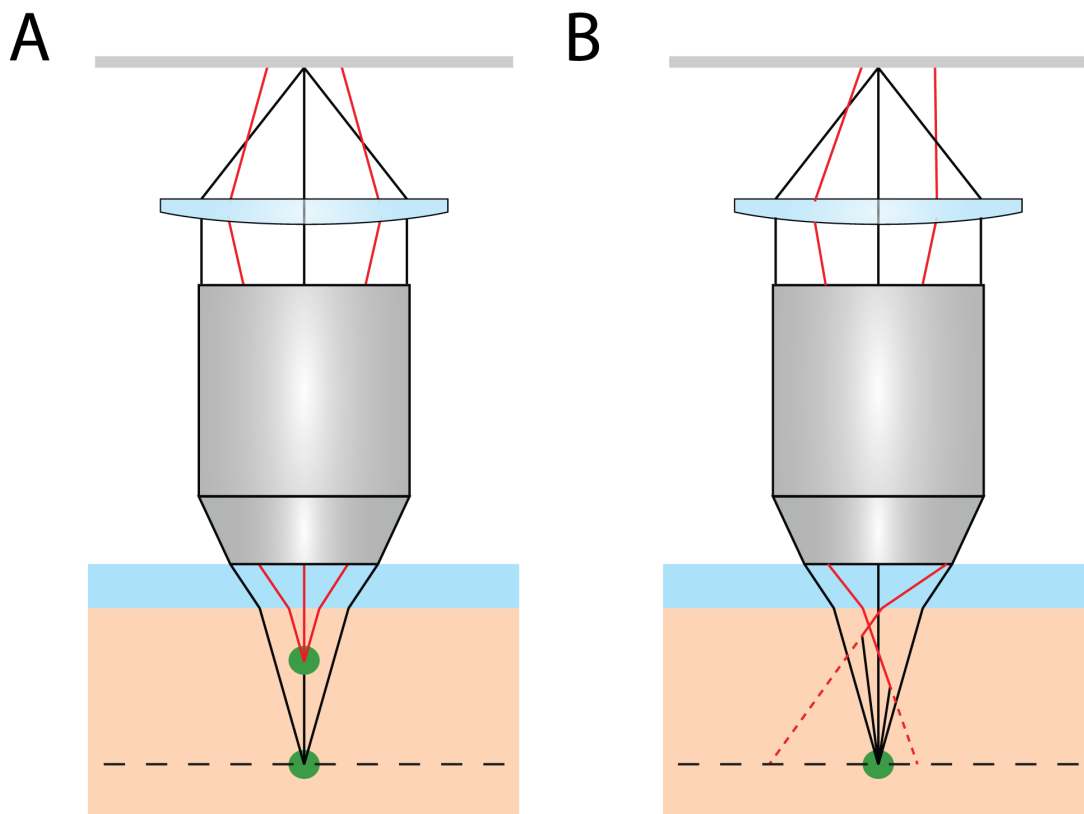


**Figure 1.7: The challenges of 3D imaging in biological tissue** a) Techniques which are not optically sectioning suffer from blur caused by the collection of light from out of focus planes. b) Light rays can be scattered before exiting the tissue, changing their apparent origin. In aggregate, this leads to a blurring effect which drastically increases with depth.



on our system than would exist if we were imaging cultured cells in a well.

Firstly, brains are three-dimensional. This raises two significant issues with conventional wide-field microscopy, summarised in Figure 1.7. Due to the large axial extent of the excitation light, much fluorescence is excited out of the microscope's focal plane. When collected onto a camera chip, this out of focus light reduces the contrast of the in focus image. Worse, the labelled out of focus cells have individually varying fluorescence time courses which ends up overlaid upon the in focus time course. This makes standard wide-field fluorescence imaging with single cell resolution often untenable in densely labelled 3D samples. Shifting the focus in the Z direction in standard imaging configurations is difficult, as it typically requires moving the large mass of the objective along the optical axis.

Secondly, as discussed in 1.4.2, brains are scattering and mammalian brains, where much research is focussed, are highly scattering. This limits the imaging depth in two ways. Excitation efficiency decreases with increasing imaging depth as the excitation light is scattered and the excitation point spread function is degraded. Also, light excited in one spatial location can be scattered before collection and be detected as though arising from somewhere else. This degrades image contrast and confuses analysis of image time courses in neighbouring areas.

Techniques that are 'optically sectioning' have been developed to circumvent the first issue. Optically sectioning techniques collect light from only a single z plane and so do not suffer from the blurring effect of out of focus light. Optical sectioning can be achieved in a variety of ways, either by rejecting out of focus fluorescence or only exciting fluorescence in the focal plane. One of the first optically sectioning techniques developed was confocal laser scanning microscopy (CLSM), developed by Davidovits and Egger, 1969. CLSM uses a laser focussed to a spot to excite fluorescence in a sample. The fluorescence is then collected through a pinhole placed in a plane conjugate to the laser focus. This pinhole acts to block out of focus light, optically sectioning the sample. The pinhole also increases the lateral resolution of the system as the confocal point spread function is the product of the illumination and detection point spread functions, leading to a sharper fall off of intensity with lateral distance. Assuming similar excitation and emission fluorescence wavelengths the lateral resolution tends towards an increase by a factor of  $\sqrt{2}$  for an infinitely small pinhole (Sheppard, 2009). The laser is scanned in the sample and the fluorescence sampled at each point to build up a 2D image. Although CLSM is widely used to image biological systems it suffers from a number of disadvantages. The system is not light

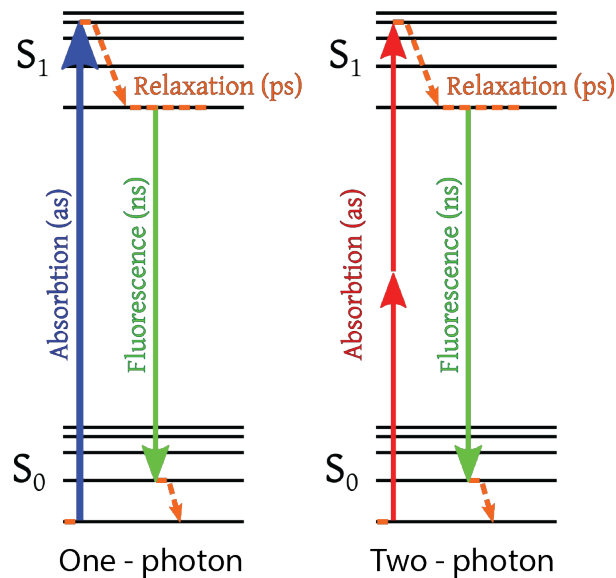


**Figure 1.8: Jablonski diagrams of one- and two-photon excitation.** One-photon fluorescence occurs when a single photon excites an electron to a higher energy level which subsequently relaxes, emitting a photon of longer wavelength. Two-photon excitation occurs when two photons of approximately half the transition energy are quasi-simultaneously absorbed by the electron, which relaxes as before emitting a photon of similar frequency as the one-photon case, of shorter wavelength than the two-photon excitation. Adapted from an image by [Alex M. Mooney, CC BY-SA 3.0](#).

efficient; emitted light scattered after originating from the focus is not collected and much fluorescence is excited out of plane. This uses up the ‘photon budget’ of the indicator and reduces the amount of useful imaging. Secondly, the imaging depth is limited by scattering in the sample. At large depths, excitation is very inefficient and an increasing proportion of light excited at the focus will be rejected by the pinhole. This limits confocal microscopy to depths of a few 100 microns in mammalian brain tissue (Combs, 2010). Finally, as CLSM is a laser scanning technique it must trade off fluorescence excitation, temporal resolution and spatial sampling. Longer pixel dwell times to increase photon flux and SNR necessitate decreased temporal resolution, a reduced FOV or coarser spatial sampling. Serial point scanning techniques have a limited imaging bandwidth, which can be divided according to the experimental requirements.

Other techniques achieve optical sectioning by exciting fluorescence only from the plane of interest. Two-photon laser scanning microscopy (2PLSM) has become widespread since its demonstration in 1990 (Denk, Strickler, and Webb, 1990). Two-photon microscopy techniques excite fluorescence via a different interaction to standard one-photon fluorescence. Instead of the fluorophore’s electron absorbing a single photon and transitioning to an excited state, it (almost) simultaneously absorbs two photons of a longer wavelength whose energy sums to the same as the single photon, as shown in Figure 1.8. The electron then de-excites via normal

fluorescence emission. The probability of this excitation process scales quadratically with the excitation intensity (Boyd, 2008). This can be thought of as due to the combined probability of two photons arriving at the same time and place. This is highly unlikely and so it requires very high photon fluxes to excite reasonable amounts of fluorescence. 2PLSM exploits this non-linear dependence on intensity to achieve optical sectioning. Focussing a pulsed laser to a diffraction limited spot results in fluorescence being excited in a femtolitre volume around the focal spot. Mode-locked Ti:Sapphire lasers with  $\approx 100$  fs pulses and 80 MHz repetition rates (and consequently very low duty cycles) are commonly used for excitation so that high peak powers can be achieved whilst keeping average power delivered into the tissue low. The excited fluorescence can be collected without any pinholes and assigned unambiguously to the excitation volume. As with CLSM an image is built up by scanning the spot and sampling the fluorescence at each point. 2PLSM is more efficient at photon collection than CLSM as it can sample all the fluorescence collected by the objective. As no fluorescence is excited out of the focal plane, phototoxicity and photobleaching are reduced.

Most importantly, 2PLSM is much more resistant to scattering for two reasons. Firstly, the longer excitation wavelengths used are less scattered in tissue, as can be seen from Figure 1.6. Secondly, emitted fluorescence that is scattered can still be collected, as long as it is within the collection cone of the objective. This enables 2PLSM to image at depths up to  $\approx 1$  mm in brain tissue (Combs, 2010). 2PLSM, as a scanning modality, suffers from the same intrinsic drawback as CLSM that the imaging bandwidth must be split to trade off between temporal resolution, fluorescence excitation and spatial sampling. Much effort has been expended developing improved strategies for using 2PLSM or adapting it to suit specific problems. The work in Chapter 3 concerns extensions to standard 2PLSM implementations, and so these are discussed in detail in section 1.4.3.

Another conceptual category of optical sectioning techniques are planar illumination techniques, known as 'lightsheet' microscopy (Mertz, 2011). In these microscopes optical sectioning is achieved by directly shaping the excitation light into a thin sheet. Imaging then occurs perpendicularly to the excitation optical axis. This removes the need to scan a single point in the sample, greatly increasing imaging speed and photon excitation rates (Huisken et al., 2004). Two-photon excitation can be used to increase resistance to scattering (Truong et al., 2011). A major drawback of this technique is that the imaging optics sit at right angles to the excitation optics. This geometry limits this form of lightsheet to small samples such as embryos that can

fit between the optics. The lightsheet also has to propagate through the tissue and so is disrupted by highly scattering samples. Oblique collection geometries, however, enable imaging in large, thick samples by using the same objective to deliver the lightsheet and collect fluorescence (Dunsby, 2008). A particularly successful implementation sweeps the oblique lightsheet and confocally collects the descanned excitation, achieving volume rates of 10 Hz over volumes of  $600 \times 600 \times 134 \mu\text{m}$  (Bouchard et al., 2015).

Structured illumination can also achieve optical sectioning in thick samples by numerical postprocessing (Mertz, 2011). Multiple images are collected under different illumination conditions which are then synthesised to generate a sectioned image. These techniques are based on the observation that it is the DC component of the image which does not attenuate with defocus (Neil, Juškaitis, and Wilson, 1997). Techniques of this kind have been implemented to perform calcium imaging in zebrafish (Lauterbach et al., 2015), however these approaches are limited when detecting small signals due to the numerical subtraction of the out of focus background. The mean of the background is subtracted, but the variance remains. If the background is then too bright compared to the structures of interest, the remaining variance will swamp the varying fluorescent indicator signal to be resolved (Mertz, 2011). Structured illumination approaches have therefore not become widespread in mammalian functional imaging where the samples are large.

A final technique sections the sample via a detector-side modification of the lightpath. Light field microscopy (Levoy et al., 2006) achieves optical sectioning by separating spatial frequencies as they arrive onto the microscope image plane with a microlens array. This technique is used in this thesis, and an in depth introduction is provided in section 1.4.4.

## Two Photon Scanning Strategies

Due to excellent performance in mammalian tissue *in vivo* and in slice, various techniques have been developed to improve 2PLSM's temporal resolution and SNR during functional imaging. One approach started with the recognition that the standard raster approach to building up an image is inefficient under some functional imaging conditions. Many calcium imaging experimental paradigms are interested only in imaging transients at cell somata, which in many cortical calcium imaging preparations are fairly sparse and separated by areas not of much interest. If cells to be monitored can be identified before imaging is carried out by, for example, a single 2D fluorescence image, more efficient scanning strategies can be used. This approach

was first implemented by Lillis et al., 2008 by generating a simple path between selected soma. Improvements to speed and dwell time were made by optimising the path length using the travelling salesman algorithm (Sadovsky et al., 2011) or by compensating for galvanometer inertia by scanning in spiral patterns (Schuck et al., 2018).

Another approach is to replace the galvanometers with acousto-optic pointing devices (AODs), (Salomé et al., 2006). These devices steer light via diffraction from refractive index variations in crystals caused by acoustic waves. AODs enable random access pointing with a switching speed, governed by the velocity of sound in the crystal, of  $\sim 10 \mu\text{s}$ . Driving AODs with chirped acoustic waves also enables scanning in  $z$  for 3D random access scanning (Duemani Reddy et al., 2008). AODs are hampered by generating only small deflection angles, limiting FOV or spatial sampling, and by being highly dispersive and expensive.

Scanning strategies are very effective at imaging with high temporal resolution and SNR, but the requirement of *a priori* target selection means that they are not applicable to all experimental paradigms.

### Two photon parallelisation approaches 1: Fluorescence excitation constraints

Since the main drawback of 2PLSM is due to the serial image acquisition, parallelisation approaches have been widely explored to increase the imaging speed and SNR. Instead of more intelligently apportioning bandwidth to regions of interest as scanning strategies do, these techniques increase the total available bandwidth, enabling better functional imaging. Increasing the degree of parallelisation, however, typically decreases 2PLSM's resistance to scattering as light can no longer be unambiguously assigned to a single point of origin. Often the optical sectioning capability is also compromised if the full numerical aperture (NA) of the objective is not used in order to increase the axial spread of the excitation beam. Finally, increasing the degree of parallelisation requires splitting the beam pulse energy over a larger spatial area,<sup>1</sup> decreasing the peak intensity and therefore the fluorescence excitation quadratically. A simple scaling calculation demonstrates this well. The number of absorbed photons per fluorophore,  $N$  in two-photon microscopy is proportional to (Rupprecht et al., 2016):

$$N \propto \frac{P_0^2 \lambda^2}{f \tau} \frac{\Delta t}{A^2} \propto N_0 \frac{\Delta t}{A^2} \quad (1.10)$$

<sup>1</sup>Except for time-multiplexed multifocal systems and Bessel beam imaging.

Where  $P_0$  is the average incident laser power at the sample,  $f$  is the laser repetition rate,  $\tau$  the laser pulse length,  $\lambda$  the laser wavelength,  $A$  the excited area and  $\Delta t$  the dwell time. Here we have separated this expression into factors depending on the excitation laser used,  $N_0$ , and factors affected by parallelisation,  $\Delta t/A^2$ . Consider imaging a sample with the same fluorophore distribution using imaging modalities with four different degrees of parallelisation: point scanning, point spanning with  $k$  spots, line scanning and wide-field imaging and considering the total evoked photon flux, the square root of which defines the SNR. The field of view (FOV),  $F$ , is imaged into  $n \times n$  pixels during an imaging period of  $T$ , the inverse of the frame rate. The table below shows  $A$  and  $\Delta t$  for equivalent imaging conditions for the four modalities along with the resulting signal multiplier representing the scaling of the baseline evoked fluorescence from the sample during a single frame acquisition:

Parallelisation degree	$A$	$\Delta t$	Resulting excitation efficiency factor
Single spot	$F/n^2$	$T/n^2$	$n^2$
$k$ spots	$F/kn^2$	$T/kn^2$	$n^2/k$
Line	$F/n$	$T/n$	$n$
Area	$F$	$T$	$1$

Clearly as the available dwell time increases linearly with area and the excitation power scales inversely quadratically with area the photon flux evoked decreases quadratically with pixel area. This decrease in excited photon flux must be compensated by increasing  $N_0$  in order to maintain SNR for parallelised imaging to be viable.

How this is achieved depends on available laser technology and tissue damage thresholds. The wavelength used for TPLSM is governed by the two-photon absorption spectra of the indicators used and so cannot be changed anywhere near enough to compensate for these scaling factors. Similarly, the pulse length,  $\tau$ , is limited by the bandwidth of the mode-locked laser and cannot be decreased to compensate. Ti:Sapphire oscillators are often operated giving 100 fs pulses where the bandwidth is already nearly 10 nm for a pulse centred at 800 nm. Pulse durations down to 5.5 fs have been achieved (Sutter et al., 1999), although these would be impractical to use for TPLSM due to dispersion and the fact that the bandwidth is around 170 nm, broader than many excitation spectra. This leaves the average power  $P_0$  and laser repetition rate,  $f$ , as variable factors that can compensate for the diminished signal.

A simple way to increase  $N_0$  is to increase the average power delivered to the sample. Whether this is effective depends on whether tissue damage for a single spot is dominated by

non-linear or linear processes. If tissue damage is limited by the total power applied to the tissue, then parallelisation will not enable greater photon fluxes. On the other hand, if the limiting damage mechanisms are non-linearly dependent on the peak intensity then it is possible to use multiple points, or a line or blob, with the same peak power but greater overall total power to evoke more fluorescence from the sample (Bewersdorf, Egner, and Hell, 2006). The degree of parallelisation can be increased until the linear (heating) mechanisms become dominant or you run out of laser power. Damage mechanisms found experimentally have an intensity dependence to the power of between 2 and 3 (Bewersdorf, Egner, and Hell, 2006). Practically, assuming the power to a diffraction limited spot of  $\sim 10$  mW and diameter  $d \sim 1$   $\mu\text{m}$ , the area can be increased to  $d\sqrt{250/10} = 5$   $\mu\text{m}$  in diameter before tissue damage becomes significant *in vivo* at powers of 250 mW (Podgorski and Ranganathan, 2016). *Ex vivo* preparations such as acute brain slices are able to tolerate higher powers as most of the laser energy passes straight through the slice and is not deposited in the tissue. Clearly, however, for both *in-* and *ex vivo* increasing laser power in the sample cannot enable a high degree of parallelisation.

Decreasing the laser pulse repetition rate (PRR), equivalent to increasing the energy per laser pulse, can increase the evoked photon flux without increasing the required average power. Increasing the pulse energy increases the peak intensity and therefore greatly increases non-linear excitation. The lower limit for decreasing the PRR is affected by various aspects of the imaging system and sample. Firstly, as decreasing the PRR increases the peak intensity, non-linear effects become more important. Non-linear damage mechanisms could start to dominate, reducing parallelisation's effectiveness. Secondly, for scanning techniques the PRR must be sufficiently high to deliver at least a single pulse to each pixel (and more if careful synchronisation of image acquisition with the laser is to be avoided). A Ti:Sapphire laser operating at 80 MHz can deliver  $\sim 300$  pulses per pixel per second to a  $512 \times 512$  FOV. Reducing the PRR to 10 MHz would limit the imaging system to less than 40 Hz, removing one of the key benefits of parallelisation, imaging speed increase, although parallelisation might enable decreased pixel number, counteracting this effect. Finally, as always, PRR is limited by the available laser technology. A laser's PRR is inversely proportional to cavity length and so there exist constraints which create a practical lower limit.

## Two photon parallelisation approaches 2: techniques

A number of different techniques to parallelise two-photon microscopy have been, and are continuing to be, developed. Particularly interesting are ‘projection’ techniques, where information over one spatial dimension is folded into another to speed up acquisition, and computational techniques are used to unmix the subsequent signals.

A recently reported method of this kind, SLAPMi (Kazemipour et al., 2018), collects tomographic projections by scanning differently oriented lines in the  $x, y$  plane through the sample. Using 4 lines, they can image at kilohertz rates over  $\sim 250 \times 250 \mu\text{m}$  FOVs at up to  $300 \mu\text{m}$  depths. Functional signals are extracted using an adapted compressive-sensing Richardson-Lucy deconvolution algorithm incorporating priors from previously acquired structural images and the time course of the functional indicators used.

Another projection method is Bessel beam imaging (Botcherby, Juškaitis, and Wilson, 2006), where an elongated PSF is engineered to increase the imaging depth of field. This enables a volume scan with a standard raster pattern, parallelising the excitation in  $z$ . As the excitation light is tightly laterally confined this technique does not suffer from the power scaling issues discussed before. Combined with sparse activity and indicators, this technique does not require significant computational image reconstruction, and has enabled video rate imaging of synaptic calcium events (Lu et al., 2017). Although this technique is not axially sectioning in the conventional sense, the PSF shape and non-linear excitation does not lead to the same issues as non axially sectioned wide field single photon imaging.

A more straightforward approach to parallelising TPLSM is to split the excitation beam into multiple beamlets and scan them simultaneously in the sample, an approach known as multifocal two-photon microscopy (MTPM). Using multiple beams allows more excitation power to be applied to the sample before damage commences, exciting a greater total photon flux. Multifocal configurations can be split into two conceptually different categories: spatially resolving and non-spatially resolving. In a spatially resolving system the excitation from the multiple beamlets is imaged onto a spatially resolved detector. Non spatially-resolved systems, alternatively, collect all fluorescence onto a single PMT as with standard TPLSM and use temporal multiplexing approaches to demix the signals from different foci. As two-photon excitation is pulsed and fluorophores de-excite and emit fluorescence for typically a few nanoseconds, fluorescence emission in two photon imaging is pulsed (Cheng et al., 2011). Ti:Sapphire lasers



often used in TPLSM typically have a repetition rate of 80 MHz and therefore a period of 12.5 ns. By delaying parts of the beam by fractions of the period and using fast electronics to time resolve emitted fluorescence pulses it is possible to image separate parts of the sample simultaneously (Amir et al., 2007; Cheng et al., 2011) These multiplexing schemes can image multiple planes or FOVs simultaneously by adjusting the divergence or angle of the beams respectively. The multiplexing factor that can be achieved is limited by the ratio of the laser period to the fluorophore lifetime and is typically around 4 (Cheng et al., 2011), fewer than is optimal considering non-linear and linear optical damage thresholds (Bewersdorf, Egner, and Hell, 2006).

In spatially resolving systems the single beam is split into multiple beams which are scanned in the sample, and the fluorescence is either descanned and collected on a PMT (Kim et al., 2007) or simply collected onto a camera (Bewersdorf, Pick, and Hell, 1998). This form of multifocal microscopy is discussed in the introduction to Chapter 3. It is important to note that spatially resolved detection comes at the price of vulnerability to scattering. As there are multiple sources of light in the sample, it is no longer unambiguous from where photons detected have arisen. Increasing the degree of parallelisation, line and sheet excitation has been used for functional imaging, removing the need for one or both scanning axes, increasing fluorescence excitation. With increasing parallelisation, however, scattering becomes more of a problem.

#### 1.4.4 Light field imaging

In some cases, even highly parallelised two-photon approaches are simply unable to excite enough fluorescence to resolve small signals, primarily when dealing with voltage indicators. Wide-field single photon fluorescence efficiently excites fluorescence in parallel from a 3D FOV that extends along the optical axis. With conventional epifluorescent detection, this is a disadvantage as the out of focus light collected is blurred and degrades contrast and functional SNR as described before. Single-photon excitation also bleaches samples quickly due to it being easily absorbed, meaning the imaging quality of any other z plane is degraded after imaging the first. This makes it difficult to find the functional 3D structure of a signal.

Light field microscopy (Levoy et al., 2006) presents a way around this problem by enabling reconstruction of 3D volumes in a single shot from a 2D camera image. Based on an idea originally conceived over 100 years ago (Lippmann, 1908; Dudnikov, 1970), light field imaging captures information about the propagation direction of light as well as the spatial intensity distribution which is captured during the normal imaging process. This enables reconstruction

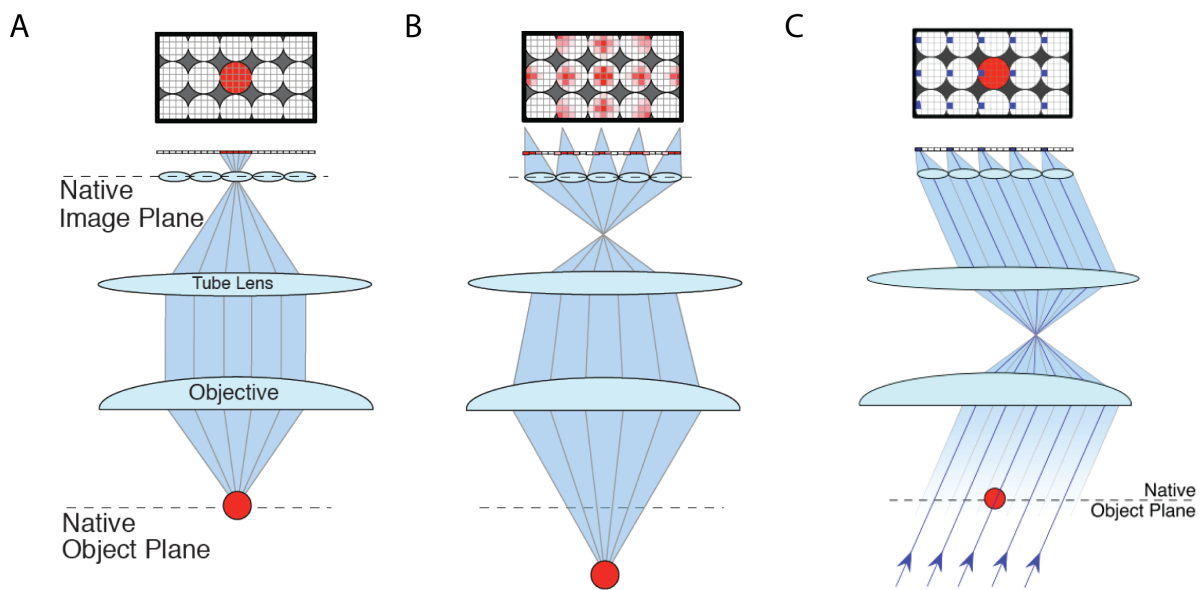


**Figure 1.9: A light field microscope diagram** A) The light field microscope differs from a standard wide-field microscope by the addition of a microlens array at the native image plane. The camera sensor is then placed at the back focal plane of the microlens array. B) Sources in 3D space generate unique spatial distributions of light on the camera, enabling volume reconstructions from the resulting image. C) Each pixel location under the microlens images consist of orthographic projections through the sample at specific angles. Different pixel locations correspond to different angular samplings. Reprinted with permission from (Broxton et al., 2013), OSA.

of a 3D volume around the microscope’s focal plane resulting in an extremely light-efficient imaging modality compared to standard wide-field fluorescence microscopy, as photons excited away from the focal plane can be usefully assigned to a 3D spatial location.

3D imaging is achieved by placing a microlens array at the native image plane of the microscope, where the sensor would be usually, and placing the sensor in the back focal plane of the microlens array, as shown in Figure 1.9. This splits light arriving onto the native image plane by propagation angle. The collected image consists of circular sub-images (Fig. 1.10A), with the macroscopic structure of the sub-images resembling an undersampled version of the standard camera image, with each circular image representing the angular content of the light at the specific spatial location. Considering the system in terms of geometric optics, the image therefore represents a sampling of the 4D lightfield function representing each ray’s propagation through the system,  $\mathcal{L}(x, y, \theta, \phi)$ , where  $x$  and  $y$  correspond to spatial locations in the object space, and  $\theta, \phi$  to propagation angles. In the lightfield literature  $\theta, \phi$  are parameterised instead by two spatial locations in a complementary plane to  $x, y$ , known as  $u, v$ . In lightfield microscopy we use  $u = f \sin(\theta) \cos(\phi)$  and  $v = f \sin(\theta) \sin(\phi)$ . Examining closely a lightfield

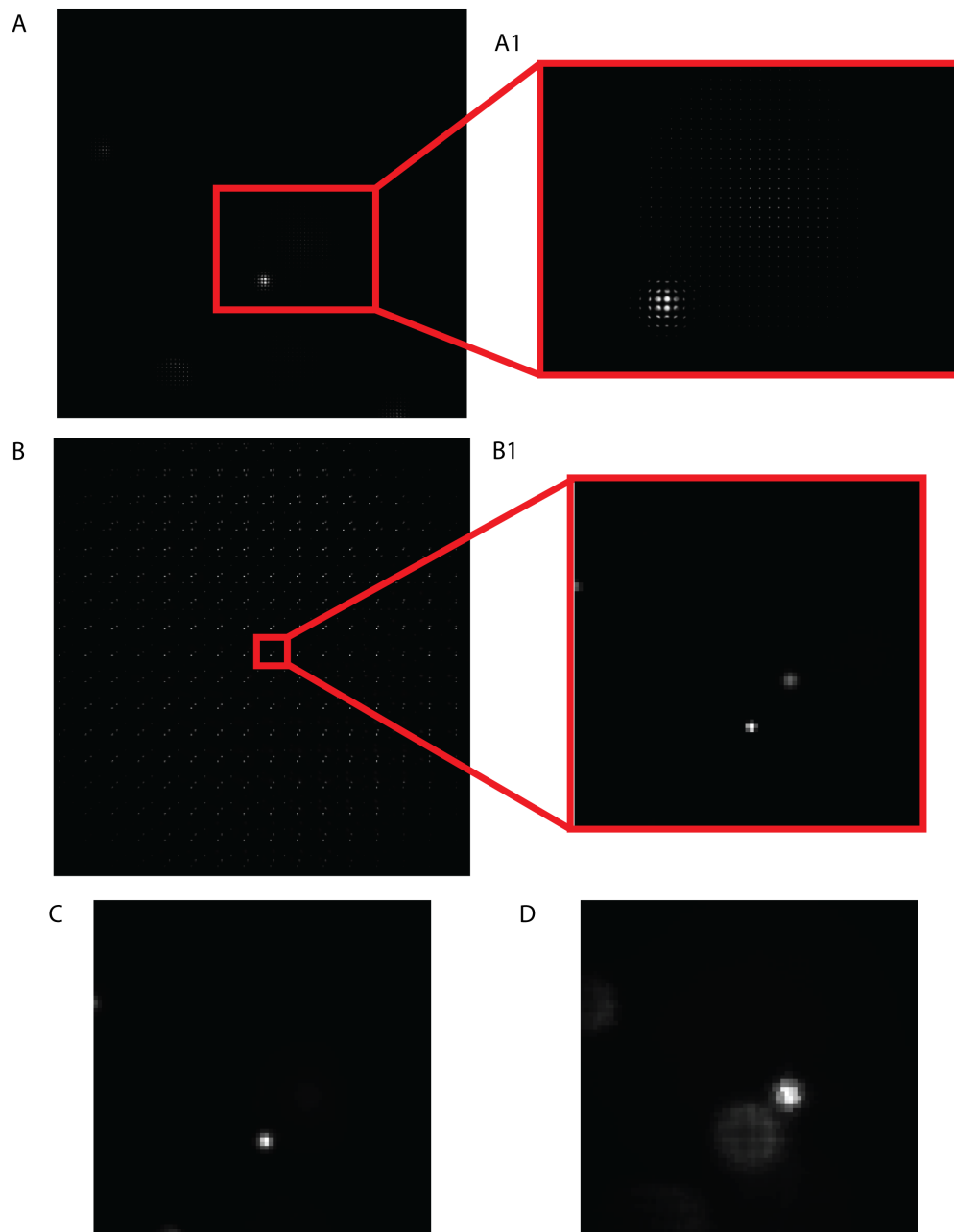


**Figure 1.10: Light field images** A) A full and (A1) enlarged section of a raw light field image captured on a camera. The individual spots can be thought of as a decomposition in spatial frequency in that spatial location. B) A tiling of orthographic projections of sub-aperture images generated by selecting the same pixel from underneath each microlens corresponding to a specific propagation angle through the sample. Each image results from the selection of a different pixel and a parallax effect can be seen across the tiling. B1) Shows a single projection. Note that the depth of field is large due to the small synthetic acquisition aperture and that the spatial resolution is low. C) Shows a light field synthetically refocused at  $z = 0 \mu\text{m}$ . The second bead is now out of focus as the synthetic collection aperture is the full objective NA. D) An image synthetically refocused  $22 \mu\text{m}$  above the native focal plane. The first bead is out of focus and the second in focus. The quality of focussing is worse due to the falloff in spatial frequency transfer with defocus of the objective.

image of two beads (Fig. 1.10A1) each individual circular spot can be thought of as samples of  $\mathcal{L}(x = x', y = y', u, v)$  for a specific  $x', y'$ . This treatment assumes that rays propagating through the object are not greatly attenuated or amplified, otherwise a full 5D lightfield,  $\mathcal{L}(x, y, z, u, v)$  is required to model the system. Taking a single pixel from behind each microlens represents a sampling of the lightfield at a specific value of  $\theta$  and  $\phi$ , and therefore represent an orthographic projection of the object through that specific angle, as shown in Figure 1.9C. Each pixel behind each microlens provides a projection at a different angle through the object, and so each captured lightfield is essentially a limited angle tomography measurement. This can also be seen in Figure 1.10B, which consist of a tiling of these orthographic projections or ‘sub-aperture images’, which are generated by selecting the same pixel from behind each microlens. These images can be thought of as  $\mathcal{L}(x, y, u = u', v = v')$  for a specific value of  $u', v'$ . Parallax can be seen between different parts of the tiling as the viewing angle changes. A single sub-aperture image is seen in Fig 1.10B1. The spatial resolution is decreased, and is defined by the pitch of the microlens array in the sample. The depth of field of the image is very large as the aperture used to collect it is a pinhole (seen between the two main lenses in Fig. 1.9C). The individual images are therefore quite noisy as they only use a fraction of the light collected by the objective. It is possible to combine these sub-aperture images to synthesise refocused images as if the microscope was focussed at a different location in  $z$  (Figs. 1.10C & D). These images are generated using all of the sub-aperture images and so use all the light collected by the microscope, increasing the SNR. An image at the microscope native focal plane is generated by simply adding all of the sub-aperture images (Fig. 1.10). To refocus at a different plane, each image must be shifted proportionally to the obliquity of the viewing angle before summation. A simple geometric picture helps to understand this process.

Figure 1.11 shows a geometric intuition behind synthetic refocussing. A focussed image corresponds to the case where all the light rays for a pixel meet at a specific  $z$  plane, i.e. at the native focus in 1.11. Adding all the unshifted projections from Figure 1.10C corresponds to this case. To refocus at a different  $z$  plane we need to sum rays that meet at that  $z$  plane. Shifting the rays away from the optical axis by an amount proportional to their propagation angle enables us to bring them together at a deeper focus. This corresponds to translating the individual sub-aperture images before summation. A refocussed image can therefore be calculated as

$$I(x, y) = \sum_{u, v} L(x + u(1 - 1/\alpha), y + v(1 - 1/\alpha), u, v), \quad (1.11)$$

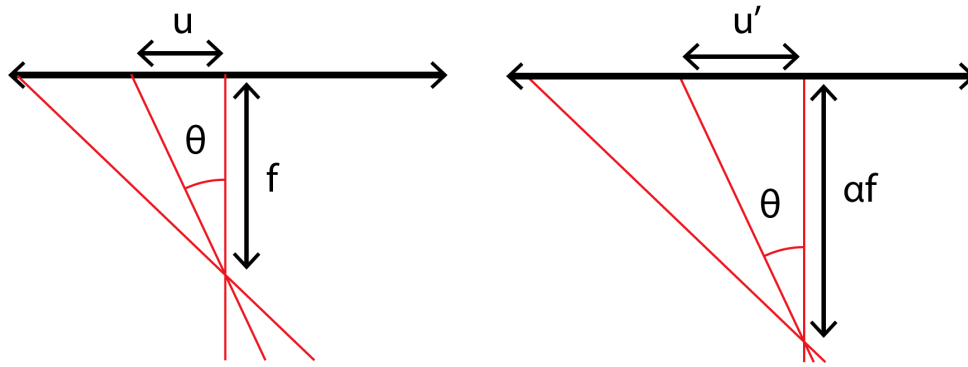


**Figure 1.11: Synthetic refocusing** Changing the plane of focus of the microscope requires sampling the rays that intersect at the desired focal plane. Individual pixels under each microlens correspond to different propagation angles,  $\theta$ . Summing the pixels under each microlens corresponds to the case on the left, where the rays meet at the objective focal plane. This will generate an image focused at the native focal plane sampled at the pitch of the microlens in the sample. Shifting rays by an amount proportional to their propagation angle makes them come to a focus at a different  $z$  plane. Summing these shifted rays results in a synthetically refocused image.

where  $\alpha = f'/f$ , the new focal distance as a fraction of the native distance and we neglect an overall spatial scaling with refocus (Ng, 2006).

Understanding this picture of lightfield as tomography helps to illustrate the core trade-off at the heart of lightfield design. Increasing the microlens pitch increases the number of pixels underneath each one, allowing for a finer angular sampling of the object. This increases the effectiveness of synthetic refocusing, enabling finer reconstructions of the object in  $z$ . Increasing the pitch, however, decreases the lateral spatial resolution as each angular sample arises from a projection through a cylinder of greater diameter in the object. The lateral resolution is the demagnified microlens pitch in the sample plane, i.e. the spatial sampling frequency is at  $M/d$ . In order to maximise the usable sensor area the NA of the MLA must be chosen to match the demagnified NA of the objective. This means that, neglecting diffraction, an in-focus object will generate circles on the sensor that just touch, minimising unused pixels, whilst ensuring that they do not overlap. This fixes the ratio of pitch to focal length, and so pitch is the only free parameter to vary to choose the desired spatial and angular resolution trade-off. The angular resolution is limited by the number of diffraction-limited spots that can be fit under a single microlens; assuming fine enough pixel sampling the number of resolvable angles,  $N$ , is related to the microlens pitch,  $d$ , the magnification,  $M$  and the objective NA limited Airy disk size in the sample,  $w$ , as

$$N = \frac{d}{Mw}. \quad (1.12)$$

This angular resolution defines the number of unique synthetically refocused slices that can

be obtained from a focal stack in the light field. Increasing the number of slices (the axial resolution) decreases the lateral resolution and vice versa.

Interestingly, more advanced reconstruction techniques enable improving on this resolution limit in some circumstances. Broxton et al., 2013 showed that using 3D deconvolution of the light field image using a forward model obtained from a wave optics model of the microscope was able to achieve up to an order of magnitude increase in resolution compared to the simple reconstruction. This was enabled by the projections finer sampling of the object than the microlens pitch. At the native focal plane, however, the ray sampling is degenerate and this method fails to increase the resolution above the aforementioned limit. This technique is unfortunately much more computationally expensive than the synthetic refocussing algorithm above, due to the need to iteratively deconvolve the 3D volume with a spatially variant PSF with Richardson-Lucy deconvolution.

### 1.4.5 Deconvolution

As deconvolution arises a number of times throughout this thesis I shall provide a brief introduction here. No measurement instrument collects and records the measured signal perfectly. The signal,  $x$ , is often changed by the instrument by convolution with its impulse response,  $h$ , such that the measured signal,  $y$ , is equal to

$$y = h * x \quad (1.13)$$

and we are often able to measure the impulse response of our instrument before our measurement. In standard optical imaging, for example, our impulse response is the 3D point spread function of the system arising due to diffraction. Due to the convolution theorem, equation 1.13 is equivalent to a multiplication in Fourier space

$$\hat{y} = \hat{h}\hat{x} \quad (1.14)$$

where  $\hat{y}$ ,  $\hat{h}$  and  $\hat{x}$  are the Fourier transforms of  $y$ ,  $h$  and  $x$  respectively. In incoherent optical imaging  $\hat{h}$  is the modulation transfer function and is band limited due to the limited numerical aperture of the system. Equation 1.14 would suggest a simple division in frequency space could account for the measurement system's response and restore the uncorrupted signal, however

this naive approach almost invariably fails due to the measurement noise inherent to physical systems. We measure in general a signal related to  $g$  by the relation

$$y = h * x + \epsilon, \quad (1.15)$$

where  $\epsilon$  is our measurement noise. It is clear to see that a straight division in frequency space will return a corrupted version of our original signal. Worse, our impulse responses often take the form of low pass filters, and so when we are trying to restore high frequency fine details in our image by straight deconvolution we amplify the noise which arrives unfiltered through our system.

Deconvolution techniques accounting for the noise inherent to measurement have been developed to overcome this problem. In the case of optical imaging, among others, shot noise due to photon detection is the main noise source. We can develop a maximum likelihood estimate of our source signal,  $x$ , given our known impulse response,  $h$  and the form of our noise. We write eq. 1.13 as a matrix operation for clarity in this discussion so that each pixel,  $y_i$ , is given by

$$y_i = (Hx)_i, \quad (1.16)$$

where  $x$  is a vector of observations and  $H$  is the matrix representing the forward model.

Assuming we are working with a camera image of  $i$  pixels arising from our fluorescent object the likelihood function,  $L(x)$  is the probability of observing pixel value  $y_i$  given the source distribution  $x$  and the impulse response  $H$ ,

$$L(x) = P(y|x) = \prod_i \frac{[(Hx)_i]^{y_i}}{y_i!} \exp[-(Hx)_i] \quad (1.17)$$

which is simply the product of the individual Poisson probabilities of observing a pixel with photon count  $y_i$  due to the underlying emission rate of  $(Hx)_i$  (Lanteri, Soummer, and Aime, 1999). It can be shown (Shepp and Vardi, 1978) that the iterative Expectation-Maximisation algorithm (Dempster, Laird, and Rubin, 1977) will converge on a source distribution  $x$  maximising the likelihood function if the following iterative update is used:

$$x_i^{k+1} = \frac{1}{a_i} \left[ H^T \frac{y}{Hx^k} \right]_i x_i^k, \quad (1.18)$$

where the fraction  $y/Hx^k$  is computed element-wise and  $a_i = \sum_j H_{j,i}$ . Intuitively, this update can be understood as follows. The collected data and the data predicted from the current expected source distribution are compared in the aforementioned fraction. The ratio of the two are then inverse transformed into the object space and used to update the current estimate of the source distribution. This deconvolution is called Richardson-Lucy deconvolution after the two people who originally independently described it (Richardson, 1972; Lucy, 1974).

This deconvolution method effectively restores images blurred by a known kernel. As an iterative method however, it suffers from a heavy computational cost due successive convolutions. These can be efficiently implemented as fast Fourier transforms (FFTs), but even so can become burdensome for large datasets. Secondly, the deconvolution is not regularised and so tends to amplify noise as the number of iterations grows too large. A number of extensions to address these issues have been put forward (Dey et al., 2006).

## 1.5 Advanced optical methods in GEVI imaging: state of the art

Due to its overwhelming SNR advantage, single photon wide field imaging is used almost exclusively for neuronal GEVI imaging. In this section I will review the studies which utilised or developed more advanced optical techniques to meet a specific need. As discussed previously, single spot two-photon voltage imaging seems eminently unsuitable for GEVI imaging. Nevertheless, two-photon voltage imaging was achieved *in vivo* in single cells in 2012 (Ahrens et al., 2012) and at the single trial level in populations of cells in 2013 (Akemann et al., 2013). These studies imaged extremely small areas in order to achieve high enough frame rates to resolve voltage signals. The ASAP family of GEVIs is best suited to two-photon excitation as it does not lose its sensitivity under two-photon illumination, as many others do (Chamberland et al., 2017). Interestingly, 2P lifetime imaging was demonstrated as a method of measuring absolute voltage changes in ASAP1 (Brinks, Klein, and Cohen, 2015). Imaging fast enough to resolve spikes, however, requires fast random access measurements of the membrane with acousto-optic scanning, which precluded *in vivo* use, as motion artefacts disrupt the scan pattern. Optimisations to the probe's sensitivity and two-photon excitation, along with a novel scanning strategy using non-stationary wave driven acousto-optic scanners has enabled *in vivo* detection of spikes deep in the mouse brain for up to 4 cells (Chavarha et al., 2018).



Single-photon excitation is much more commonly used with GEVIs. The recently reported Voltron GEVI (Abdelfattah et al., 2018) is sufficiently bright and sensitive that 30 cells in layer 2/3 can be imaged simultaneously in wide field, although this requires soma restricted sparse expression to ensure that membrane signal mixing does not destroy the SNR. To achieve single-cell performance *in vivo* with paQuasar3 (Adam et al., 2018), researchers combined single photon imaging with DMD patterned photoactivation and soma restricted expression. Light field microscopy has been used to image GEVIs in *Drosophila* (Aimon et al., 2018) and larval zebrafish (Cong et al., 2017) as part of whole brain imaging setups alongside calcium imaging. It has however not been applied to GEVI imaging in mammalian tissue or at single cell resolution.

Confocal microscopy has been used to image the GEVI ASAP1 in zebrafish spinal cords (Maruyama et al., 2018), although has not been applied to functional imaging in the mammalian cortex, likely due to increased scattering.

## Chapter 2

# Methods

### 2.1 Introduction

This chapter contains methods common to multiple chapters to reduce repetition in the individual methods sections. All animal work in this study was carried out in accordance with the recommendations of UK Animals (Scientific Procedures) Act 1986 under Home Office Project and Personal Licenses (project licenses 70/7818 and 70/9095).

### 2.2 Slice preparation

All functional microscopy in this thesis was carried out in acute slice preparation. This preparation preserves some of the structure in the brain, whilst allowing easier experimentation than *in vivo* due to multiple factors. Firstly, structures that are 'optically deep' for both one- and two-photon excitation can be exposed to within the scattering length of the illumination. This enables, for example, simple two-photon imaging of sub-cortical structures or one-photon imaging of deeper cortical layers without strong scattering. Secondly, there is greatly reduced physiological noise from haemodynamic signals or sample movement. The clear drawbacks from this are that the brain is no longer intact, introducing confounds into study of neuronal activity. Secondly, the possibility of studying behavioural or sensory questions is obviously removed, as the brain is no longer connected to the rest of the body. Preparing acute brain slices of adequate quality to study neuronal function can be challenging, and a number of different methods have been developed and are in use. Throughout my work I have mainly used a simplification of the method described by Ting et al., 2014, where the simplification is described on the website of the group ([www.brainslicemethods.com](http://www.brainslicemethods.com)). I have found that this method gives good quality slices with many healthy cells for mice well into adulthood (up to 1 year old).

### 2.2.1 Solutions

Two solutions are required to prepare brain slices using the aforementioned method: standard artificial cerebro-spinal fluid (ACSF) for slicing and recording, and N-methyl D-glucamine (NMDG) supplemented ACSF in which the slices rest for a short period after cutting.

**Table 2.1: Sodium-containing ACSF recipe.**

	Concentration (mM)
NaCl	125
NaHCO <sub>3</sub>	25
Glucose	20
KCl	2.5
NaH <sub>2</sub> PO <sub>4</sub>	1.25
MgCl <sub>2</sub>	2
CaCl <sub>2</sub>	2

**Table 2.2: Secondary Sodium-containing ACSF recipe.**

	Concentration (mM)
NaCl	124
NaHCO <sub>3</sub>	24
Glucose	12.5
KCl	2.5
NaH <sub>2</sub> PO <sub>4</sub>	1.2
HEPES	5
MgCl <sub>2</sub>	2
CaCl <sub>2</sub>	2

**Table 2.3: NMDG ACSF recipe.**

	Concentration (mM)
NMDG	110
NaHCO <sub>3</sub>	25
Glucose	25
KCl	2.5
NaH <sub>2</sub> PO <sub>4</sub>	1.2
MgCl <sub>2</sub>	10
CaCl <sub>2</sub>	0.5

**Table 2.4: Intracellular solution recipe.**

	Concentration (mM)
K-gluconate	120
KCl	7
ATP-Mg	4
GTP-Na	0.3
Phosphocreatine-Na	10
HEPES	10

### 2.2.2 Protocol

The following protocol is for preparation of mouse acute brain slices. Before slicing, all solutions must be brought to the correct temperature as detailed below and oxygenated with 95% O<sub>2</sub>/5 % CO<sub>2</sub>.

1. Anaesthetise the mouse in 5% isoflurane in oxygen and decapitate;
2. Remove brain and place in ice cold Na-ACSF (Tables 2.1 or 2.2);
3. Slice 400  $\mu$ m slices at 80 Hz and 1 mm vibration on the microtome in ice cold Na-ACSF;
4. Place each slice as it is cut into NMDG-ACSF (Table 2.3) at 37°;
5. After 12 minutes, transfer slices into room temperature Na-ACSF;
6. Allow slices to rest for 1 hour before recording.

## Chapter 3

# Multifocal Two-photon Microscopy

### 3.1 Introduction

In this chapter I describe the design and testing of a multifocal two-photon microscope (MTPM) for imaging of functional neuronal signals in slice. In section 3.2, which reproduces large sections of my work previously published in Quicke et al., 2018 (original, CC BY 4.0), I describe the microscope and a novel control and image processing algorithm designed to increase MTPMs resistance to scattering. In section 3.3 I then go on to use the multifocal system to image a genetically encoded voltage indicator in slice, showing that the MTPM system can resolve signals in both populations of cells and single cells. I finally summarise the feasibility of imaging EPSPs with this specific multifocal system.

### 3.2 Development and testing of a source localisation algorithm

#### 3.2.1 Introduction

Two-photon laser scanning microscopy (2PLSM, (Denk, Strickler, and Webb, 1990)) is widely used in neuroscience due to its ability to image cellular and subcellular structures at high spatial resolution with low phototoxicity and photobleaching. In combination with intracellular calcium indicators, it allows readout of neuronal action potentials (APs) from single cells in highly scattering mammalian brain tissue. The inherent optical sectioning from nonlinear fluorescence excitation also enables the discrimination of different activity amongst densely packed neurons.

As a laser scanning technique, 2PLSM has to trade off temporal resolution, spatial sampling and fluorescence excitation. Resonant galvanometers, improved scanning strategies (Schuck et

al., 2018), point spread function sculpting (Prevedel et al., 2016) and temporal multiplexing (Cheng et al., 2011) offer improved temporal performance. In its basic implementation, however, frame rates for most neuroscience applications are limited to around 10 Hz for fields of view (FOV) of up to  $500 \times 500 \mu\text{m}$ . This is adequate to detect slow calcium transients if low temporal precision on the inference of the underlying AP timing is sufficient. However, there is evidence that AP timing and frequency play a crucial role in sensory encoding and processing (Luczak, McNaughton, and Harris, 2015), and increasing imaging temporal resolution whilst maintaining signal-to-noise ratio (SNR) decreases the error in AP timing estimation (Schuck et al., 2018; Reynolds et al., 2018). Secondly, the faster dynamics and smaller size of signals such as membrane potential or neurotransmitter release and reuptake limit standard 2PLSM's applicability to these signals.

Spatial multiplexing has been widely explored as a strategy to improve two-photon imaging's temporal resolution without sacrificing pixel dwell time and fluorescence excitation (Schultz et al., 2017). Digital holography allows up to 100% duty cycles by shaping light only over regions of interest, but requires preselecting specific structures and ignoring others (Ducros et al., 2013; Yang et al., 2015; Castanares et al., 2016; Foust et al., 2015; Nikolenko, 2008; Bovetti et al., 2017; Tanese et al., 2017; Pozzi et al., 2015). MTPM parallelizes two-photon acquisitions by scanning multiple beamlets and allows dense sampling without target preselection. Multifocal microscopes have been implemented using microlens arrays (Bewersdorf, Pick, and Hell, 1998), diffractive optical elements (Sacconi et al., 2003), etalons (Fittinghoff, Wiseman, and Squier, 2000), beamsplitters and mirrors (Nielsen et al., 2001), and spatial light modulators (Shao et al., 2012). Longer pixel dwell times and therefore total excited photon flux can be achieved with MTPM without reducing the frame rate. This increases Poisson-noise limited SNR compared to single-spot two-photon for equivalent imaging speeds, with SNR scaling as  $\sqrt{N} \cdot \text{SNR}_0$ , for  $N$  additional equal foci and a single spot SNR of  $\text{SNR}_0$ . This has been exploited to image calcium in neural cells with high SNR (Yuan et al., 2007; Watson, Nikolenko, and Yuste, 2009; Kurtz et al., 2006). Spatial multiplexing of two-photon excitation, however, removes the ability to assign excited fluorescence to a single spatial location with total certainty. The imaged fluorescence is susceptible to crosstalk, degrading contrast in highly scattering tissue such as the mammalian brain. This limits achievable imaging depths and mixes functional signals from different cells, confusing analysis of their underlying activity. Previous MTPM implementations improved robustness to scattering by descanning fluorescence onto

multianode photomultiplier tubes (PMTs) (Kim et al., 2007) and developed reassignment algorithms for photons collected on the wrong anode (Cha et al., 2014). The descanned collection, however, reduces photon collection efficiency due to the additional collection optics by 15-50% and, even if non-descanned (Cha et al., 2015), must use relatively low quantum efficiency (QE) multianode PMTs (16% QE at 550 nm (H7546, Hamamatsu)) compared to the sCMOS cameras used in wide-field detection (82% QE at 550 nm (Orca Flash 4.0 V2, Hamamatsu)), decreasing functional SNR.

We have developed a novel photon source localization and MTPM strategy implemented with non descanned epifluorescent collection for fast functional imaging of neural signals. This has allowed us to maintain the increased SNR of MTPM whilst mitigating the effects of scattering on the recording. In this paper, we describe our MTPM implementation and algorithm and show that it increased image contrast at depth and reduced functional crosstalk between pixels in neural imaging data. We also analyzed the effect of source localization on the SNR and found it was maintained for densely labeled samples.

### 3.2.2 Methods

#### Multifocal two-photon setup

We built a custom MTPM for functional neural imaging (Fig. 3.1). A Ti:Sapphire laser beam (Mai Tai HP, Spectra Physics), tuned at 800 nm with a 80 MHz repetition rate, passed through a half wave plate and polarising beam cube to control the power, typically between 400 and 700 mW at the sample. A 6:5 Keplerian telescope (focal lengths +300 mm, Thorlabs AC508-300-B; and +250 mm, Edmund Optics G322 311 525) reduced and relayed the beam waist to the downstream optics. A second telescope consisting of a +700 mm cylindrical lens, a -20 mm cylindrical lens, and a +50 mm spherical lens (Thorlabs, LJ1836L1-B, LK1085L1-B and LA1131-B) shaped the beam into a line before it entered a microlens array (MLA, 0.15 mm pitch, 0.26 mm focal length, Ultra Precision and Structured Surfaces (UPS2)) which split it into beamlets. Sandwiching the MLA between two 1" glycerol-filled glass coverslips increased its focal length to +0.975 mm to achieve the desired objective fill fraction of 0.8. The shape of the beam into the MLA determined the envelope of the beamlet line array in the sample (Fig. 3.2(a)). Each beamlet rastered a rectangle in the sample, with the rectangle's long axis perpendicular to the beamlet line's axis (see Fig. 3.2(d)). This allowed efficient utilization of the CMOS camera's

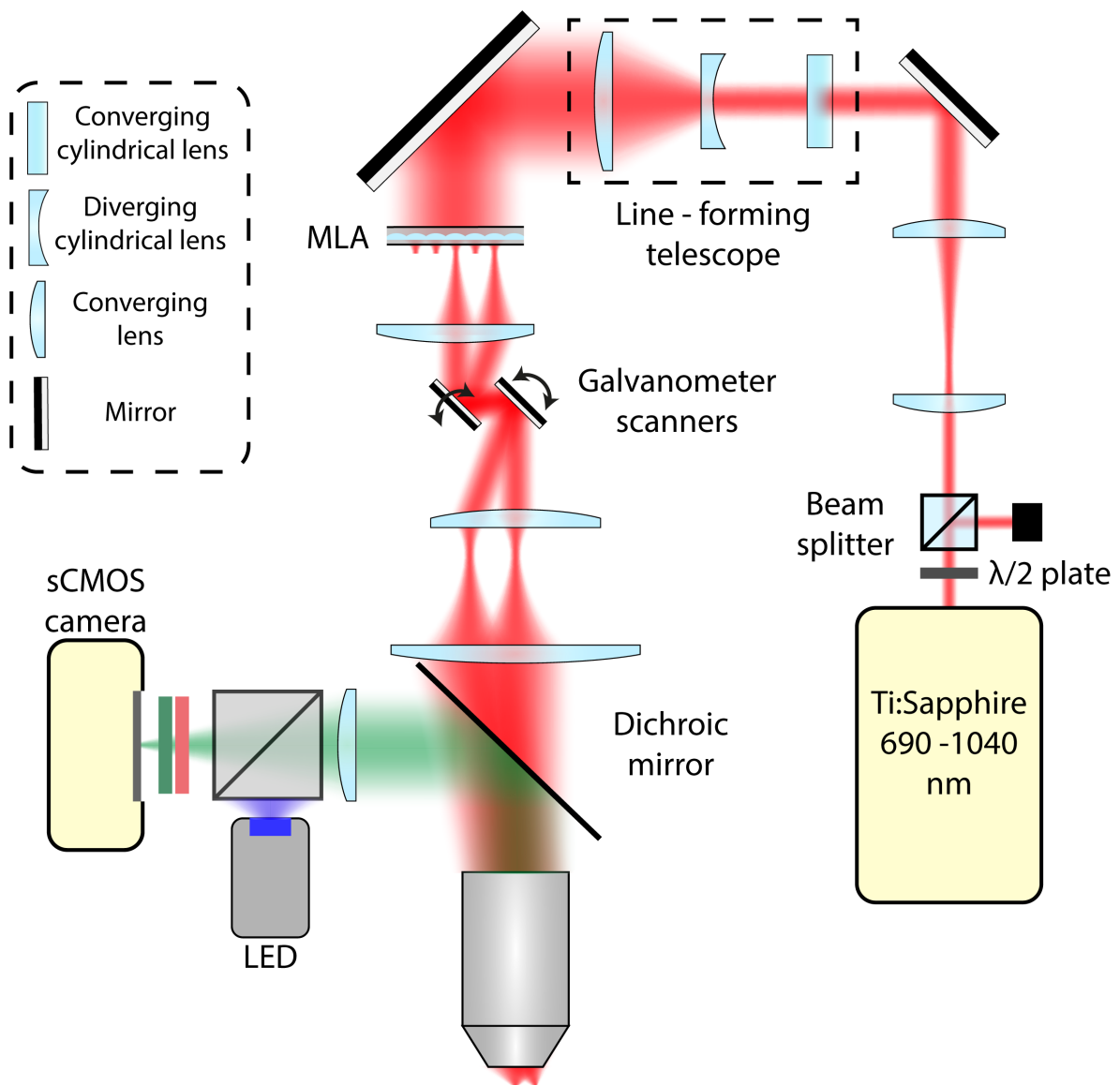


**Figure 3.1: The multifocal apparatus.** The laser beam is shaped into a line by an asymmetric telescope before passing through a microlens array which splits it into multiple beamlets. Individual beamlets are collimated and directed onto galvanometer mirrors which are conjugate with the back focal plane of the objective lens. The beamlets are rastered in the sample forming an image which is collected onto a CMOS camera synchronised with the galvanometers. A wide-field LED excitation path is used for comparison with the multifocal excitation.



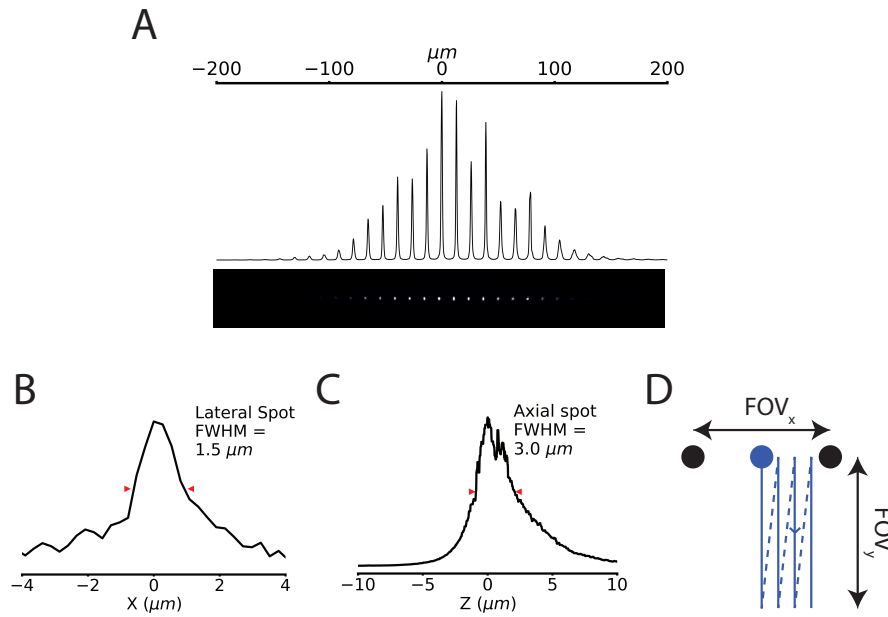


**Figure 3.2: Optical characteristics of the multifocal array.** a) Example image of a line beamlet array on a thin fluorescent slide. b) Lateral and c) axial cross sections of a single beamlet scanned through a thin fluorescent layer. d) An illustration of the scanning strategy used. Each beamlet is rastered in a rectangle orthogonal to the beamlet axis to build up the image. The temporally oversampled images used in the source localization process consist of one image per vertical raster line, in this illustration, four images.

central section and therefore maximized the frame rate. It is important that the line lies centrally on a single line of microlenses to achieve maximum excitation efficiency in the sample. A +20 mm lens (Thorlabs, LA1074-B) collimated the beamlets into galvanometer mirrors (Cambridge Technology) before they passed through the scan (+75 mm, Thorlabs AC254-075-B), tube (+300 mm, Thorlabs AC508-300-B) and objective (1.0 NA water immersion, 25 $\times$ , Olympus XLPlan N) lenses into the sample. A 670 nm dichroic (Chroma, ZT670rdc) directed non-descanned epifluorescence through a +180 mm tube lens (Thorlabs, AC508-180-A) onto the CMOS camera (Orca Flash 4.0 V2, Hamamatsu). We filtered emission with 525/50 nm bandpass (Chroma, ET 525/50) and 750 nm short pass (Semrock, FF01-750/SP-25) filters. A blue light-emitting diode (LED; Thorlabs M490L3, excitation filter Semrock FITC-Ex01-Clin-25), collimated with a 16 mm focal length aspheric lens (Thorlabs ACL25416U-A) and reflected to the sample with a long pass dichroic mirror (Semrock FF495-DI03-25X36), excited one-photon epifluorescence in wide-field mode.

A National Instruments DAQ (PCIe-6321) and custom LabVIEW code controlled the galvanometers, and Micromanager (Edelstein et al., 2014) controlled the camera acquisition. Spike2 electrophysiology software and a Power1401 digitizer (Cambridge Electronic Design) controlled

the excitation shutter, electrophysiological stimuli and master timing of the galvanometer's scans and camera acquisitions. To acquire a synchronous imaging and electrophysiology run, the digitizer triggered the camera in 'free run' mode at the beginning of each acquisition. The digitizer recorded the camera readout start signal and triggered each full frame scan of the galvanometer mirrors. For functional imaging, we rastered each beamlet in a rectangle with 8 lines filling the beamlet pitch to fully cover the field of view. An illustration of an equivalent 4-line scan pattern is shown in Fig. 3.2(d). For a standard image, we set the exposure time to just over the scan time. As the beamlets have an approximately Gaussian envelope (Fig. 3.2(a)), the resulting image has a Gaussian intensity profile parallel to the beamlet axis. To apply the source localization process, we imaged at approximately 8 times this frame rate so that in each frame a single line from each beamlet was imaged (i.e. one image per vertical line in Fig. 3.2(d), example images shown in Fig. 3.3(a)). The exposure time of the camera was adjusted to synchronize it with the galvanometers. All analysis and image processing was carried out using Python 3 and results are reported as mean  $\pm$  standard error of the mean.

### Image reconstruction

To improve MTPM's resistance to scattering, we developed a source-localization process to reassign scattered photons to their likely original emitted locations. Instead of exposing the camera for the full 8 line scan pattern, we imaged at  $8\times$  the scan speed to generate a set of 8 'streak' images per time point, one for each line (see Fig. 3.2(d) for equivalent 4-line diagram, example 'streak' images in Fig. 3.3(a)). Taking the mean of these frames is equivalent to exposing the camera for a full scan. Due to the structured illumination in each 'streak' image, any light collected off the streaks is known to be scattered. A 100-iteration Richardson-Lucy deconvolution ((Richardson, 1972; Lucy, 1974), implemented in scikit-image (Walt et al., 2014)), estimated the emitter distribution in the absence of scattering, using a deconvolution kernel derived from Monte Carlo modeling of photon propagation in scattering tissue. We initialized the deconvolution with a flat prior and updated the image using the equation

$$u_{t+1} = u_t \cdot \left( \frac{d}{u_t \otimes p} \otimes \hat{p} \right), \quad (3.1)$$

where  $u$  is the deconvolved image,  $t$  the current iteration number,  $d$  the measured image,  $p$  the point spread function and  $\hat{p}$  the point spread function mirrored along the  $x = y$  axis. This is

the same iteration scheme as described in section 1.4.5. Reflectively padding the boundaries reduced edge artefacts in the final image.

We generated the PSF using Monte Carlo simulation in a similar manner to (Rupprecht et al., 2015) by simulating the propagation of photons from a point source at  $(x, y, z) = 0$  through a slab of scattering tissue extending from  $0 \leq z \leq z_h$ . We simulated photons with an initial propagation angle drawn from a uniform distribution over the elevation and azimuthal angles corresponding to a NA of 1 to match the objective used in this experiment. The contribution from photons outside of this range was assumed to be negligible. The photons were propagated through the tissue for a length drawn from an exponential distribution with a characteristic scattering length  $\mu = 20 \text{ mm}^{-1}$  (Rupprecht et al., 2015). If  $z < z_h$ , we simulated a scattering event by drawing a new propagation angle from a uniform distribution between 0 and  $2\pi$  in azimuth and from a Henyey-Greenstein phase function (Henyey and Greenstein, 1941) with a forward scattering anisotropy of  $g = 0.9$  in elevation (Rupprecht et al., 2015). The propagation and scattering steps were then repeated until the photon left the tissue. The photon was then backprojected along its final propagation angle to find its  $(x, y)$  position for  $z = 0$  (Fig. 3.3(b)). We assigned the photon to a camera pixel according to its location and repeated the process for  $10^8$  photons to sample the kernel. This analysis did not consider the effect of the PSF of the microscope upon the deconvolution.

Multiple PSFs were generated for different modeled depths and applied to test data to decide upon a final PSF and iteration number to use in the reconstructions. We manually reviewed the contrast and high spatial frequency content of a test image after deconvolution with different PSFs and found the best results when using a scattering kernel for a tissue depth of  $z_h = 190 \mu\text{m}$ , although good results were observed for depths of 100 to 200  $\mu\text{m}$ , the maximum depth modeled. We show a cross section through the PSF in Fig. 3.3(c). Although the same deconvolution parameters were applied to all data for comparison, tailoring the PSF and deconvolution parameters to an acquisition's specific parameters could improve performance. Deconvolving the streak images suppressed off-streak illumination while increasing the brightness of the illuminated features on the line as shown in Fig. 3.3(a). For some deeper, lower contrast images a one-dimensional median filter parallel to the streaks was applied after the deconvolution to suppress noise and improve contrast. Complete frames for each time point were then recovered by taking a maximum intensity projection through each set of 8 deconvolved streak images.

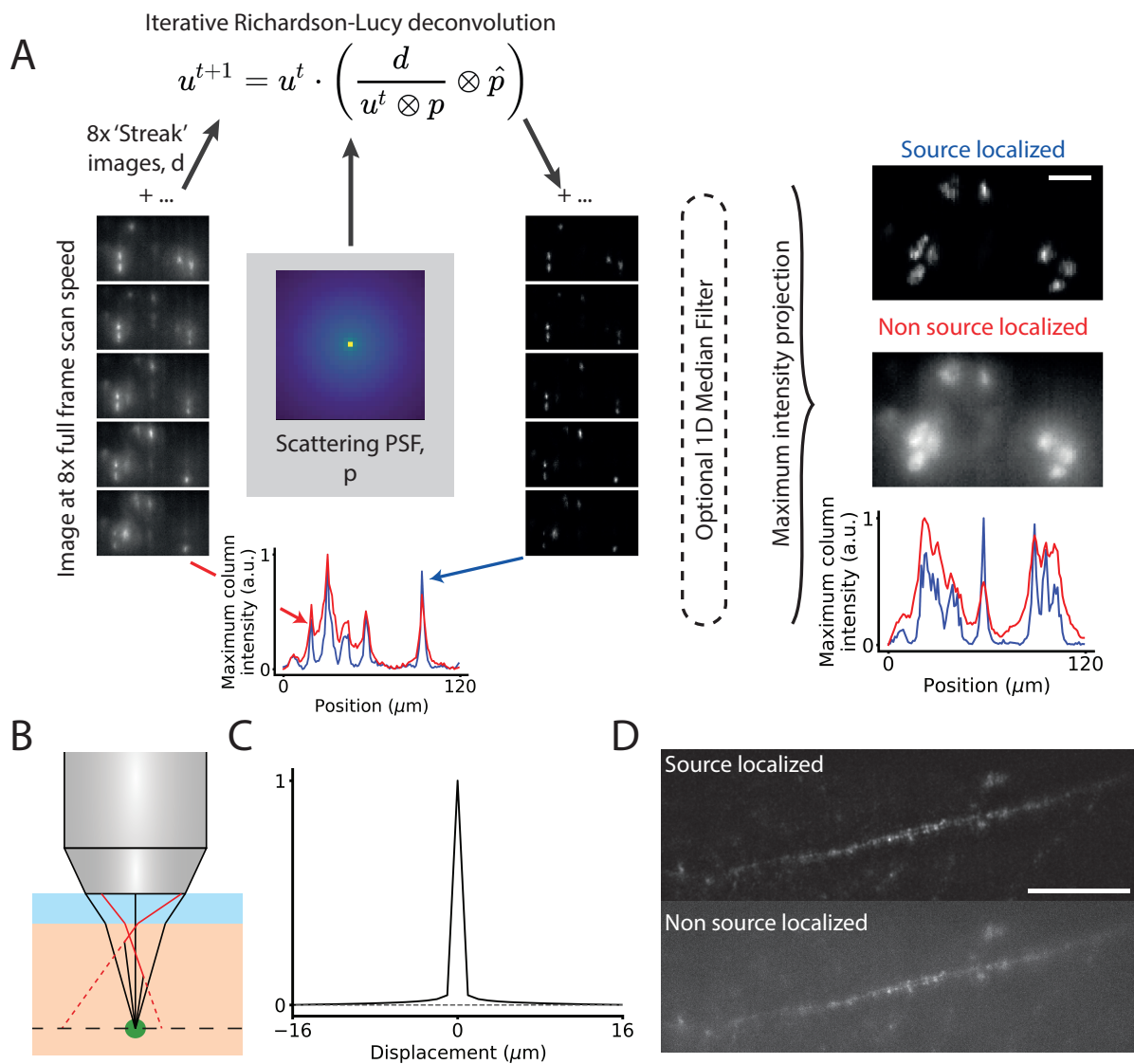


**Figure 3.3: The source localization process.** a) To generate a single source-localized frame, eight temporally oversampled images are acquired, corresponding to a single line scan from each beamlet. A subset of these are shown in the leftmost column of 'streak' images. Any illumination arriving onto the camera not on the line has arisen from scattering of the emission. We use Richardson-Lucy deconvolution to reassign the light back to its probable origin. The right column of 'streak' images shows the deconvolved images. Below these columns is a maximum intensity projection in  $y$  of the bottom 'streak' image showing the increase in contrast due to source localization. Once the light is reassigned, we take a maximum intensity projection through the temporally oversampled frames to recover a single frame. The two right-most images show a comparison between a source localized frame and an unprocessed image and below them a maximum intensity projection in  $y$  to show the increased contrast from source localization. Scale bar  $20 \mu\text{m}$ . b) A diagram of the Monte Carlo method used to generate a deconvolution kernel for the Richardson-Lucy deconvolution. Photons from a point source (green dot) were propagated through a scattering medium and backprojected when they reached the surface. Red rays were scattered and the dotted lines show backprojection to their apparent origin. Black rays are unscattered light. c) A cross section through the scattering PSF used for the deconvolution. The sampled PSF was approximately radially symmetric. d) A source localized (top) and non-source localized (bottom) image of a layer 2/3 pyramidal cell's apical dendrite labeled with membrane-targeted GFP. 12 lines per frame, scale bar  $50 \mu\text{m}$

### Analysis of depth penetration

To determine whether source localization reduced the effects of scattering at depth in brain tissue, we took depth stacks through fixed brain slices containing cells expressing membrane localized GFP. We used the Michelson contrast metric (Michelson, 1927) to measure the relative contrast of the cells and their background, defined as

$$C = \frac{I_{max} - I_{min}}{I_{max} + I_{min}}, \quad (3.2)$$

where  $C$  is the contrast,  $I_{max}$  is the maximum pixel intensity of a cell and  $I_{min}$  is the minimum intensity of the cell's surroundings, the background. Scattering will tend to increase the intensity of the background and decrease the intensity of the cell, reducing this contrast metric. In order to correctly identify  $I_{max}$  and  $I_{min}$  as cellular GFP signal and extracellular space and not from, e.g., uneven illumination, we segmented the cells and their surrounds from the image and measured the intensities from these areas. To segment the cells we thresholded the image, choosing the pixels with intensities above the 80% cutoff of the maximum of the image histogram and removed small objects by 4 binary erosion iterations followed by 4 dilation iterations. The contrast was set to zero if all or no pixels were segmented. We calculated  $I_{max}$  and  $I_{min}$  as the 99.9th percentile and 10th percentile of the segmented intensities respectively. The metric was robust to changes in the percentiles used.

### Modeling the effect of foci separation on contrast at depth

To assess the effect of varying the foci separation on the source localization process we modeled the contrast reduction with depth for different spacings and tissue scattering coefficients. We used tissue scattering values of  $\mu = 10, 20$  and  $40 \text{ mm}^{-1}$ . We split a reference single-spot two-photon image of GFP-expressing cells into sets of images consisting of vertical lines analogous to the 'streak' images in Fig. 3.3(a), using a different streak separation for each set. These are equivalent to the temporally oversampled images used in the source localization process with the oversampling factor required the line separation in pixels. We convolved these images with scattering kernels for different depths and scattering coefficients generated using our Monte-Carlo model. Noise was added by replacing each pixel intensity value,  $I_0$ , with a value drawn from a Gaussian distribution,  $P(I | \mu, \sigma)$ , with  $\mu = I_0$  and  $\sigma = I_0/10$ . To generate a set of source localized images we applied Richardson-Lucy deconvolution to the noisy line

image series using the scattering kernels we used previously cropped to  $32 \times 32$  pixels. We then generated our final images for comparing source-localized and standard MTPM by taking a sum projection through the noisy line images and a maximum intensity projection through the deconvolved images, respectively. For each line separation and scattering coefficient we estimated the expected 50% contrast cutoff depth by fitting a 3<sup>rd</sup> order polynomial to the contrast depth profile.

### Preparation of brain slices for functional imaging

To test our multifocal setup and source localization algorithm on time-resolved image series, we collected neuronal data from mouse acute brain slices. We used two different preparations: slices where many cells were labeled with bath application of an acetoxymethyl-ester (AM-ester) calcium dye (referred to as multi-cell labeling), and slices where a single cell was intracellularly loaded with calcium dye potassium salt (single-cell labeling).

We used the slicing procedure described in Chapter 2. After the slices were prepared they were then labelled with either an AM-ester or potassium salt dye as follows. For multi-cell labeling 50  $\mu\text{g}$  of Cal-520 AM ((Tada et al., 2014), AAT-Bioquest) was dissolved in 10  $\mu\text{l}$  of DMSO with 10% w/v Pluronic F-127 (Invitrogen) and 0.5% v/v Kolliphor EL (Sigma-Aldrich) (Francoville et al., 2011). The slices were then incubated for 40 minutes at 34 °C in 2 ml of Na-ACSF (Table 2.1) with the Cal-520 AM/DMSO mixture pipetted onto the surface of each slice. The 2 ml of Na-ACSF was kept oxygenated by blowing 95% O<sub>2</sub>/5% CO<sub>2</sub> onto its surface. After loading, the slices rested in Na-ACSF for at least 20 minutes before recordings were taken.

We recorded single cell responses to excitatory stimulation for both multi-cell and single-cell labeled slices. For multi-cell labeled slices, a concentric bipolar electrode was placed at the cortical layer 6 and white matter boundary to extracellularly stimulate for 0.5 ms at 1 Hz. Responding cells were found by imaging in nearby areas of cortical layers 2/3 and 5. We adjusted the current delivered to the threshold required to evoke an AP-induced calcium transient. Imaging trials were performed at 20 and 50 Hz using MTPM and LED illumination.

To image single-cell labelled cells, cortical cells were patched using 4 - 7 MOhm patch pipettes containing intracellular solution described in table 2.4 to which 0.1 mM Cal-520 potassium salt (AAT-Bioquest) was added. Trials were rejected when resting membrane potential exceeded -60 mV with zero injected current. After sealing and breaking in, the calcium dye

diffused into the cell for 30 minutes while access resistance was kept below 15 M $\Omega$  by suction. After intracellular loading, imaging trials were taken at 10, 20, 50, 100 and 200 Hz using MTPM and LED illumination for two different trial types. The first trial consisted of eliciting pairs of APs with differing time separation. Six pairs of spikes were stimulated with 0.5 ms current injections with 0.3, 0.2, 0.1, 0.05, 0.02 and 0.01 s between the start of each stimulus and 6 s between the start of each pair. The second trial used 0.5 ms current injections to elicit trains of spikes with identical inter stimulus intervals. 1, 3, 5, 7 and 9 spikes were elicited with 0.05 s between stimuli and 6 s between trains.

All MTPM imaging trials were taken at room temperature with a power under the objective of 400 - 700 mW. Imaging cells during whole-cell patch clamp recordings did not affect resting membrane potential, input resistance or cell capacitance at these power levels. Trial order was generated randomly for each cell to control for the effects of photobleaching and physiological rundown.

### **Analysis of calcium imaging videos 1: Pixel crosstalk**

To determine the effect of the source localization algorithm on functional neural imaging data, we first tested whether source localization would reduce the crosstalk between the fluorescent signals from different cells caused by scattering. To quantify this, we selected regions of interest (ROIs) containing a single responsive cell and quantified the contribution of the intracellular functional time course to the background in the surrounding pixels. If this contribution was high, then time courses from other cells in the ROI would be contaminated by scattered light from the central cell. We analyzed both multi-cell and single-cell labeled data. While the technique is optimized for multi-cell imaging, the single-cell image series enable discernment between fluorescence arising from network activity and fluorescence scattered from a single, active cell.

For multi-cell labeling, cells responsive to stimulation surrounded by non-responsive cells were identified by hand and  $\sim 30 \times 30 \mu\text{m}$  regions of interest (ROIs) selected for the analysis. We segmented the intracellular ROIs from the source-localized video series using local correlation maps. We generated a 2D image by calculating the Pearson correlation of every pixel with its 8-connected neighbors. This was then thresholded using the method in (Yen, Chang, and Chang, 1995). Binary closing and 2-round opening was applied to remove smaller objects. If more than one region remained, the largest connected component was chosen as

the intracellular ROI. For each cell, we chose a mean segmentation by combining the segmentation results from individual video series and choosing pixels that were included in more than a quarter of them. Intracellular time courses were extracted from MTPM, source-localized MTPM, and LED image series by taking the mean values of the cellular ROIs generated using the source-localized MTPM. Extracellular traces were generated by averaging the pixels in the surrounding area, not including the cellular ROIs. We generated  $\Delta F/F_0$  traces by dividing the time courses by the mean of the baseline brightness minus the average dark frame value. Intracellular calcium concentration dynamics can be inferred from calcium indicator  $\Delta F/F_0$  traces. We measured the signal localization due to the source localization algorithm as the average size of the ratio between the intracellular ROI calcium transient and the extracellular ROI calcium transient, which we called the signal localization ratio (SLR).

Segmenting the single-cell labeled data was simpler due to the lack of background staining. We segmented the cells by generating and thresholding a 2D variance map of the pixel time courses and similarly removed small objects by binary closing and opening. We calculated the extracellular ROI by extending for 5 pixels in  $x$  and  $y$  around the bounds of the segmented cell to avoid a ringing artefact from the deconvolution in the single-cell labeled images where there was a small anticorrelated signal. This artefact is due to the highly localized single-cell labeling and would not occur in densely labeled tissue due to the maximum projection step in the reconstruction. To avoid overestimating the power of our technique we used this smaller ROI and counted anticorrelated ringing as unreassigned signal. We carried out the same analysis as for extracellularly loaded data, excluding signal from the dye inside the patch pipette.

### Analysis of calcium imaging videos 2: Signal-to-noise ratio

We examined whether the reconstruction process affected the SNR of the functional time courses as noise amplification can be a side effect of Richardson-Lucy deconvolution. For intracellular data for which we acquired simultaneous whole-cell patch clamp electrophysiology, we estimated the single-spike signal amplitude by fitting a model of the indicator dynamics.<sup>1</sup> We model a fluorescence signal consisting of  $K$  spikes at times  $\{t_k\}_{k=1}^K$  as

$$f(t) = \sum_{k=1}^K A c_{\alpha,\gamma} \left( e^{-\alpha(t-t_k)} - e^{-\gamma(t-t_k)} \right) u(t - t_k), \quad (3.3)$$

<sup>1</sup>This fitting was done by a collaborator on this project, Dr. Stephanie Reynolds.



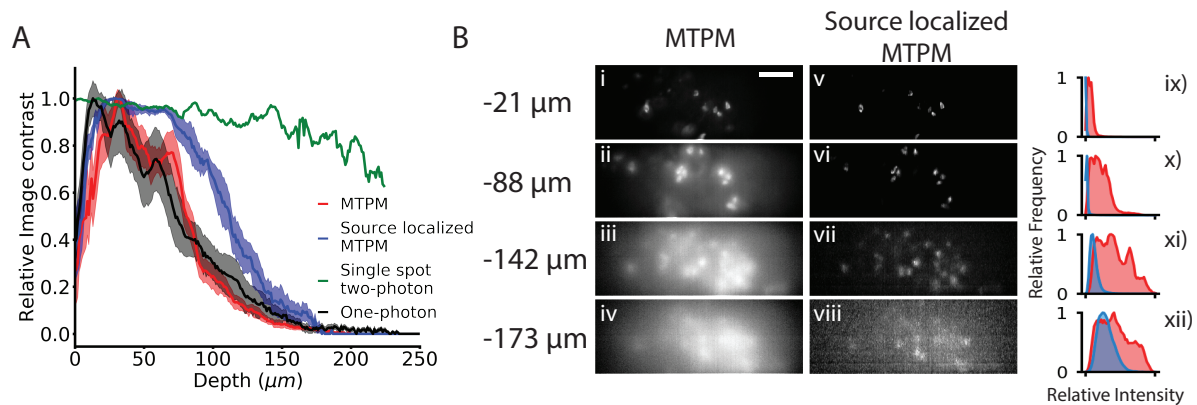


**Figure 3.4: Characterization of the increased depth penetration from source localization.** a) Image contrast plotted against depth from the tissue surface for one-photon wide-field LED illumination, MTPM, source localized MTPM and two-photon point scanning. Plotted as mean  $\pm$  s.e.m. b) Example frames taken at different depths in fixed brain tissue without (i - iv) and with (v - viii) source localization. To the right ix) - xii) are the histograms of the normalized images, in red without source localization and blue with source localization. Scale bar  $50 \mu\text{m}$

where  $u(\cdot)$  is the indicator or step function, which is equal to zero for negative arguments and one otherwise, and the parameters  $\{A, \alpha, \gamma, c_{\alpha, \gamma}\}$  define the shape of the calcium transient. The speed of the pulse's rise and decay is determined by the parameters  $\alpha$  and  $\gamma$ , which were estimated from (Tada et al., 2014) to be  $3.18 \text{ s}^{-1}$  and  $34.39 \text{ s}^{-1}$  respectively. The factor  $c_{\alpha, \gamma}$  is a normalization constant, which ensures that the peak amplitude of a calcium transient is at  $A$ . The signal samples,  $y[n]$ , are assumed to be corrupted by additive noise in the acquisition process, such that  $y[n] = f[n] + \epsilon[n]$ , where  $f[n] = f(nT)$  are samples of the fluorescence signal with time resolution  $T$  and  $\epsilon[n]$  are samples from a zero-mean normal distribution with standard deviation  $\sigma$ . The noise level of each trace,  $\sigma$ , was estimated from the sample standard deviation of the final 0.2 s of the trace in which there was no spiking activity. Given knowledge of the spike timings from the electrophysiology and the signal samples, the amplitude parameter,  $A$ , was fit to Eq. (3.3) using a linear least squares program. For the extracellularly loaded data we were unable to fit a model as we did not have simultaneous 'ground truth' electrophysiology and so we estimated the signal size,  $A$ , as the peak intensity in a short window after the stimulus was applied. We measured the trace noise level by taking the standard deviation of the final 0.3 s of the trace when there was no activity. The peak signal-to-noise ratio (PSNR) of the data is then calculated as  $A^2/\sigma^2$ .

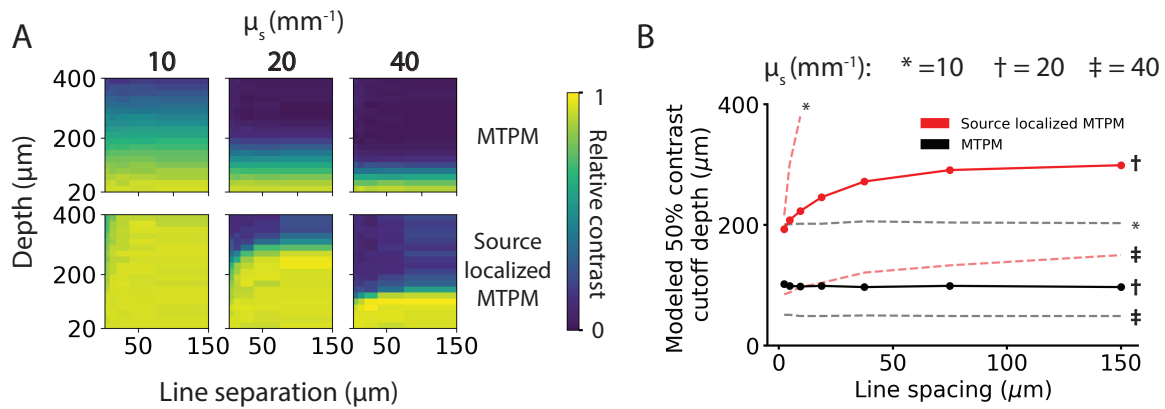


**Figure 3.5: The predicted effect of changing foci separation on depth penetration.** a) False color plots of relative contrast modeled at different depths for varying line spacing for standard MTPM and source localized MTPM for three different scattering coefficients b) A plot of the depths corresponding to a 50% decrease in relative contrast for MTPM (black) and source localized MTPM (red) for different line spacings. Solid lines show the data for the scattering coefficient used in the reconstructions of the experimental data, while dashed lines were modeled using different scattering coefficients. Source localization increases maximum imaging depth compared to standard MTPM, improving contrast more at larger line separations. Increased depth penetration must be traded off against increased imaging speed or SNR.

### 3.2.3 Results

#### Source localization increases contrast at depth

Source localization decreases blur from scattering at depth in tissue. We took depth stacks through fixed cortical tissue containing cells labeled with GFP to determine whether our source localization procedure increased image contrast at depth. We calculated the changing contrast with depth for 5 different cortical fields of view for wide-field LED illumination, MTPM and source localized MTPM, (Fig. 3.4), along with a single area for a typical 2PLSM for comparison. The data shows a drop off of contrast quickly with depth for all 3 modalities compared to a standard 2PLSM, as expected. The 50% cutoff for the source localized case of  $112 \pm 5 \mu\text{m}$  is significantly deeper than for the non source-localized ( $80 \pm 3 \mu\text{m}$ ,  $z = 0.0$ ,  $p = 0.04$ , Wilcoxon signed rank,  $n = 5$  areas, mouse age 42 days) or LED illumination ( $72 \pm 6 \mu\text{m}$ ,  $z = 2$ ,  $p = 0.009$ , Wilcoxon ranked sum test,  $n = 5$  areas, mouse age 42 days).

To investigate how changing the spacing between the foci might affect the depth penetration of source localized MTPM, we modeled the contrast loss with depth for foci separations from 2.3 - 150  $\mu\text{m}$  for three different scattering coefficients between 10 and 40  $\text{mm}^{-1}$ . Smaller line separations allow for greater parallelization of the acquisition and therefore an increase in SNR for the same imaging speed. As shown in Fig. 3.5(a) & (b), source localization increases

the maximum imaging depth compared to standard MTPM for all scattering coefficients and line separations. Source localization's depth penetration increases asymptotically relative to standard MTPM with increasing line spacing. The asymptote value and rate of approach decrease with increasing scattering coefficient. At small line separation the deconvolution is less effective at reassigning scattered photons to their correct location. At the line separation implemented in this paper and expected experimental scattering coefficient ( $12.5 \mu\text{m}$  and  $20 \text{mm}^{-1}$  respectively) our model predicts a 50% contrast cutoff at  $98 \mu\text{m}$  for MTPM and  $230 \mu\text{m}$  for source localized MTPM. These cutoffs are deeper than those found experimentally. This could be due to the modeling of the scattering medium as a homogeneous block, or an underestimation of the scattering coefficient of the tissue.

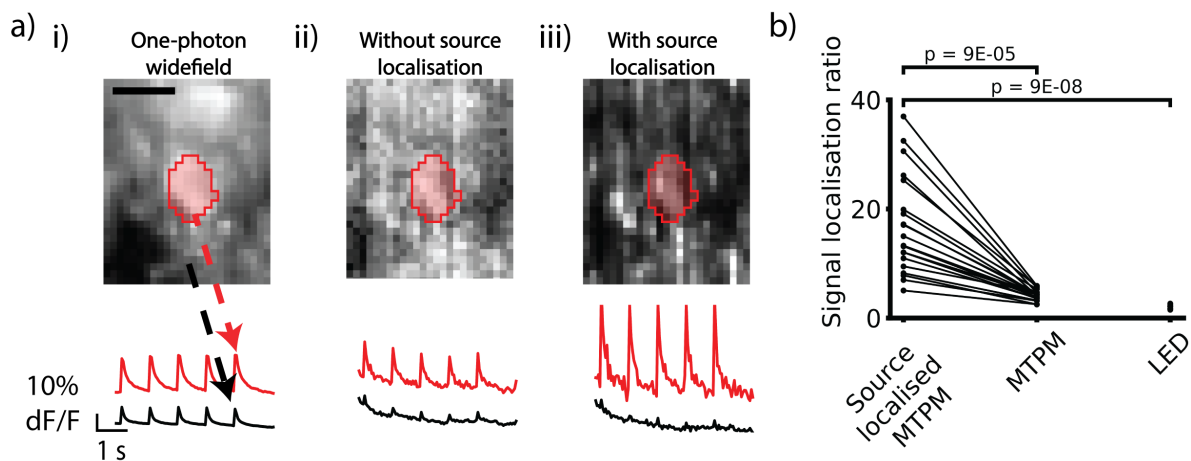


**Figure 3.6: Source localization decreases the functional crosstalk between adjacent neuronal structures.** a) Example ROIs and fluorescence time courses of multi-cell labeled neuronal tissue with a single responsive cell using i) wide-field LED, ii) MTPM and iii) source localized MTPM. Red traces are the average of the red intracellular region and black traces of the entire region outside the red area. In both the wide-field LED and MTPM case there is a significant component of the intracellular time course contaminating the extracellular pixels. This leads to difficulty discriminating between cells in areas with multiple active cells. Source localization drastically reduces the relative contribution of the intracellular time course to the extracellular region. b) Summary data showing the ratio of peak intracellular to extracellular response to excitatory stimulus (the signal localization ratio) over 20 trials. This is significantly higher for source localized MTPM compared to MTPM or wide-field LED illumination. Scale bar  $10 \mu\text{m}$ .

### Source localization decreases functional crosstalk

Source localization reduces spurious functional signals from scattered light. Scattered in and out of focus light impedes single-cell resolution wide-field functional imaging in densely labeled samples. It is difficult to demix time courses from different cells, especially when the activity has a low SNR or is spatiotemporally dense. To test whether our source localization

strategy reduced the contamination of extracellular pixels with functional signal, we compared the ratios of peak  $\Delta F/F_0$  signal sizes from the mean time courses of segmented intracellular regions to the mean time courses of surrounding extracellular areas, the signal localization ratio (SLR, Fig. 3.6(a)). A larger ratio indicates a smaller contamination of the extracellular pixels. Comparing the same raw data with and without source localization shows a significant increase in the SLR when source localization is applied, with the mean SLR increasing from  $4.2 \pm 0.2$  to  $16.9 \pm 2.0$  ( $z = 0.0$ ,  $p = 9E-5$ , Wilcoxon signed rank,  $n = 20$  trials, mouse age 36 days, power used 700 mW, Fig. 3.6(b)). The SLR for the LED illumination in equivalent trials was found to be  $2.03 \pm 0.08$ , significantly lower than the source localized MTPM ( $z = 5.3$ ,  $p = 9E-8$ , Wilcoxon rank sums,  $n = 18$  trials, mouse age 36 days).

To ensure that these results were not confounded by neuropil or multicellular signal excited by the field stimulation, we repeated these experiments with single-cell labeled data. The above analysis produced similar results, with source-localized MTPM increasing the SLR from  $1.0 \pm 0.03$  to  $3.9 \pm 0.3$ , ( $z = 0.0$ ,  $p = 2E-8$ , Wilcoxon signed rank,  $n = 41$  trials, mouse age 28 days, power used 600 mW). The sourced localized SLR was also significantly greater than the LED SLR of  $1.16 \pm 0.04$  ( $z = 7.7$ ,  $p = 1E-14$ , Wilcoxon rank sums,  $n = 41$  trials, mouse age 28 days). This indicated that the source localization does indeed reduce signal crosstalk by reassignment of scattered signal photons back to their emitted location. The smaller SLR seen in the single-cell labeled data is likely due to two factors. Firstly, the extracellular ROI used in the analysis is smaller to eliminate effects from reconstruction artefacts as discussed in the previous section. As scattering is highly forward biased, the closer pixels are likely to contain a higher quantity of signal and increase the extracellular signal size. Secondly, the increase in peak signal due to source localization is much higher in the multi-cell labeling case, likely because in this case the reassignment of scattered photons not only increases signal photon collection but also reduces non signal-containing extracellular photon collection in the intracellular ROI.

### Source localization's impact on PSNR is labeling and frame rate dependent

The MTPM system captured neuronal calcium fluorescence transients at frame rates up to 200 Hz, with source-localization for frame rates up to 100 Hz (Fig. 3.7(a)). Above 100 Hz the temporal oversampling required for source localization made the FOV with our camera prohibitively small. We wanted to ensure that source localization did not reduce the SNR increase of MTPM over single spot 2P by introducing additional noise to the recordings. To do this we compared

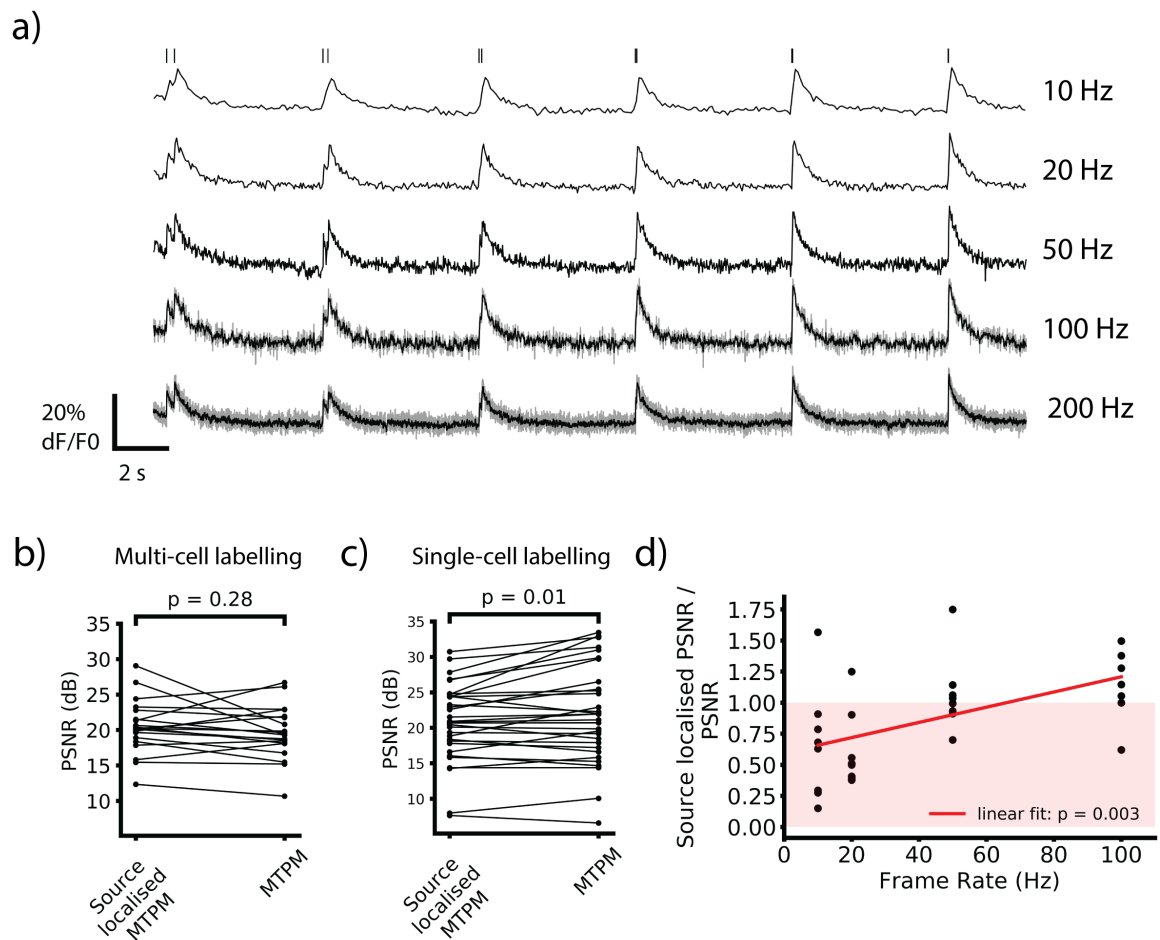


**Figure 3.7: The effect of source localization on PSNR is labeling and frame rate dependent.** a) Example single-cell labeled traces acquired at different frame rates. Traces are source localized for all but 200 Hz where no temporal oversampling or source localization was used. A binomial filter was applied to 100 and 200 Hz traces, and the raw trace is shown in gray. b & c) Comparisons of PSNR with and without source localization for all frame rates for multi-cell labeling (b) and single-cell labeling (c). Single-cell labeling shows a significant decrease in SNR when source localization is applied due to noise introduced in the deconvolution. This is not seen when imaging with densely labeled samples as the signal increase is much larger due to the reduction in non-signal-containing scattered light collected in the intracellular ROI. c) The ratio of source localized PSNR to non source-localized PSNR plotted against frame rate. This increases at higher frame rates as Poisson noise dominates over noise introduced in the deconvolution. Red area indicates worse performance for source localized videos.

the change in SNR between source localized and non source localized time courses. If the SNR is not decreased, then source localized MTPM increases signal through parallelization while reducing the drawbacks of wide-field detection in scattering samples. Source localization did not change the PSNR for multi-cell labeling significantly. The PSNR rose from  $126 (21.0 \text{ dB}) \pm 26$  to  $162 (22.1 \text{ dB}) \pm 40 \text{ dB}$  ( $z = 76$ ,  $p = 0.28$ , Wilcoxon signed rank,  $n = 20$  trials, mouse age 36 days, power used 700 mW, Fig. 3.7(b)). The peak signal and the noise were increased proportionately by the Richardson-Lucy deconvolution process.

Applying source localization to the single-cell labeled traces significantly decreased the PSNR when looking at the pooled data from  $443 (26.5 \text{ dB}) \pm 114$  to  $224 (23.5 \text{ dB}) \pm 48 \text{ dB}$  ( $z = 119$ ,  $p = 0.011$ , Wilcoxon signed rank,  $n = 31$ , mouse age 28 days, power used 700 mW, Fig. 3.7(c)). The difference between the two results can be accounted for by a larger increase in the signal amplitude for the source localized MTPM when using multi-cell labeling. With multi-cell labeling the source localized signal size is  $2.29 \pm 0.09$  times greater than for non source localized traces, whereas the increase for single-cell labeling is  $1.28 \pm 0.012$  ( $z = 6.25$ ,  $p = 4E-10$ , Wilcoxon rank sums,  $n = 20$ , mouse age 36 days, power used 600 mW). As discussed in the previous section, source localization is more beneficial to multi-cell labeled samples. This is because the deconvolution process not only reassigns light scattered from the interior of the cell back inside, increasing the signal, it also reassigns light scattered from other bright areas into the interior of the cell back out again, reducing the background.

The decrease in PSNR due to source localization in single-cell labeled samples is inversely correlated with frame rate (Fig. 3.7(d)). When looking at frame rates above 50 Hz, there is no decrease in PSNR when using source localization. Below 50 Hz there is a significant decrease in PSNR. The peak signal increases at all frame rates when source localization is applied. The increase in the noise level during the source localization process is greater below 50 Hz. This suggests that the deconvolution is introducing a noise component that is frame rate independent. At low frame rates this is larger than the Poisson noise intrinsic to fluorescence imaging and makes up a large fraction of the total noise. Here the noise increase exceeds the increase in signal, reducing the PSNR. At high frame rates, Poisson noise dominates and the fraction of the total noise that the deconvolution contributes is small. The increase in signal amplitude then compensates, leaving an unchanged PSNR. As this decrease is only seen in singly-labeled cells, it will not be an issue for most typical use cases for multifocal imaging. If labeling is sufficiently

sparse then high SNR one-photon excitation becomes a more viable imaging alternative. Multifocal imaging is best suited for situations where one-photon imaging would be impractical due to a large background fluorescence signal from non-target cells.

### 3.2.4 Conclusion

We have shown that exploiting the structured illumination inherent in multifocal two-photon microscopy can mitigate the effects of scattering that previously limited the extent of its application to mammalian brain imaging. The source localization process described here increases the image contrast at depth in scattering brain tissue, increasing the number of cells that can be sampled compared to regular MTPM. In brain slices, this can improve access to intact cells, synapses, and processes away from the cut surface. Future *in vivo* studies can also benefit as layer 2/3 of the mouse cortex lies at depths comparable to the 50% cutoffs for source localized MTPM. Although our implementation requires average powers known to heat brain tissue *in vivo*, future systems can avoid this problem with increased numerical apertures, higher laser pulse energies at decreased repetition rates, or dispersion compensation.

Source localization also reduces the mixing of signals from adjacent neuronal structures due to scattering. This is essential when neuronal activity is visualized by voltage indicators, as low amplitude fluctuations in their time course contain information about sub-threshold membrane potential dynamics. Their time course also cannot be modeled simply by a convolution of AP times with a characteristic pulse shape. Avoiding aliasing of this signal requires increasing the imaging frame rate.

Source localization does not decrease the PSNR of functional traces for densely labeled samples. The increase in brightness, which would usually increase PSNR, is offset by noise amplification during the deconvolution process. This could be mitigated by more sophisticated deconvolution algorithms, such as damped Richardson-Lucy (White, 1994). The quality of the deconvolution could also be improved by refining the PSF estimate, or using blind deconvolution to adjust the PSF to each individual imaging location (Fish et al., 1995).

As the source localization process requires temporally oversampling the image series, currently the FOV height is limited by the camera speed and the oversampling factor for source-localized MTPM. The FOV can therefore be increased with faster cameras or a reduction in the temporal oversampling factor, although this would likely reduce the deconvolution efficacy, as discussed in section 3.2.3. A second limitation is the computational cost of Richardson-Lucy

deconvolution. This is currently around 0.8 s per frame for an  $391 \times 80 \mu\text{m}$  FOV, leading to long computation times for high frame rate or long imaging sessions. Both the deconvolution itself and individual frame processing are parallelizable and so can improve with GPU or cluster based processing.

MTPM fills a gap between the commonly used imaging modalities of wide-field LED imaging and 2PLSM. MTPM achieves a speed and SNR closer to that of wide-field one-photon imaging without the large, out-of-focus background which swamps single-cell fluorescent transients and precludes cellular resolution population imaging. Source localized MTPM increases the scope of MTPM by mitigating its vulnerability to scattering. Source localized MTPM could prove particularly useful for two-photon voltage imaging with genetically encoded voltage indicators, which has so far struggled to achieve widespread use due to fast indicator temporal dynamics and small fluorescent responses.

### 3.3 Multifocal two-photon voltage imaging

#### 3.3.1 Introduction

In the previous section I discussed the design of a MTPM system and the development and testing of a technique to improve resistance to scattering. This was motivated by the poor performance of TPLSM in imaging voltage signals. Single-photon imaging is another alternative which will be explored in this thesis, however that technique does have a number of drawbacks which make it worthwhile to explore alternative imaging methods. Although wide-field single-photon imaging offers the highest SNR of functional imaging techniques, certain characteristics make it difficult to use for searching a 3D volume for small signals. Due to the high excitation rates and lack of optical sectioning, 1P imaging rapidly bleaches out a cylindrical volume above and below the focal plane. This makes iteratively imaging the processes of a cell with a 3 dimensional dendritic arbour at different depths to search for EPSP activation difficult, as the cell will likely be bleached a few slices into the search. Standard single-photon wide-field imaging techniques are therefore not particularly suitable for connectivity mapping experiments. Two photon imaging, on the other hand, is well suited to the acquisition of depth resolved stacks due to the excitation's axial confinement. Only the structures in focus are bleached and so repeats at different Z planes are possible with no SNR loss. A second issue, which will be explored in depth in chapter 4, is that the overlap of membranes in densely labelled tissue makes



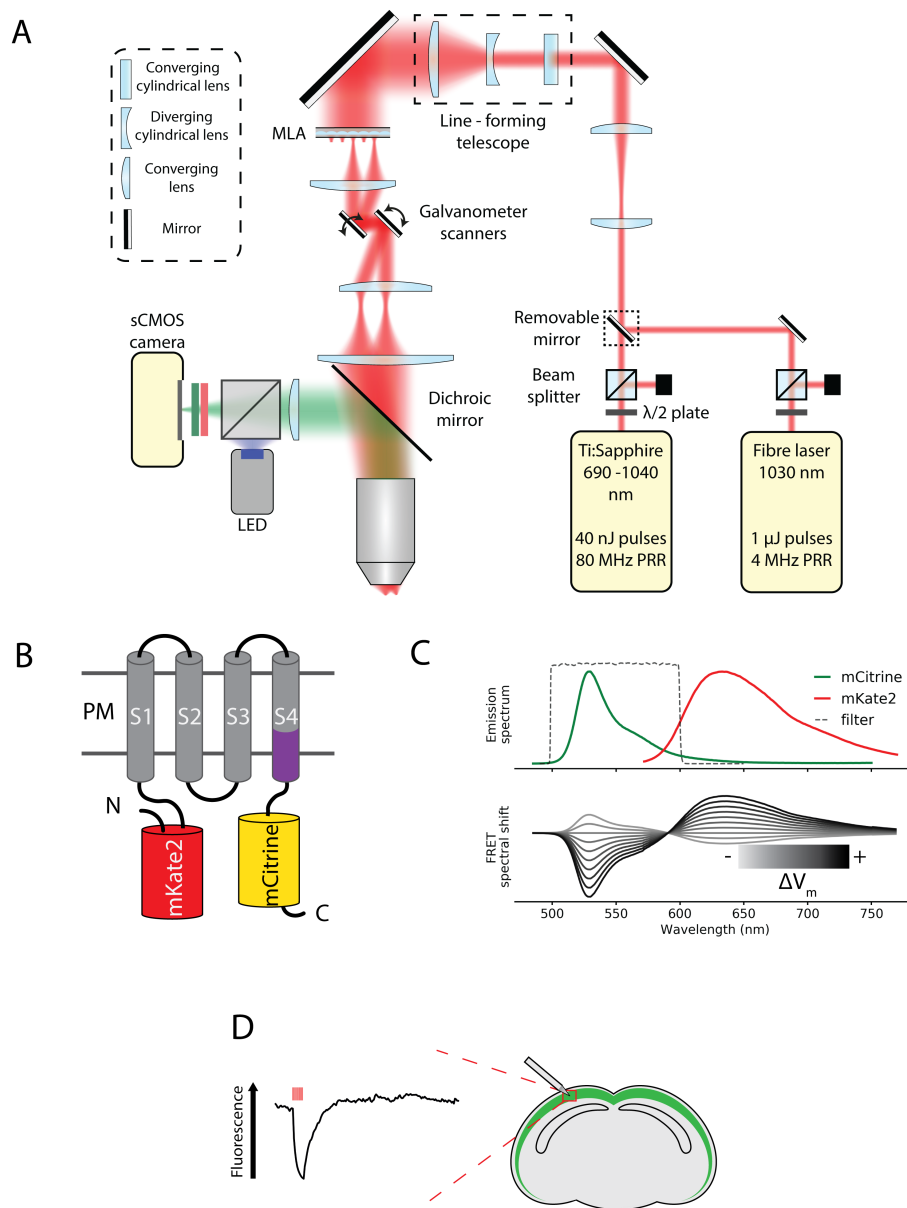


**Figure 3.8: Voltage imaging with MTPM.** A) The same multifocal setup was used with an additional laser source incorporated. The fibre source generated much higher peak powers, increasing excitation efficiency in the sample. B) A schematic of the voltage sensor chimeric VSFP-Butterfly. Changes in polarisation of the plasma membrane (PM) changes the separation of the two fluorescent proteins, changing the FRET efficiency between them. Drawn with reference to Akemann et al., 2012. C) Spectral characteristics of the GEVI. Top: the emission spectra of the proteins in the GEVI and the passband of the collection filter. Bottom: a cartoon of the shift in relative emission of the two FPs as the membrane hyper- and depolarises. Data from Chroma Technology Corporation, 2018. D) Collection of fluorescence from the FRET donor leads to a decrease in signal during stimulation of neurons.

single photon single-cell resolution imaging impossible due to the large unactive fluorescent signal excited from non-target neurons. Due to the reduced excitation volume, a much larger fraction of fluorescence excited with this technique when single-cell imaging would be signal containing, and so two-photon imaging could enable this. In this chapter I describe the results of experiments to determine if the multifocal two-photon microscopy system described in the previous section could be used for effectively imaging GEVIS from the VSFP family. The source localisation technique described previously was not applied to these acquisitions, as the first aim was to determine the baseline signals that could be achieved.

### 3.3.2 Methods

We used the same multifocal multiphoton optical setup as described previously in the chapter to image both brain slices expressing VSFP GEVIs. As shown in figure 3.8A, we added a second laser source co-aligned with the Ti:Sapphire used previously. The laser source used was a high power fixed-wavelength fibre laser emitting  $\approx 1 \mu\text{J}$ , 300 fs pulses at 1030 nm centre wavelength at 4 MHz pulse repetition rate. The maximum power emitted from the laser was 4 W, however due to the differing beam divergence the maximum power in the sample was limited to  $\approx 480$  mW, less than the maximum power in the sample afforded by the Ti:Sapphire with a maximum output of 3 W.

Slices were prepared as described in chapter 2 from mice densely expressing chimeric-VSFP-Butterfly Yellow-Red (Fig. 3.8B, (Mishina et al., 2014), 'pan-pyramidal') and mice sparsely expressing VSFP-Butterfly 1.2 (Quicke et al., 2019; Song et al., 2017) ('sparse'). A full discussion of the differences between these expression strategies can be found in chapter 4. Briefly, all cortical pyramidal neurons in 'pan-pyramidal' expressing mice express the indicator, whilst only a random subset of layer 2/3 neurons in sparse mice express the GEVI. This sparse expression allows identification of individual cellular responses apart from population responses. The indicators used report voltage by varying the FRET efficiency between two fluorescent proteins, mCitrine and mKate2. During imaging we collected a band of fluorescence encompassing mainly emission from mCitrine (Fig. 3.8C). In these GEVIs, the FRET donor decreases its emission on membrane depolarisation as the FRET efficiency increases, and therefore a decrease in fluorescence is seen during electrical stimulation (Fig. 3.8D).

We examined population responses for LED and MTPM signals in pan mice. Population

signals were evoked with a concentric bipolar electrode (10 pulses at 20 Hz) and imaged using one-photon and two-photon excitation. We examined single cell responses in sparse mice. Individual cells were patched and imaged over multiple trials whilst being intracellularly stimulated with current injections through the patch pipette.

### 3.3.3 Results

#### Predictions of laser performance

Two-photon excitation is much less efficient at exciting fluorescence compared to one-photon. As discussed in the chapter 1, high pulse energy lasers improve fluorescence excitation without increasing average power delivered to the sample. Commonly used commercial Ti:Sapphire oscillators such as that used in the previous section typically emit pulses at 80 MHz, and emit a peak power of a few Watts at around 800 nm (Newport, 2018). The mode-locked PRR is inversely proportional to the cavity round trip time. Decreasing the PRR therefore requires the use of increased cavity lengths. Fibre laser cavities can be simply extended by increasing the fibre length and so are economical to use when a lower PRR is required. Ytterbium doped fibre lasers are commonly used for high power mode-locked applications due to their wide gain bandwidth allowing short pulses (Kaluza et al., 2012). The gain bandwidth structure of these lasers limits their operation to a small number of wavelengths, typically either 1030 nm or 1050 nm, without the tuning capability offered by the broad gain of Ti:Sapphire (Kaluza et al., 2012). The benefits of the more efficient excitation must therefore be weighed against the disadvantage of imaging with a wavelength that is quite far from the excitation peak for most probes.

FRET probes add additional considerations when choosing suitable excitation wavelengths. The functional signal in these probes arises from non-radiative transfer of energy from an electron in an excited state of the donor protein to an electron in the ground state of the acceptor (Fig. 3.9A). Measurement of the emission of either or both proteins shows an anticorrelated change which reflects protein separation. Direct excitation of the acceptor must be kept to a minimum as this makes the acceptor protein unable to accept the FRET energy transfer. This renders that particular FRET pair non-functional for the duration of the acceptor state lifetime. FRET based GEVIs such as VSFP are designed with 1P excitation in mind and the acceptor and

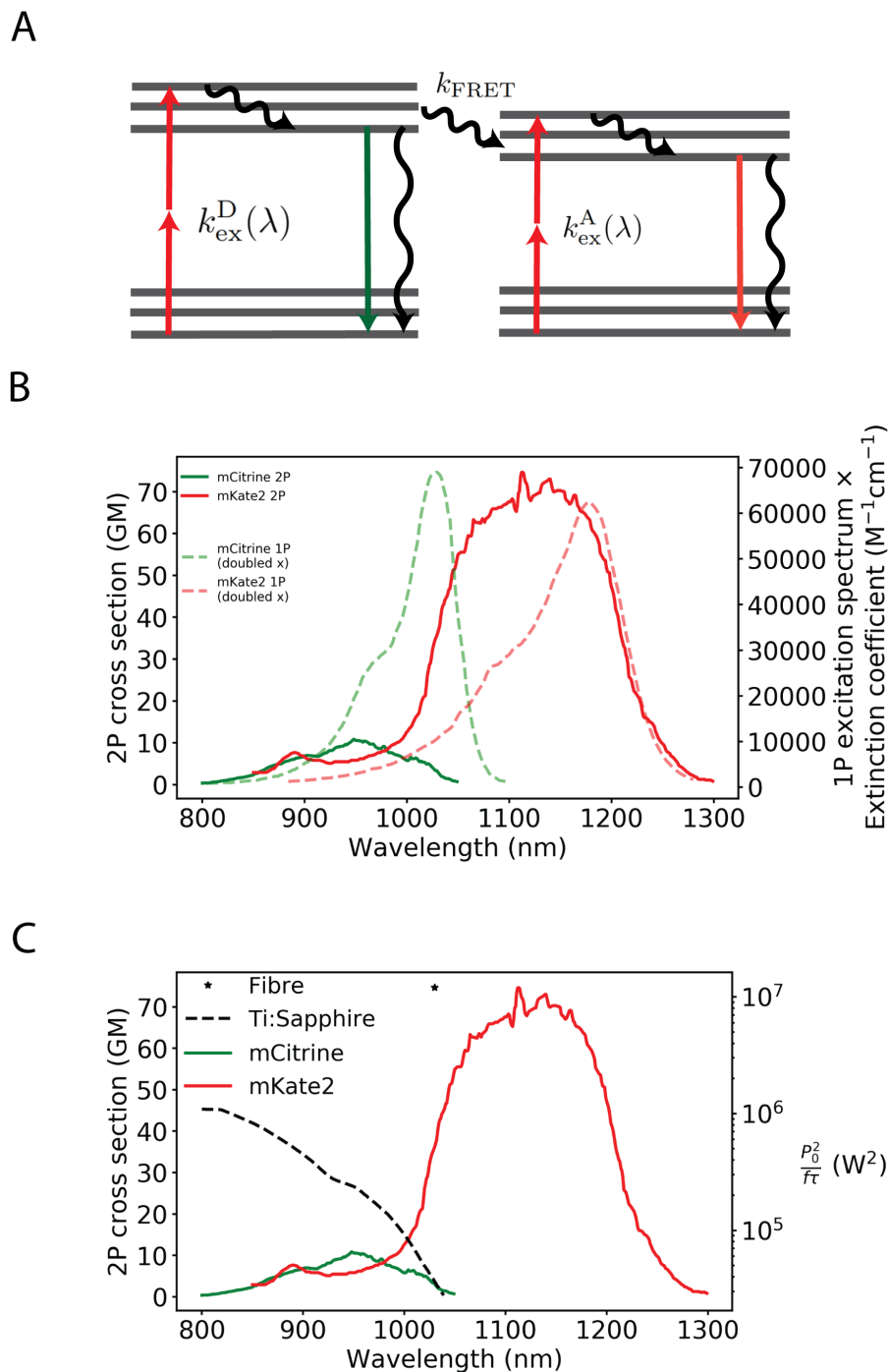


**Figure 3.9: The two-photon excitation spectrum of VSFP-Butterfly.** A) A Jablonski diagram of the two-photon FRET process. Due to the increased spectral overlap of two-photon spectra, there is often more direct acceptor excitation with two-photon excitation. B) A comparison of the two-photon and one-photon cross sections. The one-photon spectra are plotted on a doubled x-axis for comparison. Data from (Chroma Technology Corporation, 2018). The GEVI probe was designed for use with one-photon excitation, and is clearly sub-optimal for two-photon excitation as the donor cross section is small. C) A plot of the 2P excitation spectra alongside a figure of merit for two-photon excitation for a pulsed laser (note the logarithmic scale). The fibre laser figure of merit is  $\sim 10\times$  greater than the peak Ti:Sapphire value, but can only be used at 1030 nm, a highly inefficient excitation wavelength for the donor fluorophore. Two photon spectra reproduced from (Drobizhev et al., 2011).

donor excitation spectra are therefore well separated (Fig. 3.9B, dashed spectra on doubled x-axis, (Drobizhev et al., 2011; Chroma Technology Corporation, 2018)). Two-photon spectra are in general broader than one-photon spectra and blue shifted, and one-photon brightness does not well predict two-photon absorption cross section (Drobizhev et al., 2011). Carefully designed probes for one-photon excitation may therefore become less efficient under two-photon illumination. Figure 3.9B compares the excitation spectra of the two fluorescent proteins, mCitrine (green/yellow, data from Chroma Technology Corporation, 2018) and mKate2 (red, data from Chroma Technology Corporation, 2018) in the FRET pair of the GEVI used in these experiments (Akemann et al., 2012). Under one-photon excitation their magnitude is almost equal and they are well separated such that an excitation filter with a cutoff around 490 nm would overwhelmingly excite the donor. On the other hand under two-photon excitation they overlap significantly. The acceptor has a much greater peak cross section and also has a long blue tail and secondary peak, such that the absorption of the donor is greater than the acceptor only in a window between approximately 900 and 980 nm. Figure 3.9C shows a figure of merit for two-photon excitation,  $P^2/f\tau$ , where  $f$  is PRR and  $\tau$  the pulse length, against wavelength on a logarithmic scale for two lasers used in these experiments. The Ytterbium fibre laser rates an order of magnitude higher due to its decreased repetition rate, however at its operating wavelength it excites the FRET pair donor around 11 times more efficiently than the acceptor.

### **Voltage responses are resolved at sub optimal excitation wavelengths**

We were able to resolve voltage signals in response to extracellular stimulation in the pan slices with the Ti:Sapphire oscillator (Fig. 3.10A). Single trial signals could be clearly resolved at 20 and 50 Hz with signal sizes up to 1.5%  $\Delta F/F_0$ . Imaging sparsely expressed cells with the Ti:Sapphire oscillator yielded extremely dim signals in which we were unable to resolve voltage responses even after >200 averages. Signals from sparse slices are much dimmer than pan slices firstly, as only a single set of membranes is illuminated and secondly, the sparsely expressed GEVI was an older-generation GEVI than the pan GEVI, which is also dimmer in individual cells, likely due to less efficient membrane trafficking (Mishina et al., 2014).

Interestingly, in a single cell sparse voltage responses could be resolved using the fibre laser emitting at 1030 nm central wavelength (Fig. 3.10B). In response to intracellular current stimulation evoking 50 ms and 100 ms long depolarisations, a low SNR voltage signal could be convincingly resolved. This was surprising as, as discussed before, at this wavelength the

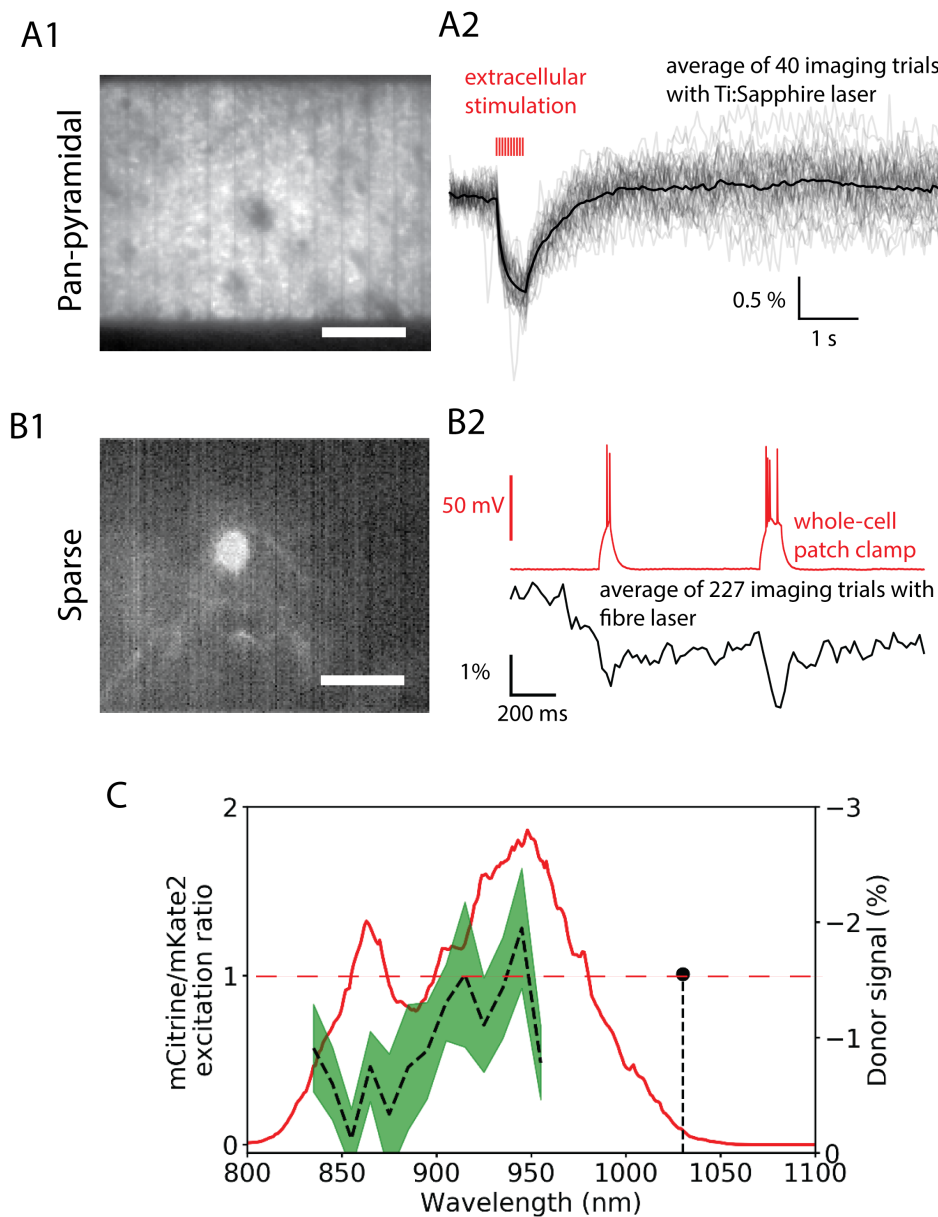


**Figure 3.10: MTPM can resolve voltage signals in dense and sparse slices** A) Population signals can be resolved in single trial with MTPM. A1) A mean image of a pan-pyramidal slice taken with the MTPM system using the Ti:Sapphire oscillator. A2) Individual traces (grey,  $n = 40$ ) and mean trace (black) taken at 20 Hz at 935 nm excitation wavelength. B) Sparse signals can only be resolved with high power excitation. B1) A mean image of a cell expressing VSFP-Butterfly in a sparse slice. Note the fixed pattern noise visible due to the extremely dim signal. B2) Intracellular (red) and optical (black) traces. The voltage signal can be resolved with poor SNR after 227 averages. A response was only detected from this single cell. C) plot of signal size measured for population signals measured with the Ti:Sapphire (dotted line, single trial signal error estimate plotted as green band) and single-cell signal measured with the fibre laser (point) against the mCitrine/mKate2 excitation ratio (red line). Red dashed line indicates the threshold below which the acceptor has a higher excitation cross section. A signal as large as that measured at the mCitrine/mKate2 excitation peak was measured when the donor excitation was  $\sim 11$  times smaller than the acceptor. Scale bars 40  $\mu\text{m}$ .

acceptor is around 11 times more efficiently excited than the donor (Fig. 3.10C). This reduces the effective probe concentration by making the acceptor unavailable for FRET. Due to the extremely low 2P excitation probability, however, it is likely that the overlap between excited donor proteins and acceptor proteins is small, as the overall excitation probability is small. Sub-optimal excitation wavelengths can therefore be used for these FRET probes when using low-efficiency excitation like two-photon, although one-photon excitation must still be carefully chosen to avoid direct acceptor excitation, as the fraction of excited probes in that case is much higher.

We also measured the size of the acceptor signal whilst varying the Ti:Sapphire tuning wavelength (Fig. 3.10C, black dotted line). We found that the largest signal near the donor/acceptor excitation ratio peak at 940 nm. The signal appeared to reduce concurrently with the ratio, unlike with the fibre laser, although due to the reduced fluorescence excitation at the less efficient wavelengths, the signal was much harder to measure.

### **2P voltage signals are larger than 1P voltage signals**

The two-photon population voltage signals we recorded were large compared to previously recorded (Mishina et al., 2014) and so we compared them to similar evoked signals recorded with one-photon excitation (Fig. 3.11). MTPM signals (Fig. 3.11A) had much lower single trial SNR compared to LED signals (Fig. 3.11B), due to the much lower fluorescence excitation efficiency of two-photon. Interestingly, the two-photon peak signal size was over twice as large compared to one-photon excitation (Fig. 3.11C) (mean signal increased from  $0.42 \pm 0.08$  to  $1.13 \pm 0.44$ ,  $z = 4.15$ ,  $p = 3E-5$ , Wilcoxon rank sums,  $n = 7$  LED trials and 40 MTPM trials). This is likely because the one-photon signal arises from a volume extending deep into the slice, where the extracellular stimulus has not reached. This reduces the responsive indicator fraction in the optical trace, reducing the overall size of the change in fluorescent signal.

## **3.4 Chapter Conclusion**

In this chapter I described the design and build of a multifocal two-photon system designed to acquire high frame-rate functional imaging traces. I described a novel source localisation algorithm to improve MTPMs resistance to scattering, published in Quicke et al., 2018. This

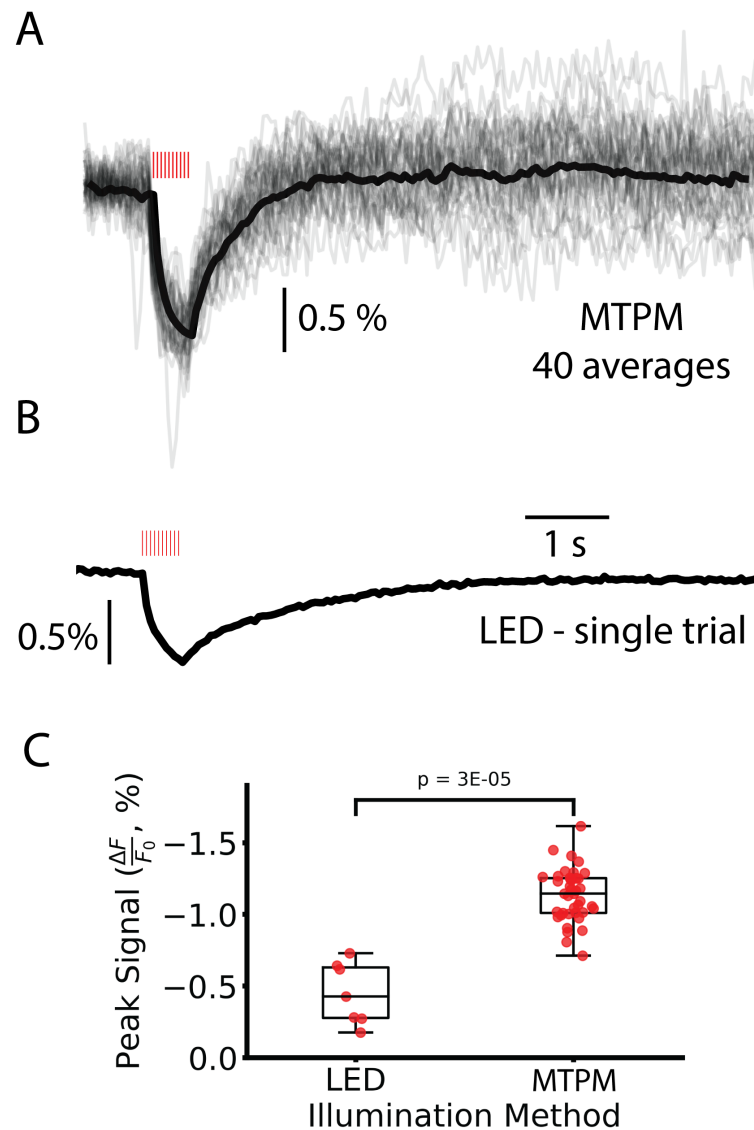


**Figure 3.11: A comparison of 2P and 1P population signal sizes.** A) MTPM population signals at 20 Hz in response to extracellular stimulation. Mean (black) and single trial (grey) traces. B) Single trial LED signal in response to the same stimulation as the MTPM. C) a comparison of single-trial signal sizes between LED and MTPM illumination. LED signal size could be reduced due to collection of non-signalling fluorescence from deep in the slice.



algorithm, based around deconvolution of temporally oversampled frames was shown to improve depth penetration and decrease functional crosstalk in calcium imaging traces. I was interested in examining whether MTPM would enable acquisition of high SNR voltage imaging traces. In the second section I first demonstrated that, despite the poor suitability of the FRET probe for two-photon excitation, both population signals with densely expressed GEVIs and single cell signals with sparsely expressed signals can be resolved. We then compared the signal sizes for different 2P excitation wavelengths compared to the mCitrine/mKate2 excitation ratio, and compared the signal sizes for one- and two-photon excitation. Despite the ability of MTPM to resolve voltage signals in slice, I decided that the low fluorescent excitation rates precluded effective study of voltage signals in slice. Single cell signals from sparse slices in particular required hundreds of averages to resolve. Single cell signals, particularly in the context of synaptic mapping, are the signals of interest and so a different approach is required. In the next chapter I will demonstrate that the use of the sparse expression strategy mentioned previously in this chapter enables resolution of single cell level voltage signals in slice with single-photon excitation.

## Chapter 4

# Wide-field single-photon voltage imaging with sparse indicators

We have seen in the previous chapter that, despite the increase in fluorescence excitation over standard single point-scanning systems, multifocal two-photon microscopy with VSFP-type GEVIs does not provide bright enough signals for most studies of physiological relevance. In this chapter we therefore turn to the highest SNR imaging modality - wide-field single photon imaging. As discussed in the introduction, multi-cell, single-cell resolution voltage imaging has been stymied by overlapping labelled membranes in the sample washing out small voltage signals. In this chapter I demonstrate that a genetic strategy for sparse expression enables single-cell resolution voltage imaging of a densely expressed cell class. The sparse expressions strategy greatly reduces the density of labelled membranes, enabling single-cell signals to be seen. This Chapter reproduces results published in Quicke et al., 2019 (original, CC BY 4.0) along with some additional material.

### 4.1 Introduction

Over the last decade, functional fluorescence imaging has become a key technology in cellular and systems neurosciences (Allen et al., 2017; Chen et al., 2017; Knöpfel, 2012; Knöpfel et al., 2006; Otis et al., 2017; Scanziani and Häusser, 2009; Yang and Yuste, 2017). The most prominent applications include *in vivo* imaging of genetically encoded calcium indicators such as GCaMPs (Chen et al., 2013; Nakai, Ohkura, and Imoto, 2001) that have enabled studies of large numbers of single cells longitudinally (Chen et al., 2012; Mank et al., 2008). Imaging of genetically encoded voltage indicators is less widespread despite being a longstanding goal driven

by high expectations. The lag between the development of calcium imaging approaches and voltage imaging technologies is because the latter is more demanding due to several intrinsic constraints (Kulkarni and Miller, 2017). Firstly, in contrast to calcium indicators which are localized in the cytosol of the cells of interest, voltage indicators are localized to their plasma membranes, which account for a tiny fraction of their volume. This limits the number of indicator molecules that can be employed and hence the flux of signaling photons that can be generated. Secondly, voltage signals of interest are typically much faster than the signals provided by calcium indicators and therefore must be imaged at higher frame rates. This is not only an instrumentation challenge but also translates, along with the limited number of dye molecules, into a signal-to-noise ratio (SNR) challenge, as a sufficiently high SNR requires a large number of photons sampled per spatiotemporal bin (e.g. 10,000 photons are required in order for a fluorescence change of 1% to have an SNR of 1).

Improvement of SNR has been the driving force for much of the previous work on voltage imaging. Recently, new photostable low molecular weight voltage sensitive dyes and genetically encoded voltage indicators (GEVIs) have been developed (Abdelfattah et al., 2018; Adam et al., 2018; Chavarha et al., 2018; Gong et al., 2015; Piatkevich et al., 2018; Sepehri Rad et al., 2017; Xu, Zou, and Cohen, 2017; Yi et al., 2018). These have greatly increased sensitivity (fluorescence change with change in membrane voltage), considerably increasing achievable SNRs.

Another feature of voltage indicators adds a third issue that needs to be resolved: as a consequence of their plasma membrane localization, optical voltage signals from adjacent cells cannot be resolved without imaging at sub-micrometer resolution, which is largely impractical for functional fluorescence imaging across multiple neurons. Calcium signals, in contrast, are more easily resolved in intact brain tissue as ‘blinking’ cell bodies that can readily be segregated. Hence, alongside low SNRs, allocation of optical voltage signals to individual cells in intact brain tissue is an inherent problem for voltage imaging.

Formally, the issue of single cell resolution can be described as follows: an optical signal from a cell of interest is compromised by shot noise generated by non-signaling fluorescence emanating from the membranes of other fluorescent cells and tissue autofluorescence (the ‘background’). The fractional change in collected fluorescence,  $\Delta F/F$ , will be reduced to  $(1 - f_b)\Delta F/F$  where  $f_b$  is the fraction of fluorescence arising from non-signaling structures.

Background fluorescence also has a detrimental effect on SNR. In a shot noise limited imaging system, SNR will be reduced proportionally to the SNR measured in the absence of background fluorescence ( $SNR_0$ ) as  $\sqrt{(1 - f_b)}SNR_0$ . Reducing the excitation volume in an attempt to minimize the contribution of fluorescent membranes of adjacent cells and their processes, for instance by using highly localized two-photon laser scanning (2PLS) excitation, reduces the amount of non-signaling fluorescence collected at the cost of very low rates of signal-carrying fluorescence excitation resulting in low SNRs. This makes 2PLS microscopy a poor choice for most voltage imaging applications, although it has been used successfully in some experimental paradigms (Ahrens et al., 2012; Akemann et al., 2013; Chamberland et al., 2017; Chavarha et al., 2018).

In voltage imaging applications aimed at single-cell resolution, instead of limiting fluorescence excitation to small volumes, a practical approach to maximize the contribution of a single cell to the fluorescence measured across an ROI is to limit the spatial overlap of fluorescence from different cells. Targeting a voltage indicator to single or multiple spatially segregated cells has been achieved by intracellular injection or electroporation of low molecular weight dyes (Antic, 2003; Roome and Kuhn, 2018). This approach, however, is limited to a single or a few cells in the microscopic field of view (FOV). Therefore voltage imaging based on low molecular weight voltage indicators is practically limited to single dye-injected cells or, using unselective staining procedures, to population imaging without single-cell resolution (Antic, Empson, and Knöpfel, 2016; Grinvald et al., 2003). We reasoned that sparse labelling of neurons using genetic methods applicable to GEVIs could provide a practical intermediate experimental paradigm allowing multi-cell voltage imaging at single cell resolution (Song et al., 2017). Sparse labelling has the advantage of the single cell labelling approach of reducing or eliminating unwanted background fluorescence, whilst still labelling multiple cells in a FOV. Sparse labelling neurons will create opportunities for multi-cell, single cell resolution imaging aimed towards understanding signal processing in neuronal networks.

Single-cell resolution genetically encoded voltage indicator (GEVI) imaging requires not only sparse, but also strong expression to enable an adequate collected photon flux. Gene delivery via intracortical injection of viruses produces expression patterns where the expression strength and likelihood decreases with increasing distance from the injection site and virus titre. Sparse expression can therefore be achieved with modifications to injection protocols, albeit in a local and highly variable way and with low expression levels (on average less than 1

virus particle per cell and therefore often only 1 virus per expressing cell). Another strategy to limit the density of indicator expressing membranes is the targeting of a GEVI to specific compartments of the cell. Recent works showed that, indeed, soma targeting of GEVIs can reduce the number of labelled membranes and enable single-cell signals to be extracted from sequences of images (Abdelfattah et al., 2018; Adam et al., 2018). Voltage imaging of naturally sparse cell populations, such as cortical interneurons, at single cell resolution is achievable with standard transgenic mouse lines (Bayguinov et al., 2017). Dual component expression strategies based on Cre-lox (Sauer and Henderson, 1988) and tetracycline response elements (TRE) (Gossen and Bujard, 1992) are especially useful for GEVI imaging experiments aimed at cortical circuit analyses, as these expression strategies label all cells of a genetic class with high expression levels (Madisen et al., 2015). In the case of non-sparse cell classes, in particular cortical pyramidal cells, sparse stochastic targeting can be achieved by controlling activation of a strong expression cassette via the titratable activity of destabilized Cre (Sando et al., 2013; Song et al., 2017). This strategy has been previously demonstrated at the morphological level, which demonstrated sparse but strong ('Golgi-staining like') expression from a GEVI in a transgenic mouse line (Song et al., 2017). Here we validate this approach for functional voltage imaging which requires higher expression levels than simple anatomical imaging. We show that d-Cre based stochastic expression strategies enables single-cell resolution GEVI imaging in cortical pyramidal cells in acute mouse brain slices. We compare recordings from tissue of mice sparsely expressing in cortical pyramidal cells ('sparse PC line') with recordings from mice which express the GEVI in all pyramidal cells ('pan PC line') using wide-field imaging (Fig. 4.1A). We evaluate the achievable SNR, discuss optimal GEVI imaging frame rates and also quantify the functional spread of signals to guide experimenters' choice of the sparsity level. We used early generation GEVIs (VSFP Butterfly 1.2 (Akemann et al., 2012) and chimeric VSFP Butterfly YR (Mishina et al., 2014)) for which transgenic mice suitable for a fully genetic approach were readily available. Our principal conclusions should hold true, and quantifications could be extrapolated, for all recently developed GEVIs covering a spectrum of voltage sensitivities, temporal dynamics, and brightness.

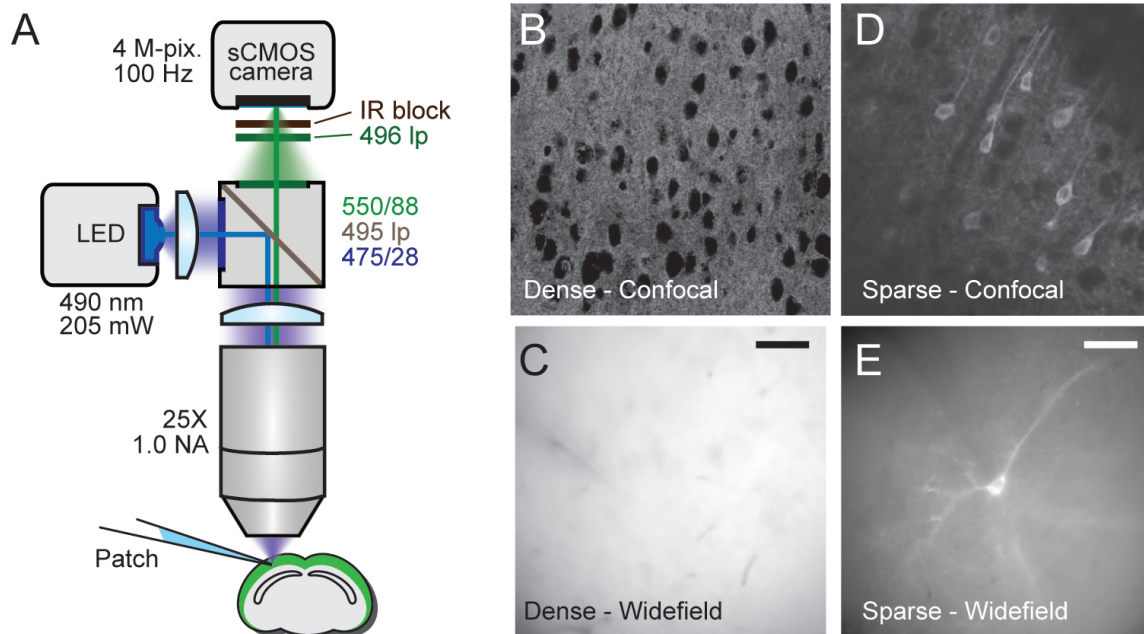


**Figure 4.1: Comparison of densely and sparsely expressed GEVIs.** A) The microscope set up for wide-field imaging. We used a standard epifluorescence microscope configuration to image patched cells expressing GEVIs in sparsely and densely expressing brain slices. B) A confocal image of a brain slice densely expressing chimeric VSFP-butterfly. Assignment of fluorescence to individual neurons is impossible due to expression in overlapping membranes. C) A wide-field image of a brain slice with the same expression strategy. The problem of assignment is compounded by the lack of optical sectioning, making even cell bodies difficult to discern. D) A confocal image of a brain slice sparsely expressing VSFP butterfly via destabilized-Cre modulated expression. Processes and soma from individual GEVI-expressing cells can be clearly resolved. E) Wide-field image of a brain slice with the same expression strategy. Contrast is decreased due to lack of optical sectioning, but single cells and processes can still be resolved. Scale bar 40  $\mu\text{m}$ . Images in B) and D) captured by a collaborator on this project, Chenchen Song.

## 4.2 Methods

### 4.2.1 Animals

Transgenic mice were bred to express VSFP Butterfly 1.2 in cortical layer 2/3 pyramidal neurons under the intersectional control of TetO and Cre-recombinase (Fig. 4.2B, 'sparse PC line', Rasgrf2-dCre; CaMK2A-tTA; Ai78 (Harris et al., 2014; Madisen et al., 2015; Mayford et al., 1996)). To induce sparse expression through stochastic re-stabilization of destabilized Cre, a titrated total dose of  $2 \times 10^{-4}$  mg/kg Trimethoprim (TMP, Sigma) was given via multiple intraperitoneal injections over two consecutive days as described in (Song et al., 2017).<sup>1</sup> For comparison, transgenic mice densely expressing chimeric VSFP-Butterfly in all pyramidal cells were used ('pan PC line', CaMK2A-tTA; tetO-chiVSFP (Song et al., 2018)).

### 4.2.2 Slice Preparation

Slices from transgenic mice were prepared at least 2 weeks post TMP injection using the protocol described in Chapter 2.

### 4.2.3 Imaging

Healthy fluorescent cells were identified using gradient contrast IR and fluorescence optics. Patch pipettes were pulled to a resistance between 3 and 10 MOhms when filled with the solution detailed in Chapter 2. Cells were patched using a Multiclamp 700B amplifier and signals were digitized using a Power 1401 digitizer. Current pulses were injected to elicit action potentials and fluorescence was imaged at 50 - 100 Hz using a custom-built epifluorescence microscope (optical path shown in Fig 4.1A).

We excited donor fluorescence of the VSFP FRET fluorescent protein pair with a 490 nm LED (M490L4, Thorlabs) powered by a current driver (Keithley Sourcemeter 1401), collimated with an  $f = 16$  mm aspheric lens (ACL25416U0-A, Thorlabs) and filtered with a 475/28 nm excitation filter (FITC-EX01-CLIN-25, Semrock). Intensity at the sample was between 4 and 30 mW/mm<sup>2</sup>. Fluorescence was collected using a 495 nm long pass dichroic (FF495-Di03, Semrock) along with a 550/88 nm collection filter (FF01-550/88, Semrock), 496 long pass filter (Semrock FF01-496/LP) and IR blocking filter (Semrock, FF01-750/SP) onto a sCMOS camera (512 x 512 pixels with 4 x 4 binning, Orca Flash 4 V2, Hamamatsu). This collected fluorescence from

<sup>1</sup>Mouse husbandry and injection were performed by a collaborator, Chenchen Song.

the FRET pair donor fluorophore (mCitrine), meaning membrane depolarizations resulted in decreased fluorescence emission as FRET efficiency increased. Imaging data were acquired using Micromanager (Edelstein et al., 2014). Images recorded at room temperature.

For 500 Hz voltage imaging,<sup>2</sup> a water immersion LUMPlanFI 40x objective with NA 0.8 (Olympus, Japan) was used. Fluorescence was excited with CoolLED, UK, 473 nm. Optical filters were purchased from Chroma Technology (Rockingham, VT, USA). The filter cube contained an exciter 480/40, dichroic 510DRLP, and emitter 535/50 nm. Voltage signals were sampled at 500 Hz with a NeuroCCD camera (80x80 pixel configuration) (RedShirtImaging, Decatur, GA). Analysis of optical data, including spatial averaging, high-pass and low-pass filtering, was conducted with Neuroplex v. 8.0.0 (RedShirtImaging). Images were recorded at 34 C.

#### 4.2.4 Image analysis

Imaging trials were repeated between 5 and 20 times and the individual trial image sequences averaged. Linear fits,  $f_i$ , were calculated for each pixel,  $p_i$ , to control for bleaching and the  $\Delta F/F_0$  time course was calculated as  $(p_i[n] - f_i[n]) / (f_i[n] - 1600)$ , where 1600 is the camera offset for 4x4 binning and  $n$  is the frame number. Only averaged traces were analyzed and all traces plotted are averages unless explicitly noted. Number of averages for traces are noted in captions. We plot all fluorescence traces on inverted y axes.

Image analysis was conducted with Python. Activation maps were found by considering  $\Delta F$  image sequences calculated pixel-wise as  $(p_i[n] - f_i[n])$ . The image time series was downsampled to 50 Hz by averaging to improve the SNR. To create maps for visualization and segmentation the image sequences were spatiotemporally filtered with a Gaussian filter with sigma of 1 time point/1 pixel 20 ms/1.04  $\mu\text{m}$  and for functional spread characterization they were temporally filtered with a 3 point median filter. 2D activation maps were then found from 3D image sequences by summing the frames collected during stimulation periods. ROIs for time series analysis were found by segmenting the activity maps. Each map was thresholded using an automatic criterion (Yen, Chang, and Chang, 1995), before a single round of binary closing and then dilation. The largest connected component was then selected as the

---

<sup>2</sup>These data were acquired by collaborators, Dr. Eric J. Mckimm, Dr. Milena M. Milosevic and Professor Srdjan Antic.



somatic ROI. For trials where a long depolarizing stimulus was used the signal size was calculated as the 5<sup>th</sup> percentile value of the fluorescence time course during the stimulus period with the median value of the previous 10 time points subtracted. For single spike trials the signal size of the first spike in a spike train was calculated differently to the others due to the easier estimation of the fluorescence value immediately preceding. The first spike signal size was calculated as the maximum value in the 50 ms after the stimulus (the stimulus period) with the median value of the preceding 10 time points subtracted. For subsequent spikes in the spike train the signal size was calculated as the minimum of the 50 ms following the stimulus with the maximum of the 20 ms time points before the stimulus subtracted. The noise level of traces was calculated as the standard deviation of 20 samples before the stimulus was applied.

### Frame rate analysis

To examine the effect of decreased sampling rate on GEVI traces we took an example  $\Delta F/F_0$  trace acquired at 500 Hz and downsampled it by averaging. To avoid overestimating the noise level for larger averaging periods we first flattened the trace to remove bleaching remnants by dividing it by a polynomial fit to the trace with the voltage signals removed. We then calculated  $n$  downsampled traces for downsampling by integer factors of 1, 2, 3, 4, 5, 10 and 20, where each of the  $n$  traces corresponds to a different downsampling phase. We calculated the noise level as the standard deviation of  $100/n$  points with no voltage signal and the signal level as the peak value during the stimulus period subtracted by the median value of the  $20/n$  preceding points. AP timing detection jitter was calculated as the imaging frame period multiplied by the range in frame number of the location of the optical AP signal peak. Least-squares log-log-linear fits were then calculated for the noise and 1-signal size.

### Crosstalk analysis

We estimated the sparsity level required to separate signals between adjacent cells using the mean autocorrelation of the activation maps. To derive the relevance of the autocorrelation for measuring signal crosstalk, consider two identically shaped neurons separated by a distance  $d$ , labelled as 1 and 2. We are interested in measuring the time course of neuron 1 without measuring the signal from neuron 2. The signal containing pixels imaged onto the camera are given by  $f_1(x, y, t)$  and  $f_2(x, y, t)$ . We assume that the neurons are of equal brightness, spatially identical and homogeneous so that we can separate the response functions into  $f_1 = f(x, y)p(t)$

and  $f_2 = f(x + d, y)q(t)$ . We also assume that the functional signal from the neurons decays with distance from the soma. The signal is given by  $s = f_1 + f_2$ . We wish to calculate the fraction of signal power arising from neuron 1 when integrating over a region of interest (ROI),  $R$ , covering the majority of neuron 1. The total signal power arising from the ROI is given by

$$\begin{aligned} P_T &= \int_0^\infty \int_R S^2 dx dy dt \\ &= \int_0^\infty \int_R f_1^2 + f_2^2 + 2f_1f_2 dx dy dt \\ &= \int_0^\infty p^2(t) dt \int_R f^2(x, y) dx dy + \int_0^\infty q^2(t) dt \int_R f^2(x + d, y) dx dy + \\ &\quad 2 \int_0^\infty p(t)q(t) dt \int_R f(x, y)f(x + d, y) dx dy. \end{aligned}$$

If the region  $R$  encompasses enough of  $f(x)$  then we can approximate the final integral with the 2 dimensional autocorrelation function,

$$ACF(x, y) = \int_{-\infty}^\infty \int_{-\infty}^\infty f(x, y)f(x + x', y + y') dx' dy', \quad (4.1)$$

evaluated at the point  $(d, 0)$ . Voltage imaging temporal signals consist of few-percentage fluctuations on a significant background and we can write them in the form  $k_0 + k_1(t)$ , where  $k_1 \ll k_0$ . To continue with our calculation we assume that the power in the temporal fluctuations of the neuron's time courses is equal and that they are uncorrelated. We can therefore factorise the integral in time as

$$\int_0^\infty p^2(t) dt = \int_0^\infty q^2(t) dt \approx \int_0^\infty p(t)q(t) dt = K \quad (4.2)$$

and write the total power in region  $R$  as

$$P_T = K(S_1 + S_2 + 2 ACF(d, 0)), \quad (4.3)$$

Where  $S_1 = \int_R f^2(x, y) dx dy$  and  $S_2 = \int_R f^2(x + d, y) dx dy$ . We wish to calculate the fraction of power arising from neuron 1, given by

$$\begin{aligned} \frac{P_1}{P_T} &= \frac{P_1}{K(S_1 + S_2 + 2 ACF(d, 0))} \\ &= \frac{S_1}{(S_1 + S_2 + 2 ACF(d, 0))}. \end{aligned}$$

If the separation,  $d$ , is sufficiently large such that  $f(x + d, y)$  is much less than 1 over the region  $R$  then  $S_2 \ll 2 ACF(d, 0) \ll S_1$  and we can approximate the power ratio as

$$\frac{P_1}{P_T} \approx \frac{S_1}{(S_1 + 2 ACF(d, 0))}. \quad (4.4)$$

$S_1$  is equal to the autocorrelation function evaluated at the origin and we can therefore normalise this to 1 with no loss of generality:

$$\begin{aligned} \frac{P_1}{P_T} &\approx \frac{ACF(0, 0)}{(ACF(0, 0) + 2 ACF(d, 0))} \\ &= \frac{1}{(1 + 2 ACF(d, 0))} \end{aligned}$$

Similarly, considering the impact of multiple cells at positions  $\vec{r}_i$  we can calculate the fraction of power arising from the target neuron as:

$$\frac{P_1}{P_T} \approx \frac{1}{(1 + 2 \sum_i ACF(\vec{r}_i))}. \quad (4.5)$$

### Experimental autocorrelation measurements

Autocorrelations of spatially unfiltered maps were calculated and a 1-pixel central peak arising from noise in the image was removed by replacing the central pixel with the mean of the surrounding pixels. The autocorrelation images were then normalized to between 0 and 1, rotated such that their longest axis faced the same direction before taking an average over all cells. This generated a roughly elliptical autocorrelation image with orthogonal axes representing our estimate of the largest and smallest signal mixing lengths. In the previous section we calculated the amplitude of the crosstalk for a neuron at the origin due to other neurons at positions  $r_i$  to be equal to  $1 - \sqrt{P/P_T} \approx 1 - \sqrt{1/(1 + 2 \sum_i ACF(r_i))}$ . We can therefore use the longest and shortest axis of our measured ACF to estimate the best and worst-case mixing fraction respectively.

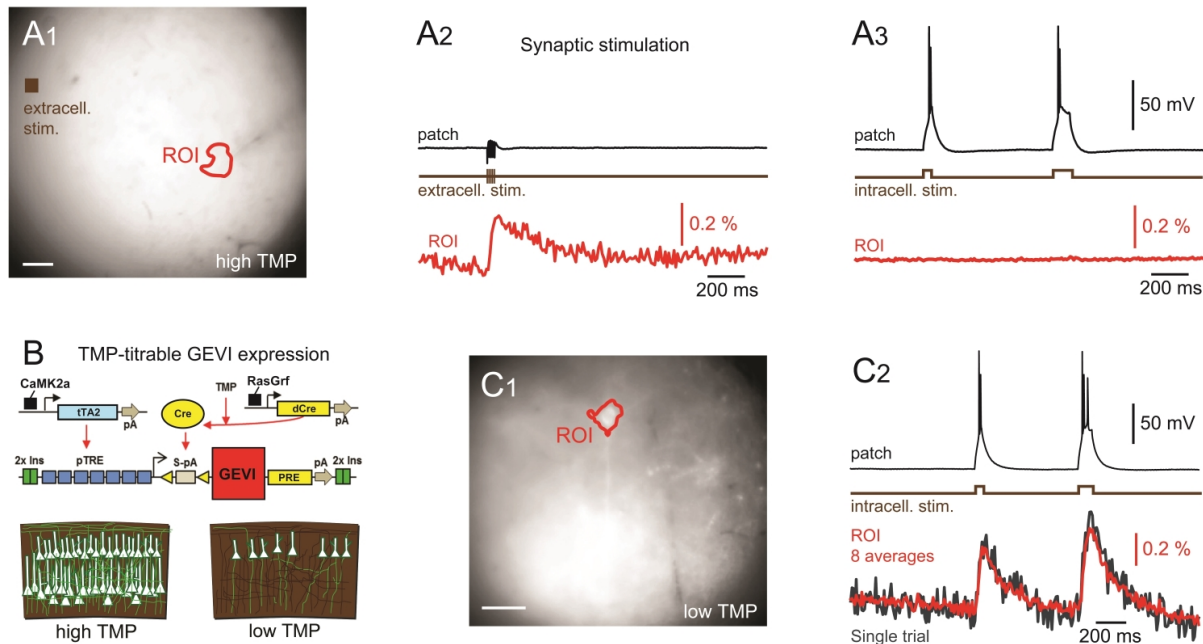


**Figure 4.2: d-Cre modulated sparse expression strategies enable single-cell resolution functional imaging.** A) Population, but not single-cell, voltage signals are resolved with densely expressed GEVIs. A1) A wide-field image showing the patched cell's location and the ROI used to generate the voltage imaging trace. An extracellular stimulation electrode was located as indicated. A2) A train of extracellular stimulation evoked responses from many cells, leading to a clear population voltage response in the cellular ROI. A3) No single cell voltage signal could be resolved despite averaging of 80 repeated trials of extracellular stimulation. B) The expression strategy used to generate sparse expression in layer 2/3 pyramidal cells. TMP stabilizes destabilized Cre recombinase enabling TRE driven GEVI expression. C1) A wide-field image of sparsely expressed GEVI showing the ROI used to calculate the voltage time course. C2) Single-cell voltage transients can be clearly resolved with sparse expression. Red time course shows an average of 8 repeats, grey shows single trial response. Fluorescence traces shown on inverted y axes. Scale bars 40  $\mu\text{m}$ . Panel B) created by a collaborator on this project, Srdjan D. Antic.

## 4.3 Results

### 4.3.1 Voltage imaging with densely and sparsely targeted GEVIs

As explained in the introduction, it is difficult to optically resolve fluorescent plasma membranes if a GEVI is targeted to all cells in a dense population of neurons, such as cortical pyramidal cells. To illustrate this, Figure 4.1 shows a comparison of images obtained from two transgenic mouse models using confocal and wide-field microscopy (Fig 4.1A). In the first mouse line, the GEVI is targeted to all cortical pyramidal cells ('pan PC line', see methods). In the second line of mice, the GEVI is targeted to a small subset of (mainly) layer 2/3 pyramidal cells ('sparse PC line', (Harris et al., 2014)). In the case of the non-sparsely targeted tissue ('pan PC'), confocal microscopy resolves individual cells bodies by negative contrast of their non-fluorescent cytosol (Fig. 4.1B). Plasma membranes of adjacent cells cannot be differentiated and the bulk of fluorescence emerges from neuronal processes (dendrites and axons) that are not structurally resolved (Fig. 4.1B). Wide-field microscopy of this tissue ('pan PC') reveals a sea of fluorescence with virtually no cellular structural details (Fig. 4.1C). In contrast, images of cortical tissue from the sparse PC line resolve the plasma membranes of cell bodies and processes both in confocal (Fig. 4.1D) and in wide-field microscopy (Fig. 4.1E). To demonstrate that optical voltage signals can readily be recorded in slices from pan PC mice using wide-field imaging, we employed synaptic activation of a large number of optically unresolved neurons (Fig. 4.2A1). Optical voltage signals were resolved in single trials over a cell body sized region of interest (ROI) in response to extracellular electrical stimulation (5, 0.5 ms pulses at 100 Hz, electrode  $\sim 360 \mu\text{m}$  from cell body, Fig. 4.2A2). This experiment demonstrates that population voltage signals can be recorded across 'cell body sized' ROIs in the brain slices of pan PC mice. We then tested whether the optical signal of a single cell can be resolved in the same preparation using wide-field imaging. To this end we patched a layer 2/3 cortical pyramidal cell in current clamp mode. Imaging during intracellular injection of positive current pulses (two pulses of 50 and 100 ms duration, current amplitude adjusted to induce spiking) did not reveal an optical signal across the cellular ROI despite a noise floor of only  $0.004\% \Delta F/F_0$  after averaging the images from up to 80 trials (Fig. 4.2A3). This suggests that single cell-level optical voltage signals are masked by the large shot noise produced by the non-signaling fluorescence of neighboring cells.

To verify this prediction, we switched to tissue from the sparse PC line (Fig. 4.2B), where

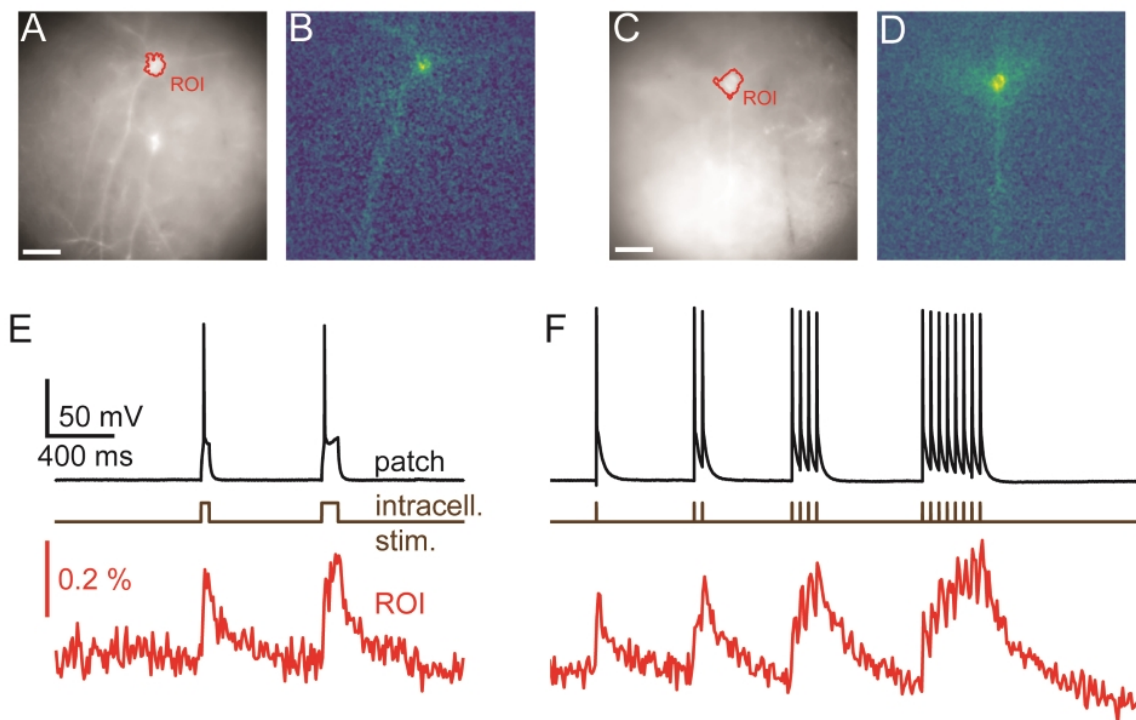


**Figure 4.3: Imaging reveals dendritic structure** Wide-field (A & C) and activity maps (B & D) of two cortical pyramidal cells. Activity maps were generated by calculating the integral over stimulated video frames and pick out an individual cells dendritic structure, including basal and apical dendrites, from adjacent cells. (E & F) the average time courses from the videos used to calculate the activity maps. Optical traces are averages of 12 (E) and 10 (F) repeats, scale bars 40  $\mu\text{m}$ . Fluorescence traces shown on inverted y axes.

single cells can be resolved even with wide-field epi-illumination fluorescence microscopy (Fig. 4.2C1). As with the above experiments using pan PC tissue, we patched a single fluorescent cell and imaged while the cell was depolarized by direct current injection through the patch electrode, readily resolving optical voltage signals at the single cell level (Fig. 4.2C2). In response to long lasting depolarizing current injections (50 to 500 ms, adjusted to induce one or more APs), we resolved voltage signals in single trials ( $n=12$  out of 15 cells attempted). In response to short single spike-triggering current pulses (0.5 ms current injections to induce spiking at 20 Hz), we observed signals ( $n = 4$  cells out of 4 cells attempted), with 2 cells with a signal-to-noise ratio consistent with spike detection without trial averaging (see below). Overall, we resolved single cell voltage signals in 13 patched cells in 13 slices at imaging depths of up to 77  $\mu\text{m}$ .

Interestingly, maps of GEVI responses ( $\Delta F$  images, see methods) reveal cellular structures that are not always readily apparent in raw wide-field images. Maps of GEVI responses allow identification of processes belonging to active cells (Fig. 4.3). We calculated response maps (Fig. 4.3 B & D) from our  $\Delta F$  image series by averaging 7 - 30 frames during stimulus periods,

depending on the stimulus length. As the GEVI fluorescence decreases on membrane depolarization, pixels containing signal have a negative value in response to the stimulus whilst pixels containing only noise average to zero (see methods section 3). The response maps clearly reflect the anatomy of the patched cells; dendrites and their branches can also be seen when they lie in the plane of focus. 6/13 cells were imaged with one or more other cells in the FOV and in these cases the active cell can be clearly distinguished in the activity map from the adjacent GEVI-labelled cells (Fig. 4.3, see also below, Fig. 4.7). We used these activity maps to automatically segment the cell soma from the image sequences by thresholding the activity maps. We then calculated the cell's fluorescence time course as the mean time course of the pixels within the segmented region (Fig. 4.3 E & F).

### 4.3.2 Signal-to-noise ratio

Comparing experimentally assessed SNR values between different imaging systems and preparations is complicated by differing fluorescence collection efficiencies, illumination conditions, and GEVI expression levels. Optical signals collected with high quality sCMOS cameras operating in a high photon count regime ( $\gg 10$  photons per pixel per frame (Li et al., 2016)) are shot noise limited. With our measured baseline noise levels  $< 1\%$ , we clearly image in this regime. This means that we can write the SNR as  $SNR \propto \Delta F / F \sqrt{n}$ , where  $\Delta F / F$  is the fractional change in fluorescence, or GEVI sensitivity, and  $n$  is the number of collected fluorescence photons. Increasing the illumination intensity increases the number of photons collected, increasing SNR, but in doing so increases the rate of bleaching of the sample, thus reducing the available imaging time. This makes fair GEVI evaluation and selection difficult as data from disparate labs must be collated and compared. A practical way to increase comparability of data from different systems, is to take the rate of photobleaching into account. Bleach rates can be used to normalize across different illumination intensities and facilitate comparison across different GEVIs with different photostabilities. The bleach rate,  $dC/dt$ , is proportional to  $-I_{ex}\Phi_B C$ , where  $I_{ex}$  is the illumination intensity,  $\Phi_B$  the bleaching quantum yield, and  $C$  the concentration of unbleached GEVIs. Ideally the quantum yield of bleaching would be measured for each GEVI as it would allow independent comparison of expression density; however, this is not known for the GEVI used in this study or, to our knowledge, any other GEVI. Normalizing the SNR to the bleach rate, however, can help to control for the GEVIs bleaching propensity and concentration along with the illumination level in one step with an easily calculable number.

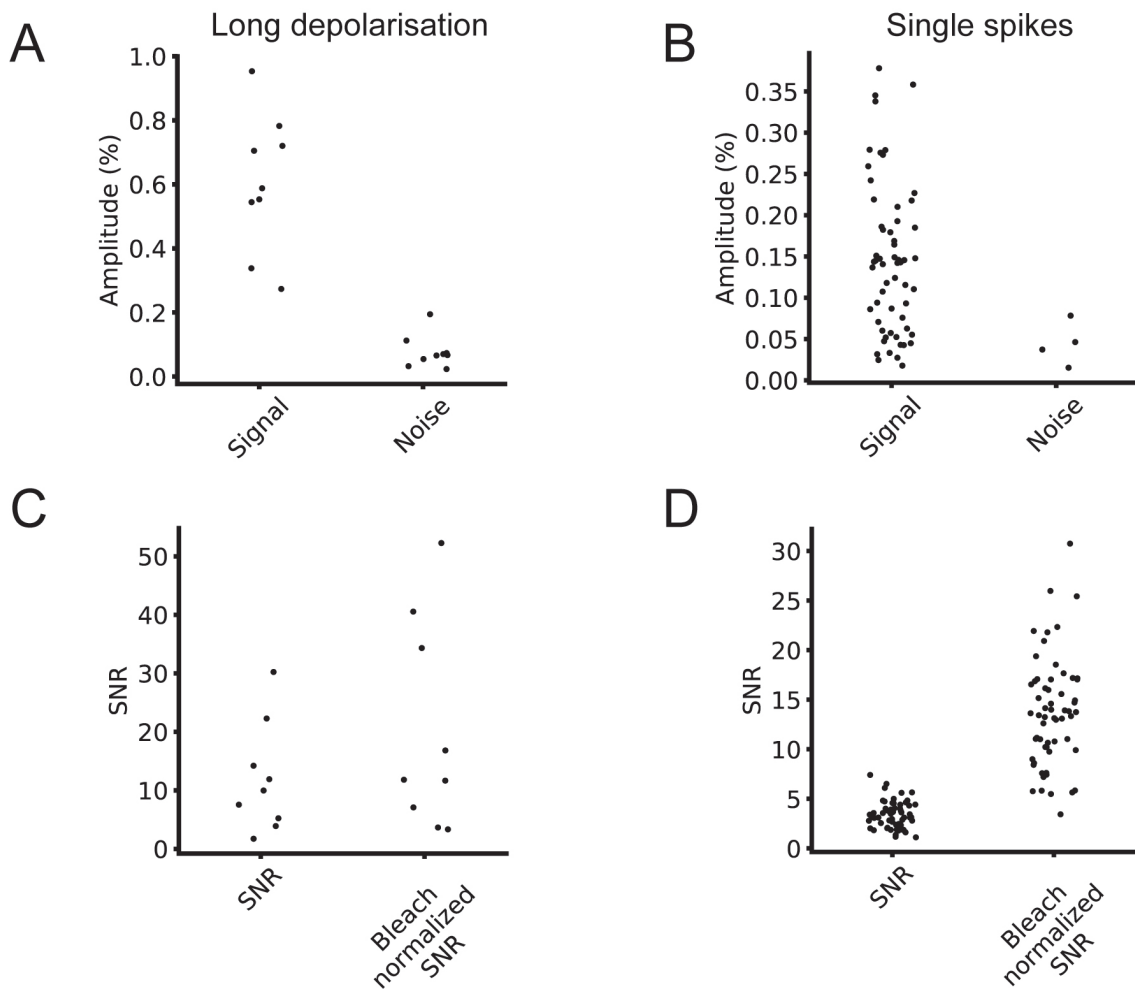


**Figure 4.4: Signal and noise levels.** A) Average signal and noise amplitudes for individual cells for 5 repeats at 100 Hz. B) Single spike signal amplitude and noise amplitude for 5 repeats at 100 Hz. C) SNR and bleach corrected SNR for long depolarizing stimulus. D) SNR and bleach normalized SNR for single spike stimulus.



Table 4.1: Sparse imaging SNR results

Stimulus type	Signal size (%)	Noise level (%)	SNR	Bleach corrected SNR	Number of cells
100 ms depolarization	0.59 [0.33,0.82]	0.07 [0.03,0.13]	10.0 [3.5,23.9]	11.8 [3.6,42.4]	9
Action potential	0.14 [0.04,0.28]	0.04 [0.02,0.07]	3.1 [1.8,4.8]	13.5 [7.1,21.0]	4

To this end, we estimated the signal size, the bleaching rate and the SNR of the optical signals across a segmented ROI. The median bleach rate over the cellular ROIs was 0.52%/s and the 90th and 10th percentiles were 0.98 and 0.23 %/s (calculated using a linear fit of baseline fluorescence). We calculated the signal and noise levels for 9/15 cells for which we collected data at 100 Hz with comparable stimulus regimes, and used image sequences of the average of four trials for each cell in the analysis. Table 4.1 summarizes the signal, noise, SNR and bleach corrected SNR values measured for long depolarizing stimuli (100 ms pulse duration, Fig. 4.3E) and AP inducing stimuli (Fig. 4.3F). The values are reported as median [10<sup>th</sup> percentile, 90<sup>th</sup> percentile]. We plot the individual measured values in Figure 4.4.

These SNR values come from an early generation GEVI with low sensitivity. As SNR increases linearly with indicator sensitivity, our values and conclusions can easily be scaled for more recent GEVIs with much higher reported sensitivity under similar experimental conditions.

### 4.3.3 Effect of sampling rate

Optical voltage signals need to be imaged at a frame rate sufficient to resolve the signals of interest (e.g. action potentials or subthreshold fluctuations of membrane voltage). However, the appropriate GEVI imaging sampling rate further depends on the time course of the optical signal generated by the GEVI used. Due to the non-instantaneous kinetics of GEVIs the optical signal is generally low-pass filtered relative to fast voltage signals (i.e. action potentials). Imaging at rates higher than necessary degrades SNR by increasing the proportion of time spent on image readout relative to signal integration and increases accumulated read noise. Increasing frame rates without reducing the SNR also necessitates an increase in illumination intensities, which will increase the bleach rate and reduce the available imaging time. Imaging at frame

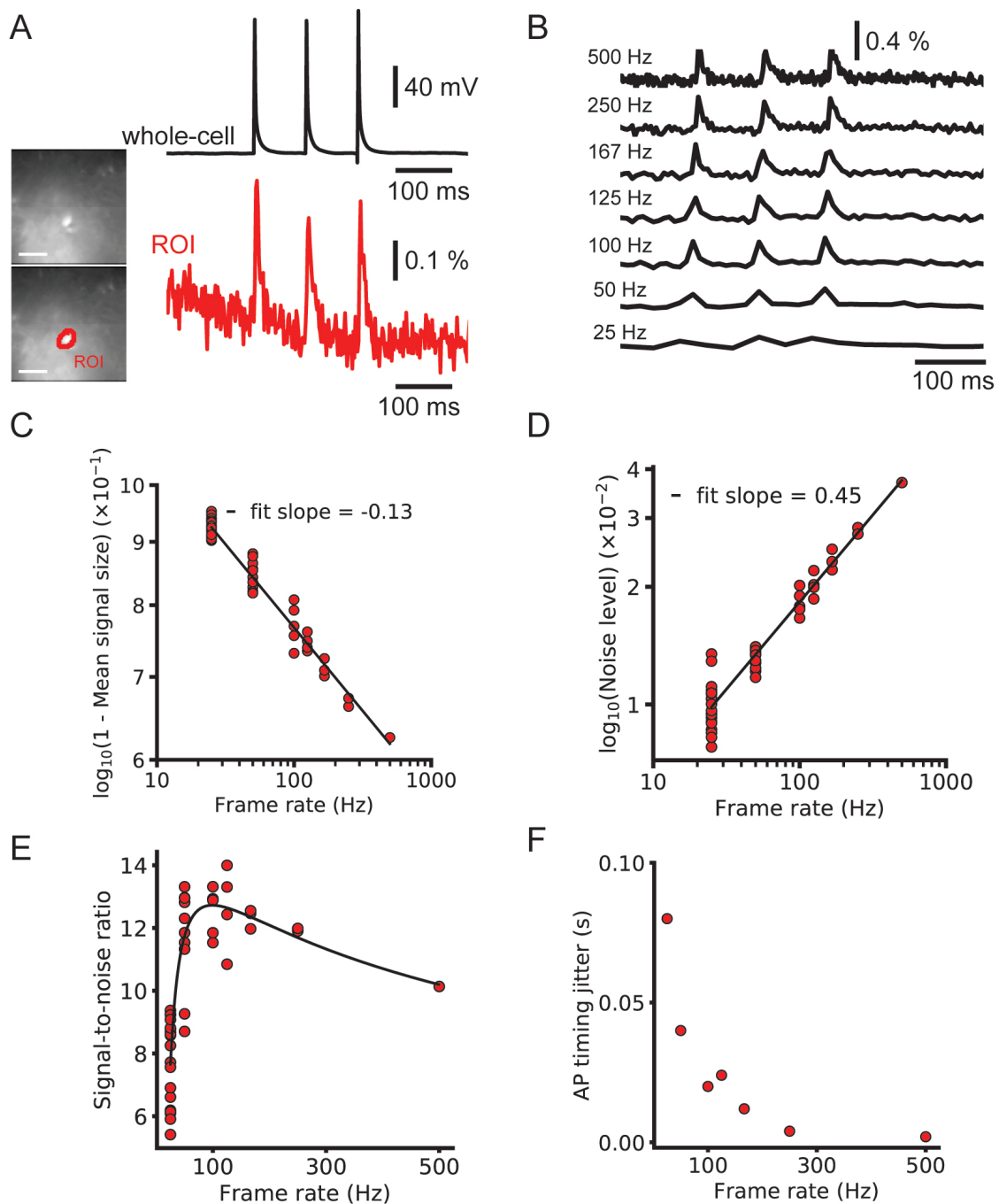


**Figure 4.5: Effect of frame rate on SNR and spike timing estimation.** Decreasing the imaging rate in wide-field imaging reduces the temporal accuracy and AP shape information but increases the SNR. A) Image of a brain slice from sparse GEVI mouse obtained at 500 Hz frame rate (80 x 80 pixels). Simultaneous electrical recording from cell body (black) and optical recording (red). Average of 9 trials. B) A 500 Hz  $\Delta F/F$  trace with 3 single-spike transients and down samples by averaging. Signal size, noise level and AP timing estimation accuracy all decrease with mean downsampling. C) and D) Power law fits to 1 - signal size and the noise level. The noise level scales approximately with the square as expected from Poisson statistics. E) The signal to noise ratio and power law fits plotted on linear axes. Fits give an optimal frame rate for spike detection SNR of 99 Hz. Note that this curve is the result of the division of the log-log linear fits in C) and D) and not a fit to the plotted points. F) The bounds on spike timing estimation for different frame rates. Fluorescence traces shown on inverted y axes. Data in A) collected by collaborators in this project, Dr. Eric J. McKimm, Dr. Milena M. Milosevic, and Professor Srdjan D. Antic.

rates above 100 Hz is also limited by image sensor technology and often requires using fast, low pixel-number charge coupled-device (CCD) cameras, or pixel sub-arrays from most modern sCMOS cameras.

When imaging with wide-field illumination, photons are integrated throughout virtually the whole frame period, and therefore fast fluorescent transients can be detected even if the imaging rate is below the nominal Nyquist rate of the optical signal. This is because the integration of detected photons over the frame period applies a low-pass filter to the collected fluorescence signal, as we shall see below. This contrasts with laser scanning illumination techniques where photons are collected for each pixel for only a short fraction of the frame rate, and a frame rate above the Nyquist frequency must be used to ensure detection of fast transients. That is, a neuron's action potential may escape detection if it occurs between visits of the neuron by the laser spot in LSM. The choice of wide-field imaging speed appropriate to the indicator and experimental question is therefore important.

With wide-field imaging therefore, due to the integration of photons during the whole frame period slow camera frame rates may be compatible with GEVI-based AP detection, especially for experiments that can tolerate low precision of AP onset timing. To investigate these predictions, we imaged at 500 Hz using a fast, low resolution (80 x 80 pixel) CCD camera (Fig. 4.5A, images)<sup>3</sup>. Three brief current pulses (pulse duration = 2 ms, pulse interval = 100 ms) were delivered via a patch pipette to drive a triplet of action potentials (Fig. 4.5A, whole-cell). We examined the peak SNR of AP related signals for a voltage imaging trace imaged at 500 Hz and integer downsamples by  $n$  of the  $n$ -point moving average. A fluorescent time course containing 3 AP-evoked fluorescence transients was downsampled by averaging to frequencies as low as 25 Hz (Fig. 4.5B) and the signal and noise were measured (Fig. 4.5 C & D). The noise and signal varied with the relative phase of the downsampling. The mean downsampled noise level was well fit by a power law model of the form  $A_2 x^{b_2}$  (log-log linear  $r^2 = 0.999$ ), with  $b_2 = 0.45 \sim 0.5$  as predicted by theory (Gans and Gill, 1983). The mean downsampled peak signal was also well fit by a power law fit of  $1 - A_1 x^{b_1}$  ( $r^2 = 0.995$ ), with  $b_1 = -0.13$ . Combining these and plotting against the SNR gave a predicted ideal imaging speed for spike detection of 99 Hz (Fig. 4.5E). We note, however, that the ideal imaging speed may be much higher if precise information about AP shape or spike timing (see spike jitter as a function of imaging

<sup>3</sup>These data were collected by collaborators, Dr. Eric J. Mckimm, Dr. Milena M. Milosevic and Professor Srdjan Antic.

rate, Figure 4.5F) is desired and a hypothetical GEVI with very fast kinetics is used.

We validated this analysis by modelling the GEVI signal as a series of decaying exponentials (Fig. 4.6A). A voltage signal from an action potential at  $t = 0$  s of unit power can be reasonably well modelled by a mono-exponential function of the form

$$s(t) = \frac{e^{-t/t_0}}{t_0} \cdot u(t), \quad (4.6)$$

$u(\cdot)$  is the indicator or step function, which is equal to zero for negative arguments and one otherwise, and  $t_0$  is the characteristic decay rate of the indicator under the specific conditions encountered. We are interested in the amount of aliased power in the signal and SNR as we vary the sampling frequency,  $f_s$ . For a simple signal such as (4.6) it is possible to calculate values for these analytically by considering the frequency domain representation of these signals. Defining the Fourier transform of the signal  $s(t)$  as  $\hat{s}(2\pi f)$ , the measured signal power spectrum will be given by

$$|\hat{s}'|^2 = |\hat{F}\hat{s}|^2, \quad (4.7)$$

where  $\hat{F}$  is the sampling filter spectrum, in our case a sinc function. The transform of an exponential is a Lorentzian and so our sampled signal has a spectrum given by

$$\hat{s}' = \frac{\text{sinc}\left(\frac{\pi f}{f_s}\right)}{\sqrt{2\pi}(i + 2\pi f t_0)} i. \quad (4.8)$$

We plot the signal and filter spectra in Fig. 4.6C. If we model our noise as purely Poissonian, which has a constant power spectrum, then our measured noise power spectrum is given by

$$\hat{n}' = k \cdot \text{sinc}\left(\frac{\pi f}{f_s}\right), \quad (4.9)$$

where  $k$  represents the noise power spectral density, in this case proportional to the rate of photon collection (Rice, 2016). We can then calculate the SNR as

$$SNR = \frac{\int_0^\infty |\hat{s}'|^2 df}{\int_0^\infty |\hat{n}'|^2 df'}, \quad (4.10)$$

where in this case we count aliased signal as 'usable' signal as we are interested in event detection. We could alternatively define the numerator as an integral to  $f_N = f_s/2$ , the Nyquist rate,

to place a greater emphasis on measurement of optical trace shape. We can similarly calculate the un-aliased signal power fraction as

$$P_{UA} = \frac{\int_0^{f_N} |\hat{s}'|^2 df}{\int_0^{\infty} |\hat{s}'|^2 df}. \quad (4.11)$$

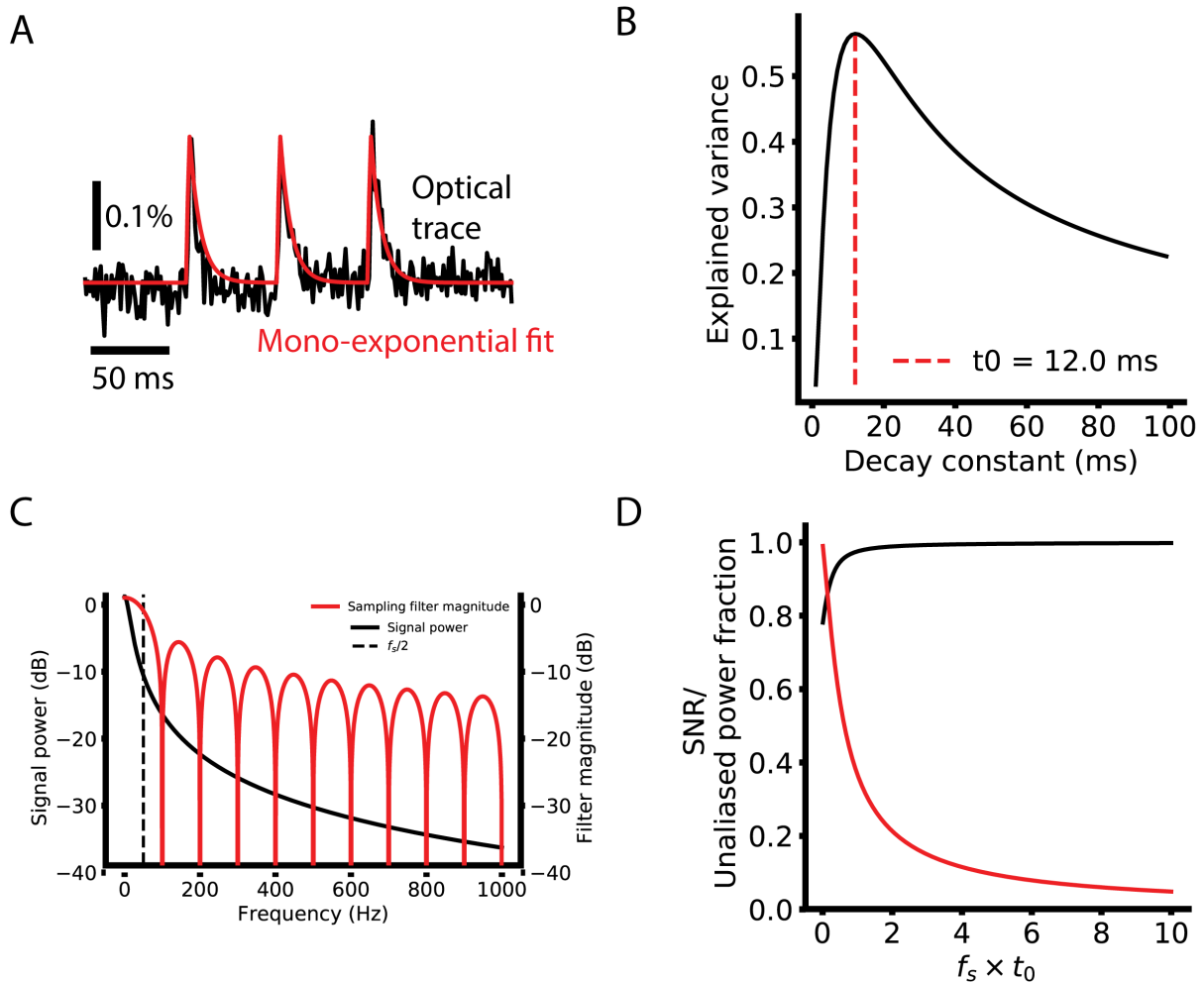
These integrals can both be analytically evaluated, although the latter cannot be written in terms of elementary functions. The results can be parameterised in terms of a dimensionless number  $w = f_s \cdot t_0$ , as could be reasonably expected as these quantities will vary with the sampling rate as a proportion of the signal decay rate.

Figure 4.6D plots  $SNR$  and  $P_{UA}$  as a function of  $w$ . The aliased power fraction starts to precipitously decline below  $w \approx 2$ . This shows that severe aliasing occurs when the sampling period used is more than approximately half the decay constant of the optical signal. The signal in Figure 4.5A was well fit with an exponential decay with a time constant of 12.0 ms. This predicts a frame rate of around 167 Hz is sufficient to avoid significant aliasing. The optical signals recorded at 100 Hz are slower, as they were recorded at room temperature, as opposed to 34 C for the 500 Hz traces. For these, 100 Hz imaging is sufficiently high to prevent significant aliasing.

#### 4.3.4 Signal spread

In order to guide future levels of sparsity we developed a method to estimate the level of signal mixing between cells as a function of distance. Neurons are highly variable in shape and, in the cortex, their extent varies with the orientation of the imaging focal plane relative to the cortical column. Figure 4.7A shows an example ROI containing a patched, stimulated cell adjacent to unpatched cells. The fluorescent voltage response in 6B shows a clear transient in the time course over the patched cell. Fluorescent time courses from ROIs over adjacent unpatched cells show a small amount of crosstalk, disappearing for more distant cells. This indicates that time courses from adjacent cells can be discriminated, albeit with some signal mixing depending on distance.

In order to quantify the expected level of this signal mixing we considered how the time course of one neuron of interest would be affected by being surrounded by  $i$  other neurons separated by distances,  $r_i$ , of the same shape and with similar fluorescent time courses. We wanted to quantify crosstalk, that is the signal amplitude (square root of the signal power,



**Figure 4.6: Theoretical treatment of sampling rate.** A) Single-AP optical traces are reasonably well modelled by a mono-exponential function. B) Estimation of the exponential decay rate for the 500 Hz trace. Curve shows the proportion of explained variance in the optical trace for exponentials of different decay rates. A clear peak can be seen at  $t_0 \approx 12$  ms. C) The signal power spectrum (black) for  $t_0 = 12$  ms and sampling filter response magnitude (red) for wide-field imaging at 100 Hz. The sampling Nyquist frequency is shown as the dotted line. All power beyond this frequency not removed by the filter is aliased into the signal. D) A plot of the un-aliased power fraction (black) and theoretical SNR metric (red, see text) as a function of dimensionless number  $f_s \times t_0$ . The choice between reduced aliasing and increased SNR must be made in choosing a sampling frequency as a fraction of the exponential decay rate.

$P, \sqrt{P} = \sqrt{\int s^2 dt}$ , arising from adjacent neurons when averaging signal from a ROI over a target neuron as a fraction of the total signal. This crosstalk was calculated (section 4.2.4) to be given by  $1 - \sqrt{P/P_T} \approx 1 - \sqrt{1/(1 + 2\sum_i ACF(r_i))}$ , where  $ACF(r)$  is the spatial autocorrelation function of the neurons' activity ( $\Delta F$ ) map, such as in Figs. 4.3B, 4.3D and 4.7C, evaluated at distance  $r$ .  $P$  and  $P_T$  correspond to the signal power from the target neuron and total measure power respectively. We calculated autocorrelations from the activation maps of signal-containing pixels (Fig. 4.7C), which allowed us to simply average different cells together. We averaged all the autocorrelations together after aligning their longest axes to average out cell-structure specific features caused by different dendritic shapes (Fig. 4.7E). To quantify the amount of crosstalk expected in sparse imaging we first calculated the width for each cell where the autocorrelation fell to 50% of its central value (Fig. 4.7F). This 50% cutoff represents the distance at which the crosstalk it contributes to an adjacent neuron would be 50% of the signal power or 25% of signal amplitude (where signal amplitude is the square root of the signal power). The 50% cut-offs of the neurons recorded ranged from 15 to 135  $\mu\text{m}$ . The large range in the values can be attributed to differences in imaging depth and dendritic structure. We plot the mean falloff in the autocorrelation in Fig. 4.7G. Using this, we calculated the crosstalk for two cells separated by 100  $\mu\text{m}$  the proportion of the total signal amplitude accounted for by the cell of interest when trying to image a single cell as between 20% and 22%. For cells on a hexagonal grid of side length 100  $\mu\text{m}$  the crosstalk was found to be 52% to 55%.

## 4.4 Discussion

We have shown that destabilized Cre recombinase (dCre) based expression strategies enable single-cell resolution voltage imaging of cortical pyramidal cells in acute brain slices. This expands the current repertoire of single-cell voltage imaging from interneurons and other naturally sparse cell classes to non-sparse layer 2/3 cortical pyramidal cells. We have not verified this approach with other cell classes, although we expect no differences in the strategy relevant to functional imaging. This powerful approach allows the sparsity of expression to be varied by the titration of the dosage of TMP which stabilizes the dCre and, in combination with strong transgene inducers systems such as tetO, enables sparse but strong GEVI expression. Different levels of sparsity allow the experimenter to trade off the level of population sampling and functional crosstalk between cellular voltage traces. The level of sparsity can also be adapted to

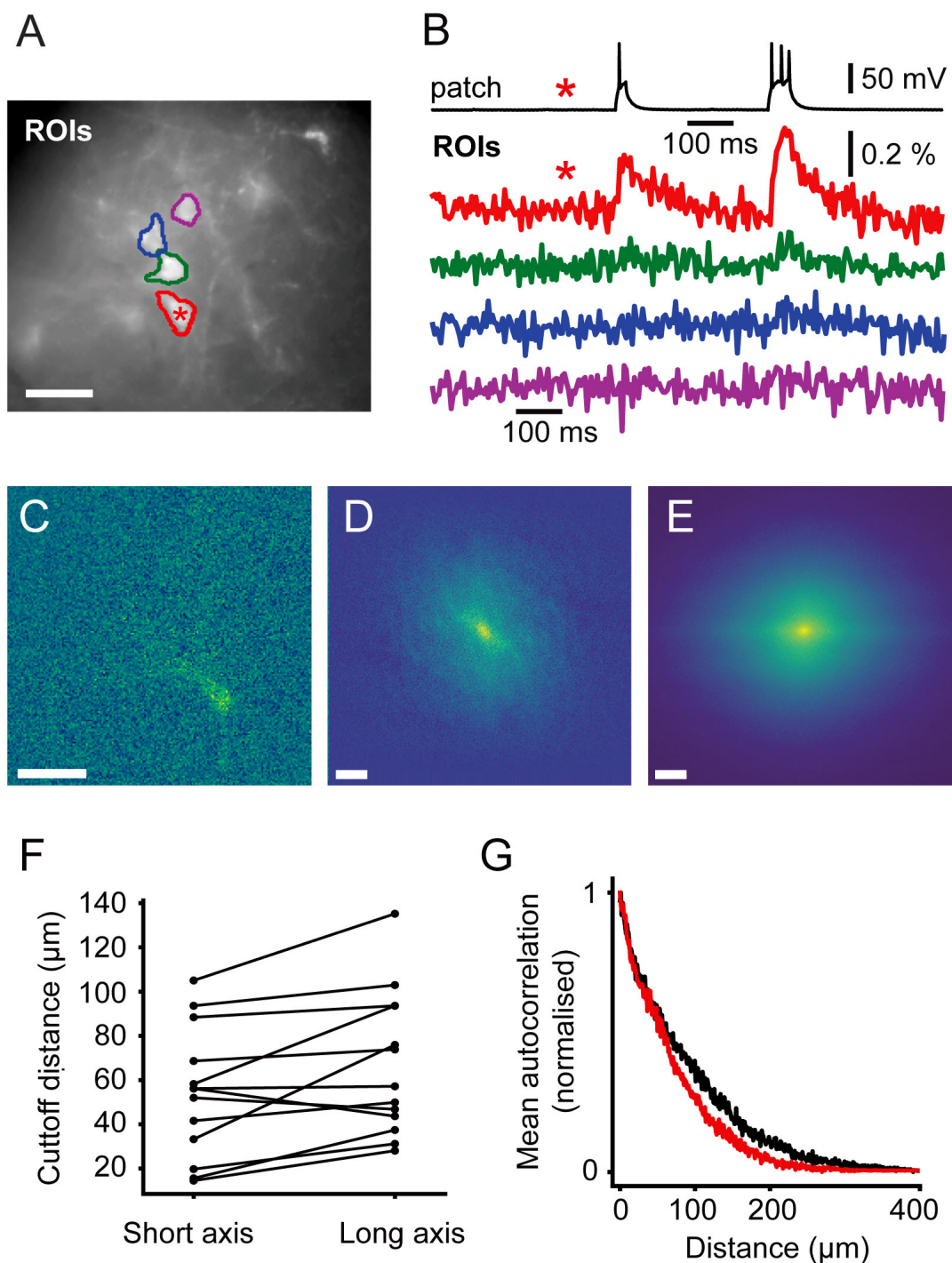


**Figure 4.7: Signal Spread.** Autocorrelation of activity maps can be used to estimate crosstalk. A) Wide-field image of a patched neuron (red roi) with other neurons in the FOV. B) Electrophysiological and fluorescent trace from the patched active cell (red and black) and fluorescent traces from ROIs over adjacent cells (green, blue and magenta). A small amount of crosstalk can be seen in the time courses of the adjacent cells. C) A spatially unfiltered activity map of the same neuron calculated by measuring the sum over frames during the depolarizing stimulus. D) The 2D spatial autocorrelation of the activity map. This represents the fraction of signal power arising from the patched neuron at different separations. E) The mean of rotationally aligned autocorrelations of all measured cells. F) The length of the long and short 50% cut-offs for all cells. G) The profile of the mean autocorrelation for the long (black) and short (red) axes. Scale bars 40  $\mu\text{m}$ .



the imaging approach used, with increased specificity from, for example, holographic imaging allowing denser cellular expression (Foust et al., 2015).

Although in this specific implementation, signal averaging was often needed in order to resolve single-AP voltage transients, an issue common to many voltage imaging applications due to low sensitivity of earlier generation GEVIs such as those used here. However, this genetic approach is, at least conceptually, not restricted to particular GEVIs, and could be used with any of the more sensitive GEVIs that have been recently reported (Abdelfattah et al., 2018; Adam et al., 2018; Piatkevich et al., 2018; Yi et al., 2018). We anticipate that these new GEVIs, combined with the sparse transgenic strategy used in the current study, will yield better single trial spike detection performance.

As wide-field single photon excitation was used, the imaging depth was limited by the scattering of both excitation and emission light. We were able to record from cells at depths up to 77  $\mu\text{m}$  in slice, although at these depths there was severe broadening of the functional signal due to scattering. This scattering will limit wide-field *in vivo* imaging in mice to superficial cortical layers. Two-photon excitation would improve this performance, however, this would require optimizing both the GEVI for two-photon excitation, and also using improved imaging methods to increase traditional two-photon imaging's meagre photon budget (Chavarha et al., 2018; Cheng et al., 2011; Prevedel et al., 2016; Quicke et al., 2018; Schuck et al., 2018). Contributing to the difficulties of two-photon voltage imaging, as each pixel is sampled for only a short fraction of the frame rate, full Nyquist-rate sampling of the indicator kinetics must be used to avoid aliasing of high frequency voltage transients.

Soma targeting of voltage indicators, as seen in recent GEVI studies (Abdelfattah et al., 2018; Adam et al., 2018) is likely to greatly reduce the mixing of functional signals by restricting the possible spatial sources of contaminating signal. This comes at the cost, however, of eliminating the ability to reveal somato-dendritic physiology. In multi-site voltage imaging experiments, successful soma targeting will eliminate important clues about input signals generated by dendritic neuropil.

We analyzed how far functional signals from fully labelled (not soma-targeted) active cells spread in order to guide future experimental designs. To choose a specific sparsity level, however, experimenters must also consider other factors such as the characteristics of the membrane dynamics of the studied cell class, as well as the specific experimental question. More

crosstalk can be tolerated, and therefore more dense cells studied, if factors such as AP amplitude can be used to discriminate between signals from different cells and subthreshold fluctuations are less important.

Sparse transgenic approaches could also be beneficial to opsin photostimulation approaches. Light shaping methods using computer generated holography (Papagiakoumou et al., 2008; Pégard et al., 2017) or generalized phase contrast (Papagiakoumou et al., 2010) can benefit from sparsely expressed opsins to better confine excitation to a single cell or subsets of cells. Previous studies have already used soma-restricted expression (Shemesh et al., 2017) or exploited naturally sparse cell classes (Papagiakoumou et al., 2013; Ronzitti et al., 2017) to improve single-cell targeting with optogenetic actuation. Sparse expression strategies as used here could also help with excitation confinement whilst enabling holographic dendritic stimulation of individual cells (Yang et al., 2011).

## 4.5 Chapter conclusion

We have seen how sparsely expressed genetically encoded voltage indicators enable single-cell resolution imaging in dense cell classes like cortical pyramidal cells. We required wide-field single-photon imaging to resolve these small signals in single trials. As discussed in Chapter 1, wide-field single photon is an extremely inefficient imaging technique that suffers from a lack of optical sectioning. A connectivity mapping experiment that would, for example, like to map the inputs to a fluorescent cell by dendritic location, would likely only be able to map inputs in a single plane before the cell was bleached. We therefore need a technique that enables high SNR, 3D imaging in a light efficient manner. As discussed in the introduction, light field microscopy seems like an excellent candidate for this. In the final results chapter, we will therefore explore the powerful combination of the sparse genetic strategy discussed here and that interesting optical technique.

## Chapter 5

# Lightfield voltage imaging

Light field microscopy (LFM) is an extremely light efficient 3D microscopical technique that seems to offer many benefits for voltage imaging. In this chapter I describe the first reported single-cell voltage imaging results and examine LFM's suitability for these experiments. LFM is a computational imaging technique; images acquired on a light field microscope must be reconstructed to generate micrographs of the type with which we are familiar. The specifics of the reconstruction technique impact upon the temporal and spatial resolution and SNR. To facilitate understanding and inform future studies this chapter compares and contrasts the benefits and drawbacks of different reconstruction techniques. Results are also included assessing the viability of synaptic mapping with LFM. Unfortunately, due to my misunderstanding when collecting the data, the LFM was misaligned for the GEVI wavelengths when doing functional GEVI imaging, discussed in section 5.2.1. These results therefore currently rest on imperfect data and correct data can not be collected in the timescale of this thesis due to the required animal husbandry. Improvements in the microscope alignment should only improve the results presented, and so this chapter should be a guide to the lower limits of achievable performance with this GEVI.

## 5.1 Introduction

Cellular resolution voltage imaging enables direct observation of neural computation. Indeed, voltage imaging experiments have spatially and temporally resolved the generation and propagation, both active and passive, of action potential and synaptic potentials throughout dendritic and axonal arbors (Foust et al., 2010; Popovic et al., 2014; Holthoff, Zecevic, and Konnerth, 2010; Palmer and Stuart, 2009). Wide-field, single photon imaging is overwhelmingly

the primary imaging modality for neuronal voltage imaging due to the high photon fluxes required to image small voltage signals at high speeds. Imaging neuronal processes in wide-field is challenging due to the requirement that the imaged membranes must all lie in the microscope's focal plane. Typically, these experiments are performed in slice and the requirement for flat, in plane cells sets a high bar for experimenters to clear before acquiring data. Secondly, in any slice preparation only a few cells will be oriented correctly, greatly reducing throughput, and only certain cell types have shapes that can be sampled well in a single plane. Anselmi et al., 2011 implemented remote focusing to image calcium transients along tilted dendrites, although this flexibility costs half of the fluorescence photon flux and is limited to a single tilted plane.

Even worse, out of focus structures contribute polluting signal to the image sequences due to one-photon imaging's lack of optical sectioning, making allocation of signals to axially separated processes difficult. Traditional optical sectioning techniques such as confocal and two-photon microscopy cannot resolve this issue as they are point scanning techniques; as each pixel must be sequentially sampled, fast imaging requires short dwell times and therefore few photons collected. This caps shot-noise limited SNR to extremely low levels hence making point scanning voltage imaging untenable in most circumstances. Fluorescence excitation parallelization into multiple spots (Quicke et al., 2018), lines (Žurauskas et al., 2017; Kazemipour et al., 2018) and sheets (Ahrens et al., 2013; Bouchard et al., 2015) increases the photon budgets, enabling functional volumetric imaging or single-plane imaging at increased speeds. These techniques feature optical sectioning through axially confined fluorescence excitation, with reduced robustness to scattering compared to single-point scanning modalities. Alternatively, 3D two-photon imaging with elongated Bessel beams (Botcherby, Juškaitis, and Wilson, 2006; Lu et al., 2017) excites a narrow column of fluorescence and relies on temporal and spatial sparsity of labelling and activity to demix time courses from different  $z$  planes. This increases the volume rate but still addresses each columnar pixel sequentially. These techniques have been used to image calcium fluorescence transients but not yet voltage.

Light field microscopy (LFM, Levoy et al., 2006) is a technique that enables multiple axial planes from single frames to be resolved, maintaining the high fluorescence excitation and collection efficiency of wide-field microscopy. LFM places a microlens array at the native microscope image plane to disperse the angular components of the collected image (Fig. 5.1A). The collected image consists of circular subimages (Fig. 5.1B), with the macroscopic structure of the

subimages resembling an undersampled version of the standard camera image, and each circular image representing the angular content of the light at the specific spatial location. Lightfield images are typically parameterized by the 4D function  $\mathcal{L}(u, v, x, y)$ , where each lenslet subimage is  $\mathcal{L}(u, v, \cdot, \cdot)$  and the same specific pixel under each subimage is  $\mathcal{L}(\cdot, \cdot, x, y)$ . Each pixel in the image can be thought of as the tomographic projection through the object volume. The object is sampled with a lateral resolution (the ‘native LFM resolution’) given by the microlens pitch divided by the objective magnification, much worse than the corresponding wide-field resolution.

Two prominent algorithms for reconstructing source volumes from LFM images have been described, synthetic refocusing (Levoy et al., 2006) and 3D deconvolution (Broxton et al., 2013). Synthetic refocusing reconstructs a single image representing the image generated by a wide-field microscope focused at that plane. By reconstructing multiple planes, a focal stack is generated similar to that generated by a standard z-stack on a microscope. This procedure is fast, as each pixel in the output image can be calculated as the weighted sum of a subset of pixels in the lightfield image. Significantly, objects not in focus in the reconstructed single plane appear as blur in the refocused image, and so this technique suffers from some of the same limitations as wide-field imaging. Deconvolution approaches, on the other hand, calculate a forward model based on a wave optics model of the LFM and use iterative deconvolution methods such as Richardson-Lucy (RL, Richardson, 1972; Lucy, 1974) or Image Space Reconstruction Algorithm (ISRA, Daube-Witherspoon and Muehllehner, 1986) to reconstruct the source volume. Interestingly, this technique is able to reconstruct source volumes at volume sampling rates higher than the LFM’s native sampling rate, the demagnified MLA pitch. The individual projections through the volume sample the object more finely than the microlens array apart from at specific depths where the ray sampling is degenerate, notably at the LFM native focal plane (Broxton et al., 2013), although newer designs have circumvented this limitation (Li et al., 2019). The source volume is reconstructed with less axial blur than in the refocused case, increasing the discriminability of axially separated signals.

Reduced lateral pixel size is not a big drawback for voltage imaging. Electrical length constants in neurons are on the scale of tens of microns, therefore imaging at or below the optical diffraction limit spatially over-resolves membrane potential fluctuations. Trading spatial resolution to increase speed and/or SNR is thus a sensible choice. For example, many voltage imaging studies use lower readout noise, higher sensitivity CCD sensors with low pixel counts,

meaning pixel size is typically large. Due to the low sensitivity of some probes, if higher pixel count detectors are used, multiple pixels are often averaged together to increase SNR to levels amenable to analysis. Deconvolution of voltage imaging volumes could therefore use lower lateral oversampling to reduce computational cost without sacrificing desired resolution.

LFM has been applied with great success to calcium imaging of large volumes in *C. Elegans* and zebrafish (Prevedel et al., 2014), and in mice, both head-fixed and behaving (Grosenick et al., 2017; Nöbauer et al., 2017; Skocek et al., 2018). LFM has also been applied to voltage imaging in *Drosophila* (Aimon et al., 2018) and larval zebrafish (Cong et al., 2017) as part of whole brain imaging setups alongside calcium imaging. These studies do not resolve individual neurons, however LFM seems well suited to dealing with some of the GEVI imaging issues encountered previously in this thesis. LFM benefits from the same high fluorescence excitation and collection rates of single-photon wide-field imaging, which enabled single-sweep voltage imaging in the previous chapter. It should also benefit from improved axial sectioning, enabling resolution of 3D neuronal structures.

In this study we apply LFM to GEVI imaging in acute mouse brain slices. We combine this technique with a recently reported transgenic strategy driving sparse expression in a random subset of layer 2/3 cortical pyramidal neurons which enables the resolution of single-cell level voltage signals in neuronal soma and dendrites (Quicke et al., 2019; Song et al., 2017). We show that LFM is able to bring axially separated fluorescent dendritic structures into clear focus, enabling single-shot capture of GEVI fluorescence transients in the 3D dendritic arbour.

We compare and evaluate deconvolution and synthetic refocusing for different GEVI imaging applications, whilst using a coarse deconvolution approach with no lateral oversampling to reduce computational cost. We also describe a simple adaptation of calculation of light field PSFs applicable to high NA objectives and which enables simple modelling of non-ideal microscope performance. We compare the achievable SNR for LFM and wide-field microscopy and finally show that LFM enables 3D localization of dendritic and somatic GEVI voltage signals.

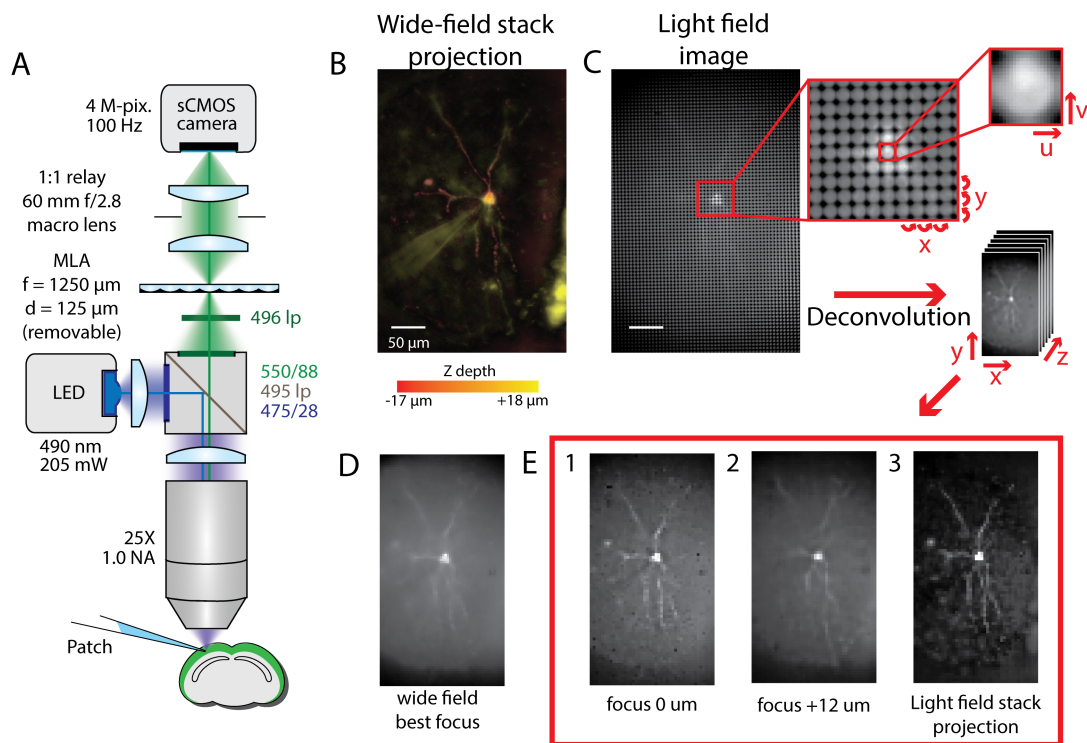


**Figure 5.1: Light field microscopy enables simultaneous focusing on axially separated dendrites.** (A) LFM Diagram (B) A pseudocolour z-projection of a wide-field image stack through a GEVI labelled cell. Redder areas are shallower and yellow areas deeper. Individual dendrites follow tortuous paths in all 3 dimensions, making simultaneous focussing on them all impossible in wide-field microscopy. (C) A light field image of the same cell showing the structure of light field images. Each spot in the light field image is a spatial sampling (coordinates  $x,y$ ) of the angular distribution of rays (coordinates  $u,v$ ) at that point. This angular and spatial information can be used to reconstruct a volume from a single image. (D) A best focus wide-field image of the single cell showing partially in focus dendritic structures. (E) Three different images recovered from the LFM image showing extractable information. 1 & 2) Single plane focus images at different planes showing in focus images of individual dendrites seen out of focus in the wide-field image. 3) A z-projection through the recovered light field volume image showing the in-focus sections of dendrites recovered.

## 5.2 Methods

### 5.2.1 Light field microscope design<sup>1</sup>

We designed our LFM following the principles set out in Levoy et al., 2006. We adapted a wide-field imaging system by placing a microlens array (MLA) at the microscope image plane, and used a 1:1 relay lens (Nikon 60 mm f/2.8 D AF Micro Nikkor Lens) system to image the MLA back focal plane onto our camera chip (ORCA Flash 4 V2, 2048 × 2048 pixels, 6.5 μm pixel size, Hamamatsu, see Figure 5.1A.). The lateral resolution is given by the pitch of the MLA in the sample divided by the magnification of the objective. Using our 25× objective (1.0 NA, XLPLN25XSVMP, Olympus) we chose our system to have 5 μm lateral pixels, dictating a microlens pitch of 125 μm.

The axial resolution is defined by the number of resolvable diffraction-limited spots behind each microlens (Levoy et al., 2006). Assuming a central emission wavelength of 550 nm for mCitrine, the FRET donor in VSFP-Butterfly 1.2 (Akemann et al., 2012), the spot size in the camera plane is 6.46 μm using the Sparrow criterion. With an 125 μm pitch MLA, we are able to resolve  $N_{\mu} = 19$  distinct spots under each microlens. The depth of field when synthetically refocussing our LFM can therefore be calculated as 7.81 μm (Levoy et al., 2006).

To efficiently use the camera sensor, the exit pupil of the objective should map through the MLA to produce circles on the light field plane that are just touching, requiring that the objective image-side f-number (f/12.5) equal the MLA f-number. We chose an f/10 MLA (MLA-S125-f10, RPC Photonics), an off-the-shelf part which came close to matching whilst being a larger aperture.

### Light field microscope misalignment

For the GEVI data collected for this chapter, the LFM microscope system was aligned using an IR LED with peak emission around 780 nm (Thorlabs, M780L2). Due to chromatic aberration in the LFM, when imaging the FRET donor and collecting fluorescence in a band from 506 to 594 nm, the MLA was slightly misaligned. This caused the lenslet images to overlap slightly in the camera plane as the MLA - camera chip distance was more than the MLA focal length (Fig. 5.2A). This is likely caused by dispersion in the MLA (Fig. 5.2B). Unfortunately, I had not realised the real reason for this overlap and so corrected for it by reducing the relay lens

<sup>1</sup>This design was done by a collaborator on this project, Dr. Carmel Howe - thanks! :)



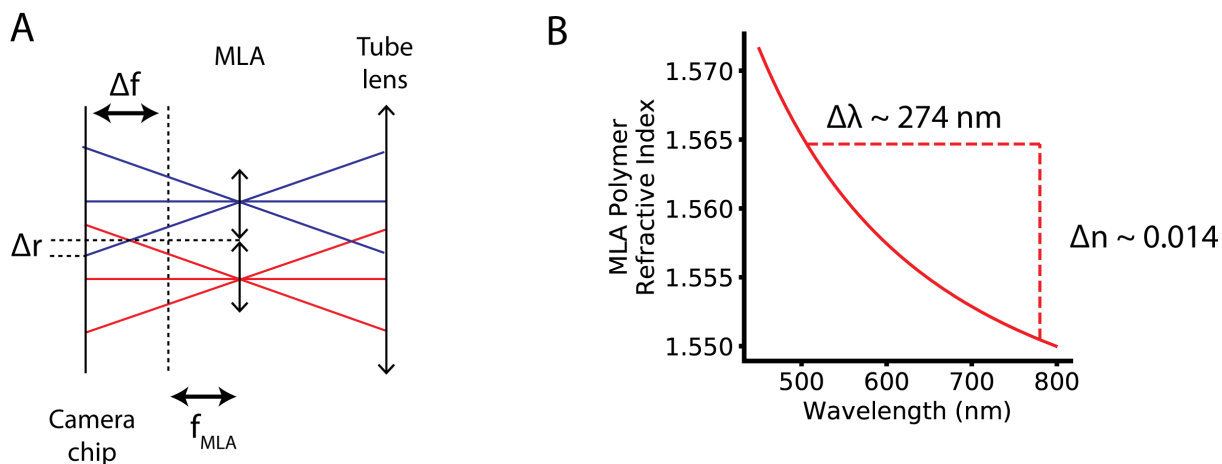


**Figure 5.2: Lightfield Chromatic Aberration.** LFM in the configuration used here is aligned when the camera chip is conjugate with the MLA back focal plane. If the camera is too far from the MLA then light from adjacent microlenses will overlap, impeding reconstruction. For the data in this thesis the LFM was misaligned as the system was aligned with 780 nm light and imaged fluorescence between 506 and 594 nm. B) The dispersion curve of the polymer-on-glass MLA polymer coating. The refractive index shift between 506 and 780 nm is around 0.014. This alone is not sufficient to cause the focus shift observed when aligning at different wavelengths, and so likely other components contribute additional chromatic aberration.

aperture, reducing the numerical aperture of the collected light. This blocks the higher angle rays, reducing the light collection of the microscope and reducing the number of resolvable angular samples.

The LFM is aligned using transmitted Köhler illumination from a substage condenser (Fig. 5.3A). During slice experiments, this substage apparatus is used with oblique illumination to image cells in the upper section of the slice, and NIR illumination increases scattering resistance, enabling visualisation of deeper cells. To align the LFM microscope, the camera is first aligned without the MLA so that it is imaging an alignment target in the microscope focal plane illuminated by the substage optics. The condenser is set such for Köhler illumination, with the camera imaging the field diaphragm, and the condenser diaphragm is stopped down as far as possible. The MLA is then introduced to the system and aligned along the optical axis so that it is conjugate with the camera chip. This is achieved by observing the camera image. When the MLA is in the microscope image plane, the illumination is not focused and an image of the focal plane can be seen, with just a checkerboard pattern from the microlenses and no focusing of the illumination. The camera is then translated away from the MLA using a linear stage until the illumination is focused into spots, as each microlens forms an image of the condenser aperture. A small section of the alignment image when the system is aligned using a 780 nm LED in Figure 5.3B. Changing the Köhler illumination to use an LED emitting at a 490 nm peak

(Thorlabs, M490L2), the image of the condenser aperture is clearly defocused (Fig. 5.3C). This defocus can be corrected by moving the camera approximately 750  $\mu\text{m}$  towards the MLA (Fig. 5.3D). The direction of this misalignment is consistent with the dispersion curve of common optical glasses and the polymer coating on the MLA that forms the microlenses (Fig. 5.2B). The total focal shift, however, is larger than that predicted purely by considering dispersion in the polymer-air interface. The focal shift due to the difference in refractive index in the MLA polymer can be estimated assuming a spherical lens surface using the formula

$$f = \frac{R}{n - 1}, \quad (5.1)$$

where  $R$  is the MLA radius of curvature and  $n$  the polymer refractive index. Using the manufacturer's supplied dispersion curve and the design focal length of 1250  $\mu\text{m}$  at 633 nm, the difference in focal length between 490 and 780 nm can be estimated as 32  $\mu\text{m}$ . This is much less than the observed difference. As the alignment uses Köhler illumination, the chromatic aberration in the rest of the system should affect this focal difference minimally. The observed difference between the predicted and actual focal shift could be caused by dispersion in the relay or imperfect illumination set up.

The effect of this misalignment on collected LFM images is clear. To demonstrate this, broadband fluorescence was excited from a thick fluorescent block. When imaging with a 550/88 nm yellow/green filter and the system aligned using the 780 nm LED, the lenslet images severely overlap in the camera plane with an open relay lens aperture (Fig. 5.3F). As the relay lens aperture is stopped down, reducing the collection NA below the design value, the overlap decreases and disappears. At the design NA the overlap is around 60  $\mu\text{m}$ . This is larger than the overlap predicted by the ray optics picture of around 30  $\mu\text{m}$ , possibly due to diffraction at the microlens apertures.

With a redder collection filter (692/40 nm) but an identically aligned setup and same fluorescence emitter, the overlap is greatly reduced in the camera plane (Fig. 5.3G). The relay lens needs to be stopped down less before no overlap is observed. If however, the system is aligned using a 490 nm LED, imaging fluorescence using the same filter as for GEVI imaging results in non-overlapping lenslet images on the camera chip with a fully open relay lens system, as the system was designed to form (Fig. 5.3H). When imaging the GEVI, the overlap was slightly better than in Figure 5.3F, likely due to a different emission spectrum compared to the

fluorescent slab, and so a more open relay aperture was used.

The data are reconstructed with two different PSFs, one calculated as if the LFM were correctly aligned, and one calculated with an additional propagation distance between the microlens and the sensor of  $412\ \mu\text{m}$  (33% of the MLA focal length). The computational cost of deconvolving the dataset precludes a comprehensive parameter sweep, but this defocus is approximately the defocus when scaling the focal shift measured with the 780 nm and 490 nm LEDs to the center of the fluorescence collection band using the MLA dispersion curve. Further work would include trying additional defocus values to see if better results could be achieved.

The error when using the aligned PSF should not be too large at smaller propagation angles as the ray displacement error should be small, and, as we shall see, reasonable reconstructions can be obtained for functional and structural images with both PSFs. This misalignment will, however, affect both the quality of the reconstruction and, as the limiting aperture of the collection path was reduced, the SNR of the GEVI recordings. For the recordings used, the relay lens aperture was reduced from  $f/2.8$  to  $f/4$  or  $f/5.6$ , blocking either  $1/2$  or  $3/4$  of the incoming light. This will reduce the shot-noise limited SNR by a factor of  $\sqrt{2}$  to 2. Although the high NA rays were blocked by this limiting aperture, the angular samples were not reduced as much as this would suggest, as the lower angle rays were split over more pixels and therefore more finely sampled. The number of resolvable angular samples was reduced as the spot size in the sensor was increased due to the reduced light numerical aperture. The number of resolvable angular spots in the sample was reduced to  $\sim 9$  instead of  $\sim 19$  for a relay lens aperture of  $f/4$ , and, assuming the misalignment is not so severe as to invalidate synthetic refocussing (which, as we shall see, is not the case), the depth of field of the synthetically refocused system increases to around  $17\ \mu\text{m}$ . As the modelled and actual transfer function of the system will diverge, the reconstructed depths will likely be slightly displaced from their actual positions, however a qualitative understanding of the power of LFM for GEVI imaging can still be achieved. Future work will include collecting similar GEVI data with a correctly aligned system, however the following analysis should provide a lower limit on the quality and SNR of achievable reconstructions.

### 5.2.2 Imaging

Slices were made from 3 ‘sparse’ mice described in the previous chapter. The mice were aged 31, 32 and 175 days. Fluorescent cells were patched under oblique IR illumination (780 nm)

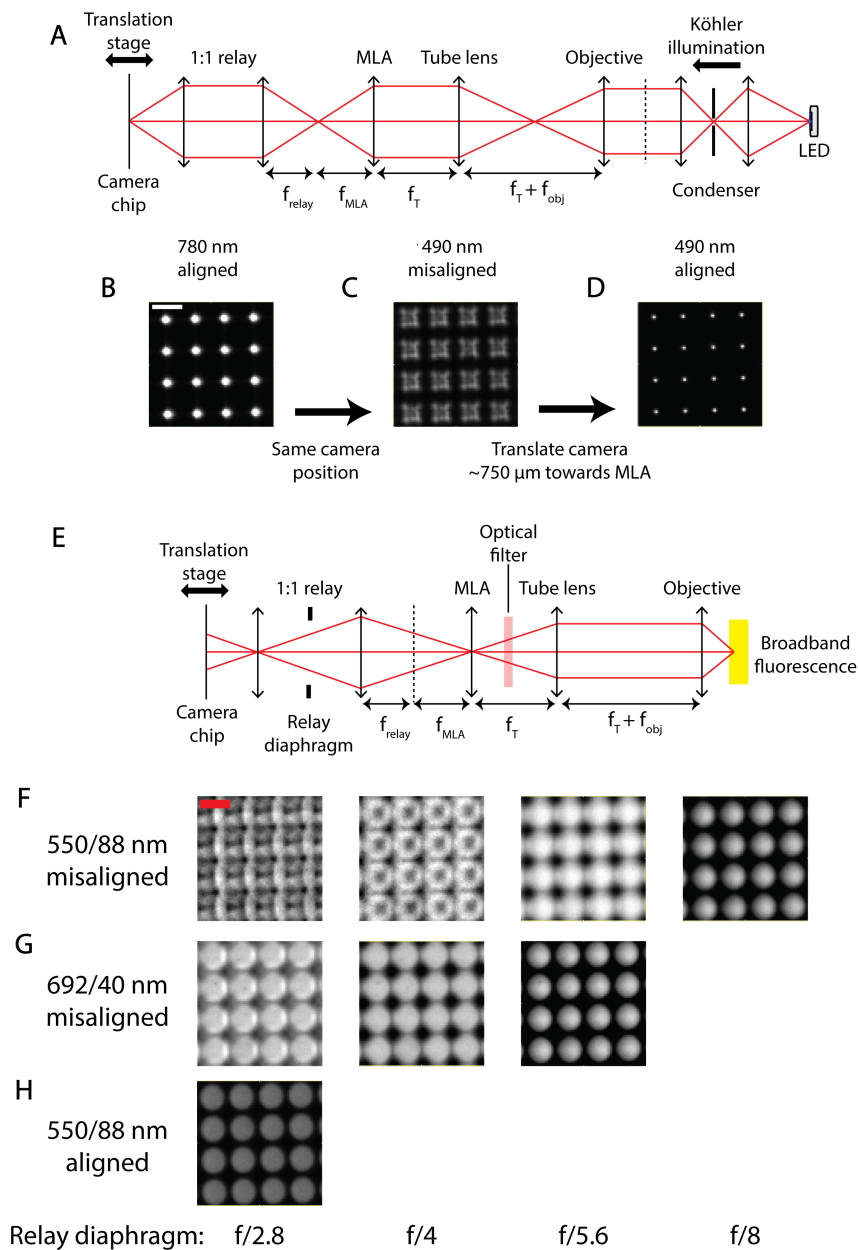


**Figure 5.3: Light field alignment.** A) The LFM is aligned using transmitted Köhler illumination from a substage condenser. The condenser diaphragm is stopped down to its lowest value and a transmissive alignment target imaged. B) When the camera is conjugate with the MLA back focal plane the illumination is focussed to small spots at the center of each microlens, each an image of the condenser aperture. C) Replacing the 780 nm Köhler illumination with 490 nm illumination results in defocused squares in the camera plane. D) Translating the camera towards the MLA brings the spots back into focus. E) To characterise the misalignment, broadband fluorescence is excited from a thick alignment slide. F) When the LFM is misaligned as in B) and C), yellow / green fluorescence results in overlapping lenslet images in the camera plane. Stopping down the relay lens aperture removes high NA light, eliminating the overlap. G) Imaging red fluorescence from the same emitter in the same configuration results in less overlap due to reduced difference in the alignment and imaging wavelengths. H) When the system is aligned with 490 nm light as in D), imaging the same yellow / green fluorescence results in non-overlapping lenslet images with an open aperture.

with pipettes of resistance between 3 and 10 MOhms when filled with intracellular solution containing: (in mM) 130 K-Gluconate, 7 KCl, 4 ATP - Mg, 0.3 GTP - Na, 10 Phosphocreatine - Na, 10 HEPES. We used a Power 1401 digitiser (Cambridge Electronic Design) to record signals from a Multiclamp 700B amplifier (Axon Instruments). We imaged at room temperature at 100 Hz for 2.5 s whilst injecting current pulses of 50 and 100 ms to elicit trains of action potentials. We used a 490 nm LED (M490L4, Thorlabs) powered by a constant current source (Keithley Sourcemeter 1401) to illuminate the sample at 3 mW/mm<sup>2</sup>. We averaged between 4 and 8 sweeps per imaging condition. The LED was collimated with an  $f = 16$  mm aspheric lens (ACL25416U0-A, Thorlabs) and filtered with a 475/28 nm excitation filter (FITC-EX01-CLIN-25, Semrock). Fluorescence was collected using a 495 nm long pass dichroic (FF495-Di03, Semrock) along with a 550/88 nm collection filter (FF01-550/88, Semrock) and 496 long pass filter (Semrock FF01-496/LP) to attenuate any excitation light transmitted by the dichroic. Imaging data were acquired with Micromanager (Edelstein et al., 2014). Imaged cell's somata lay between 18 and 55  $\mu\text{m}$  below the slice surface, with a median depth of 41  $\mu\text{m}$ .

### 5.2.3 Light field reconstruction

We reconstructed source volumes using different techniques to compare their performance for single-cell voltage data. We calculated  $(x,y,z,t)$  volume time series using synthetic refocussing (Levoy et al., 2006), and Richardson-Lucy deconvolution (Broxton et al., 2013; Richardson, 1972; Lucy, 1974) with two different PSFs as described before. The image space reconstruction algorithm (Prevedel et al., 2016; Daube-Witherspoon and Muehlechner, 1986) was also tested on the data, however little discernible difference in the results were observed.

#### Lightfield PSF calculation

We calculated LFM PSFs differently to previously described (Broxton et al., 2013). In the following the alignment is assumed to be perfect, and to calculate a misaligned PSF a simple additional factor is included into the Fresnel propagation term in eq. (5.2). In previous studies, the electric field magnitude in the camera plane was calculated as

$$h(\mathbf{x}, \mathbf{p}) = \mathcal{F}^{-1} \left[ \mathcal{F} [U_i(\mathbf{x}, \mathbf{r}) \Phi(\mathbf{x})] e^{2\pi i f_\mu \lambda (k_x^2 + k_y^2)} \right], \quad (5.2)$$

where  $\mathcal{F}$  denotes the Fourier transform,  $U_i(\mathbf{x}, \mathbf{r})$  is the electric field in the tube lens focal plane,  $f_\mu$  is the microlens array focal length, and  $\Phi(\mathbf{x})$  is a phase mask modelling the transmission of the microlens array.

We used the same model to calculate the propagation of the field from the microscope native focal plane to camera plane, however we used a different method to calculate the field at the native focal plane,  $U_i$ . Our calculation extends the validity of the calculation of LFM PSFs to high NA objectives and enables simple extension to add aberrations into the PSF.

To calculate the field in the native microscope focal plane, we consider how a high NA objective lens collects the field from an oscillating electric dipole at position  $\mathbf{r}$  near the microscope focus,  $|\mathbf{r}| \ll f$ , at the origin (Fig. 5.4A). We assume that we can model the behaviour of a point source consisting of randomly oriented fluorescent molecules as the incoherent sum of dipoles along 3 orthogonal directions. In the far field, the field magnitude of an oscillating dipole oriented along  $\mathbf{p}$  is given by

$$\mathbf{E} \propto \left(\frac{f}{k_0}\right)^2 \mathbf{k} \times \mathbf{p} \times \mathbf{k}, \quad (5.3)$$

Where  $\mathbf{k}$  is the wavevector of the plane wave component travelling along  $(\theta, \phi)$  and we neglect multiplicative factors (Sheppard and Török, 1997). If we assume that the dipole does not move far from the objective focus, then the electric field magnitude will not change with  $\mathbf{r}$ , but the displacement will add a phase shift to the field given by  $\exp(i\mathbf{k} \cdot \mathbf{r})$

The objective lens maps the field on a circular cap of a sphere centred at the origin into a disk in its back aperture, with the field components transformed using the matrix (Sheppard and Wilson, 1982; Clegg, 2016)

$$\frac{1}{\sqrt{\cos \theta}} \begin{pmatrix} \cos \theta \cos^2 \phi + \sin^2 \phi & (\cos \theta - 1) \cos \phi \sin \phi & -\cos \phi \sin \theta \\ (\cos \theta - 1) \cos \phi \sin \phi & \cos^2 \phi + \cos \theta \sin^2 \phi & -\sin \phi \sin \theta \\ \cos \phi \sin \theta & \sin \phi \sin \theta & \cos \theta \end{pmatrix}. \quad (5.4)$$

In our model the component of the field orthogonal to the focal sphere's surface in the object space and parallel to the optical axis in the objective pupil are identically zero due to the cross product in equation (5.3), however we include the terms in the third row of the previous matrix for completeness.

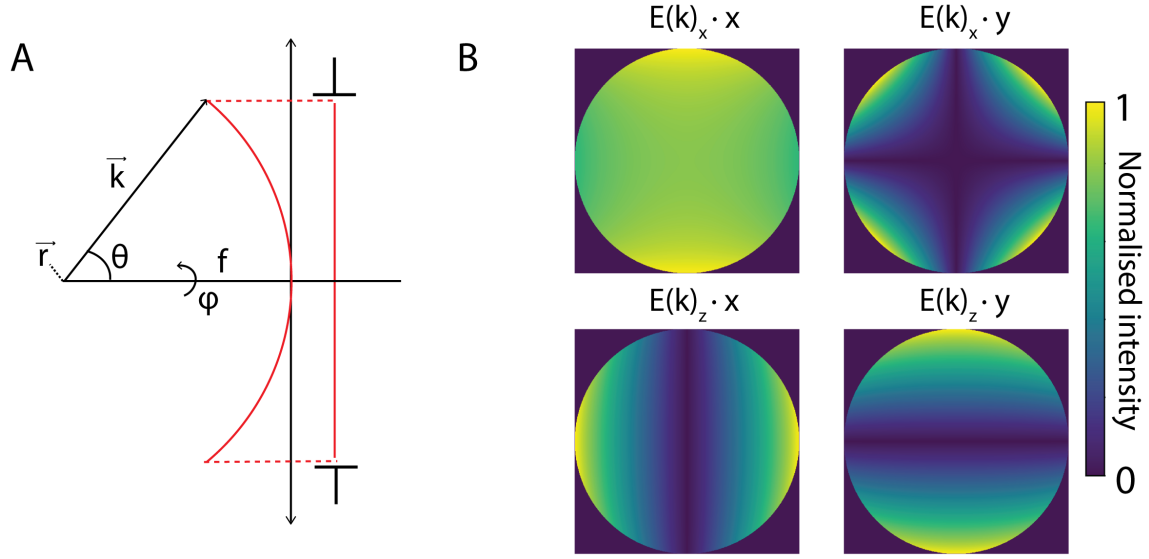


**Figure 5.4: PSF calculation method** A) A diagram showing the coordinate space for the calculation of the pupil functions for the vectorial PSF modelling. The Electric field on the surface of the red spherical cap are transformed by the lens to the pupil disc. A small displacement of the dipole by the vector  $\mathbf{r}$  results in an additional phase equal to  $\mathbf{k} \cdot \mathbf{r}$ . B) The electric field intensity in the objective pupil for dipoles along  $x$  and  $z$ . The intermediate PSFs in the microlens plane are found by calculating the Fourier transform of these multiplied by the phase factor due to the dipoles displacement from the origin.

Following a similar method to Boruah and Neil, 2009, we can re-write this in terms of the  $\mathbf{k}$ -components of the field as

$$\sqrt{\frac{k_0}{k_z}} \begin{pmatrix} (k_z k_x^2 + k_0 k_y^2) / (k_0 k_r^2) & (k_x k_y (k_z / k_0 - 1)) / k_r^2 & -k_x / k_0 \\ (k_x k_y (k_z / k_0 - 1)) / k_r^2 & (k_0 k_x^2 + k_y^2 k_z) / (k_0 k_r^2) & -k_y / k_0 \\ k_x / k_0 & k_y / k_0 & k_z / k_0 \end{pmatrix}. \quad (5.5)$$

where we note that  $\cos \theta = \frac{k_z}{k_0}$ ,  $\sin \theta = \frac{k_r}{k_0}$ ,  $\cos \phi = \frac{k_x}{k_r}$ , and  $\sin \phi = \frac{k_y}{k_r}$ , where  $k_r^2 = k_x^2 + k_y^2$ . The  $z$  component  $k_z = \sqrt{k_0^2 - k_r^2}$  is constrained such that the magnitude of the  $\mathbf{k}$  vector is equal to  $k_0 = 2n\pi/\lambda$ , and the radial component is constrained such that  $k_r \leq k_0 \text{NA}/n$ .

Denoting the vectorial electric field arising from a dipole oriented along, e.g.,  $\hat{z}$  as  $\mathbf{E}(\mathbf{k})_z$  we can then write the electric fields in the objective back focal plane as

$$\mathbf{E}(\mathbf{k})_x = \frac{f^2}{k_0 k_r^2 \sqrt{\frac{\sqrt{k_0^2 - k_r^2}}{k_0}}} \left( k_x^2 \sqrt{k_0^2 - k_r^2} + k_0 k_y^2, k_x k_y \left( \sqrt{k_0^2 - k_r^2} - k_0 \right), 0 \right) \quad (5.6)$$

and

$$\mathbf{E}(\mathbf{k})_z = \frac{f^2}{k_0 \sqrt{\frac{\sqrt{k_0^2 - k_r^2}}{k_0}}} (-k_x, -k_y, 0), \quad (5.7)$$

and we can calculate  $\mathbf{E}(\mathbf{k})_y$  by applying a rotation matrix to (5.6). The  $x$  and  $y$  components of the field intensity in the objective pupil are plotted in Figure 5.4B.

We can simply evaluate these expressions for the pupil field once, and then calculate  $U_i(\mathbf{x}, \mathbf{p} = \mathbf{p}')$  by calculating the DFT of the field multiplied by the additional phase due to the source shift. Additional effects from aberration could also easily be incorporated by expressing them as Zernike polynomials in the objective back aperture (Boruah and Neil, 2009). Alternatively, if no aberrations were incorporated, further computational savings can be made by assuming that the PSF is spatially invariant for small lateral source shifts, such that only source  $z$ -shifts need to be calculated. If this is assumed, the 2D FFT can be reduced to a 1D integral, which can be quickly numerically evaluated.

This can be achieved by following a similar procedure to Richards and Wolf, 1959. For ease of notation we write the four electric field components contributing to the PSF that we need to calculate in the microscope image plane as  $E_j(k_x, k_y)$ ,  $j \in 1, 2, 3$ , where we calculate a single component of  $\mathbf{E}(\mathbf{k})_z$  and two components of  $\mathbf{E}(\mathbf{k})_x$ . For a source point on the optical axis at defocus  $d$ , the PSF component due to field component  $E_i$  is given by the inverse Fourier transform of the field and defocus phase,

$$U_i^j(x, y) = \int_{-\infty}^{\infty} \int_{-\infty}^{\infty} E_j(k_x, k_y) e^{iz\sqrt{k_0^2 - k_r^2}} e^{-i2\pi(k_x x + k_y y)} dk_x dk_y. \quad (5.8)$$

We can re-write this in polar coordinates as

$$U_i^j(r, \gamma) = \int_0^{2\pi} \int_0^{\infty} E_j(k_r, \phi) e^{iz\sqrt{k_0^2 - k_r^2}} e^{-i2\pi k_r r \cos(\phi - \gamma)} k_r dk_r d\phi. \quad (5.9)$$

For each of our field components we are able to integrate over  $\phi$  immediately using a relationship derived in Richards and Wolf, 1959, valid for integer values of  $n$ :

$$\int_0^{2\pi} \cos(n\phi) e^{i\rho \cos(\phi - \gamma)} d\phi = 2\pi i^n J_n(\rho) \cos(n\gamma) \quad (5.10)$$

$$\int_0^{2\pi} \sin(n\phi) e^{i\rho \cos(\phi - \gamma)} d\phi = 2\pi i^n J_n(\rho) \sin(n\gamma), \quad (5.11)$$



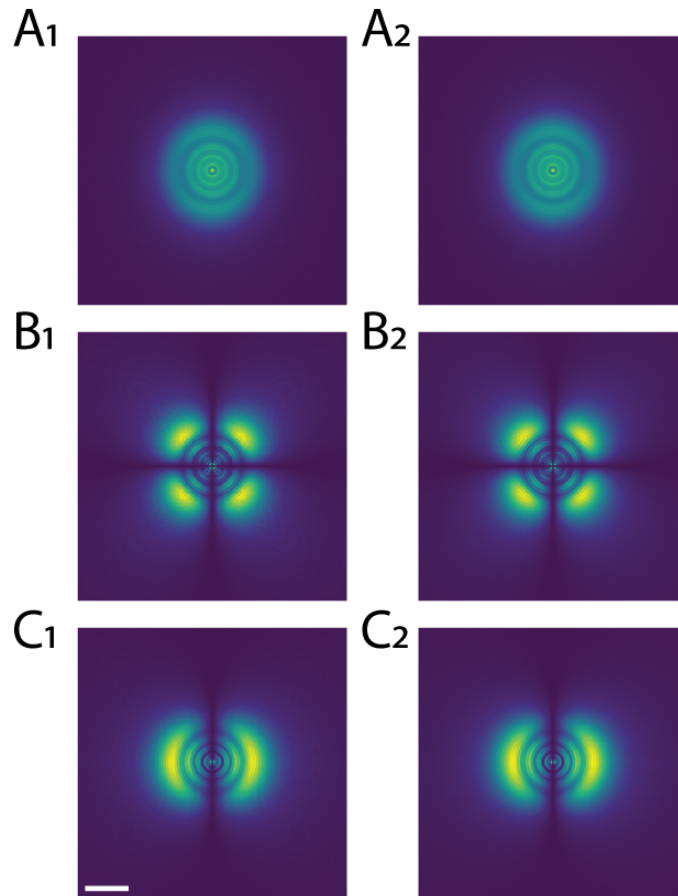


**Figure 5.5: Numerical PSF Calculation** Field components in the microscope native focal plane calculated using (A) 1D trapezoidal integration and (B) 2D FFTs for  $d = 5 \mu\text{m}$ . (1)  $U_i^1$ , (2)  $U_i^2$ , (3)  $U_i^3$ . Scale bar  $4 \mu\text{m}$  in the object space.

where  $J_n(\rho)$  is a Bessel function of the first kind of order  $n$ . In the following we will derive for each of our desired field components the 1D radial integral required to calculate them.

Our first component is

$$\begin{aligned}
 E_1 &= \frac{k_r^{-2}(k_o^2 - k_r^2)^{-1/4}}{\sqrt{k_0}} \left( k_x^2 \sqrt{k_o^2 - k_r^2} + k_0 k_y^2 \right) \\
 &= \frac{(k_o^2 - k_r^2)^{-1/4}}{\sqrt{k_0}} \left( \cos^2(\phi) \sqrt{k_o^2 - k_r^2} + k_0 \sin^2(\phi) \right). \tag{5.12}
 \end{aligned}$$

Using the identities  $\sin^2(\phi) = (1 - \cos(2\phi))/2$  and  $\cos^2(\phi) = (1 + \cos(2\phi))/2$ , we can write eq. (5.12) as

$$\begin{aligned} E_1 &= \frac{(k_o^2 - k_r^2)^{-1/4}}{2\sqrt{k_o}} \left( (1 + \cos(2\phi)) \sqrt{k_o^2 - k_r^2} + k_o (1 - \cos(2\phi)) \right) \\ &= \frac{(k_o^2 - k_r^2)^{-1/4}}{2\sqrt{k_o}} \left( k_o + \sqrt{k_o^2 - k_r^2} + \cos(2\phi) \left( \sqrt{k_o^2 - k_r^2} - k_o \right) \right) \\ &= f_1(k_r) \cos(0\phi) + g_1(k_r) \cos(2\phi), \end{aligned} \quad (5.13)$$

where

$$f_1 = \frac{\sqrt{k_o^2 - k_r^2} + k_o}{2\sqrt{k_o}(k_o^2 - k_r^2)^{1/4}} \quad (5.14)$$

and

$$g_1 = \frac{\sqrt{k_o^2 - k_r^2} - k_o}{2\sqrt{k_o}(k_o^2 - k_r^2)^{1/4}}. \quad (5.15)$$

Combining eqs. (5.9), (5.10) & (5.13), the PSF is given by

$$U_i^1(r, \gamma, d) = 2\pi \int_0^{k_o NA/n} (f_1(k_r) J_0(rk_r) - \cos(2\gamma) g_1(k_r) J_2(rk_r)) k_r e^{id\sqrt{k_o^2 - k_r^2}} dk_r. \quad (5.16)$$

Our second component is

$$\begin{aligned} E_2 &= \frac{k_r^{-2}(k_o^2 - k_r^2)^{-1/4}}{\sqrt{k_o}} \left( k_x k_y \left( \sqrt{k_o^2 - k_r^2} - k_o \right) \right) \\ &= \frac{(k_o^2 - k_r^2)^{-1/4}}{\sqrt{k_o}} \left( \cos(\phi) \sin(\phi) \left( \sqrt{k_o^2 - k_r^2} - k_o \right) \right) \\ &= \frac{(k_o^2 - k_r^2)^{-1/4}}{2\sqrt{k_o}} \left( \sin(2\phi) \left( \sqrt{k_o^2 - k_r^2} - k_o \right) \right) \\ &= f_2(k_r) \sin(2\phi), \end{aligned} \quad (5.17)$$

where we have used the identity  $\cos(\phi) \sin(\phi) = \sin(2\phi)/2$ , and

$$f_2 = \frac{\sqrt{k_o^2 - k_r^2} - k_o}{2\sqrt{k_o}(k_o^2 - k_r^2)^{1/4}} \quad (5.18)$$

Combining eqs. (5.9), (5.10) & (5.17), the PSF is given by

$$U_i^2(r, \gamma, d) = -2\pi \sin(2\gamma) \int_0^{k_o NA/n} f_2(k_r) J_2(rk_r) k_r e^{id\sqrt{k_o^2 - k_r^2}} dk_r. \quad (5.19)$$

Our third component is

$$\begin{aligned} E_3 &= \frac{(k_0^2 - k_r^2)^{-1/4}}{\sqrt{k_0}} (-k_x) \\ &= f_3(k_r) \cos(\phi), \end{aligned} \quad (5.20)$$

where

$$f_3 = \frac{k_r}{2\sqrt{k_0}(k_0^2 - k_r^2)^{1/4}} \quad (5.21)$$

Combining eqs. (5.9), (5.10) & (5.20), the PSF is given by

$$U_i^3(r, \gamma, d) = i2\pi \cos(\gamma) \int_0^{k_0^{NA/n}} f_3(k_r) J_1(rk_r) k_r e^{id\sqrt{k_0^2 - k_r^2}} dk_r. \quad (5.22)$$

For completeness, our fourth and final component is

$$\begin{aligned} E_4 &= \frac{(k_0^2 - k_r^2)^{-1/4}}{\sqrt{k_0}} (-k_y) \\ &= f_3(k_r) \sin(\phi), \end{aligned} \quad (5.23)$$

and so

$$U_i^4(r, \gamma, d) = i2\pi \sin(\gamma) \int_0^{k_0^{NA/n}} f_3(k_r) J_1(rk_r) k_r e^{id\sqrt{k_0^2 - k_r^2}} dk_r. \quad (5.24)$$

Example intermediate PSFs in the microlens plane for a defocus of 5  $\mu\text{m}$  are plotted in Figure 5.5 for the different field components calculated using both the 2D FFT and 1D integral method.

This integral method is still mildly more computationally intensive than the single integral evaluation used in Broxton et al., 2013, as it requires 4 complex numerical integration steps rather than 1. For the deconvolutions used in this chapter, the 2D FFT calculation method was used to calculate the PSFs. We measured experimental point spread functions from sub LFM resolution fluorescent beads (Fig. 5.6A) to compare with the modelled results. At positive, negative and no defocus the PSFs qualitatively match well with experiment (5.6B). There are qualitative differences between the calculated and measured PSFs, which could be due to measurement noise, differences in source position, aberrations, or inaccuracies in the models assumptions.

We calculated the PSF for GEVI imaging deconvolution for 550 nm light with the LFM elements used in the design for perfect alignment and for the camera displaced from perfect

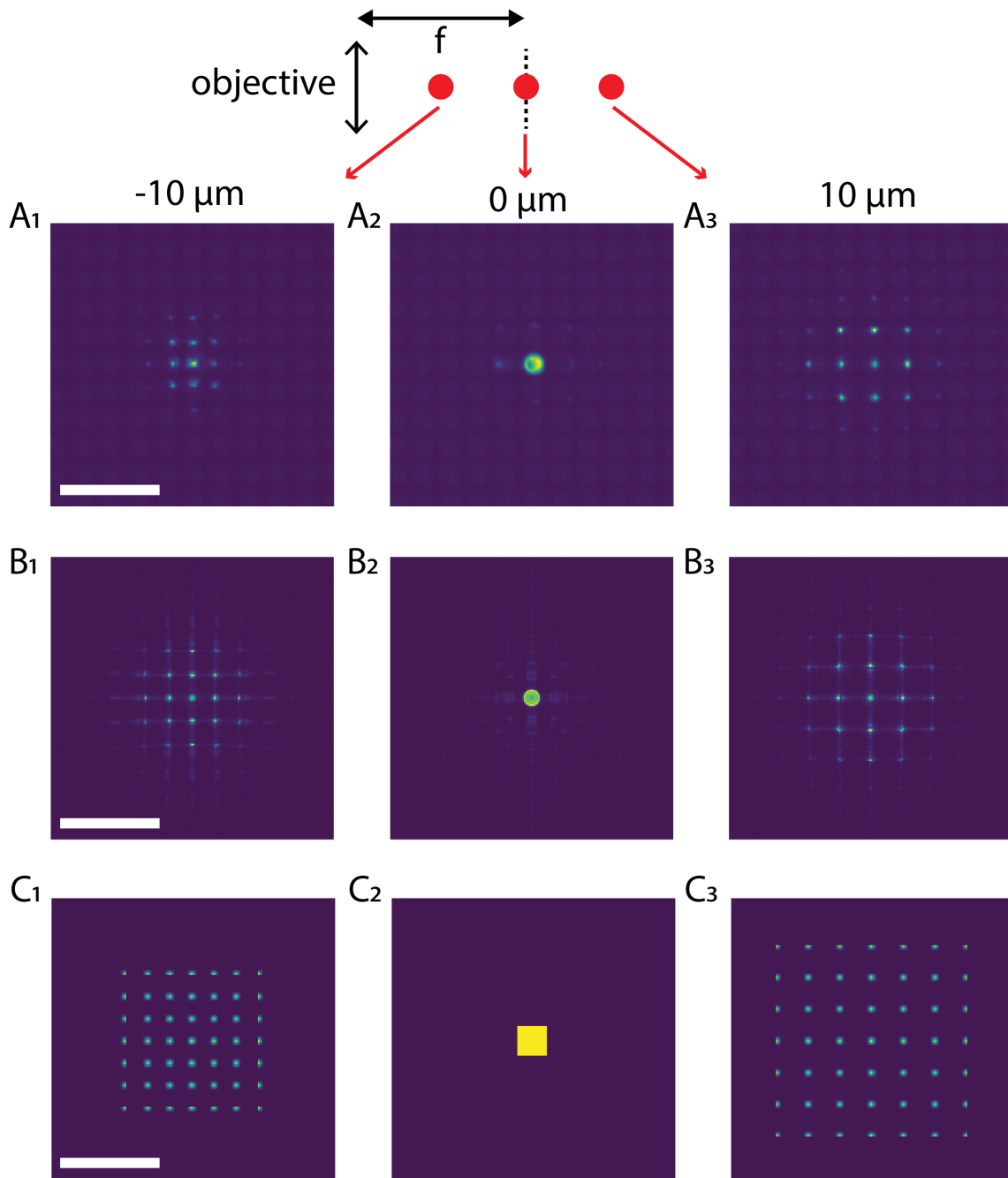


**Figure 5.6: Measured and modelled point spread functions** A) Measured light field point spread functions for A1)  $d = -10 \mu\text{m}$  (i.e. the source point is closer to the objective than the focus) A2)  $d = 0 \mu\text{m}$  and A3)  $d = 10 \mu\text{m}$  (point farther from the objective than focus). PSFs measured with  $2 \mu\text{m}$  beads emitting at peak wavelength  $660 \text{ nm}$ . B) PSFs simulated using the method described in the text for  $\lambda = 660 \text{ nm}$  and the same defocus as the measured PSFs. The contrast and dynamic range of the measured PSFs is quite low due to the low fluorescence intensity of single sub-resolution microbeads. C) Visualisation of the pixel weights used to synthetically refocus a lightfield pixel - the synthetic refocussing 'point spread function'. Scale bar  $20 \mu\text{m}$  in the object space.

alignment by 33% of the MLA focal length ( $\sim 412 \mu\text{m}$ , 'misaligned PSF') We deconvolved image volumes at the light field native resolution laterally and at  $1\text{-}5 \mu\text{m}$  spacing axially. We did not oversample the deconvolution as resolving voltage signals generally requires averaging pixels to approximately the native LFM resolution anyway. We therefore generated a single light field kernel for each depth by averaging over kernels sampled for point sources at different lateral positions under the microlens, weighting each point in the average by a 2D Hamming window function of a width equal to our microlens' pitch. We averaged over kernels sampled at 5 times the native microlens resolution. The Richardson-Lucy iteration scheme was used to deconvolve the data.

### Volume reconstructions

Having obtained our downsampled point spread function we deconvolved our volume using a similar procedure to previous studies. A key difference is that only a single 2D convolution was required for each depth in the reconstructed volume for the forwards and backwards projections, respectively. We applied the deconvolution scheme independently to each frame of the image time sequences, using a cluster to parallelize the data processing. Deconvolution of a single frame took around 30 - 40 minutes for a 21 iteration deconvolution of 21 z-planes on a single CPU. We employed a large cluster to process the individual frames simultaneously, enabling 5000 frames to be processed overnight. We did not use a parallel algorithm within each deconvolution by using, e.g. GPU processing, as the computing resources available to us were better suited to data parallelism. As with previous studies this would greatly increase the rate of individual frames, although it would also likely reduce the number of simultaneous frames that could be deconvolved for typical cluster setups.

Synthetic refocusing, based on a ray optics model of light field image formation, is a simpler approach to volume reconstruction that is also much less computationally intensive. Images focused at different z-depths can be constructed by combining individual perspective views using the formula derived in (Ng et al., 2005). Using linear interpolation in this summation results in each pixel being the weighted sum of pixels of the original light field image. Example weights for a single pixel (i.e. a 'refocusing PSF') can be seen in Fig. 5.6C. This reconstruction is much faster than the iterative deconvolution methods and also does not suffer from issues surrounding noise amplification (Thiébaud, 2005).

## 5.2.4 Volume time series analysis

### Effect of reconstruction on SNR

To compare the effect of different reconstruction techniques on voltage signal's SNR we reconstructed single planes from volumes at the light field microscope focal plane. We compared synthetically refocussed time series with time series deconvolved using RL deconvolution for different iteration numbers using the two PSFs, aligned and misaligned (defocused). ROIs were manually chosen over the soma and its surround and the same ROIs were used for each reconstruction technique.

As we were collecting fluorescence from the FRET donor, fluorescence decreased upon membrane depolarisation. To measure SNR we calculated the signal as the 5<sup>th</sup> percentile value during a stimulus and relaxation period of 200 ms with the median value of the 100 ms before the stimulation period subtracted. The noise level was calculated as the standard deviation of a 350 ms period during no intracellular current stimulus.

### Comparison of light field and wide-field SNR

We compared the SNR between trials of the same cell for image sequences taken with wide-field and light field imaging systems. We compared the SNR between refocused and wide-field images for the same number of repeats using ROIs calculated to be the same for both imaging modalities. We also calculated a compensation factor for imaging order and additional apertures in the light field system by calculating the square root of the sum brightness of the first image frame of the first repeat for the light field and wide-field trials.

## 5.3 Results

### 5.3.1 Light field microscopy enables simultaneous imaging of axially separated dendrites.

To compare LFM and wide-field imaging's ability to resolve axially separated dendrites we imaged a cell with a complex 3D dendritic structure using wide-field (Fig. 5.1B) and LFM (Fig. 5.1C). No single plane wide-field images were able to simultaneously bring all the dendrites into a good focus (Fig 5.1D), however when we reconstructed a volume from the LFM image by deconvolution, different planes from the reconstruction clearly resolved different dendritic

structures (1E1 & 1E2). A projection image through the recovered stack (Fig. 5.1E3) shows the same structure as the projection through the complementary wide-field stack.

### 5.3.2 Comparison of the effect of different reconstruction methods on SNR

LFM requires computational reconstruction to extract source volumes from raw images. Different approaches offer different advantages and disadvantages and must be evaluated for the specific problem at hand. SNR is of key importance in low-sensitivity GEVI imaging applications and so we first compared the effect of deconvolution and refocusing on functional single-cell GEVI image traces. We reconstructed volume time series for 11 cells and extracted optical time courses from ROIs over the individual cell's soma at the native focal plane (Fig. 5.7A). We then compared for each cell the effect of iteration number and PSF type on the trace SNR, using the refocused images as the baseline due to the simplicity of extracting the in focus refocused image. We found that for all iteration numbers the noise and signal level was increased by deconvolution (Figs. 5.7B-E). The contrast of the deconvolved volumes was increased, leading to a linear increase in signal and noise levels. The deconvolution does however increase noise levels above and beyond the increased brightness as is demonstrated in figure 5.7B. The deconvolved and refocused traces are highly correlated, however there remains a residual variance after removing the linear relationship. The increase of the slope of the linear fit to the points can also be directly interpreted as the increased sensitivity due to the deconvolution. We measured the increased signal and noise levels whilst varying the number of deconvolution iterations in the reconstruction (Figs. 5.7C - E). Increasing the number of iterations does increase the signal and noise levels, with the noise increasing faster than the signal. This is a known phenomenon with Richardson-Lucy deconvolution, as the maximum-likelihood solution to the problem can overfit noise peaks (White, 1994). These peaks appear and disappear in subsequent frames, introducing temporal noise. The noise level is generally increased more than the signal level for iteration number greater than one, and so increasing iterations decreases the SNR relative to the refocused case. The SNR for both deconvolved cases was significantly worse at 23 iterations compared to the refocused case, with no significant difference when using correctly aligned or misaligned PSFs (refocused-RL-RL misaligned Friedman  $\chi^2$  with post hoc Bonferroni-corrected Wilcoxon signed-rank tests.  $\chi^2 = 16.5$ ,  $p = 0.0002$ , RL-RL misaligned  $z = 22$ ,  $p = 0.33$ , RL-refocused  $z = 0.0$ ,  $p = 0.003$ , RL misaligned-refocused  $z = 0.0$ ,  $p = 0.003$ ). This decrease in SNR

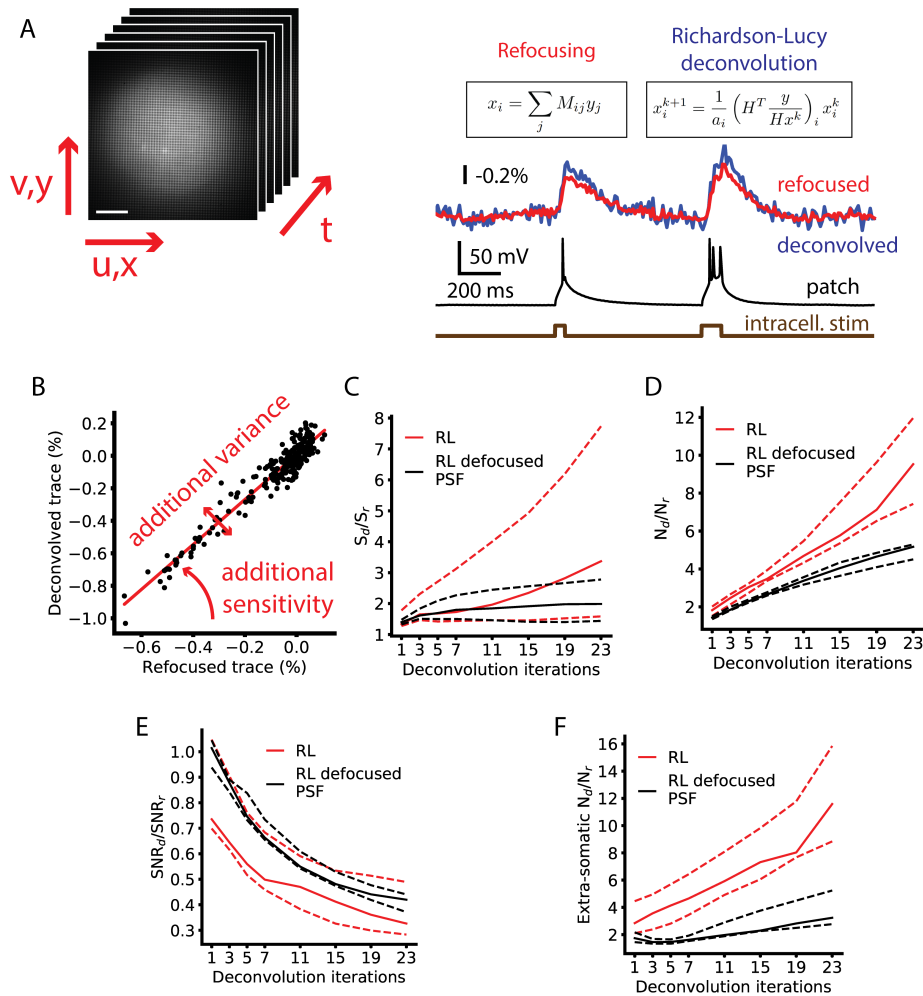


**Figure 5.7: Comparison of the effect of different reconstruction methods on SNR.** (A) We reconstructed sequences of light field images using synthetic refocusing and deconvolution methods. Volumes were deconvolved with an aligned PSF and a PSF with modelled defocus of  $412 \mu\text{m}$ . Deconvolution can provide better axial sectioning but suffers from long computational times and noise amplification. Resulting optical traces in response to intracellular stimulation are plotted for refocused and RL deconvolved cases. Deconvolution increases contrast and cellular brightness, increasing the signal size but also the noise level (5 deconvolution iterations). (B) Deconvolved and refocused signals are strongly linearly correlated, as can be seen from plotting the individual trace time points. The additional noise variance due to deconvolution can be identified as the residual from the linear fit. The increased signal level can be seen as the increased fit gradient over unit slope. (C) Deconvolution signal size normalized to refocused signal size as a function of iteration number. The in-focus PSF starts to diverge at high iteration number, whilst the slightly defocused PSF seems to converge to approximately constant. Solid lines median of  $n = 11$  cells, dashed lines indicate 25<sup>th</sup> and 75<sup>th</sup> percentile values. (D) Deconvolution noise increase over refocused noise. (E) Deconvolution SNR as a fraction of refocused SNR. At low iteration number the deconvolution and refocusing are very similar, as the methods are related. At large iteration number the SNR is decreased relative to refocused, however the increased axial sectioning may still motivate the use of deconvolution methods. (F) The noise level from ROIs over dim areas away from cell's somata. Noise is increased more over the refocused case compared to in bright areas.



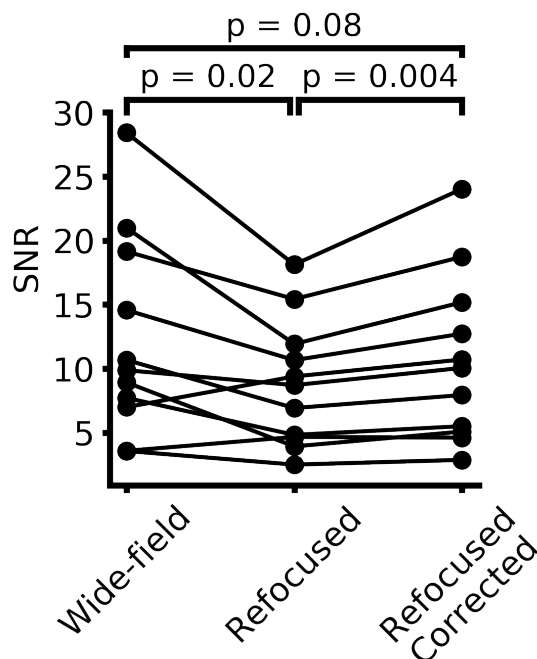


**Figure 5.8: Comparison of Light field and wide-field SNR.** SNR is significantly decreased using LFM. This is likely due to trial order and the reduced aperture due to misalignment as discussed in section 5.2.1. Correcting the traces by multiplying by the square root of the relative sum intensity collected removes any difference in SNR.

is unfortunate for deconvolution, especially for voltage imaging, however deconvolution may offer advantages in other areas that make the reduction in SNR worthwhile.

We also analysed ROIs surrounding but excluding the active somata. These were typically dimmer, and we wanted to investigate if noise amplification was worse in dimmer areas. We calculated the noise levels for these ROIs (Fig. 5.7F) and found that the increase in noise over the refocused case was indeed higher than in the somatic ROIs. This seems to be driven by a subset of the cells, where the noise is greatly increased. In particular, temporal oscillations could be seen to start to appear in time courses, likely an artefact from the line-by-line CMOS readout amplified by the deconvolution process. This is likely to be impactful when imaging particularly dim objects or at high frame rates. Interestingly, RL deconvolution performed significantly worse with the in-focus PSF for high iteration numbers in these traces, and the oscillations can be seen to be qualitatively worse (refocused-RL-RL misaligned PSF Friedman  $\chi^2$  with post hoc Bonferroni-corrected Wilcoxon signed-rank tests.  $\chi^2 = 22$ ,  $p = 2 \times 10^{-5}$ , RL-RL misaligned  $z = 0$ ,  $p = 0.0033$ , RL-refocused  $z = 0.0$ ,  $p = 0.003$ , RL misaligned-refocused  $z = 0$ ,  $p = 0.0033$ ). RL median (IQR) noise: 0.08% (0.07%, 0.1%), RL misaligned median (IQR) noise: 0.027% (0.025%, 0.032%), refocused median (IQR) noise: 0.008% (0.005%, 0.010%).

### 5.3.3 Comparison of wide-field and light field SNR

We compared refocused reconstructed LFM traces with paired wide-field trials to compare SNR between light field and wide-field imaging modalities. Using refocused traces removed confounds due to the chosen deconvolution method. We found that the LFM traces had significantly lower SNR than wide-field traces collected from the same cell (Fig. 5.8A), reducing the SNR from 9.9 (7.3, 16.8) (median (IQR)) to 8.7 (4.7, 11.2). This is likely due to two factors: firstly, when cells were initially patched the wide-field imaging traces were collected first to easily check if the correct cell had been patched and so light field trials were taken after some initial bleaching had occurred. Secondly, and more importantly, an additional aperture was introduced into the light field system due LFM misalignment. This reduced the total transmission of the LFM system significantly (apertures between 1/2 and 1/4 the design aperture used). As this is an artefact of poor experimental practice, we also report a corrected SNR comparison between LFM and wide-field modalities. We correct the LF SNR by adjusting it to  $\sqrt{(\sum(p_{WF}) / \sum(p_{LF}))}$ , where  $p_{WF}$  and  $p_{LF}$  are the wide-field and lightfield pixel intensities of the first frame of the first imaging sweep for each acquisition mode respectively. This is a correction factor for reduced shot noise limited SNR due to lower measured light intensities. Applying this correction factor removed the significant decrease when using LFM, increasing the mean SNR to 10.0 (5.3, 13.9) (wide-field - refocused - refocused corrected Friedman  $\chi^2$  with post hoc Bonferroni-corrected Wilcoxon signed-rank tests (significant at  $p < 0.017$ ).  $n = 11$  cells from 11 slices from 3 mice. Friedman  $\chi^2 = 9.45$ ,  $p = 0.009$ . Post-hoc tests: wide-field-refocused  $z = 6$ ,  $p = 0.016$ , wide-field - refocused corrected  $z = 13$ ,  $p = 0.075$  (n.s.), refocused - refocused corrected  $z = 1.0$ ,  $p = 0.004$ ).

### 5.3.4 Light field microscopy resolves 3D localised voltage signals

Tracking propagating voltage signals in 3D is a key advantage of LFM and therefore signals from different planes must be discriminable in volume reconstructions. This is dependent on factors intrinsic to the LFM, such as depth of field, and also extrinsic factors, such as cellular localisation and signal spread due to tissue scattering. To test whether voltage signals could be localized in 3D we reconstructed 4D space-time volumes and compared time courses from ROIs over different dendritic and somatic structures. Figure 5.9 shows an example region with a patched, active cell and an inactive cell. We plot traces from deconvolved and refocused

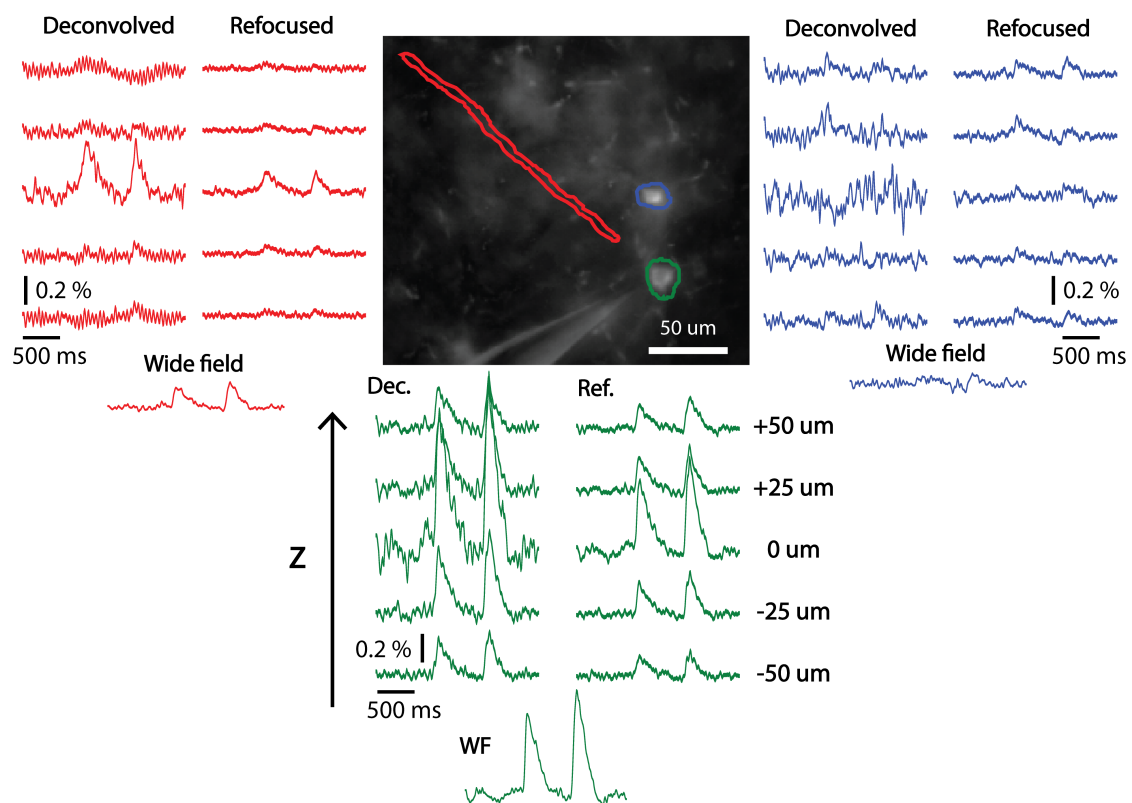


**Figure 5.9: Light field microscopy resolves 3D localised voltage signals.** An example cell with optical traces plotted from three ROIs plotted at different axial depths (LFM) and at best focus (wide-field). Individual traces are plotted from reconstructed volumes at planes at -50 to +50  $\mu\text{m}$ . The ROI around the cell's apical dendrite (red) shows much higher 3D localisation as it lies in a single plane compared to trace plotted from an ROI around the soma (green) which extends in three dimensions. Traces are also plotted from an ROI around an adjacent unstimulated cell (blue). This shows a small amount of optical crosstalk from the stimulated cell likely caused by scattering or collection of signal from basal dendrites.

volumes at different depths and in focus wide-field traces from ROIs over the active cell's soma, inactive cell's soma and active cell's apical dendrite. Traces from the deconvolved volume show a large signal from the cell's soma that peaks in size at the native focal plane where the cell is positioned. A significant signal extends for a large  $z$  region above and below the soma. A ROI positioned over the apical dendrite shows a much sharper transition, with a functional signal appearing and disappearing rapidly as the dendrite comes into focus. The ROI over the inactive cell shows little functional signal, with just a small amount of crosstalk likely from basal dendritic signals or emission photon scattering. Similar results were achieved with both PSF types used in the deconvolution.

The refocussed volumes seemed to exhibit a larger axial PSF width compared to the deconvolved traces, meaning signals are smeared out and it is difficult to distinguish between functional signal from different planes. To quantify this effect we generated volumes showing the distribution of functional signal. We generated a time course from an in focus somatic ROI and calculated the temporal correlation coefficient of every pixel in the volume for refocussed and deconvolved volume time series. Pixels with high correlation coefficients are interpreted as having a large response to the intracellular current injection, and so a volume map of these reveals the cell's structure. Activation maps from wide-field imaging trials show extensive blurring around the soma from out of focus basal dendrites (Fig. 5.10A). Comparatively,  $z$ -projections from a 30  $\mu\text{m}$  region around the soma generated from the deconvolved activation volume reveals the structures that cause this blur. Similar treatment of the refocused volume also shows significant blurring from the poor axial sectioning of this reconstruction technique. We quantified the effect of the 3D signal spread with the 3D autocorrelation of these activation maps. The value of the 3D autocorrelation at any point is proportional to the signal power that the cell contributes to that location's time course and previous studies have quantified this effect in two dimensions (Quicke et al., 2019). We examined how the mean autocorrelation changed in the axial dimension to study the functional signal localisation. Axial smearing can be seen in reconstructions from both deconvolution and refocusing (Fig. 5.10E), although the effect is much more severe in refocused traces. This can be seen in the axial autocorrelation as side lobes away from the central peak (Fig. 5.10F). These lobes can be seen to decrease with increasing deconvolution iteration number (Fig. 5.10F & G), thus increasing the axial sectioning ability. The defocused PSF (Fig. 5.10G) seemed to have slightly reduced axial spread compared to the aligned PSF deconvolution (Fig. 5.10F). This could be due to the reduced

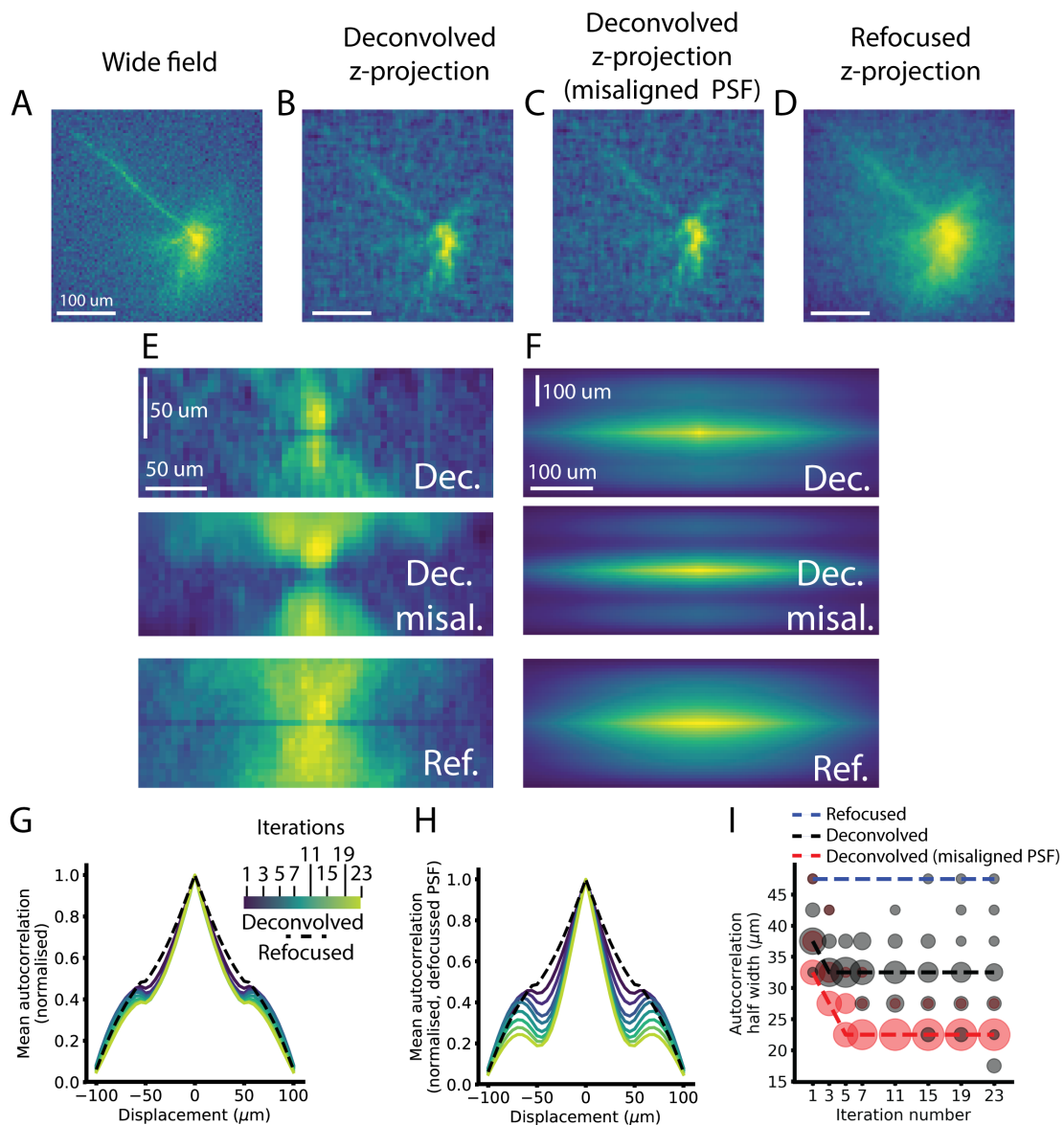


**Figure 5.10: Mapping dendritic signals.** (A) wide-field activation image. (B) Deconvolved activation image, mean projection from -15 to +15 μm, 21 deconvolution iterations. (C) Deconvolved activation image using a defocused PSF, mean projection from -15 to +15 μm. (D) Refocused activation image, mean projection from -15 to +15 μm. (E) x-z projections through deconvolved (top), deconvolved with a misaligned PSF (middle) and refocused (bottom) activation images showing the different axial sectioning. (F) Mean x-z projections through the autocorrelations. (G) Normalised mean autocorrelation for different depths from refocused and deconvolved LFM activation volumes. (H) Similar to (G), but from data deconvolved with a defocused PSF. The secondary peaks arise from the elongated axial PSF, and these can be seen decreasing as the iteration number increases. (I) Autocorrelation axial half width for  $n = 11$  cells with iteration number. Black circles, aligned PSF, red circles misaligned PSF. Dashed lines represent median value. Area of circles indicates number of cells.

noise levels in the misaligned PSF deconvolution. The autocorrelation axial half widths can be seen to decrease with number until  $\approx 5$  iterations (Fig. 5.10G). The deconvolved autocorrelation half widths decrease from 37.5  $\mu\text{m}$  (37.5  $\mu\text{m}$ , 40.5  $\mu\text{m}$ ) at 1 iteration to 32.5  $\mu\text{m}$  (25.0  $\mu\text{m}$ , 35.0  $\mu\text{m}$ ) at 23 deconvolution iterations. The misaligned PSF deconvolved autocorrelation half widths decrease from 32.5  $\mu\text{m}$  (32.5  $\mu\text{m}$ , 37.5  $\mu\text{m}$ ) at 1 iteration to 22.5  $\mu\text{m}$  (22.5  $\mu\text{m}$ , 35.0  $\mu\text{m}$ ) at 23 deconvolution iterations. The refocused autocorrelation axial half width median (IQR) was 47.5  $\mu\text{m}$  (47.5  $\mu\text{m}$ , 47.5  $\mu\text{m}$ ). Comparing the values at the final iteration step between deconvolved, deconvolved with misaligned PSF and refocused found no significant difference between the two deconvolution types, however, although they were both significantly narrower than the refocused case. This used a Friedman  $\chi^2$  with post hoc Bonferroni-corrected Wilcoxon signed-rank tests (significant at  $p < 0.017$ ).  $n = 11$  cells from 11 slices from 3 mice. Friedman  $\chi^2 = 17.6$ ,  $p = 0.0001$ . Post-hoc tests: deconvolved - deconvolved misaligned  $z = 4$ ,  $p = 0.027$  (n.s.), deconvolved-refocused  $z = 0$ ,  $p = 0.005$ , deconvolved misaligned - refocused  $z = 0.0$ ,  $p = 0.0009$ ). A trade off must be made whether to increase the iteration number and improve axial resolution, or use reduced iterations for increased SNR.

## 5.4 Conclusion

We have shown that LFM enables 3D single cell GEVI imaging of somatic and dendritic structures. This could enable easier studies of dendritic integration or synaptic mapping. Even with imperfect alignment, the LFM was able to resolve dendritic and somatic voltage signals in three dimensions. We anticipate that with correct alignment the reconstructions would have both better axial resolution and SNR on parity with wide-field microscopy. We are currently working towards collecting this data. Alternatively, reconstruction methods taking the misalignment into account could be developed to make the most of the imperfect data.

For this study we used an earlier generation GEVI, VSFP-Butterfly 1.2, for practical reasons. Although the GEVI exhibits lower sensitivity than recently reported probes, we were able to use it with a recently described technique for sparse but strong expression enabling single-cell GEVI imaging (Quicke et al., 2019; Song et al., 2017). The kinetics of this probe also happen to represent a good compromise in response kinetics, with the ability to resolve action potentials without being so fast as to suffer severe aliasing at 100 Hz imaging rates. Although we could resolve single-sweep signals, signal averaging was required to resolve smaller dendritic signals

with adequate SNR. More recently reported probes offer increased SNR over VSFP-Butterfly 1.2 (Abdelfattah et al., 2018; Adam et al., 2018; Piatkevich et al., 2018; Yi et al., 2018). These GEVIs could be combined with LFM for single-sweep dendritic signal tracking. One issue that may be encountered using newer GEVIs with faster kinetics with LFM is the increased sampling rate they require to avoid significant signal aliasing. These GEVIs are much faster than VSFP-Butterfly 1.2 and are typically imaged at 500 - 1000 Hz. Megapixel image sensors with full-frame readout at 1 kHz would be required to make full use of these GEVIs with LFM. With CMOS cameras like that used in this study, this requires reducing the FOV to a small strip in the center of the camera. This impacts LFM more strongly than wide-field microscopy for two reasons. Firstly, lateral resolution is already reduced relative to wide-field, and so there are fewer pixels to spare. Secondly, information about the source volume is distributed widely across the camera sensor, especially for objects away from the native focal plane. Light, and therefore signal, from these will be lost if only a subset of rows on the sensor are sampled. We anticipate that this issue will be steadily ameliorated as newer CMOS sensor technology is developed.

We compared how different reconstruction techniques offer different benefits with respect to signal localization and SNR. Refocusing offers increased SNR over deconvolution, but performs poorly when axial localization of signal is desired. Deconvolution, however, has two major disadvantages: computational cost and noise amplification. The LFM point spread function (PSF) is in general shift invariant, however it displays a periodicity when shifting a source laterally by integer multiples of the microlens pitch. This means that deconvolution can be performed efficiently with FFT-based convolution, however, even with modest oversampling compared to the native LFM resolution the computational cost is very high. Reconstruction of a volume at  $n_z$  z-planes and with a lateral oversampling of  $m$  requires  $2 \times n_z \times m^2$  2D convolutions per iteration, which rapidly becomes extremely burdensome, especially when deconvolving individual frames at high frame rate. Secondly, both Richardson-Lucy and ISRA tend to amplify noise in their outputs due to their lack of regularization (Dey et al., 2006). For high-SNR calcium imaging the additional noise introduced by these methods may not be significant, however when imaging small, dim voltage signals these effects may become increasingly important. As newer GEVIs with increased SNR are used, the additional noise introduced in the deconvolution process may become less of a problem. Alternatively, more

sophisticated deconvolution approaches incorporating regularization could improve the deconvolution's performance. Imaging at faster frame rates with newer GEVIS would drastically increase the computational resources required for volume reconstructions. Approaches have been developed for calcium imaging which do not require reconstruction of volume time series (Nöbauer et al., 2017), however, these rely upon the temporal and spatial characteristics of neuronal calcium signals, and so may not be appropriate to apply to voltage signals which are smaller, less temporally sparse and arise from more intricate 3D structures than neuronal somata.

## 5.5 Prospects for synaptic mapping

Does the combination of VSFP-Butterfly 1.2 and the current LFM setup have high enough SNR to resolve synaptic signals? We can use the data collected as part of this thesis to estimate the level of averaging needed to resolve dendritic inputs.

We can model the synaptic input as a square pulse. Somatic EPSPs range in size up to approximately 10 mV. Dendritic EPSPs, however, where voltage imaging will measure them, are much larger due to the dendrite's geometry and electrical properties (Etherington et al., 2010). For an approximate calculation, we can assume generously a 20 mV, 10 ms square wave dendritic input.

The length constant of a cylindrical dendrite of diameter  $d$  is given by

$$\lambda = \sqrt{\frac{dR_M}{4R_A}}, \quad (5.25)$$

where  $R_M$  is the specific membrane resistance and  $R_A$  the specific axial resistance through the cytoplasm along the dendrite (Bower and Beeman, 2003). For a 1  $\mu\text{m}$  diameter dendrite with  $R_M = 10\,000 \Omega\text{cm}^2$  and  $R_A = 100 \Omega\text{cm}$ ,  $\lambda \sim 500 \mu\text{m}$ . We can integrate over pixels with an area proportional to the electrical length constant multiplied by the width of a dendrite.

The red ROI shown in 5.9 is a good test ROI for this calculation, with a similar order of magnitude area. LFM at the focal plane can achieve an SNR of 4.7 for a square input pulse of length 50 ms from a depolarisation of 50 mV at the soma (where we assume the AP is filtered by the GEVI response). Averaging the 50 mV depolarisation along the dendrite using the length constant estimated previously, we calculate a mean depolarisation of  $50 \times 0.63 = 32 \text{ mV}$ .



EPSPs, however, do not occur on every presynaptic spike. Assuming 50% transmission rate we therefore need to reduce the mean SNR by 2.

The SNR of a Poissonian rate change of length  $\Delta t$  is proportional to  $\Delta t^{-1/2}$ . We can therefore estimate the SNR of a dendritic EPSP from 8 trial averages as  $4.7 \times \sqrt{\frac{10}{100}} \times \frac{20}{32} \times 1/2 \approx 0.46$ . An SNR of 1 would therefore be achieved by averaging a further 24 sweeps. Considering the imperfect alignment of the system, as discussed before, this could likely be reduced in a well aligned system. This is within the realms of possibility, however the chances would be much improved by using more sensitive and newer GEVIs.

## Chapter 6

# Conclusion and future directions

In this thesis different optical and genetic techniques to improve GEVI imaging in brain slice have been presented. GEVI imaging is a fast growing and changing field, with exciting developments arising from a multitude of different approaches. With this thesis I hope that I have, in an extremely limited way, helped to advance the field so that the full potential of neuronal GEVI imaging can be realised.

The development of this thesis broadly tracks the development of my understanding of the challenges of voltage imaging and my appreciation of the possible. In the first chapter I described a multifocal two-photon system developed with fast GEVI imaging in mind. In order to increase the resistance of MTPM to scattering and better resolve GEVI signals in tissue, I developed a source localization control and processing algorithm to reassign scattered light back to its likely origin. This algorithm works by temporally oversampling a scanned multifocal line array, before using iterative deconvolution with a scattering PSF to reassign scattered light back to its likely origin. Further work is required to improve the computational efficiency of the algorithm, which requires iterative deconvolution of temporally oversampled frames. A possibility which I briefly explored is to first project the 'streak' images onto a single column of pixels per spot, and then deconvolve along a single axis parallel to the streak direction. This would greatly reduce the computational time at the loss of a small amount of lateral detail. A second continuation would be to apply more sophisticated deconvolution techniques to reduce the additional noise introduced by the deconvolution process. Including additional terms in the iterative deconvolution cost function to penalise, for example, very high frequency variations that likely arise from noise, could reduce the noise amplification during the deconvolution. Alternatively, techniques to estimate both the deconvolved image and PSF could be applied, adapting the PSF to each specific imaging location.

After developing the MTPM system I then applied the MTPM to image GEVI signals in slice, resolving both single-cell and population signals. Interestingly, voltage signals could be resolved with a fibre laser operating at a wavelength that excited the FRET acceptor around 11 times more than the FRET donor. Direct acceptor excitation is generally thought to reduce the signal size, as directly excited acceptors are unavailable for FRET. In this case, however, it is likely that the fraction of excited molecules, both donor and acceptor, are so low that the probability of exciting both in the same molecule is negligible. I also observed larger voltage signals under two photon excitation than single photon excitation, likely due to the optical sectioning meaning a higher fraction of excited fluorescence arising from molecules in depolarised membranes. Despite this, I quickly realised that the small signal size and dim indicators would not result in anywhere near high enough SNRs to do physiologically useful imaging, and so I did not move forwards with collecting temporally oversampled data and applying the source localisation algorithm. Newer, two-photon optimised GEVIs or synthetic voltage probes would likely benefit from multifocal implementations.

After seeing the high noise levels and low imaging speeds of even multifocal two-photon I became convinced that single photon imaging was the best way to image VSFP-Butterfly signals in slice. Luckily, sparsely expressed VSFP-Butterfly mice had been demonstrated by a collaborator, Chenchen Song, although functional signals were still yet to be properly verified. In chapter 4 I demonstrated that this sparse transgenic technique did indeed enable single cell resolution GEVI imaging. I was also able to explore the characteristics of GEVI signals and examine what spatial and temporal sampling regimes might be useful. Exploring the minimum sparsity of cells required for a specific value of signal mixing between them enables future experimenters to titrate the dCre stabilisation to a level that suits them.

I wanted to collect 3D activation stacks in wide-field as a first step towards mapping synaptic input onto a neuron, however when imaging I realised that the 3D imaging requirement along with sample bleaching meant that I would not be able to acquire enough high SNR images to do this. Fortunately a collaborator, Dr. Carmel Howe, had just designed and built a light field microscope system for calcium imaging. I realised that this could be the high-SNR 3D imaging technique which could enable the kind of experiments I imagined. I acquired a dataset of single-cell GEVI lightfield functional images and reconstructed them in different ways to evaluate the attainable results. As the previous wave-optics based deconvolution PSF was valid only for low to moderate-NA objectives, I calculated a vectorial PSF for the LFM

valid for high-NA fluorescence correction. A key advantage of this PSF calculation method is the ability to easily include aberrations in the LFM PSF by expressing them as Zernike polynomials in the objective pupil. In future work, it would be interesting to see if improved reconstructions could be achieved by measuring and including any relevant aberrations present to enable post-hoc aberration correction.

Reconstructing 3D GEVI imaging volumes, I was pleased to observe that GEVI signals could be identified and localised to somatic and dendritic structures. I characterised the effect of different reconstruction techniques on achievable SNR and axial confinement. Deconvolution approaches were found to decrease axial blur, but introduce additional noise into the functional traces. Unfortunately, as with the previous deconvolution, the iterative deconvolution methods had a tendency to amplify noise, making choosing the best reconstruction technique a challenge. Again, regularised or damped deconvolution methods would be the next thing to try to ameliorate this issue.

Late in the process, after I had designed and carried out the data analysis, I realised that the data I had collected were from a misaligned LFM microscope. I was puzzled why my lenslet images were overlapping when GEVI imaging when the design had set the MLA numerical aperture higher than the objective NA. By the time I realised that the problem was simply that the alignment and imaging wavelengths were different and therefore the system was slightly misaligned, no more mice with the required genetics were being bred, meaning correct data could not be acquired. More mice are currently planned, but the complex breeding means the data cannot be included in this thesis. As this misalignment was slight, I was able to reconstruct volumes, albeit they were likely a worse quality than if the LFM was aligned correctly. This data needs to be collected to properly evaluate LFM for single cell GEVI imaging and this is currently being arranged.

The GEVI imaged in this study is fairly slow, allowing us to image at 100 Hz without significant aliasing. Newer GEVIs with higher intensity signals require imaging at higher rates, however experimental tricks could enable us to image them at 100 Hz in some paradigms. If we already average over multiple time-locked stimuli, we could vary the phase of the stimulus with respect to the camera readout, achieving temporal super-resolution time courses from which high frequency unaliased time courses could be deconvolved. A second important route of enquiry is to develop new reconstruction techniques, analogous to SID for calcium imaging (Nöbauer et al., 2017), that work well for single-cell imaging GEVI datasets. This will enable

higher throughput analysis without the heavy computational cost of frame-by-frame deconvolution.

There is much work to do, and much has been achieved. The future of optical electrophysiology is bright!

## 6.1 Summary of novel contributions

In this section I list the high-level novel achievements from each of my results chapters.

- Multifocal two-photon microscopy
  - Development and testing of a novel source localisation algorithm for MTPM.
  - Single-cell resolution and population GEVI imaging with a MTPM.
- Wide field GEVI imaging
  - Demonstration that transgenic sparsity enables wide-field single-cell resolution GEVI imaging.
- Lightfield GEVI imaging
  - Development of extended model for calculation of high-NA LFM point spread functions.
  - Single-cell resolution GEVI imaging with a LFM.

## 6.2 List of publications arising from this thesis

- Quicke P., Howe, C. L., Verinaz Jadan, H., Song, P., Knöpfel, T., Dragotti, P. L., Neil, M., Schultz, S. R., Foust, A. J., (In preparation). Lightfield voltage imaging.
- Quicke P., Howe, C. L., Song, P., Knöpfel, T., Schultz, S. R., Dragotti, P. L., Foust, A. J., Neil, M., (accepted). Calculation of high numerical aperture lightfield point spread functions.
- Song, P., Verinaz Jadan, H., Quicke, P., Howe, C. L., Foust, A. J., Dragotti, P. L., (accepted). Location Estimation for Light Field Microscopy based on Convolutional Sparse Coding.

- Quicke P., Song, C., McKimm, E. J., Milosevic, M. M., Howe, C. L., Neil, M., Schultz, S. R., Antic, S. D., Foust, A. J., Knöpfel, T., (2019). Single-neuron level one-photon voltage imaging with sparsely targeted genetically encoded voltage indicators. *Frontiers in Cellular Neuroscience*, 13, 39.
- Soor, N. S., Quicke, P., Howe, C. L., Pang, K. T., Neil, M., Schultz, S. R., Foust, A. J. (2019). All-optical crosstalk-free manipulation and readout of Chronos-expressing neurons. *Journal of Physics D: Applied Physics*.
- Quicke, P., Reynolds, S., Neil, M., Knöpfel, T., Schultz, S. R., Foust, A. J. (2018). Source Localised Multifocal Multiphoton Microscopy for High Speed Functional Imaging. *Biomedical Optics Express*, 9, 3678-3693.
- Quicke, P., Barnes, S. J., Knöpfel, T. (2017). Imaging of Brain Slices with a Genetically Encoded Voltage Indicator. In: Markaki Y., Harz H. (eds) *Light Microscopy. Methods in Molecular Biology*, vol 1563. Humana Press, New York, NY
- Schultz, S. R., Copeland, C. S., Foust, A. J., Quicke, P., Schuck, R. (2017). Advances in two-photon scanning and scanless microscopy technologies for functional neural circuit imaging. *Proceedings of the IEEE*, 105(1), 139-157.
- Schuck, R., Quicke, P., Copeland, C., Garasto, S., Anecchino, L. A., Hwang, J. K., Schultz, S. R. (2015). Rapid three dimensional two photon neural population scanning. In *Engineering in Medicine and Biology Society (EMBC), 37th Annual International Conference of the IEEE* (pp. 5867-5870).

# Bibliography

- Abdelfattah, Ahmed S et al. (2018). "Bright and photostable chemigenetic indicators for extended in vivo voltage imaging". In: *bioRxiv*. DOI: [10.1101/436840](https://doi.org/10.1101/436840).
- Adam, Yoav et al. (2018). "All-optical electrophysiology reveals brain-state dependent changes in hippocampal subthreshold dynamics and excitability". In: *bioRxiv*, p. 281618. DOI: [10.1101/281618](https://doi.org/10.1101/281618).
- Ahrens, Kurt F et al. (2012). "Two-photon scanning microscopy of in vivo sensory responses of cortical neurons genetically encoded with a fluorescent voltage sensor in rat." In: *Frontiers in neural circuits* 6.March, p. 15. ISSN: 1662-5110. DOI: [10.3389/fncir.2012.00015](https://doi.org/10.3389/fncir.2012.00015).
- Ahrens, Misha B et al. (2013). "Whole-brain functional imaging at cellular resolution using light-sheet microscopy". In: *Nat Methods* 10.5, pp. 413–420. ISSN: 1548-7105. DOI: [10.1038/nmeth.2434](https://doi.org/10.1038/nmeth.2434).
- Aimon, Sophie et al. (2018). "Fast near-whole brain imaging in adult *Drosophila* during responses to stimuli and behavior". In: *bioRxiv*, p. 033803. DOI: [10.1101/033803](https://doi.org/10.1101/033803).
- Akemann, Walther et al. (2012). "Imaging neural circuit dynamics with a voltage-sensitive fluorescent protein." In: *Journal of neurophysiology* 108.8, pp. 2323–37. ISSN: 1522-1598. DOI: [10.1152/jn.00452.2012](https://doi.org/10.1152/jn.00452.2012).
- Akemann, Walther et al. (2013). "Two-photon voltage imaging using a genetically encoded voltage indicator". In: *Scientific reports* 3.223, pp. 1–7. DOI: [10.1038/srep02231](https://doi.org/10.1038/srep02231).
- Allen, William E et al. (2017). "Thirst-associated preoptic neurons encode an aversive motivational drive." In: *Science (New York, N.Y.)* 357.6356, pp. 1149–1155. ISSN: 1095-9203. DOI: [10.1126/science.aan6747](https://doi.org/10.1126/science.aan6747).
- Amir, Wafa et al. (2007). "Simultaneous imaging of multiple focal planes using a two-photon scanning microscope." In: *Optics letters* 32.12, pp. 1731–3. ISSN: 0146-9592. DOI: [10.1117/12.731868](https://doi.org/10.1117/12.731868).
- Amit, Daniel J. (1989). *Modeling brain function : the world of attractor neural networks*. Cambridge University Press, p. 504. ISBN: 0521361001.

- Anastasiades, Paul G., Andre Marques-Smith, and Simon J.B. Butt (2018). "Studies of cortical connectivity using optical circuit mapping methods". In: *Journal of Physiology* 596.2, pp. 145–162. ISSN: 14697793. DOI: [10.1113/JP273463](https://doi.org/10.1113/JP273463).
- Anselmi, F. et al. (2011). "Three-dimensional imaging and photostimulation by remote-focusing and holographic light patterning". In: *Proceedings of the National Academy of Sciences* 108.49, pp. 19504–19509. ISSN: 0027-8424. DOI: [10.1073/pnas.1109111108](https://doi.org/10.1073/pnas.1109111108).
- Antic, Srdjan D. (2003). "Action potentials in basal and oblique dendrites of rat neocortical pyramidal neurons". In: *Journal of Physiology* 550.1, pp. 35–50. ISSN: 00223751. DOI: [10.1113/jphysiol.2002.033746](https://doi.org/10.1113/jphysiol.2002.033746).
- Antic, Srdjan D, Ruth M Empson, and Thomas Knöpfel (2016). "Voltage imaging to understand connections and functions of neuronal circuits." In: *Journal of neurophysiology* 116.1, pp. 135–52. ISSN: 1522-1598. DOI: [10.1152/jn.00226.2016](https://doi.org/10.1152/jn.00226.2016).
- Baker, Christopher A et al. (2016). "Cellular resolution circuit mapping in mouse brain with temporal-focused excitation of soma-targeted channelrhodopsin". In: *eLife* 5, e14193. ISSN: 2050-084X. DOI: [10.7554/eLife.14193](https://doi.org/10.7554/eLife.14193).
- Bayguinov, Peter O. et al. (2017). "Imaging Voltage in Genetically-Defined Neuronal Subpopulations with a Cre Recombinase-Targeted Hybrid Voltage Sensor". In: *The Journal of Neuroscience*, pp. 1363–17. ISSN: 0270-6474. DOI: [10.1523/JNEUROSCI.1363-17.2017](https://doi.org/10.1523/JNEUROSCI.1363-17.2017).
- Berridge, Michael J, Peter Lipp, and Martin D Bootman (2000). "The versatility and universality of calcium signalling." In: *Nature reviews. Molecular cell biology* 1.1, pp. 11–21. ISSN: 1471-0072. DOI: [10.1038/35036035](https://doi.org/10.1038/35036035).
- Bewersdorf, Jörg, Alexander Egner, and Stefan W Hell (2006). "Multifocal Multi-Photon Microscopy". In: *Handbook Of Biological Confocal Microscopy*. Boston, MA: Springer US, pp. 550–560. ISBN: 038725921X. DOI: [10.1007/978-0-387-45524-2\\_{\\\_}29](https://doi.org/10.1007/978-0-387-45524-2_{\_}29).
- Bewersdorf, Jörg, Rainer Pick, and Stefan W Hell (1998). "Multifocal multiphoton microscopy." In: *Optics letters* 23.9, pp. 655–7. ISSN: 0146-9592.
- Bloodgood, Brenda L and Bernardo L Sabatini (2007). "Ca<sup>2+</sup> signaling in dendritic spines". In: *Current Opinion in Neurobiology* 17.3, pp. 345–351. ISSN: 09594388. DOI: [10.1016/j.conb.2007.04.003](https://doi.org/10.1016/j.conb.2007.04.003).
- Blunck, R., B. Chanda, and F. Bezanilla (2005). "Nano to micro - Fluorescence measurements of electric fields in molecules and genetically specified neurons". In: *Journal of Membrane Biology* 208.2, pp. 91–102. ISSN: 00222631. DOI: [10.1007/s00232-005-0822-z](https://doi.org/10.1007/s00232-005-0822-z).



- Boruah, B. R. and M. A.A. Neil (2009). "Focal field computation of an arbitrarily polarized beam using fast Fourier transforms". In: *Optics Communications* 282.24, pp. 4660–4667. ISSN: 00304018. DOI: [10.1016/j.optcom.2009.09.019](https://doi.org/10.1016/j.optcom.2009.09.019).
- Botcherby, E. J., R. Juškaitis, and T. Wilson (2006). "Scanning two photon fluorescence microscopy with extended depth of field". In: *Optics Communications* 268.2, pp. 253–260. ISSN: 00304018. DOI: [10.1016/j.optcom.2006.07.026](https://doi.org/10.1016/j.optcom.2006.07.026).
- Bouchard, Matthew B. et al. (2015). "Swept confocally-aligned planar excitation (SCAPE) microscopy for high-speed volumetric imaging of behaving organisms". In: *Nature Photonics* 9.2, pp. 113–119. ISSN: 1749-4885. DOI: [10.1038/nphoton.2014.323](https://doi.org/10.1038/nphoton.2014.323).
- Boucsein, C. (2005). "Controlling Synaptic Input Patterns In Vitro by Dynamic Photo Stimulation". In: *Journal of Neurophysiology* 94.4, pp. 2948–2958. ISSN: 0022-3077. DOI: [10.1152/jn.00245.2005](https://doi.org/10.1152/jn.00245.2005).
- Bovetti, Serena et al. (2017). "Simultaneous high-speed imaging and optogenetic inhibition in the intact mouse brain". In: *Scientific Reports* 7.1, p. 40041. ISSN: 20452322. DOI: [10.1038/srep40041](https://doi.org/10.1038/srep40041).
- Bower, James M. and David Beeman (2003). *The Book of GENESIS*.
- Boyd, Robert W. (2008). *Nonlinear Optics*. 3rd ed. Elsevier Inc.
- Brinks, Daan, Aaron J. Klein, and Adam E. Cohen (2015). "Two-Photon Lifetime Imaging of Voltage Indicating Proteins as a Probe of Absolute Membrane Voltage". In: *Biophysical Journal* 109.5, pp. 914–921. ISSN: 15420086. DOI: [10.1016/j.bpj.2015.07.038](https://doi.org/10.1016/j.bpj.2015.07.038).
- Broxton, Michael et al. (2013). "Wave optics theory and 3-D deconvolution for the light field microscope". In: *Optics Express* 21.21, p. 25418. ISSN: 1094-4087. DOI: [10.1364/OE.21.025418](https://doi.org/10.1364/OE.21.025418).
- Brunel, Nicolas (2016). "Is cortical connectivity optimized for storing information?" In: *Nature Neuroscience*. ISSN: 1097-6256. DOI: [10.1038/nn.4286](https://doi.org/10.1038/nn.4286).
- Bryant, S H and Julian M Tobias (1952). "Changes in light scattering accompanying activity in nerve." In: *Journal of cellular physiology* 40.2, pp. 199–219. ISSN: 0021-9541.
- Castanares, Michael Lawrence et al. (2016). "Efficient multi-site two-photon functional imaging of neuronal circuits." In: *Biomedical optics express* 7.12, pp. 5325–5334. ISSN: 2156-7085. DOI: [10.1364/BOE.7.005325](https://doi.org/10.1364/BOE.7.005325).
- Cha, Jae Won et al. (2014). "Reassignment of scattered emission photons in multifocal multiphoton microscopy." In: *Scientific reports* 4, p. 5153. ISSN: 2045-2322. DOI: [10.1038/srep05153](https://doi.org/10.1038/srep05153).

- Cha, Jae Won et al. (2015). "Non-descanned multifocal multiphoton microscopy with a multi-anode photomultiplier tube." In: *AIP advances* 5.8, p. 084802. ISSN: 2158-3226. DOI: [10.1063/1.4916040](https://doi.org/10.1063/1.4916040).
- Chalfie, M et al. (1994). "Green fluorescent protein as a marker for gene expression." In: *Science (New York, N.Y.)* 263.5148, pp. 802–5. ISSN: 0036-8075.
- Chamberland, Simon et al. (2017). "Fast two-photon imaging of subcellular voltage dynamics in neuronal tissue with genetically encoded indicators". In: *eLife* 6, pp. 1–35. ISSN: 2050-084X. DOI: [10.7554/eLife.25690](https://doi.org/10.7554/eLife.25690).
- Chan, Ken Y et al. (2017). "Engineered AAVs for efficient noninvasive gene delivery to the central and peripheral nervous systems". In: *Nature Neuroscience* 20.8, pp. 1172–1179. ISSN: 15461726. DOI: [10.1038/nn.4593](https://doi.org/10.1038/nn.4593).
- Chavarha, Mariya et al. (2018). "Fast two-photon volumetric imaging of an improved voltage indicator reveals electrical activity in deeply located neurons in the awake brain". In: *bioRxiv*, p. 445064. DOI: [10.1101/445064](https://doi.org/10.1101/445064).
- Chen, Jerry L et al. (2013). "Online correction of licking-induced brain motion during two-photon imaging with a tunable lens." In: *The Journal of physiology* 591.Pt 19, pp. 4689–4698. ISSN: 1469-7793. DOI: [10.1113/jphysiol.2013.259804](https://doi.org/10.1113/jphysiol.2013.259804).
- Chen, Qian et al. (2012). "Imaging Neural Activity Using Thy1-GCaMP Transgenic Mice". In: *Neuron* 76.2, pp. 297–308. ISSN: 08966273. DOI: [10.1016/j.neuron.2012.07.011](https://doi.org/10.1016/j.neuron.2012.07.011).
- Chen, Tsai Wen et al. (2017). "A Map of Anticipatory Activity in Mouse Motor Cortex". In: *Neuron* 94.4, pp. 866–879. ISSN: 10974199. DOI: [10.1016/j.neuron.2017.05.005](https://doi.org/10.1016/j.neuron.2017.05.005).
- Cheng, Adrian et al. (2011). "Simultaneous two-photon calcium imaging at different depths with spatiotemporal multiplexing." In: *Nature methods* 8.2, pp. 139–42. ISSN: 1548-7105. DOI: [10.1038/nmeth.1552](https://doi.org/10.1038/nmeth.1552).
- Chroma Technology Corporation (2018). *Chroma Spectra Viewer*.
- Clegg, James (2016). "Polarisation microscopy of single emitters". PhD thesis. Imperial College London.
- Cohen, Lawrence B., Richard D. Keynes, and Bertil Hille (1968). "Light scattering and birefringence changes during nerve activity". In: *Nature* 218.5140, pp. 438–441. ISSN: 00280836. DOI: [10.1038/218438a0](https://doi.org/10.1038/218438a0).
- Combs, Christian A (2010). *Fluorescence microscopy: A concise guide to current imaging methods*. DOI: [10.1002/0471142301.ns0205s00](https://doi.org/10.1002/0471142301.ns0205s00).

- Cong, Lin et al. (2017). "Rapid whole brain imaging of neural activity in freely behaving larval zebrafish (*Danio rerio*)". In: *eLife* 6. ISSN: 2050084X. DOI: [10.7554/eLife.28158](https://doi.org/10.7554/eLife.28158).
- Dana, Hod et al. (2018). "High-performance GFP-based calcium indicators for imaging activity in neuronal populations and microcompartments". In: DOI: [10.1101/434589](https://doi.org/10.1101/434589).
- Daube-Witherspoon, Margaret E. and Gerd Muehllehner (1986). "An Iterative Image Space Reconstruction Algorithm Suitable for Volume ECT". In: *IEEE Transactions on Medical Imaging* 5.2, pp. 61–66. ISSN: 1558254X. DOI: [10.1109/TMI.1986.4307748](https://doi.org/10.1109/TMI.1986.4307748).
- Davidovits, Paul and M. David Egger (1969). *Scanning laser microscope*. DOI: [10.1038/223831a0](https://doi.org/10.1038/223831a0).
- Davila, H. V. et al. (1973). "A large change in axon fluorescence that provides a promising method for measuring membrane potential". In: *Nature New Biology* 241.109, pp. 159–160. ISSN: 00900028. DOI: [10.1038/newbio241159a0](https://doi.org/10.1038/newbio241159a0).
- Dempster, A P, N M Laird, and D B Rubin (1977). *Maximum Likelihood from Incomplete Data via the EM Algorithm*. Tech. rep. 1, pp. 1–38.
- Denk, W, J. Strickler, and W. Webb (1990). "Two-photon laser scanning fluorescence microscopy". In: *Science* 248.4951, pp. 73–76. ISSN: 0036-8075. DOI: [10.1126/science.2321027](https://doi.org/10.1126/science.2321027).
- Denk, Winfried and Heinz Horstmann (2004). "Serial block-face scanning electron microscopy to reconstruct three-dimensional tissue nanostructure". In: *PLoS Biology* 2.11. ISSN: 15449173. DOI: [10.1371/journal.pbio.0020329](https://doi.org/10.1371/journal.pbio.0020329).
- Dey, Nicolas et al. (2006). "Richardson-Lucy Algorithm with Total Variation Regularization for 3D Confocal Microscope Deconvolution". In: *Microscopy Research & Technique* 69.4, pp. 260–266.
- Djurisic, Maja et al. (2003). "Optical monitoring of neural activity using voltage-sensitive dyes". In: *Methods in Enzymology* 361, pp. 423–451. ISSN: 00766879. DOI: [10.1016/S0076-6879\(03\)61022-0](https://doi.org/10.1016/S0076-6879(03)61022-0).
- Drobizhev, Mikhail et al. (2011). "Two-photon absorption properties of fluorescent proteins." In: *Nature methods* 8.5, pp. 393–399. ISSN: 1548-7105. DOI: [10.1038/nmeth.1596](https://doi.org/10.1038/nmeth.1596).
- Ducros, Mathieu et al. (2013). "Encoded multisite two-photon microscopy." In: *Proceedings of the National Academy of Sciences of the United States of America* 110.32, pp. 13138–43. ISSN: 1091-6490. DOI: [10.1073/pnas.1307818110](https://doi.org/10.1073/pnas.1307818110).
- Dudnikov, Yu A (1970). "Autostereoscopy and Integral Photography". In: *OPTICAL TECHNOLOGY* 37.7.

- Duemani Reddy, Gaddum et al. (2008). "Three-dimensional random access multiphoton microscopy for functional imaging of neuronal activity". In: *Nature Neuroscience* 11.6, pp. 713–720. ISSN: 1097-6256. DOI: [10.1038/nn.2116](https://doi.org/10.1038/nn.2116).
- Dunsby, C. (2008). "Optically sectioned imaging by oblique plane microscopy". In: *Optics Express* 16.25, p. 20306. ISSN: 1094-4087. DOI: [10.1364/OE.16.020306](https://doi.org/10.1364/OE.16.020306).
- Edelstein, Arthur D et al. (2014). "Advanced methods of microscope control using  $\mu$ Manager software." In: *Journal of biological methods* 1.2, p. 10. ISSN: 2326-9901. DOI: [10.14440/jbm.2014.36](https://doi.org/10.14440/jbm.2014.36).
- Empson, Ruth M. et al. (2015). "Validation of optical voltage reporting by the genetically encoded voltage indicator VSFP Butterfly from cortical layer 2/3 pyramidal neurons in mouse brain slices". In: *Physiological Reports* 3.7, e12468. ISSN: 2051-817X. DOI: [10.14814/phy2.12468](https://doi.org/10.14814/phy2.12468).
- Etherington, Sarah J et al. (2010). "Synaptic Integration". In: *Encyclopedia of Life Sciences*. Chichester, UK: John Wiley & Sons, Ltd. DOI: [10.1002/9780470015902.a0000208.pub2](https://doi.org/10.1002/9780470015902.a0000208.pub2).
- Finbarr Hayes (2003). "The function and organisation of plasmids". In: *E. Coli Plasmid Vectors: Methods and Applications*. Ed. by Nicola Casali and Andrew Presto. Humana Press.
- Fish, D. A. et al. (1995). "Blind deconvolution by means of the Richardson-Lucy algorithm". In: *Journal of the Optical Society of America A* 12.1, p. 58. ISSN: 1084-7529. DOI: [10.1364/JOSAA.12.000058](https://doi.org/10.1364/JOSAA.12.000058).
- Fittinghoff, D, Paul Wiseman, and Jeffrey Squier (2000). "Widefield multiphoton and temporally decorrelated multifocal multiphoton microscopy." In: *Optics express* 7.8, pp. 273–9. ISSN: 1094-4087. DOI: [10.1364/OE.7.000273](https://doi.org/10.1364/OE.7.000273).
- Förster, T (1965). *Delocalized Excitation and Excitation Transfer*. Tech. rep.
- Foust, A. J. and D. M. Rector (2007). "Optically teasing apart neural swelling and depolarization". In: *Neuroscience* 145.3, pp. 887–899. ISSN: 03064522. DOI: [10.1016/j.neuroscience.2006.12.068](https://doi.org/10.1016/j.neuroscience.2006.12.068).
- Foust, Amanda et al. (2010). "Action Potentials Initiate in the Axon Initial Segment and Propagate through Axon Collaterals Reliably in Cerebellar Purkinje Neurons". In: *The Journal of Neuroscience* 30.20, pp. 6891–6902. ISSN: 16130073. DOI: [10.1523/JNEUROSCI.0552-10.2010](https://doi.org/10.1523/JNEUROSCI.0552-10.2010).
- Foust, Amanda J. et al. (2015). "Computer-generated holography enhances voltage dye fluorescence discrimination in adjacent neuronal structures." In: *Neurophotonics* 2.2, p. 021007. ISSN: 2329-423X. DOI: [10.1117/1.NPh.2.2.021007](https://doi.org/10.1117/1.NPh.2.2.021007).

- Franconville, Romain et al. (2011). "Somatic calcium level reports integrated spiking activity of cerebellar interneurons in vitro and in vivo." In: *Journal of neurophysiology* 106.4, pp. 1793–805. ISSN: 1522-1598. DOI: [10.1152/jn.00133.2011](https://doi.org/10.1152/jn.00133.2011).
- Gans, Peter and J. Bernard Gill (1983). "Examination of the Convolution Method for Numerical Smoothing and Differentiation of Spectroscopic Data in Theory and in Practice." In: *Applied Spectroscopy* 37.6, pp. 515–520. ISSN: 00037028. DOI: [10.1366/0003702834634712](https://doi.org/10.1366/0003702834634712).
- Ginger, Melanie et al. (2013). "Revealing the secrets of neuronal circuits with recombinant rabies virus technology." In: *Frontiers in neural circuits* 7.January, p. 2. ISSN: 1662-5110. DOI: [10.3389/fncir.2013.00002](https://doi.org/10.3389/fncir.2013.00002).
- Gong, Yiyang et al. (2015). "High-speed recording of neural spikes in awake mice and flies with a fluorescent voltage sensor". In: *Science* 350, pp. 1361–1366. DOI: [10.1126/science.aab0810](https://doi.org/10.1126/science.aab0810).
- Gossen, M and H Bujard (1992). "Tight control of gene expression in mammalian cells by tetracycline-responsive promoters." In: *Proceedings of the National Academy of Sciences of the United States of America* 89.12, pp. 5547–51. ISSN: 0027-8424.
- Grienberger, Christine and Arthur Konnerth (2012). "Imaging calcium in neurons." In: *Neuron* 73.5, pp. 862–885. ISSN: 1097-4199. DOI: [10.1016/j.neuron.2012.02.011](https://doi.org/10.1016/j.neuron.2012.02.011).
- Grinvald, Amiram et al. (2003). "Neuronal assemblies: Single cortical neurons are obedient members of a huge orchestra". In: *Biopolymers* 68.3, pp. 422–436. ISSN: 0006-3525. DOI: [10.1002/bip.10273](https://doi.org/10.1002/bip.10273).
- Grosenick, Logan M. et al. (2017). "Identification Of Cellular-Activity Dynamics Across Large Tissue Volumes In The Mammalian Brain". In: *bioRxiv*, p. 132688. DOI: [10.1101/132688](https://doi.org/10.1101/132688).
- Grover, Vijay P B et al. (2015). "Magnetic Resonance Imaging: Principles and Techniques: Lessons for Clinicians." In: *Journal of clinical and experimental hepatology* 5.3, pp. 246–55. ISSN: 0973-6883. DOI: [10.1016/j.jceh.2015.08.001](https://doi.org/10.1016/j.jceh.2015.08.001).
- Gu, Min (1999). *Advanced Optical Imaging Theory*. 1st ed. Springer-Verlag Berlin Heidelberg.
- Guenther, Casey J. et al. (2013). "Permanent genetic access to transiently active neurons via TRAP: Targeted recombination in active populations". In: *Neuron* 78.5, pp. 773–784. ISSN: 08966273. DOI: [10.1016/j.neuron.2013.03.025](https://doi.org/10.1016/j.neuron.2013.03.025).
- Harris, Julie A. et al. (2014). "Anatomical characterization of Cre driver mice for neural circuit mapping and manipulation". In: *Frontiers in Neural Circuits* 8, p. 76. ISSN: 1662-5110. DOI: [10.3389/fncir.2014.00076](https://doi.org/10.3389/fncir.2014.00076).

- Hecht, Eugene (2017). *Optics*. 5th ed. Pearson education Limited. ISBN: 9780133977226.
- Heim, R, A B Cubitt, and R Y Tsien (1995). "Improved green fluorescence." In: *Nature* 373.6516, pp. 663–4. ISSN: 0028-0836. DOI: [10.1038/373663b0](https://doi.org/10.1038/373663b0).
- Heneyey, L. C. and J. L. Greenstein (1941). "Diffuse radiation in the Galaxy". In: *The Astrophysical Journal* 93, p. 70. ISSN: 0004-637X. DOI: [10.1086/144246](https://doi.org/10.1086/144246).
- Hill, D K (1950). "The volume change resulting from stimulation of a giant nerve fibre." In: *The Journal of physiology* 111.3-4, pp. 304–27. ISSN: 0022-3751.
- Hill, D K and R D Keynes (1949). "Opacity changes in stimulated nerve." In: *The Journal of physiology* 108.3, pp. 278–81. ISSN: 0022-3751.
- Holthoff, Knut, Dejan Zecevic, and Arthur Konnerth (2010). "Rapid time course of action potentials in spines and remote dendrites of mouse visual cortex neurons". In: *Journal of Physiology* 588.7, pp. 1085–1096. ISSN: 00223751. DOI: [10.1113/jphysiol.2009.184960](https://doi.org/10.1113/jphysiol.2009.184960).
- Hooks, B. M. et al. (2011). "Laminar analysis of excitatory local circuits in vibrissal motor and sensory cortical areas". In: *PLoS Biology* 9.1. ISSN: 15449173. DOI: [10.1371/journal.pbio.1000572](https://doi.org/10.1371/journal.pbio.1000572).
- Hopfield, J J (1982). "Neural networks and physical systems with emergent collective computational abilities." In: *Proceedings of the National Academy of Sciences of the United States of America* 79.8, pp. 2554–2558. ISSN: 0027-8424. DOI: [10.1073/pnas.79.8.2554](https://doi.org/10.1073/pnas.79.8.2554).
- Huisken, Jan et al. (2004). "Optical sectioning deep inside live embryos by selective plane illumination microscopy." In: *Science (New York, N.Y.)* 305.5686, pp. 1007–9. ISSN: 1095-9203. DOI: [10.1126/science.1100035](https://doi.org/10.1126/science.1100035).
- Huygens, Christiaan (1690). *Treatise on Light*. Trans. by Sylvanus P. Thompson. London: Macmillan.
- Jacobs, A. H. et al. (2003). "PET-based molecular imaging in neuroscience". In: *European Journal of Nuclear Medicine and Molecular Imaging* 30.7, pp. 1051–1065. ISSN: 1619-7070. DOI: [10.1007/s00259-003-1202-5](https://doi.org/10.1007/s00259-003-1202-5).
- Jacques, Steven L (2013). "Optical properties of biological tissues: a review." In: *Physics in medicine and biology* 58.11, pp. 37–61. ISSN: 1361-6560. DOI: [10.1088/0031-9155/58/11/R37](https://doi.org/10.1088/0031-9155/58/11/R37).
- Joseph W. Goodman (2005). *Introduction to Fourier Optics*. Roberts and Company Publishers.
- Kaluza, Malte C. et al. (2012). "Measurement of temperature-dependent absorption and emission spectra of Yb:YAG, Yb:LuAG, and Yb:CaF<sub>2</sub> between 20 °C and 200 °C and predictions

- on their influence on laser performance". In: *Journal of the Optical Society of America B* 29.9, p. 2493. ISSN: 0740-3224. DOI: [10.1364/josab.29.002493](https://doi.org/10.1364/josab.29.002493).
- Kannan, Madhuvanathi et al. (2018). "Fast, in vivo voltage imaging using a red fluorescent indicator". In: *Nature Methods*, (in press). ISSN: 1548-7091. DOI: [10.1038/s41592-018-0188-7](https://doi.org/10.1038/s41592-018-0188-7).
- Kazempour, Abbas et al. (2018). "Kilohertz frame-rate two-photon tomography". In: *bioRxiv*, p. 357269. DOI: [10.1101/357269](https://doi.org/10.1101/357269).
- Kim, Jinhyun et al. (2012). "mGRASP enables mapping mammalian synaptic connectivity with light microscopy." In: *Nature methods* 9.1, pp. 96–102. ISSN: 1548-7105. DOI: [10.1038/nmeth.1784](https://doi.org/10.1038/nmeth.1784).
- Kim, Ki Hean et al. (2007). "Multifocal multiphoton microscopy based on multianode photomultiplier tubes." In: *Optics express* 15.18, pp. 11658–78. ISSN: 1094-4087. DOI: [10.1364/OE.15.011658](https://doi.org/10.1364/OE.15.011658).
- Kim, Tae Kyung and James H Eberwine (2010). "Mammalian cell transfection: The present and the future". In: *Analytical and Bioanalytical Chemistry* 397.8, pp. 3173–3178. ISSN: 16182642. DOI: [10.1007/s00216-010-3821-6](https://doi.org/10.1007/s00216-010-3821-6).
- Knöpfel, Thomas (2012). "Genetically encoded optical indicators for the analysis of neuronal circuits." In: *Nature reviews. Neuroscience* 13.10, pp. 687–700. ISSN: 1471-0048. DOI: [10.1038/nrn3293](https://doi.org/10.1038/nrn3293).
- Knöpfel, Thomas et al. (2006). "Optical probing of neuronal circuit dynamics: genetically encoded versus classical fluorescent sensors." In: *Trends in neurosciences* 29.3, pp. 160–6. ISSN: 0166-2236. DOI: [10.1016/j.tins.2006.01.004](https://doi.org/10.1016/j.tins.2006.01.004).
- Kralj, Joel M et al. (2011a). "Electrical spiking in Escherichia coli probed with a fluorescent voltage-indicating protein." In: *Science (New York, N.Y.)* 333.6040, pp. 345–8. ISSN: 1095-9203. DOI: [10.1126/science.1204763](https://doi.org/10.1126/science.1204763).
- Kralj, Joel M et al. (2011b). "Optical recording of action potentials in mammalian neurons using a microbial rhodopsin." In: *Nature methods* 9.1, pp. 90–5. ISSN: 1548-7105. DOI: [10.1038/nmeth.1782](https://doi.org/10.1038/nmeth.1782).
- Kulkarni, Rishikesh U. and Evan W. Miller (2017). "Voltage Imaging: Pitfalls and Potential". In: *Biochemistry* 56.39, pp. 5171–5177. ISSN: 15204995. DOI: [10.1021/acs.biochem.7b00490](https://doi.org/10.1021/acs.biochem.7b00490).
- Kurtz, Rafael et al. (2006). "Application of multiline two-photon microscopy to functional in vivo imaging." In: *Journal of neuroscience methods* 151.2, pp. 276–86. ISSN: 0165-0270. DOI: [10.1016/j.jneumeth.2005.12.003](https://doi.org/10.1016/j.jneumeth.2005.12.003).

- Lanteri, H, R. Soummer, and C Aime (1999). "ISRA and RL algorithms used for deconvolution of AO and HST images". In: *Astronomy with adaptive optics : present results and future programs. ESO Conference and Workshop Proceedings, vol. 56.*
- Lauterbach, Marcel A. et al. (2015). "Fast Calcium Imaging with Optical Sectioning via HiLo Microscopy". In: *PLoS ONE* 10.12. Ed. by Filippo Del Bene, e0143681. ISSN: 19326203. DOI: [10.1371/journal.pone.0143681](https://doi.org/10.1371/journal.pone.0143681).
- Levoy, Marc et al. (2006). "Light field microscopy". In: *ACM SIGGRAPH 2006 Papers on - SIGGRAPH '06*. Vol. 25. 3. New York, New York, USA: ACM Press, p. 924. ISBN: 1595933646. DOI: [10.1145/1179352.1141976](https://doi.org/10.1145/1179352.1141976).
- Li, Haoyu et al. (2019). "Fast, volumetric live-cell imaging using high-resolution light-field microscopy". In: *Biomedical Optics Express* 10.1, p. 29. ISSN: 2156-7085. DOI: [10.1364/BOE.10.000029](https://doi.org/10.1364/BOE.10.000029).
- Li, Luchang et al. (2016). "Assessing low-light cameras with photon transfer curve method". In: *Journal of Innovative Optical Health Sciences* 09.03, p. 1630008. ISSN: 1793-5458. DOI: [10.1142/S1793545816300081](https://doi.org/10.1142/S1793545816300081).
- Lillis, Kyle P. et al. (2008). "Two-photon imaging of spatially extended neuronal network dynamics with high temporal resolution". In: *Journal of Neuroscience Methods* 172.2, pp. 178–184. ISSN: 01650270. DOI: [10.1016/j.jneumeth.2008.04.024](https://doi.org/10.1016/j.jneumeth.2008.04.024).
- Lippmann, G (1908). "Épreuves réversibles donnant la sensation du relief". In: *Journal de Physique Théorique et Appliquée* 7.1, pp. 821–825. ISSN: 0368-3893. DOI: [10.1051/jphystap:019080070082100](https://doi.org/10.1051/jphystap:019080070082100).
- Lu, Rongwen et al. (2017). "Video-rate volumetric functional imaging of the brain at synaptic resolution". In: *Nature Neuroscience* 20.4, pp. 620–628. ISSN: 15461726. DOI: [10.1038/nrn.4516](https://doi.org/10.1038/nrn.4516).
- Lucy, L. B. (1974). "An iterative technique for the rectification of observed distributions". In: *The Astronomical Journal* 79.3, p. 745. ISSN: 00046256. DOI: [10.1086/111605](https://doi.org/10.1086/111605).
- Luczak, Artur, Bruce L. McNaughton, and Kenneth D. Harris (2015). "Packet-based communication in the cortex." In: *Nature reviews. Neuroscience* 16.12, pp. 745–55. ISSN: 1471-0048. DOI: [10.1038/nrn4026](https://doi.org/10.1038/nrn4026).
- Lundby, Alicia, Walther Akemann, and Thomas Knöpfel (2010). "Biophysical characterization of the fluorescent protein voltage probe VSFP2.3 based on the voltage-sensing domain of Ci-VSP." In: *European biophysics journal : EBJ* 39.12, pp. 1625–35. ISSN: 1432-1017. DOI: [10.1007/s00249-010-0620-0](https://doi.org/10.1007/s00249-010-0620-0).



- Madisen, Linda et al. (2015). "Transgenic Mice for Intersectional Targeting of Neural Sensors and Effectors with High Specificity and Performance". In: *Neuron* 85.5, pp. 942–958. ISSN: 08966273. DOI: [10.1016/j.neuron.2015.02.022](https://doi.org/10.1016/j.neuron.2015.02.022).
- Manita, Satoshi, Kenichi Miyazaki, and William N Ross (2011). "Synaptically activated Ca<sup>2+</sup> waves and NMDA spikes locally suppress voltage-dependent Ca<sup>2+</sup> signalling in rat pyramidal cell dendrites". In: *Journal of Physiology* 589.20, pp. 4903–4920. ISSN: 00223751. DOI: [10.1113/jphysiol.2011.216564](https://doi.org/10.1113/jphysiol.2011.216564).
- Mank, Marco et al. (2008). "A genetically encoded calcium indicator for chronic in vivo two-photon imaging." In: *Nature methods* 5.9, pp. 805–811. ISSN: 1548-7091. DOI: [10.1038/nmeth.1243](https://doi.org/10.1038/nmeth.1243).
- Maruyama, Kazuhiro et al. (2018). "Optical interrogation of neuronal circuitry in zebrafish using genetically encoded voltage indicators". In: *Scientific Reports* 8.1, pp. 1–10. ISSN: 2045-2322. DOI: [10.1038/s41598-018-23906-1](https://doi.org/10.1038/s41598-018-23906-1).
- Mayford, M et al. (1996). "Control of memory formation through regulated expression of a CaMKII transgene." In: *Science (New York, N.Y.)* 274.5293, pp. 1678–1683. ISSN: 0036-8075. DOI: [10.1126/science.274.5293.1678](https://doi.org/10.1126/science.274.5293.1678).
- Mertz, Jerome (2011). "Optical sectioning microscopy with planar or structured illumination". In: *Nature Methods* 8.10, pp. 811–819. ISSN: 1548-7091. DOI: [10.1038/nmeth.1709](https://doi.org/10.1038/nmeth.1709).
- Michelson, A (1927). *Studies in Optics*. The University of Chicago Press.
- Mishina, Yukiko et al. (2014). "Exploration of genetically encoded voltage indicators based on a chimeric voltage sensing domain". In: *Frontiers in Molecular Neuroscience* 7.September, p. 78. ISSN: 1662-5099. DOI: [10.3389/fnmol.2014.00078](https://doi.org/10.3389/fnmol.2014.00078).
- Miyawaki, a et al. (1997). "Fluorescent indicators for Ca<sup>2+</sup> based on green fluorescent proteins and calmodulin." In: *Nature* 388.6645, pp. 882–7. ISSN: 0028-0836. DOI: [10.1038/42264](https://doi.org/10.1038/42264).
- Miyazaki, J et al. (1989). "Expression vector system based on the chicken beta-actin promoter directs efficient production of interleukin-5." In: *Gene* 79.2, pp. 269–77. ISSN: 0378-1119.
- Miyazaki, Kenichi, Satoshi Manita, and William N. Ross (2012). "Developmental profile of localized spontaneous Ca<sup>2+</sup>-release events in the dendrites of rat hippocampal pyramidal neurons". In: *Cell Calcium* 52.6, pp. 422–432. ISSN: 15321991. DOI: [10.1016/j.ceca.2012.08.001](https://doi.org/10.1016/j.ceca.2012.08.001).
- Monakhov, Mikhail V et al. (2019). "Bright near-infrared genetically encoded voltage indicator for all- optical electrophysiology". In: *bioRxiv*. DOI: [10.1101/536359](https://doi.org/10.1101/536359).

- Muller, S R et al. (1990). "Efficient transfection and expression of heterologous genes in PC12 cells." In: *DNA and cell biology* 9.3, pp. 221–9. ISSN: 1044-5498. DOI: [10.1089/dna.1990.9.221](https://doi.org/10.1089/dna.1990.9.221).
- Murata, Yoshimichi et al. (2005). "Phosphoinositide phosphatase activity coupled to an intrinsic voltage sensor". In: *Nature* 435.7046, pp. 1239–1243. ISSN: 0028-0836. DOI: [10.1038/nature03650](https://doi.org/10.1038/nature03650).
- Nakai, Junichi, Masamichi Ohkura, and Keiji Imoto (2001). "A high signal-to-noise Ca(2+) probe composed of a single green fluorescent protein." In: *Nature biotechnology* 19.2, pp. 137–41. ISSN: 1087-0156. DOI: [10.1038/84397](https://doi.org/10.1038/84397).
- Neil, M. A. A., R. Juškaitis, and T. Wilson (1997). "Method of obtaining optical sectioning by using structured light in a conventional microscope". In: *Optics Letters* 22.24, p. 1905. ISSN: 0146-9592. DOI: [10.1364/OL.22.001905](https://doi.org/10.1364/OL.22.001905).
- Newport (2018). *Mai Tai Product Specifications*.
- Ng, Ren (2006). "Digital light field photography". PhD thesis. Stanford University.
- Ng, Ren et al. (2005). *Light Field Photography with a Hand-Held Plenoptic Camera – Stanford Tech Report CTSR 2005-02*. Tech. rep., pp. 1–11. DOI: [10.1.1.163.488](https://doi.org/10.1.1.163.488).
- Nguyen, Jeffrey P et al. (2015). "Whole-brain calcium imaging with cellular resolution in freely behaving *Caenorhabditis elegans*." In: *Proceedings of the National Academy of Sciences of the United States of America*, p. 33. ISSN: 1091-6490. DOI: [10.1073/pnas.1507110112](https://doi.org/10.1073/pnas.1507110112).
- Nielsen, T. et al. (2001). "High efficiency beam splitter for multifocal multiphoton microscopy." In: *Journal of microscopy* 201.Pt 3, pp. 368–76. ISSN: 0022-2720. DOI: [10.1046/j.1365-2818.2001.00852.x](https://doi.org/10.1046/j.1365-2818.2001.00852.x).
- Nikolenko, Volodymyr (2008). "SLM microscopy: scanless two-photon imaging and photostimulation using spatial light modulators". In: *Frontiers in Neural Circuits* 2, p. 5. ISSN: 16625110. DOI: [10.3389/neuro.04.005.2008](https://doi.org/10.3389/neuro.04.005.2008).
- Nishidate, Izumi et al. (2015). "In vivo estimation of light scattering and absorption properties of rat brain using a single-reflectance fiber probe during cortical spreading depression". In: *Journal of Biomedical Optics* 20.2, p. 027003. ISSN: 1083-3668. DOI: [10.1117/1.JBO.20.2.027003](https://doi.org/10.1117/1.JBO.20.2.027003).
- Nöbauer, Tobias et al. (2017). "Video rate volumetric Ca<sup>2+</sup> imaging across cortex using seeded iterative demixing (SID) microscopy". In: *Nature Methods* 14.8, pp. 811–818. ISSN: 15487105. DOI: [10.1038/nmeth.4341](https://doi.org/10.1038/nmeth.4341).

- Oheim, Martin et al. (2001). "Two-photon microscopy in brain tissue: Parameters influencing the imaging depth". In: *Journal of Neuroscience Methods* 111.1, pp. 29–37. ISSN: 01650270. DOI: [10.1016/S0165-0270\(01\)00438-1](https://doi.org/10.1016/S0165-0270(01)00438-1).
- Otis, James M. et al. (2017). "Prefrontal cortex output circuits guide reward seeking through divergent cue encoding". In: *Nature* 543.7643, pp. 103–107. ISSN: 14764687. DOI: [10.1038/nature21376](https://doi.org/10.1038/nature21376).
- Oztas, Emin (2003). "Neuronal tracing". In: *Neuroanatomy* 2, pp. 2–5.
- Pala, Aurelie and Carl C H Petersen (2015). "In Vivo Measurement of Cell-Type-Specific Synaptic Connectivity and Synaptic Transmission in Layer 2/3 Mouse Barrel Cortex". In: *Neuron* 85.1, pp. 68–76. ISSN: 10974199. DOI: [10.1016/j.neuron.2014.11.025](https://doi.org/10.1016/j.neuron.2014.11.025).
- Palmer, Lucy M and Greg J Stuart (2009). "Membrane potential changes in dendritic spines during action potentials and synaptic input." In: *The Journal of neuroscience : the official journal of the Society for Neuroscience* 29.21, pp. 6897–6903. ISSN: 1529-2401. DOI: [10.1523/JNEUROSCI.5847-08.2009](https://doi.org/10.1523/JNEUROSCI.5847-08.2009).
- Papagiakoumou, Eirini et al. (2008). "Patterned two-photon illumination by spatiotemporal shaping of ultrashort pulses". In: *Optics Express* 16.26, p. 22039. ISSN: 1094-4087. DOI: [10.1364/OE.16.022039](https://doi.org/10.1364/OE.16.022039).
- Papagiakoumou, Eirini et al. (2010). "Scanless two-photon excitation of channelrhodopsin-2". In: *Nature Methods* 7.10, pp. 848–854. ISSN: 15487091. DOI: [10.1038/nmeth.1505](https://doi.org/10.1038/nmeth.1505).
- Papagiakoumou, Eirini et al. (2013). "Functional patterned multiphoton excitation deep inside scattering tissue". In: *Nature Photonics* 7.4, pp. 274–278. ISSN: 17494885. DOI: [10.1038/nphoton.2013.9](https://doi.org/10.1038/nphoton.2013.9).
- Pégard, Nicolas C. et al. (2017). "Three-dimensional scanless holographic optogenetics with temporal focusing (3D-SHOT)". In: *Nature Communications* 8.1, p. 1228. ISSN: 20411723. DOI: [10.1038/s41467-017-01031-3](https://doi.org/10.1038/s41467-017-01031-3).
- Perin, Rodrigo, Thomas K Berger, and Henry Markram (2011). "A synaptic organizing principle for cortical neuronal groups." In: *Proceedings of the National Academy of Sciences of the United States of America* 108.13, pp. 5419–5424. ISSN: 0027-8424. DOI: [10.1073/pnas.1016051108](https://doi.org/10.1073/pnas.1016051108).
- Piatkevich, Kiryl D et al. (2018). "A robotic multidimensional directed evolution approach applied to fluorescent voltage reporters". In: *Nature Chemical Biology* 14.4, pp. 352–360. ISSN: 1552-4450. DOI: [10.1038/s41589-018-0004-9](https://doi.org/10.1038/s41589-018-0004-9).

- Piatkevich, Kiryl D et al. (2019). "Population imaging of neural activity in awake behaving mice in multiple brain regions". In: *bioRxiv*, p. 616094. DOI: [10.1101/616094](https://doi.org/10.1101/616094).
- Podgorski, Kaspar and Gayathri Ranganathan (2016). "Brain heating induced by near-infrared lasers during multiphoton microscopy". In: *Journal of Neurophysiology* 116.3, pp. 1012–1023. ISSN: 0022-3077. DOI: [10.1152/jn.00275.2016](https://doi.org/10.1152/jn.00275.2016).
- Popovic, Marko A. et al. (2014). "Cortical dendritic spine heads are not electrically isolated by the spine neck from membrane potential signals in parent dendrites". In: *Cerebral Cortex* 24.2, pp. 385–395. ISSN: 14602199. DOI: [10.1093/cercor/bhs320](https://doi.org/10.1093/cercor/bhs320).
- Pozzi, Paolo et al. (2015). "High-throughput spatial light modulation two-photon microscopy for fast functional imaging". In: *Neurophotonics* 2.1, p. 015005. ISSN: 2329-423X. DOI: [10.1117/1.NPh.2.1.015005](https://doi.org/10.1117/1.NPh.2.1.015005).
- Prevedel, Robert et al. (2014). "Simultaneous whole-animal 3D imaging of neuronal activity using light-field microscopy." In: *Nature methods* 11.7, pp. 727–30. ISSN: 1548-7105. DOI: [10.1038/nmeth.2964](https://doi.org/10.1038/nmeth.2964).
- Prevedel, Robert et al. (2016). "Fast volumetric calcium imaging across multiple cortical layers using sculpted light." In: *Nature methods* 13.12, pp. 1021–1028. ISSN: 1548-7105. DOI: [10.1038/nmeth.4040](https://doi.org/10.1038/nmeth.4040).
- Quicke, Peter et al. (2018). "High speed functional imaging with source localized multifocal two-photon microscopy". In: *Biomedical Optics Express* 9.8, p. 3678. ISSN: 2156-7085. DOI: [10.1364/BOE.9.003678](https://doi.org/10.1364/BOE.9.003678).
- Quicke, Peter et al. (2019). "Single-neuron level one-photon voltage imaging with sparsely targeted genetically encoded voltage indicators." In: *Frontiers in Cellular Neuroscience* 13, p. 39. ISSN: 1662-5102. DOI: [10.3389/FNCEL.2019.00039](https://doi.org/10.3389/FNCEL.2019.00039).
- Reyes, A et al. (1998). "Target-cell-specific facilitation and depression in neocortical circuits." In: *Nature neuroscience* 1.4, pp. 279–285. ISSN: 1097-6256. DOI: [10.1038/1092](https://doi.org/10.1038/1092).
- Reynolds, Stephanie et al. (2018). *CosMIC: A consistent metric for spike inference from calcium imaging*. DOI: [10.1162/neco{\\\_}\\\_a{\\\_}\\\_01114](https://doi.org/10.1162/neco{\_}\_a{\_}\_01114).
- Rice, Frank (2016). "A frequency-domain derivation of shot-noise". In: *Citation: American Journal of Physics* 84, p. 4031. DOI: [10.1119/1.4934706](https://doi.org/10.1119/1.4934706).
- Richards, B. and E. Wolf (1959). "Electromagnetic Diffraction in Optical Systems. II. Structure of the Image Field in an Aplanatic System". In: *Proceedings of the Royal Society A: Mathematical,*

- Physical and Engineering Sciences* 253.1274, pp. 358–379. ISSN: 1364-5021. DOI: [10.1098/rspa.1959.0200](https://doi.org/10.1098/rspa.1959.0200).
- Richardson, William Hadley (1972). “Bayesian-Based Iterative Method of Image Restoration\*”. In: *Journal of the Optical Society of America* 62.1, p. 55. ISSN: 0030-3941. DOI: [10.1364/JOSA.62.000055](https://doi.org/10.1364/JOSA.62.000055).
- Ronzitti, Emiliano et al. (2017). “Submillisecond Optogenetic Control of Neuronal Firing with Two-Photon Holographic Photoactivation of Chronos.” In: *The Journal of neuroscience : the official journal of the Society for Neuroscience* 37.44, pp. 10679–10689. ISSN: 1529-2401. DOI: [10.1523/JNEUROSCI.1246-17.2017](https://doi.org/10.1523/JNEUROSCI.1246-17.2017).
- Roome, Christopher J. and Bernd Kuhn (2018). “Simultaneous dendritic voltage and calcium imaging and somatic recording from Purkinje neurons in awake mice”. In: *Nature Communications* 9.1, p. 3388. ISSN: 2041-1723. DOI: [10.1038/s41467-018-05900-3](https://doi.org/10.1038/s41467-018-05900-3).
- Rupprecht, Peter et al. (2015). “Optimizing and extending light-sculpting microscopy for fast functional imaging in neuroscience”. In: *Biomedical Optics Express* 6.2, p. 353. ISSN: 2156-7085. DOI: [10.1364/BOE.6.000353](https://doi.org/10.1364/BOE.6.000353).
- Rupprecht, Peter et al. (2016). “Remote z-scanning with a macroscopic voice coil motor for fast 3D multiphoton laser scanning microscopy”. In: *Biomedical Optics Express* 7.5, p. 1656. ISSN: 2156-7085. DOI: [10.1364/BOE.7.001656](https://doi.org/10.1364/BOE.7.001656).
- Sacconi, L. et al. (2003). “Multiphoton multifocal microscopy exploiting a diffractive optical element.” In: *Optics letters* 28.20, pp. 1918–20. ISSN: 0146-9592. DOI: [10.1364/OL.28.001918](https://doi.org/10.1364/OL.28.001918).
- Sadovsky, Alexander J et al. (2011). “Heuristically optimal path scanning for high-speed multiphoton circuit imaging.” In: *Journal of neurophysiology* 106.3, pp. 1591–1598. ISSN: 0022-3077. DOI: [10.1152/jn.00334.2011](https://doi.org/10.1152/jn.00334.2011).
- Salomé, R. et al. (2006). “Ultrafast random-access scanning in two-photon microscopy using acousto-optic deflectors”. In: *Journal of Neuroscience Methods* 154, pp. 161–174. ISSN: 01650270. DOI: [10.1016/j.jneumeth.2005.12.010](https://doi.org/10.1016/j.jneumeth.2005.12.010).
- Sando, Richard et al. (2013). “Inducible control of gene expression with destabilized Cre”. In: *Nature Methods* 10.11, pp. 1085–1091. ISSN: 15487091. DOI: [10.1038/nmeth.2640](https://doi.org/10.1038/nmeth.2640).
- Sauer, Brian and Nancy Henderson (1988). “Site-specific DNA recombination in mammalian cells by the Cre recombinase of bacteriophage P1”. In: *Proceedings of the National Academy of Sciences USA* 85.July, pp. 5166–5170.

- Scanziani, Massimo and Michael Häusser (2009). "Electrophysiology in the age of light." In: *Nature* 461.7266, pp. 930–939. ISSN: 1476-4687. DOI: [10.1038/nature08540](https://doi.org/10.1038/nature08540).
- Schnepel, Philipp et al. (2015). "Physiology and impact of horizontal connections in rat neocortex". In: *Cerebral Cortex* 25.10, pp. 3818–3835. ISSN: 14602199. DOI: [10.1093/cercor/bhu265](https://doi.org/10.1093/cercor/bhu265).
- Schuck, Renaud et al. (2018). "Multiphoton minimal inertia scanning for fast acquisition of neural activity signals." In: *Journal of neural engineering* 15.2, p. 025003. ISSN: 1741-2552. DOI: [10.1088/1741-2552/aa99e2](https://doi.org/10.1088/1741-2552/aa99e2).
- Schultz, Simon R. et al. (2017). "Advances in Two-Photon Scanning and Scanless Microscopy Technologies for Functional Neural Circuit Imaging". In: *Proceedings of the IEEE* 105.1, pp. 139–157. ISSN: 00189219. DOI: [10.1109/JPROC.2016.2577380](https://doi.org/10.1109/JPROC.2016.2577380).
- Sepeshri Rad, Masoud et al. (2017). "Voltage and Calcium Imaging of Brain Activity". In: *Biophysical Journal*, pp. 1–8. ISSN: 00063495. DOI: [10.1016/j.bpj.2017.09.040](https://doi.org/10.1016/j.bpj.2017.09.040).
- Shao, Yonghong et al. (2012). "Addressable multiregional and multifocal multiphoton microscopy based on a spatial light modulator." In: *Journal of biomedical optics* 17.3, p. 030505. ISSN: 1560-2281. DOI: [10.1117/1.JBO.17.3.030505](https://doi.org/10.1117/1.JBO.17.3.030505).
- Shemesh, Or A. et al. (2017). "Temporally precise single-cell-resolution optogenetics". In: *Nature Neuroscience* 20.12, pp. 1796–1806. ISSN: 15461726. DOI: [10.1038/s41593-017-0018-8](https://doi.org/10.1038/s41593-017-0018-8).
- Shepp, L.A and Y Vardi (1978). "Maximum likelihood reconstruction emission tomography". In: *MI.2*.
- Sheppard, C J R and T Wilson (1982). "The Image of a Single Point in Microscopes of Large Numerical Aperture". In: *Proceedings of the Royal Society A: Mathematical, Physical and Engineering Sciences* 379.1776, pp. 145–158. ISSN: 1364-5021. DOI: [10.1098/rspa.1982.0010](https://doi.org/10.1098/rspa.1982.0010).
- Sheppard, C. J.R. and P. Török (1997). "An electromagnetic theory of imaging in fluorescence microscopy, and imaging in polarization fluorescence microscopy". In: *Bioimaging* 5.4, pp. 205–218. ISSN: 09669051. DOI: [10.1002/1361-6374\(199712\)5:4<205::AID-BI04>3.3.CO;2-V](https://doi.org/10.1002/1361-6374(199712)5:4<205::AID-BI04>3.3.CO;2-V).
- Sheppard, Colin J R (2009). "Confocal microscopy". In: *Imaging & Microscopy*, p. 1.
- Shimomura, O, F H Johnson, and Y Saiga (1962). "Extraction, purification and properties of aequorin, a bioluminescent protein from the luminous hydromedusa, Aequorea." In: *Journal of cellular and comparative physiology* 59.3, pp. 223–39. ISSN: 0095-9898. DOI: [10.1002/jcp.1030590302](https://doi.org/10.1002/jcp.1030590302).

- Siegel, Micah S. and Ehud Y. Isacoff (1997). "A genetically encoded optical probe of membrane voltage". In: *Neuron* 19.4, pp. 735–741. ISSN: 08966273. DOI: [10.1016/S0896-6273\(00\)80955-1](https://doi.org/10.1016/S0896-6273(00)80955-1).
- Sjöström, Per Jesper and Michael Häusser (2006). "A Cooperative Switch Determines the Sign of Synaptic Plasticity in Distal Dendrites of Neocortical Pyramidal Neurons". In: *Neuron* 51.2, pp. 227–238. ISSN: 08966273. DOI: [10.1016/j.neuron.2006.06.017](https://doi.org/10.1016/j.neuron.2006.06.017).
- Skocek, Oliver et al. (2018). "High-speed volumetric imaging of neuronal activity in freely moving rodents". In: *Nature Methods* 15.6, pp. 429–432. ISSN: 15487105. DOI: [10.1038/s41592-018-0008-0](https://doi.org/10.1038/s41592-018-0008-0).
- Song, Chenchen et al. (2017). "Transgenic Strategies for Sparse but Strong Expression of Genetically Encoded Voltage and Calcium Indicators". In: *International Journal of Molecular Sciences* 18.7, p. 1461. ISSN: 1422-0067. DOI: [10.3390/ijms18071461](https://doi.org/10.3390/ijms18071461).
- Song, Chenchen et al. (2018). "Cortical signatures of wakeful somatosensory processing." In: *Scientific reports* 8.1, p. 11977. ISSN: 2045-2322. DOI: [10.1038/s41598-018-30422-9](https://doi.org/10.1038/s41598-018-30422-9).
- Song, Sen et al. (2005). "Highly nonrandom features of synaptic connectivity in local cortical circuits". In: *PLoS Biology* 3.3, pp. 0507–0519. ISSN: 15449173. DOI: [10.1371/journal.pbio.0030068](https://doi.org/10.1371/journal.pbio.0030068).
- Steinmetz, Nicholas A et al. (2017). "Aberrant Cortical Activity in Multiple GCaMP6-Expressing Transgenic Mouse Lines." In: *eNeuro* 4.5. ISSN: 2373-2822. DOI: [10.1523/ENEURO.0207-17.2017](https://doi.org/10.1523/ENEURO.0207-17.2017).
- Sutter, D H et al. (1999). "Semiconductor saturable-absorber mirror assisted Kerr-lens mode-locked Ti:sapphire laser producing pulses in the two-cycle regime." In: *Optics letters* 24.9, pp. 631–3. ISSN: 0146-9592.
- Tada, Mayumi et al. (2014). "A highly sensitive fluorescent indicator dye for calcium imaging of neural activity in vitro and in vivo." In: *The European journal of neuroscience* 39.11, pp. 1720–8. ISSN: 1460-9568. DOI: [10.1111/ejn.12476](https://doi.org/10.1111/ejn.12476).
- Tanese, Dimitrii et al. (2017). "Imaging membrane potential changes from dendritic spines using computer-generated holography". In: *Neurophotonics* 4.3, p. 031211. ISSN: 2329-423X. DOI: [10.1117/1.NPh.4.3.031211](https://doi.org/10.1117/1.NPh.4.3.031211).
- Tetzlaff, Christian et al. (2012). "Time scales of memory, learning, and plasticity". In: *Biological Cybernetics* 106.11-12, pp. 715–726. ISSN: 14320770. DOI: [10.1007/s00422-012-0529-z](https://doi.org/10.1007/s00422-012-0529-z).

- Thiébaud, Eric (2005). "Introduction to image reconstruction and inverse problems". In: *NATO Science Series II., Mathematics, Physics and Chemistry*. Ed. by R; Foy and F-C Foy. Springer, p. 397.
- Ting, Jonathan T et al. (2014). "Acute brain slice methods for adult and aging animals: application of targeted patch clamp analysis and optogenetics." In: *Methods in molecular biology (Clifton, N.J.)* 1183, pp. 221–42. ISSN: 1940-6029. DOI: [10.1007/978-1-4939-1096-0\\_{\\\_}14](https://doi.org/10.1007/978-1-4939-1096-0_{\_}14).
- Truong, Thai V et al. (2011). "Deep and fast live imaging with two-photon scanned light-sheet microscopy." In: *Nature methods* 8.9, pp. 757–60. ISSN: 1548-7105. DOI: [10.1038/nmeth.1652](https://doi.org/10.1038/nmeth.1652).
- Tsien, Roger Y (1980). "New Calcium Indicators and Buffers with High Selectivity against Magnesium and Protons: Design, Synthesis, and Properties of Prototype Structures". In: *Biochemistry* 19, pp. 2396–2404.
- Ugolini, Gabriella (2010). "Advances in viral transneuronal tracing". In: *Journal of Neuroscience Methods* 194.1, pp. 2–20. ISSN: 01650270. DOI: [10.1016/j.jneumeth.2009.12.001](https://doi.org/10.1016/j.jneumeth.2009.12.001).
- Walt, Stefan van der et al. (2014). "scikit-image: image processing in Python." In: *PeerJ* 2, e453. ISSN: 2167-8359. DOI: [10.7717/peerj.453](https://doi.org/10.7717/peerj.453).
- Wang, Xinjun et al. (2013). "Distribution of CaMKII $\alpha$  expression in the brain in vivo, studied by CaMKII $\alpha$ -GFP mice." In: *Brain research* 1518, pp. 9–25. ISSN: 1872-6240. DOI: [10.1016/j.brainres.2013.04.042](https://doi.org/10.1016/j.brainres.2013.04.042).
- Watson, Brendon O, Volodymyr Nikolenko, and Rafael Yuste (2009). "Two-photon imaging with diffractive optical elements." In: *Frontiers in neural circuits* 3, July, p. 6. ISSN: 1662-5110. DOI: [10.3389/neuro.04.006.2009](https://doi.org/10.3389/neuro.04.006.2009).
- Weishaupt, Nina (2016). "Cortical Plasticity in Response to Injury and Disease". In: *The Cerebral Cortex in Neurodegenerative and Neuropsychiatric Disorders: Experimental Approaches to Clinical Issues*. Academic Press, pp. 37–56. ISBN: 9780128019429. DOI: [10.1016/B978-0-12-801942-9.00002-1](https://doi.org/10.1016/B978-0-12-801942-9.00002-1).
- White, Richard L. (1994). "Image restoration using the damped Richardson-Lucy method". In: *The Restoration of HST Images and Spectra II*. Ed. by David L. Crawford and Eric R. Craine, pp. 1342–1348. DOI: [10.1117/12.176819](https://doi.org/10.1117/12.176819).
- Xu, Yongxian, Peng Zou, and Adam E. Cohen (2017). "Voltage imaging with genetically encoded indicators". In: *Current Opinion in Chemical Biology* 39, pp. 1–10. ISSN: 18790402. DOI: [10.1016/j.cbpa.2017.04.005](https://doi.org/10.1016/j.cbpa.2017.04.005).



- Yang, Samuel J. et al. (2015). "Extended field-of-view and increased-signal 3D holographic illumination with time-division multiplexing." In: *Optics express* 23.25, pp. 32573–81. ISSN: 1094-4087. DOI: [10.1364/OE.23.032573](https://doi.org/10.1364/OE.23.032573).
- Yang, Sunggu et al. (2011). "Three-dimensional holographic photostimulation of the dendritic arbor." In: *Journal of neural engineering* 8.4, p. 046002. ISSN: 1741-2560. DOI: [10.1088/1741-2560/8/4/046002](https://doi.org/10.1088/1741-2560/8/4/046002).
- Yang, Weijian and Rafael Yuste (2017). "In vivo imaging of neural activity". In: *Nature methods* 14.4, pp. 349–359. ISSN: 15487105. DOI: [10.1038/nmeth.4230](https://doi.org/10.1038/nmeth.4230).
- Yaroslavsky, A N et al. (2002). "Optical properties of selected native and coagulated human brain tissues in vitro in the visible and near infrared spectral range." In: *Physics in medicine and biology* 47.12, pp. 2059–73. ISSN: 0031-9155.
- Yen, Jui Cheng, F J Chang, and Shyang Chang (1995). "A new criterion for automatic multi-level thresholding." In: *IEEE transactions on image processing : a publication of the IEEE Signal Processing Society* 4.3, pp. 370–8. ISSN: 1057-7149. DOI: [10.1109/83.366472](https://doi.org/10.1109/83.366472).
- Yi, Bumjun et al. (2018). "A dimeric fluorescent protein yields a bright, red-shifted GEVI capable of population signals in brain slice". In: *Scientific Reports* 8.1, p. 15199. ISSN: 2045-2322. DOI: [10.1038/s41598-018-33297-y](https://doi.org/10.1038/s41598-018-33297-y).
- Yuan, Qi et al. (2007). "Climbing fiber-triggered metabotropic slow potentials enhance dendritic calcium transients and simple spike firing in cerebellar Purkinje cells." In: *Molecular and cellular neurosciences* 35.4, pp. 596–603. ISSN: 1044-7431. DOI: [10.1016/j.mcn.2007.05.004](https://doi.org/10.1016/j.mcn.2007.05.004).
- Yuste, Rafael (2015). "From the neuron doctrine to neural networks". In: *Nature Reviews Neuroscience* 16.8, pp. 487–497. ISSN: 1471-003X. DOI: [10.1038/nrn3962](https://doi.org/10.1038/nrn3962).
- Zeng, Hongkui and Linda Madisen (2012). "Mouse transgenic approaches in optogenetics". In: *Progress in Brain Research* 196, pp. 193–213. DOI: [10.1016/B978-0-444-59426-6.00010-0](https://doi.org/10.1016/B978-0-444-59426-6.00010-0). **Mouse.**
- Zucker, Robert S (2006). "Synaptic Plasticity: Short Term". In: *Encyclopedia of Life Sciences*. Chichester: John Wiley & Sons, Ltd. DOI: [10.1038/npg.els.0000067](https://doi.org/10.1038/npg.els.0000067).
- Žurauskas, Mantas et al. (2017). "Rapid adaptive remote focusing microscope for sensing of volumetric neural activity". In: *Biomedical Optics Express* 8.10, p. 4369. ISSN: 2156-7085. DOI: [10.1364/boe.8.004369](https://doi.org/10.1364/boe.8.004369).

## Appendix A

# Copyright permissions

**RE: Reuse of figure from Broxton et al (2013) in thesis**

pubscopyright [REDACTED]

Thu 07/03/2019 21:29

To: Quicke, Peter E H [REDACTED]; pubscopyright [REDACTED]

Dear Peter Quicke,

Thank you for contacting The Optical Society.

For the use of figures 2 b, 2 c and 3a from Michael Broxton, Logan Grosenick, Samuel Yang, Noy Cohen, Aaron Andalman, Karl Deisseroth, and Marc Levoy, "Wave optics theory and 3-D deconvolution for the light field microscope," Opt. Express 21, 25418-25439 (2013):

OSA considers your requested use of its copyrighted material to be Fair Use under United States Copyright Law. It is requested that a complete citation of the original material be included in any publication.

While your publisher should be able to provide additional guidance, OSA prefers the below citation formats:

For citations in figure captions:

[Reprinted/Adapted] with permission from ref [x], [Publisher]. (with full citation in reference list)

For images without captions:

Journal Vol. #, first page (year published) An example: Opt. Express 21, 25418 (2013)

Please let me know if you have any questions.

Kind Regards,

Rebecca Robinson

Rebecca Robinson  
March 7, 2019  
Authorized Agent, The Optical Society

**The Optical Society (OSA)**

2010 Massachusetts Ave., NW  
Washington, DC 20036 USA  
[www.osa.org]www.osa.org

**Reflecting a Century of Innovation**

---

**From:** Quicke, Peter E H [REDACTED]  
**Sent:** Monday, February 25, 2019 12:43 PM  
**To:** pubscopyright [REDACTED]  
**Subject:** Reuse of figure from Broxton et al (2013) in thesis

Dear Sir/Madam,

I would like to reuse Figure panels 2b), 2c) and 3a) from 'Wave optics theory and 3D deconvolution for the light field microscope' (full citation below) in my PhD thesis. This will be published on an online institutional repository.

Could you please let me know how I can get permission for this?

Thanks very much,

Peter Quicke

Broxton, M., Grosenick, L., Yang, S., Cohen, N., Andalman, A., Deisseroth, K., & Levoy, M. (2013). Wave optics theory and 3-D deconvolution for the light field microscope. *Optics Express*, 21(21), 25418. <http://doi.org/10.1364/OE.21.025418>.

**Re: Case # 00384056 Permission for re-use of figure in thesis**

Permissions [REDACTED]

Thu 07/02/2019 12:07

To: Quicke, Peter E H [REDACTED]

Dear Peter Quicke,

Thank you for your request to reproduce IOP Publishing material *in your thesis***Regarding:****Figure 3 - <https://iopscience.iop.org/article/10.1088/0031-9155/47/12/305>**

We are happy to grant permission for the use you request on the terms set out below.

**Conditions**Non-exclusive, non-transferrable, revocable, worldwide, permission to use the material in print and electronic form will be granted **subject to the following conditions:**

- Permission will be cancelled without notice if you fail to fulfil any of the conditions of this letter.
- You will make reasonable efforts to contact the author(s) to seek consent for your intended use. Contacting one author acting expressly as authorised agent for their co-authors is acceptable.
- You will reproduce the following prominently alongside the material:
  - the source of the material, including author, article title, title of journal, volume number, issue number (if relevant), page range (or first page if this is the only information available) and date of first publication. This information can be contained in a footnote or reference note; or
  - a link back to the article (via DOI); and
  - ***if practical and IN ALL CASES for works published under any of the Creative Commons licences the words “©Institute of Physics and Engineering in Medicine. Reproduced by permission of IOP Publishing. All rights reserved”***
- The material will not, without the express permission of the author(s), be used in any way which, in the opinion of IOP Publishing, could distort or alter the author(s)' original intention(s) and meaning, be prejudicial to the honour or reputation of the author(s) and/or imply endorsement by the author(s) and/or IOP Publishing and/or Institute of Physics and Engineering in Medicine
- Payment of £0 is received in full by IOP Publishing prior to use.

This permission does not apply to any material/figure which is credited to another source in our publication or has been obtained from a third party. Express permission for such materials/figures must be obtained from the copyright owner.

**Special Conditions – For STM Signatories ONLY (as agreed as part of the STM Guidelines)**

Any permissions granted for a particular edition will apply also to subsequent editions and for editions in other languages, provided such editions are for the work as a whole in situ and does not involve the separate exploitation of the permitted illustrations or excerpts.

I should be grateful if you would acknowledge receipt of this email.

Kind regards,

Christina

**Copyright & Permissions Team**Gemma Alaway – Senior Rights & Permissions Adviser  
Christina Colwell - Rights & Permissions Assistant

## Contact Details

E-mail: [REDACTED]

For further information about copyright and how to request permission:

<https://publishingsupport.iopscience.iop.org/copyright-journals/>See also: <https://publishingsupport.iopscience.iop.org/>

Please see our Author Rights Policy <https://publishingsupport.iopscience.iop.org/author-rights-policies/>

**Please note:** We do not provide signed permission forms as a separate attachment. Please print this email and provide it to your publisher as proof of permission.

**Please note:** Any statements made by IOP Publishing to the effect that authors do not need to get permission to use any content where IOP Publishing is not the publisher is not intended to constitute any sort of legal advice. Authors must make their own decisions as to the suitability of the content they are using and whether they require permission for it to be published within their article.

---

----- Original Message -----

From: [REDACTED]  
Sent: 05/02/2019  
To: [REDACTED]  
Subject: Permission for re-use of figure in thesis

Dear Sir/Madam,

I would like to reuse Figure 3a) from Yaroslavsky, A. N., et al. "Optical properties of selected native and coagulated human brain tissues in vitro in the visible and near infrared spectral range." Physics in Medicine & Biology 47.12 (2002): 2059 In my PhD thesis. I was unable to obtain this permission on copyright.com. Could you please let me know how I can go about getting permission for this re-use?

Thanks very much,

Peter Quicke  
ref:\_00D30omsI\_5000c1iDprP:ref

This email (and attachments) are confidential and intended for the addressee(s) only. If you are not the intended recipient please immediately notify the sender, permanently and securely delete any copies and do not take action with it or in reliance on it. Any views expressed are the author's and do not represent those of IOPP, except where specifically stated. IOPP takes reasonable precautions to protect against viruses but accepts no responsibility for loss or damage arising from virus infection. For the protection of IOPP's systems and staff emails are scanned automatically.

IOP Publishing Limited. Company Registration No. 00467514 (England & Wales).

Registered Office: Temple Circus, Temple Way, Bristol BS1 6HG

Your privacy is important to us. For information about how IOPP uses your personal data, please see our Privacy Policy <https://emea01.safelinks.protection.outlook.com/?url=http%3A%2F%2Fioppublishing.org%2Fprivacy-cookies-policy%2F&data=02%7C01%7Cpermissions%40iop.org%7Cf656215fa511432dd32a08d68c231f6>

<https://emea01.safelinks.protection.outlook.com/?url=http%3A%2F%2Fioppublishing.org%2Fprivacy-cookies-policy%2F&data=02%7C01%7Cpermissions%40iop.org%7Cf656215fa511432dd32a08d68c231f6>

[7%7Cf9ee42e6bad04e639115f704f9ccceed%7C0%7C0%7C636850479806829608&amp;sdata=wynL3cR4IR9GQt4%2FdqPIixohGalStSs2OXIoNCxby0M%3D&amp;reserved=0](https://outlook.office365.com/mail/id/AAQkAGU4ODg0MjJiLTUwNzMtNDgwMy05NWFILTA1ZTI3ZDI5YjdkYgAQAosCqquYspLrYQbE5BCyqM%...)

**RE: Permission for re-use of figure 3 in Yaroslavsky (2002) Physics in medicine Biology****Quicke, Peter E H**

Fri 08/02/2019 10:03

To: 'Yaroslavsky, Anna N.' [REDACTED]

Dear Anna,

Thanks very much!

Best wishes,

Peter

---

**From:** Yaroslavsky, Anna N. [REDACTED]**Sent:** 07 February 2019 22:26**To:** Quicke, Peter E H [REDACTED]**Subject:** Re: Permission for re-use of figure 3 in Yaroslavsky (2002) Physics in medicine Biology

Dear Peter,

I have no problem with you re-using the figure with appropriate citation.

Best,

Anna.

Anna N. Yaroslavsky, Ph.D.

Associate Professor

Department of Physics and Applied Physics

University of Massachusetts, Lowell

[REDACTED]

Massachusetts General Hospital

Wellman Center for Photomedicine

---

**From:** Quicke, Peter E H [REDACTED]**Sent:** Thursday, February 7, 2019 7:14 AM**To:** Yaroslavsky, Anna N.**Subject:** Permission for re-use of figure 3 in Yaroslavsky (2002) Physics in medicine Biology**External Email - Use Caution**

Dear Professor Yaroslavsky,

I am writing to seek permission to reuse Figure 3) from Yaroslavsky, A. N., et al. "Optical properties of selected native and coagulated human brain tissues in vitro in the visible and near infrared spectral range." *Physics in Medicine & Biology* 47.12 (2002): 2059 In my PhD thesis.

I have obtained permission from IOP publishing and a condition of their granting re-use permissions is that I contact you as corresponding author for your consent.

I would greatly appreciate if you would let me know that you were happy for me to re-use this figure.



Thanks very much,

Peter

The information in this e-mail is intended only for the person to whom it is addressed. If you believe this e-mail was sent to you in error and the e-mail contains patient information, please contact the Partners Compliance HelpLine at <http://www.partners.org/complianceline> . If the e-mail was sent to you in error but does not contain patient information, please contact the sender and properly dispose of the e-mail.

**SPRINGER NATURE LICENSE  
TERMS AND CONDITIONS**

Mar 12, 2019

This Agreement between Peter Quicke ("You") and Springer Nature ("Springer Nature") consists of your license details and the terms and conditions provided by Springer Nature and Copyright Clearance Center.

License Number	4353571405776
License date	May 21, 2018
Licensed Content Publisher	Springer Nature
Licensed Content Publication	Nature Reviews Neuroscience
Licensed Content Title	Genetically encoded optical indicators for the analysis of neuronal circuits
Licensed Content Author	Thomas Knöpfel
Licensed Content Date	Aug 30, 2012
Licensed Content Volume	13
Licensed Content Issue	10
Type of Use	Thesis/Dissertation
Requestor type	academic/university or research institute
Format	print and electronic
Portion	figures/tables/illustrations
Number of figures/tables/illustrations	1
High-res required	no
Will you be translating?	no
Circulation/distribution	<501
Author of this Springer Nature content	no
Title	Optogenetic investigation of neuronal connectivity
Instructor name	Simon R. Schultz
Institution name	Imperial College London
Expected presentation date	Mar 2019
Portions	Left hand side of Fig. 1Ba) showing the effect of membrane depolarisation on FRET efficiency in a FRET based VSFP
Requestor Location	Peter Quicke Royal School of Mines Imperial College South Kensington Campus London, SW7 2AZ United Kingdom Attn: Peter Quicke
Billing Type	Invoice
Billing Address	Peter Quicke Royal School of Mines Imperial College South Kensington Campus London, United Kingdom SW7 2AZ Attn: Peter Quicke
Total	0.00 USD
Terms and Conditions	

**Springer Nature Terms and Conditions for RightsLink Permissions**

**Springer Customer Service Centre GmbH (the Licensor)** hereby grants you a non-exclusive, world-wide licence to reproduce the material and for the purpose and requirements specified in the attached copy of your order form, and for no other use, subject to the conditions below:

1. The Licensor warrants that it has, to the best of its knowledge, the rights to license reuse of this material. However, you should ensure that the material you are requesting is original to the Licensor and does not carry the copyright of another entity (as credited in the published version).

If the credit line on any part of the material you have requested indicates that it was reprinted or adapted with permission from another source, then you should also seek permission from that source to reuse the material.

2. Where **print only** permission has been granted for a fee, separate permission must be obtained for any additional electronic re-use.
3. Permission granted **free of charge** for material in print is also usually granted for any electronic version of that work, provided that the material is incidental to your work as a whole and that the electronic version is essentially equivalent to, or substitutes for, the print version.
4. A licence for 'post on a website' is valid for 12 months from the licence date. This licence does not cover use of full text articles on websites.
5. Where '**reuse in a dissertation/thesis**' has been selected the following terms apply: Print rights for up to 100 copies, electronic rights for use only on a personal website or institutional repository as defined by the Sherpa guideline ([www.sherpa.ac.uk/romeo/](http://www.sherpa.ac.uk/romeo/)).
6. Permission granted for books and journals is granted for the lifetime of the first edition and does not apply to second and subsequent editions (except where the first edition permission was granted free of charge or for signatories to the STM Permissions Guidelines <http://www.stm-assoc.org/copyright-legal-affairs/permissions/permissions-guidelines/>), and does not apply for editions in other languages unless additional translation rights have been granted separately in the licence.
7. Rights for additional components such as custom editions and derivatives require additional permission and may be subject to an additional fee. Please apply to [Journalpermissions@springernature.com](mailto:Journalpermissions@springernature.com)/[bookpermissions@springernature.com](mailto:bookpermissions@springernature.com) for these rights.
8. The Licensor's permission must be acknowledged next to the licensed material in print. In electronic form, this acknowledgement must be visible at the same time as the figures/tables/illustrations or abstract, and must be hyperlinked to the journal/book's homepage. Our required acknowledgement format is in the Appendix below.
9. Use of the material for incidental promotional use, minor editing privileges (this does not include cropping, adapting, omitting material or any other changes that affect the meaning, intention or moral rights of the author) and copies for the disabled are permitted under this licence.
10. Minor adaptations of single figures (changes of format, colour and style) do not require the Licensor's approval. However, the adaptation should be credited as shown in Appendix below.

### **Appendix — Acknowledgements:**

#### **For Journal Content:**

Reprinted by permission from [**the Licensor**]: [**Journal Publisher** (e.g. Nature/Springer/Palgrave)] [**JOURNAL NAME**] [**REFERENCE CITATION** (Article name, Author(s) Name), [**COPYRIGHT**] (year of publication)]

#### **For Advance Online Publication papers:**

Reprinted by permission from [**the Licensor**]: [**Journal Publisher** (e.g. Nature/Springer/Palgrave)] [**JOURNAL NAME**] [**REFERENCE CITATION** (Article name, Author(s) Name), [**COPYRIGHT**] (year of publication), advance online publication, day month year (doi: 10.1038/sj.[**JOURNAL ACRONYM**].)]

#### **For Adaptations/Translations:**

Adapted/Translated by permission from [**the Licensor**]: [**Journal Publisher** (e.g. Nature/Springer/Palgrave)] [**JOURNAL NAME**] [**REFERENCE CITATION** (Article name, Author(s) Name), [**COPYRIGHT**] (year of publication)]

#### **Note: For any republication from the British Journal of Cancer, the following credit line style applies:**

Reprinted/adapted/translated by permission from [**the Licensor**]: on behalf of Cancer Research UK: : [**Journal Publisher** (e.g. Nature/Springer/Palgrave)] [**JOURNAL NAME**] [**REFERENCE CITATION** (Article name, Author(s) Name), [**COPYRIGHT**] (year of publication)]

#### **For Advance Online Publication papers:**

Reprinted by permission from The [**the Licensor**]: on behalf of Cancer Research UK: [**Journal Publisher** (e.g. Nature/Springer/Palgrave)] [**JOURNAL NAME**] [**REFERENCE CITATION** (Article name, Author(s) Name), [**COPYRIGHT**] (year of publication), advance online publication, day month year (doi: 10.1038/sj.[**JOURNAL ACRONYM**].)]

#### **For Book content:**

Reprinted/adapted by permission from [**the Licensor**]: [**Book Publisher** (e.g. Palgrave Macmillan, Springer etc)] [**Book Title**] by [**Book author(s)**] [**COPYRIGHT**] (year of publication)]

### **Other Conditions:**

Version 1.0

**Questions? [customercare@copyright.com](mailto:customercare@copyright.com) or +1-855-239-3415 (toll free in the US) or +1-978-646-2777.**

**ELSEVIER LICENSE  
TERMS AND CONDITIONS**

Feb 25, 2019

This Agreement between Peter Quicke ("You") and Elsevier ("Elsevier") consists of your license details and the terms and conditions provided by Elsevier and Copyright Clearance Center.

License Number	4517161400547
License date	Jan 27, 2019
Licensed Content Publisher	Elsevier
Licensed Content Publication	Current Opinion in Chemical Biology
Licensed Content Title	Voltage imaging with genetically encoded indicators
Licensed Content Author	Yongxian Xu,Peng Zou,Adam E Cohen
Licensed Content Date	Aug 1, 2017
Licensed Content Volume	39
Licensed Content Issue	n/a
Licensed Content Pages	10
Start Page	1
End Page	10
Type of Use	reuse in a thesis/dissertation
Portion	figures/tables/illustrations
Number of figures/tables/illustrations	1
Format	both print and electronic
Are you the author of this Elsevier article?	No
Will you be translating?	No
Original figure numbers	Figure 1 entire figure
Title of your thesis/dissertation	Optogenetic investigation of neuronal connectivity
Publisher of new work	Imperial College London
Author of new work	Simon R. Schultz
Expected completion date	Mar 2019
Estimated size (number of pages)	1
Requestor Location	Peter Quicke Royal School of Mines Imperial College South Kensington Campus London, SW7 2AZ United Kingdom Attn: Peter Quicke
Publisher Tax ID	GB 494 6272 12
Total	0.00 USD
Terms and Conditions	

## INTRODUCTION

1. The publisher for this copyrighted material is Elsevier. By clicking "accept" in connection with completing this licensing transaction, you agree that the following terms and conditions apply to this transaction (along with the Billing and Payment terms and conditions established by Copyright Clearance Center, Inc. ("CCC"), at the time that you opened your Rightslink account and that are available at any time at <http://myaccount.copyright.com>).

## GENERAL TERMS

2. Elsevier hereby grants you permission to reproduce the aforementioned material subject to the terms and conditions indicated.

3. Acknowledgement: If any part of the material to be used (for example, figures) has appeared in our publication with credit or acknowledgement to another source, permission must also be sought from that source. If such permission is not obtained then that material may not be included in your publication/copies. Suitable acknowledgement to the source must be made, either as a footnote or in a reference list at the end of your publication, as follows:

"Reprinted from Publication title, Vol /edition number, Author(s), Title of article / title of chapter, Pages No., Copyright (Year), with permission from Elsevier [OR APPLICABLE SOCIETY COPYRIGHT OWNER]."  
Also Lancet special credit - "Reprinted from The Lancet, Vol. number, Author(s), Title of article, Pages No., Copyright (Year), with permission from Elsevier."

4. Reproduction of this material is confined to the purpose and/or media for which permission is hereby given.

5. Altering/Modifying Material: Not Permitted. However figures and illustrations may be altered/adapted minimally to serve your work. Any other abbreviations, additions, deletions and/or any other alterations shall be made only with prior written authorization of Elsevier Ltd. (Please contact Elsevier at [permissions@elsevier.com](mailto:permissions@elsevier.com)). No modifications can be made to any Lancet figures/tables and they must be reproduced in full.

6. If the permission fee for the requested use of our material is waived in this instance, please be advised that your future requests for Elsevier materials may attract a fee.

7. Reservation of Rights: Publisher reserves all rights not specifically granted in the combination of (i) the license details provided by you and accepted in the course of this licensing transaction, (ii) these terms and conditions and (iii) CCC's Billing and Payment terms and conditions.

8. License Contingent Upon Payment: While you may exercise the rights licensed immediately upon issuance of the license at the end of the licensing process for the transaction, provided that you have disclosed complete and accurate details of your proposed use, no license is finally effective unless and until full payment is received from you (either by publisher or by CCC) as provided in CCC's Billing and Payment terms

and conditions. If full payment is not received on a timely basis, then any license preliminarily granted shall be deemed automatically revoked and shall be void as if never granted. Further, in the event that you breach any of these terms and conditions or any of CCC's Billing and Payment terms and conditions, the license is automatically revoked and shall be void as if never granted. Use of materials as described in a revoked license, as well as any use of the materials beyond the scope of an unrevoked license, may constitute copyright infringement and publisher reserves the right to take any and all action to protect its copyright in the materials.

9. Warranties: Publisher makes no representations or warranties with respect to the licensed material.

10. Indemnity: You hereby indemnify and agree to hold harmless publisher and CCC, and their respective officers, directors, employees and agents, from and against any and all claims arising out of your use of the licensed material other than as specifically authorized pursuant to this license.

11. No Transfer of License: This license is personal to you and may not be sublicensed, assigned, or transferred by you to any other person without publisher's written permission.

12. No Amendment Except in Writing: This license may not be amended except in a writing signed by both parties (or, in the case of publisher, by CCC on publisher's behalf).

13. Objection to Contrary Terms: Publisher hereby objects to any terms contained in any purchase order, acknowledgment, check endorsement or other writing prepared by you, which terms are inconsistent with these terms and conditions or CCC's Billing and Payment terms and conditions. These terms and conditions, together with CCC's Billing and Payment terms and conditions (which are incorporated herein), comprise the entire agreement between you and publisher (and CCC) concerning this licensing transaction. In the event of any conflict between your obligations established by these terms and conditions and those established by CCC's Billing and Payment terms and conditions, these terms and conditions shall control.

14. Revocation: Elsevier or Copyright Clearance Center may deny the permissions described in this License at their sole discretion, for any reason or no reason, with a full refund payable to you. Notice of such denial will be made using the contact information provided by you. Failure to receive such notice will not alter or invalidate the denial. In no event will Elsevier or Copyright Clearance Center be responsible or liable for any costs, expenses or damage incurred by you as a result of a denial of your permission request, other than a refund of the amount(s) paid by you to Elsevier and/or Copyright Clearance Center for denied permissions.

### **LIMITED LICENSE**

The following terms and conditions apply only to specific license types:

**15. Translation:** This permission is granted for non-exclusive world **English** rights only unless your license was granted for translation rights. If you licensed translation rights you may only translate this content into the languages you requested. A professional translator must perform all translations and reproduce the content word for word preserving the integrity of the article.

**16. Posting licensed content on any Website:** The following terms and conditions apply as follows: Licensing material from an Elsevier journal: All content posted to the web site must maintain the copyright information line on the bottom of each image; A hyper-text must be included to the Homepage of the journal from which you are licensing at <http://www.sciencedirect.com/science/journal/xxxxx> or the Elsevier homepage for books at <http://www.elsevier.com>; Central Storage: This license does not include permission for a scanned version of the material to be stored in a central repository such as that provided by Heron/XanEdu.

Licensing material from an Elsevier book: A hyper-text link must be included to the Elsevier homepage at <http://www.elsevier.com> . All content posted to the web site must maintain the copyright information line on the bottom of each image.

**Posting licensed content on Electronic reserve:** In addition to the above the following clauses are applicable: The web site must be password-protected and made available only to bona fide students registered on a relevant course. This permission is granted for 1 year only. You may obtain a new license for future website posting.

**17. For journal authors:** the following clauses are applicable in addition to the above:

**Preprints:**

A preprint is an author's own write-up of research results and analysis, it has not been peer-reviewed, nor has it had any other value added to it by a publisher (such as formatting, copyright, technical enhancement etc.). Authors can share their preprints anywhere at any time. Preprints should not be added to or enhanced in any way in order to appear more like, or to substitute for, the final versions of articles however authors can update their preprints on arXiv or RePEc with their Accepted Author Manuscript (see below).

If accepted for publication, we encourage authors to link from the preprint to their formal publication via its DOI. Millions of researchers have access to the formal publications on ScienceDirect, and so links will help users to find, access, cite and use the best available version. Please note that Cell Press, The Lancet and some society-owned have different preprint policies. Information on these policies is available on the journal homepage.

**Accepted Author Manuscripts:** An accepted author manuscript is the manuscript of an article that has been accepted for publication and which typically includes author-incorporated changes suggested during submission, peer review and editor-author communications.

Authors can share their accepted author manuscript:

- immediately
  - via their non-commercial person homepage or blog
  - by updating a preprint in arXiv or RePEc with the accepted manuscript
  - via their research institute or institutional repository for internal institutional uses or as part of an invitation-only research collaboration work-group
  - directly by providing copies to their students or to research collaborators for their personal use
  - for private scholarly sharing as part of an invitation-only work group on commercial sites with which Elsevier has an agreement
- After the embargo period
  - via non-commercial hosting platforms such as their institutional repository
  - via commercial sites with which Elsevier has an agreement

In all cases accepted manuscripts should:

- link to the formal publication via its DOI
- bear a CC-BY-NC-ND license - this is easy to do
- if aggregated with other manuscripts, for example in a repository or other site, be shared in alignment with our hosting policy not be added to or enhanced in any way to appear more like, or to substitute for, the published journal article.

**Published journal article (JPA):** A published journal article (PJA) is the definitive final record of published research that appears or will appear in the journal and embodies all value-adding publishing activities including peer review co-ordination, copy-editing, formatting, (if relevant) pagination and online enrichment.

Policies for sharing publishing journal articles differ for subscription and gold open access articles:

**Subscription Articles:** If you are an author, please share a link to your article rather than the full-text. Millions of researchers have access to the formal publications on ScienceDirect, and so links will help your users to find, access, cite, and use the best available version.

Theses and dissertations which contain embedded PJAs as part of the formal submission can be posted publicly by the awarding institution with DOI links back to the formal publications on ScienceDirect.



If you are affiliated with a library that subscribes to ScienceDirect you have additional private sharing rights for others' research accessed under that agreement. This includes use for classroom teaching and internal training at the institution (including use in course packs and courseware programs), and inclusion of the article for grant funding purposes.

**Gold Open Access Articles:** May be shared according to the author-selected end-user license and should contain a [CrossMark logo](#), the end user license, and a DOI link to the formal publication on ScienceDirect. Please refer to Elsevier's [posting policy](#) for further information.

18. **For book authors** the following clauses are applicable in addition to the above: Authors are permitted to place a brief summary of their work online only. You are not allowed to download and post the published electronic version of your chapter, nor may you scan the printed edition to create an electronic version. **Posting to a repository:** Authors are permitted to post a summary of their chapter only in their institution's repository.

19. **Thesis/Dissertation:** If your license is for use in a thesis/dissertation your thesis may be submitted to your institution in either print or electronic form. Should your thesis be published commercially, please reapply for permission. These requirements include permission for the Library and Archives of Canada to supply single copies, on demand, of the complete thesis and include permission for Proquest/UMI to supply single copies, on demand, of the complete thesis. Should your thesis be published commercially, please reapply for permission. Theses and dissertations which contain embedded PJAs as part of the formal submission can be posted publicly by the awarding institution with DOI links back to the formal publications on ScienceDirect.

### **Elsevier Open Access Terms and Conditions**

You can publish open access with Elsevier in hundreds of open access journals or in nearly 2000 established subscription journals that support open access publishing. Permitted third party re-use of these open access articles is defined by the author's choice of Creative Commons user license. See our [open access license policy](#) for more information.

#### **Terms & Conditions applicable to all Open Access articles published with Elsevier:**

Any reuse of the article must not represent the author as endorsing the adaptation of the article nor should the article be modified in such a way as to damage the author's honour or reputation. If any changes have been made, such changes must be clearly indicated.

The author(s) must be appropriately credited and we ask that you include the end user license and a DOI link to the formal publication on ScienceDirect.

If any part of the material to be used (for example, figures) has appeared in our publication with credit or acknowledgement to another source it is

the responsibility of the user to ensure their reuse complies with the terms and conditions determined by the rights holder.

### **Additional Terms & Conditions applicable to each Creative**

#### **Commons user license:**

**CC BY:** The CC-BY license allows users to copy, to create extracts, abstracts and new works from the Article, to alter and revise the Article and to make commercial use of the Article (including reuse and/or resale of the Article by commercial entities), provided the user gives appropriate credit (with a link to the formal publication through the relevant DOI), provides a link to the license, indicates if changes were made and the licensor is not represented as endorsing the use made of the work. The full details of the license are available at

<http://creativecommons.org/licenses/by/4.0>.

**CC BY NC SA:** The CC BY-NC-SA license allows users to copy, to create extracts, abstracts and new works from the Article, to alter and revise the Article, provided this is not done for commercial purposes, and that the user gives appropriate credit (with a link to the formal publication through the relevant DOI), provides a link to the license, indicates if changes were made and the licensor is not represented as endorsing the use made of the work. Further, any new works must be made available on the same conditions. The full details of the license are available at

<http://creativecommons.org/licenses/by-nc-sa/4.0>.

**CC BY NC ND:** The CC BY-NC-ND license allows users to copy and distribute the Article, provided this is not done for commercial purposes and further does not permit distribution of the Article if it is changed or edited in any way, and provided the user gives appropriate credit (with a link to the formal publication through the relevant DOI), provides a link to the license, and that the licensor is not represented as endorsing the use made of the work. The full details of the license are available at

<http://creativecommons.org/licenses/by-nc-nd/4.0>. Any commercial reuse of Open Access articles published with a CC BY NC SA or CC BY NC ND license requires permission from Elsevier and will be subject to a fee. Commercial reuse includes:

- Associating advertising with the full text of the Article
- Charging fees for document delivery or access
- Article aggregation
- Systematic distribution via e-mail lists or share buttons

Posting or linking by commercial companies for use by customers of those companies.

### **20. Other Conditions:**

v1.9

Questions? [customer care@copyright.com](mailto:customer care@copyright.com) or +1-855-239-3415 (toll free in the US) or +1-978-646-2777.

---

---